

**Developing Novel and Optimizing Available CNS Therapies: Preclinical Development of  
20-HETE Formation Inhibitors and Population Pharmacokinetics of Propofol in ICU  
patients**

by

**Chenxiao Tang**

Bachelor of Science, Capital Medical University, 2014

Master of Science, University of Pittsburgh, 2016

Submitted to the Graduate Faculty of the  
School of Pharmacy in partial fulfillment  
of the requirements for the degree of  
Doctor of Philosophy

University of Pittsburgh

2021

UNIVERSITY OF PITTSBURGH

SCHOOL OF PHARMACY

This dissertation was presented

by

**Chenxiao Tang**

It was defended on

March 19, 2021

and approved by

Samuel M. Poloyac, PharmD, PhD, Dean and James T Doluisio Regents Chair, College of  
Pharmacy, The University of Texas at Austin

Lee A. McDermott, PhD, MBA, Assistant Professor, School of Pharmacy

Mioara D. Manole, MD, Associate Professor, School of Medicine

Patrick M. Kochanek, MD, Professor, School of Medicine

Robert B. Gibbs, PhD, Professor, School of Pharmacy

Michael A. Tortorici, PhD, Executive Director, CSL Behring

Dissertation Director: Samuel M. Poloyac, PharmD, PhD, Dean and James T Doluisio Regents  
Chair, College of Pharmacy, The University of Texas at Austin

Copyright © by Chenxiao Tang

2021

# Developing Novel and Optimizing Available CNS Therapies: Preclinical Development of 20-HETE Formation Inhibitors and Population Pharmacokinetics of Propofol in ICU patients

Chenxiao Tang, PhD

University of Pittsburgh, 2021

20-hydroxyeicosatetraenoic acid (20-HETE) is a vasoconstrictive metabolite of arachidonic acid by cytochrome P450 (CYP) 4A11 and 4F2 in humans. Inhibition of 20-HETE formation produces neuroprotective effects in cardiac arrest and stroke preclinical models. Clinical evidence shows that high CSF 20-HETE level is associated with three-fold increased mortality and unfavorable outcomes in subarachnoid hemorrhage patients. These findings suggest that 20-HETE synthase inhibition is a potential therapeutic strategy for neuroprotection after brain injury. HET0016, a 20-HETE inhibitor, did not enter clinical development due to poor solubility and short half-life. Currently, a clinically relevant 20-HETE inhibitor is not available to be evaluated as a therapeutic intervention.

The primary goal of this dissertation is to develop novel 20-HETE formation inhibitors that have strong potency and favorable physicochemical, metabolic stability, selectivity, solubility, CYP inhibition, and blood-brain barrier (BBB) permeability. We developed analytical methods to facilitate metabolic stability, CYP inhibition evaluation, and quantify the novel compound in a pharmacokinetic study. After iterations of screening and *in vitro* evaluation for 143 novel compounds, **UPMP107** was identified as a preclinical candidate that had strong potency and advantage of highly metabolically stable, wide selectivity window, and good brain penetration *in vitro*. Intravenous administration of **107** to postnatal day 17 rats showed that it could penetrate

BBB and reduce brain 20-HETE levels. The 20-HETE inhibitory effect was maintained up to 9 hrs after IV administration at 20 mg/kg. **UPMP107** exhibited a biphasic plasma concentration-time profile after IV administration. It has a low clearance, an intermediate volume of distribution, and a relatively short half-life.

The secondary goal was to optimize marketed CNS therapy, propofol, to improve the neurological outcome. The pharmacokinetics of propofol in an ICU population was described using a population pharmacokinetic model. A two-compartment, zero-order infusion, first-order elimination model best described the profile. This model could be used to explore the relationship between propofol exposure and sedative response to optimize the therapy in the ICU population.

Collectively, the work identified a novel compound that inhibits 20-HETE formation and can be used in proof of concept animal studies. Propofol pharmacokinetics was characterized in the ICU population, and the model could potentially be used to explore an exposure-response relationship in the future.

## Table of Contents

Preface.....	xix
1.0 Introduction.....	1
1.1 Overview of CYP4 enzymes.....	2
1.2 Metabolism of arachidonic acid by CYP450.....	4
1.2.1 $\omega$ -hydroxylases and 20-HETE formation .....	5
1.2.2 Epoxygenases and EETs formation.....	10
1.3 Biological actions of 20-HETE .....	11
1.3.1 20-HETE and vascular tone .....	11
1.3.2 20-HETE and cerebral blood flow autoregulation.....	12
1.3.3 20-HETE and angiogenesis .....	13
1.4 Therapeutic areas for developing 20-HETE formation inhibitors .....	14
1.4.1 Cardiac arrest.....	15
1.4.1.1 Cerebral hypoperfusion after cardiac arrest .....	15
1.4.1.2 Beneficial effects of 20-HETE inhibition after cardiac arrest .....	17
1.4.2 Stroke .....	18
1.4.2.1 Cerebral hypoperfusion after ischemic stroke.....	19
1.4.2.2 Beneficial effect of 20-HETE inhibition after ischemic stroke .....	21
1.4.2.3 Cerebral hypoperfusion after SAH.....	23
1.4.2.4 Beneficial effect of 20-HETE inhibition after SAH .....	26
1.5 Medicinal chemistry efforts to develop 20-HETE formation inhibitors .....	27
1.5.1 Early 20-HETE formation inhibitors .....	27

1.5.2 Selective 20-HETE formation inhibitors.....	28
1.5.3 20-HETE mimetics .....	34
1.5.4 Repurposing drugs and supplements as 20-HETE formation inhibitors .....	39
1.5.5 Conclusions .....	44
<b>2.0 Development of Bioanalytical Assays to Support Preclinical Evaluation of Novel</b>	
<b>20-HETE Formation Inhibitors .....</b>	<b>45</b>
2.1 Introduction .....	45
2.2 Materials and Methods .....	46
2.2.1 Materials .....	46
2.2.2 Methods.....	47
2.2.2.1 Metabolic stability assay .....	47
2.2.2.2 CYP cocktail assay.....	48
2.2.2.3 Biologic sample extraction for UPMP107 and 20-HETE.....	48
2.2.2.4 Chromatographic conditions .....	49
2.2.2.5 Mass spectrometric conditions .....	50
2.2.2.6 Method validation.....	53
2.3 Results.....	53
2.3.1 Validation of metabolic stability assay experimental system.....	53
2.3.2 Chromatography and specificity for CYP probe metabolites .....	54
2.3.3 UPLC-MS/MS method validation for CYP inhibition assay .....	58
2.3.4 Validation of the CYP cocktail assay experimental system .....	60
2.3.5 Chromatography and specificity for UPMP107 and 20-HETE.....	61
2.3.6 UPLC-MS/MS method validation for UPMP107.....	63

2.4 Discussion and conclusions .....	64
3.0 <i>In vitro</i> Evaluation of Novel Compounds: Discovery of UPMP107 as a Potent and Selective Inhibitor of 20-HETE Synthesizing Enzymes.....	68
3.1 Introduction .....	68
3.2 Materials and methods.....	72
3.2.1 Materials .....	72
3.2.2 Methods.....	73
3.2.2.1 <i>In vitro</i> screening: AA metabolism.....	73
3.2.2.1.1 Incubation conditions .....	73
3.2.2.1.2 Chromatographic Analysis .....	74
3.2.2.1.3 Data analysis.....	75
3.2.2.2 Potency assessment .....	75
3.2.2.3 Selectivity assessment .....	75
3.2.2.4 Metabolic stability assay .....	76
3.2.2.4.1 Incubation conditions .....	76
3.2.2.4.2 Chromatographic analysis .....	76
3.2.2.4.3 Data analysis.....	76
3.2.2.5 CYP inhibition assay .....	77
3.2.2.5.1 Incubation conditions .....	77
3.2.2.5.2 Chromatographic analysis .....	78
3.2.2.5.3 Data analysis.....	78
3.2.2.6 Solubility assay .....	78
3.2.2.7 MDCK-MDR1 assay.....	78



3.2.2.8 <i>In vitro</i> safety pharmacology profiling.....	79
3.2.2.9 Statistical analysis.....	80
3.3 Results.....	80
3.3.1 Physicochemical property evaluation.....	80
3.3.2 Hit identification through <i>in vitro</i> screening.....	80
3.3.3 Characterization of properties for hit compounds .....	83
3.3.4 Lead optimization .....	87
3.3.4.1 Potency evaluation of UPMP010 and UPMP019 derivatives .....	87
3.3.4.2 Species difference in inhibitory activity.....	96
3.3.5 Characterization of properties for top ranked compounds .....	98
3.3.5.1 Selectivity.....	98
3.3.5.2 Solubility .....	100
3.3.5.3 Metabolic stability and preliminary prediction of human clearance .....	100
3.3.5.4 MDCK-MDR1 and BBB permeability.....	103
3.3.5.5 CYP inhibition and DDI potential.....	104
3.3.5.6 <i>In vitro</i> safety pharmacology.....	104
3.4 Discussion and conclusions .....	109
4.0 Pharmacokinetics and Pharmacodynamics of a Novel 20-HETE Formation	
Inhibitor UPMP107 in Pediatric Rats .....	118
4.1 Introduction .....	118
4.2 Materials and Methods .....	121
4.2.1 Materials .....	121

4.2.2 Animals .....	121
4.2.3 Chemicals and formulation .....	121
4.2.4 Single dose pharmacokinetic study .....	122
4.2.5 Brain distribution study .....	123
4.2.6 Plasma and brain sample preparation .....	124
4.2.7 Quantification of UPMP107 and 20-HETE .....	125
4.2.8 Pharmacokinetic analysis .....	126
4.2.9 Statistical analysis .....	127
4.3 Results.....	128
4.3.1 Animal baseline physiology .....	128
4.3.2 Analytical results .....	129
4.3.3 Noncompartmental analysis results.....	130
4.3.4 Dose proportionality .....	133
4.3.5 Brain distribution and pharmacological effect on brain 20-HETE .....	135
4.3.6 Population PK model .....	137
4.4 Discussion and conclusions .....	142
5.0 Population Pharmacokinetics of Propofol in ICU patients.....	148
5.1 Introduction .....	148
5.2 Methods .....	149
5.2.1 Analysis population.....	149
5.2.2 Bioanalytical assay .....	150
5.2.3 Data handling .....	150
5.2.4 Statistical methods .....	151

5.2.5	Population pharmacokinetic analysis.....	152
5.2.5.1	Structural model development .....	152
5.2.5.1.1	Compartmental model.....	152
5.2.5.1.2	Interindividual variability.....	153
5.2.5.1.3	Residual variability.....	153
5.2.5.2	Covariate model development .....	154
5.3	Results.....	156
5.3.1	Patient characteristics.....	156
5.3.2	Sample description and outlier analysis.....	158
5.3.3	Structural pharmacokinetic model.....	160
5.3.4	Forward selection of covariates .....	162
5.3.5	Evaluation of the full model .....	169
5.3.6	Backward elimination of covariates .....	171
5.3.7	Final model .....	172
5.4	Discussion and conclusions .....	175
6.0	Summary and Future Directions .....	178
6.1	Key research findings.....	178
6.1.1	Development and validation of bioanalytical assays.....	178
6.1.2	<i>In vitro</i> evaluation of novel 20-HETE formation inhibitors .....	180
6.1.3	<i>In vivo</i> evaluation of novel 20-HETE formation inhibitor: UPMP107 .....	181
6.1.4	Population pharmacokinetics of propofol in ICU patients .....	182
6.2	Clinical implications .....	183
6.3	Future directions .....	186

6.3.1 Future work related to <i>in vitro</i> evaluation for novel compounds .....	187
6.3.2 Future work related to <i>in vivo</i> evaluation of preclinical candidate: UPMP107 .....	189
6.3.3 Future work related to propofol model development.....	191
6.4 Conclusions .....	191
Appendix A Supplementary data for Chapter 3 - <i>In vitro</i> evaluation of 20-HETE formation inhibitors .....	193
Appendix B Supplementary data for Chapter 4 – PK and PD evaluation of UPMP107 in pediatric rats .....	200
Appendix C Supplementary data for Chapter 5 - Propofol popPK model .....	203
Bibliography .....	208

## List of Tables

Table 1.1 Summary of CYP isoforms that catalyze 20-HETE formation .....	9
Table 1.2 20-HETE formation inhibitors and 20-HETE mimetics .....	41
Table 2.1 Analytical parameters for NCEs.....	51
Table 2.2 Analytical parameters for the individual metabolites and internal standards ....	52
Table 2.3 Analytical parameters for UPMP107, 20-HETE and internal standards.....	52
Table 2.4 Validation data: within-day precision, between-day precision and accuracy (n=5) .....	59
Table 2.5 Comparison of CYP activities between our data with published data.....	60
Table 2.6 UPMP107 validation data: within-day precision, between-day precision and accuracy (n=5) .....	63
Table 3.1 Analytical parameters of eicosanoids .....	74
Table 3.2 <i>In vitro</i> screening and potency evaluation of UPMP010 and UPMP019.....	82
Table 3.3 Property comparison for compound 24, HET0016, UPMP010 and UPMP019 ...	83
Table 3.4 Criteria for Tier 1-3 to evaluate compound.....	86
Table 3.5 CYP4 inhibition of analogs with single substitution on benzene .....	87
Table 3.6 CYP4 inhibition of analogs with simple halogen substitution .....	89
Table 3.7 CYP4 inhibition of analogs with double substitutions.....	90
Table 3.8 CYP4 inhibition of analogs with extended linker.....	90
Table 3.9 CYP4 inhibition of analogs of amide derivatives .....	92
Table 3.10 CYP4 inhibition analogs UPMP113, UPMP134, UPMP139 .....	94
Table 3.11 CYP4 inhibition of UPMP021 and UPMP022 derivatives .....	95

Table 3.12 Top ranked novel compounds based on IC <sub>50</sub> in HLM.....	97
Table 3.13 Evaluation of clearance, solubility, and MDCK-MDR1 permeability of top ranked compounds.....	102
Table 3.14 Metabolic stability of UPMP060 and UPMP072 in the presence and absence of NADPH .....	103
Table 3.15 CYP inhibition for NCEs.....	104
Table 3.16 <i>In vitro</i> safety pharmacology results of UPMP107 and UPMP124.....	105
Table 3.17 UPMP124 binding to Ca <sup>2+</sup> channel.....	106
Table 4.1 Blood collection scheme for UPMP107 IV PK study at dose levels of 5, 10, and 20 mg/kg.....	123
Table 4.2 Blood and brain samples collection scheme for UPMP107 brain distribution study at dose level of 3 and 20 mg/kg .....	124
Table 4.3 Baseline physiological variables and blood gas of animals .....	129
Table 4.4 UPMP107 mean plasma concentrations after IV administration at 5, 10, and 20 mg/kg.....	131
Table 4.5 NCA results of UPMP107 following a single IV administration at dose of 5, 10, and 20 mg/kg.....	132
Table 4.6 Dose proportionality results for C <sub>max</sub> and AUC <sub>0-∞</sub> based on power model.....	134
Table 4.7 Brain to plasma ratio of UPMP107 following IV administration.....	136
Table 4.8 Parameter estimates of the final popPK model from the original dataset and from 1000 bootstrap replicates.....	141
Table 5.1 Demographic characteristics of the analysis population (continuous variables)	156
Table 5.2 Demographic characteristics of the analysis population (catogorical variables)	156

Table 5.3 Summary of outliers that were removed from the dataset.....	159
Table 5.4 Distribution of the number of PK samples per patient .....	159
Table 5.5 Parameter estimates of the base structural model.....	161
Table 5.6 Correlation matrix for the PK parameter estimates from the structural model	162
Table 5.7 Step one covariate selection for CL, V2, and Q.....	166
Table 5.8 Step two covariate selection for CL, V2, and Q .....	167
Table 5.9 Step three covariate selection for CL, V2, and Q.....	168
Table 5.10 Step four covariate selection for CL, V2, and Q .....	168
Table 5.11 Parameter estimates of the full popPK model replicates .....	171
Table 5.12 Backward elimination of covariates .....	171
Table 5.13 Parameter estimates of the final popPK model from the original dataset and from 1000 bootstrap replicates .....	174
Appendix Table 1 CYP4 inhibition of analogs with single substituiou on benzene in RLM .....	193
Appendix Table 2 CYP4 inhibition of analogs with simple halogen substitution in RLM	194
Appendix Table 3 CYP4 inbition in RLM for analogs with double substitutions .....	194
Appendix Table 4 CYP4 inhibition in RLM for analogs with extended linker .....	195
Appendix Table 5 CYP4 inhibition in RLM for analogs UPMP101 - 140.....	196
Appendix Table 6 CYP4 inhibition in RLM for derivatives of UPMP021 and 022 .....	197
Appendix Table 7 Summary of structural model development process.....	200
Appendix Table 8 Summary of structural model development process.....	203

## List of Figures

Figure 1.1 Arachidonic acid metabolism pathways .....	5
Figure 1.2 Evolution of 20-HETE formation inhibitors and pharmacophores.....	29
Figure 1.3 Various 20-HETE formation inhibitors .....	32
Figure 1.4 Chemical structures of nonselective and selective arachidonic acid analogs that inhibit arachidonic acid metabolism. ....	37
Figure 1.5 Evolution of 20-HETE antagonists .....	39
Figure 2.1 Metabolic stability for verapamil, metoprolol, and warfarin.....	54
Figure 2.2 Chromatograms of metabolites and internal standards .....	57
Figure 2.3 Chromatograms of (A) blank, (B) UPMP107, (C) SMIP004, (D) 20-HETE, and (E) 20-HETE-d6 in plasma and brain samples .....	62
Figure 3.1 Representative examples of 20-HETE formation inhibitors .....	70
Figure 3.2 A tiered approach to evaluate novel compounds.....	71
Figure 3.3 Compound 24 and possible positions for structure changes.....	81
Figure 3.4 Selectivity of 20-HETE formation inhibition versus EETs/DiHETs formation inhibition for UPMP010 and UPMP019 .....	84
Figure 3.5 Metabolic stability for compound 24, UPMP010, and UPMP019.....	84
Figure 3.6 Selectivity of 20-HETE versus EETs and DiHETs for top ranked compounds..	99
Figure 3.7 Metabolic stability of top ranked compounds in HLM.....	101
Figure 3.8 Decision tree to narrow down the preclinical candidate pool .....	108
Figure 4.1 Chromatograms in plasma samples.....	130



Figure 4.2 Plasma concentration-time profile following UPMP107 IV administration of 5, 10, and 20 mg/kg .....	132
Figure 4.3 Regression plots of UPMP107 for (A) $AUC_{0-\infty}$ and (B) $C_{max}$ .....	134
Figure 4.4 Plasma and brain concentration-time profiles of UPMP107 following IV administration .....	135
Figure 4.5 Brain 20-HETE levels after UPMP107 administration at 3 and 20 mg/kg .....	136
Figure 4.6 Goodness-of-fit plots of the final model.....	138
Figure 4.7 Visual predictive check of UPMP107 plasma concentrations versus time.....	139
Figure 5.1 Frequency distribution histograms of continuous demographics variables for the analysis population.....	157
Figure 5.2 DV versus TSLD .....	158
Figure 5.3 Frequency distribution histogram of time since last dose (TSLD) for all concentrations .....	159
Figure 5.4 Goodness-of-fit plots for the structural model.....	161
Figure 5.5 Univariate plots of various covariates versus propofol CL .....	164
Figure 5.6 Univariate plots of various covariates versus propofol V2 .....	165
Figure 5.7 Univariate plots of various covariates versus propofol Q.....	166
Figure 5.8 Goodness-of-fit plots for the full model .....	170
Figure 5.9 Visual predictive check of the final model.....	172
Figure 6.1 Steps for early drug development .....	185
Appendix Figure 1 CYP4 homology model and docking of hit compound UPMP019.....	198
Appendix Figure 2 Observed concentrations versus individual predicted concentrations for each animal .....	202

<b>Appendix Figure 3 Individual plots of observed vs. predicted concentrations .....</b>	<b>206</b>
<b>Appendix Figure 4 Frequency distribution histograms of parameter mean estimates from bootstrap analysis (n=1000) .....</b>	<b>207</b>

## Preface

The journey in pursuing the Ph.D. degree and the work presented in this dissertation would not be accomplished without the support from my family, friends, and great mentors. I would like to express my sincere gratitude for all the encouragement, support, and guidance from all of you.

I would first like to thank my advisor, Dr. Samuel Poloyac. He has been supportive since I joined his laboratory as a Master student. Dr. Poloyac is a knowledgeable scientist and a great mentor. I appreciate every opportunity to work on different projects, and I'm forever thankful for all the scientific advice, insightful suggestions, and exciting discussions that help build up the thesis. I want to say thank you for your patience, encouragement, and having confidence in me. Dr. Poloyac not only encouraged me to overcome challenges but also has given me the freedom to explore the world outside the school. I could not have completed the internships without his support. I hope that I could be as enthusiastic and passionate as him. And someday I can give a talk to the audience as well as he can.

My thesis committee guided me through all these years. I would like to thank Dr. Lee McDermott and Dr. Mioara Manole for being supportive throughout the project. They are great collaborators to work with. They have always been helpful with answering medicinal chemistry and animal study questions. I would also like to thank Dr. Robert Gibbs, Dr. Patrick Kochanek, and Dr. Michael Tortorici for their guidance, support, and time throughout my training.

I would like to thank professors, staff, graduate students, and PharmD students who helped with the projects. I would like to thank Dr. Timothy Girard and Dr. Robert Bies for providing guidance on the modeling project. I thank Tricia Miller, Patrick Oberly, and Raymond West III for helping with assays and LC-MS/MS. I thank Henry Alexander and Drew Rowley for helping with

the animal surgery. I thank Lee Ann New and Keri Feldman for teaching me H&E staining. I'm also glad to have worked with Andrew Haddad, Feiyu Ni, Andrew Atterbury, Jonathan Birabaharan, Jiali Wen, and Jessica Abbott.

I would like to thank the School of Pharmacy for providing a supportive and friendly environment for students. I thank AAPS for holding great seminar series. I thank Student Industry Organization for building a career development program for graduate students. I was lucky to take part in the Graduate Student Organization and I thank all the fun activities it holds. I thank Dr. Maggie Folan for always having an open door for students. Thank you for being supportive academically and emotionally throughout the program.

I would like to thank my friends. It is because of all of you that make this challenging journey beautiful. I thank Yoko Franchetti for being a great friend and providing advice countless times throughout my graduate school training. I would like to thank Junyi Li and Alex Prokopienko for being helpful and supportive throughout the internships. I thank Lingjue Li, Shifan Ma, Karryn Crisamore, Yuemin Bian, and Yunqi An for being there, listening to me, supporting me, and encouraging me. Thank you to all my friends that give me strength.

I would like to give my heartfelt thanks to my mom for her unconditional love, care, and tremendous support over the years. You are selfless, strong, intelligent, and hardworking. Thank you for supporting me to study at graduate school and thank you for everything you've done for me.

## 1.0 Introduction

Cardiac arrest and stroke continue to be major public health issues. Out-of-hospital cardiac arrest (OHCA) has an estimated incidence of 356,361 in adults and 7,037 in children (Virani et al. 2020). The survival to hospital discharge was about 10%. The prevalence of stroke is around 3% of the adult population. More than 795,000 people in the United States have a stroke every year, and someone dies of a stroke every 4 minutes (Virani et al. 2020). Patients who survived the initial insults often suffer from secondary brain injury, which has complex and multifaceted pathogenesis. Disturbance of cerebral blood flow and unbalance in vasoconstrictors and vasodilators are observed after cardiac arrest and stroke. Several CYP4 enzymes synthesize 20-hydroxyeicosatetraenoic acid (20-HETE) and epoxyeicosatrienoic acids (EETs) that produce a constrictive and dilative effect in regulating cerebral vascular tone. Therefore, modulation of CYP4 enzymes is a potential strategy for restoring the balance between constrictive and dilatory mediators to improve cerebral blood flow after cerebrovascular injuries. We hypothesize that 20-HETE synthase inhibitors may reduce brain injury by improving cerebral blood flow and attenuating ischemic brain damage.

The primary objective of the thesis was to develop novel 20-HETE synthase inhibitors. To date, no 20-HETE formation inhibitor enters clinical development. Therefore, developing novel 20-HETE formation inhibitors to enable them to be tested in the clinic is needed. This chapter first introduces the pathways of arachidonic acid metabolism with an emphasis on the 20-HETE formation pathway. Next, this chapter includes the biological roles of 20-HETE and rationales of targeting 20-HETE synthase enzymes as potential new treatments in cardiac arrest and stroke. Lastly, the discovery of currently available 20-HETE synthase inhibitors is summarized.

## 1.1 Overview of CYP4 enzymes

The history of discovering omega-hydroxylases dates back to the early 1930s. Omega-oxidation was first reported by Verkade et al. when saturated fatty acids or certain C8-C11 derivatives were fed to dogs or humans, dicarboxylic acids were excreted (Verkade P.E. 1933, Robbins 1968). In the early 1960s,  $\omega$ -hydroxylation was observed *in vitro* by two separate groups of researchers. Wakabayashi and Shimazono showed that sorbic acid amide was oxidized to muconic acid amide in guinea pig liver microsomes and supernatant fraction (Wakabayashi et al. 1961). Robbins demonstrated that incubation of mid-chain monocarboxylic acids in hog, dog, rat liver, and dog kidney with cofactors formed corresponding dicarboxylic acids (Robbins 1968). Later, Preiss and Bloch added evidence in the field where rat liver microsomes catalyzed  $\omega$ -1 and  $\omega$ -2 hydroxylation of fatty acids (Preiss et al. 1964). These initial seminal studies were the first to report the hydroxylation of fatty acid at the terminal and subterminal position, which led to an expansion of the research in this field as data emerged that the oxidation reaction led to bioactive eicosanoids.

One of the pathways for the bioactivation of fatty acids is through the terminal oxidation of hydrophobic fatty acid aliphatic chain. Omega-hydroxylation is the reaction where a hydroxy group is added to the terminal carbon of a hydrophobic fatty acid aliphatic chain (Baba et al. 1963, Hamberg et al. 1971). This reaction is carried out by cytochrome P450 enzymes, specifically the CYP4 family (Fer et al. 2008). Although compared to CYP1, 2, 3 families, the CYP4 family metabolize xenobiotics to a lesser extent, it is involved in the metabolism of endogenous fatty acids, eicosanoids, nutrients, xenobiotics, and carcinogens (Baer et al. 2006, Edson et al. 2013, Eun et al. 2018). In the latest human liver CYP450 “pie” updated by S. Michaels and M. Z. Wang, CYP4F subfamily accounts for 15% of the total hepatic enzymes (Michaels et al. 2014). The

estimated total amount of CYP4F protein in the human liver ranged from 18 to 128 pmol/mg liver microsomal protein comparing to 64 pmol/mg liver microsomal protein of CYP3A4. The large amount of CYP4F protein levels highlight the important emerging role of these enzymes in endogenous and xenobiotics metabolism (Jin et al. 2011, Kawakami et al. 2011).

CYP4 subfamilies, including CYP4A, CYP4B, CYP4F, CYP4V, CYP4X, CYP4Z, have been identified in humans (Kalsotra et al. 2006, Hsu et al. 2007, Hardwick 2008). Among the six subfamilies, CYP4A, 4B, and 4F subfamilies exhibit  $\omega$ -hydroxylation activity (Hardwick 2008). In humans, CYP4F subfamily includes seven isoforms CYP4F2, CYP4F3A, CYP4F3B, CYP4F8, CYP4F11, CYP4F12, and CYP4F22 (Jarrar et al. 2019). In rats, CYP4F subfamily has four isoforms, including CYP4F1, 4, 5, and 6 (Xu et al. 2004). Human CYP4A isoforms include CYP4A11 and CYP4A22 (Drolet et al. 2017). The known rat CYP4A isoforms are CYP4A1, 4A2, 4A3, and 4A8 (Xu et al. 2005).

Long-chain fatty acids are essential components of cell membranes. Fatty acids such as dodecanoic (lauric) acid (C12:0), tetradecanoic acid (C14:0), hexadecenoic acid (C16:0), arachidonic acid (C20:4), eicosapentaenoic acid (EPA) (C20:5), and docosahexaenoic acid (DHA) (C22:6) are known CYP4 substrates (Hoch et al. 2000, Arnold et al. 2010, Honda Malca et al. 2012, Scheps et al. 2013). In general, CYP4A metabolizes medium-chain fatty acids (C10 – C16) such as lauric acid, and CYP4F metabolizes long-chain fatty acids (C16 – C26) such as arachidonic acid. Arachidonic acid is recognized as an essential component of neuronal cell membrane due to its role in supporting membrane fluidity and modulating ion channels, receptors, and enzymes. Additionally, CYP-mediated arachidonic acid metabolites play an important role in various neurological disorders such as stroke and post-cardiac arrest brain injury. The following sections

will focus on the CYP-mediated arachidonic acid metabolism and the biological actions of the metabolites.

## **1.2 Metabolism of arachidonic acid by CYP450**

Arachidonic acid is a polyunsaturated  $\omega$ -6 fatty acid that can be metabolized by cyclooxygenase (COX), lipoxygenase (LOX), and CYP450 enzymes (Fig 1.1). The COX and LOX products include prostaglandins, prostacyclin, thromboxanes, and leukotrienes. These eicosanoids possess various biological functions such as vasoconstriction, vasodilation, and inflammatory responses (Moncada et al. 1979, Ricciotti et al. 2011). A third metabolism pathway was discovered in the early 1980s where arachidonic acid can also be metabolized by CYP450 enzymes into epoxyeicosatrienoic acids (EETs) and dihydroxyeicosatetraenoic acids (DiHETs) (Capdevila et al. 1981, Oliw et al. 1981). For metabolizing arachidonic acid, CYP2C19 possesses the highest catalytic activity of 32 pmol/pmol of P450/min, followed by CYP1A1, CYP4F3B, CYP4A11, and CYP4F2 (El-Sherbeni et al. 2016). The major metabolites mediated by CYP2C19 pathway mainly included 19-HETE, 8,9-EET, and 14,15-EET. CYP1A1 also mainly mediates 19-HETE formation. CYP4F3B, 4A11, and 4F2 mainly produce 20-HETE (El-Sherbeni et al. 2016).



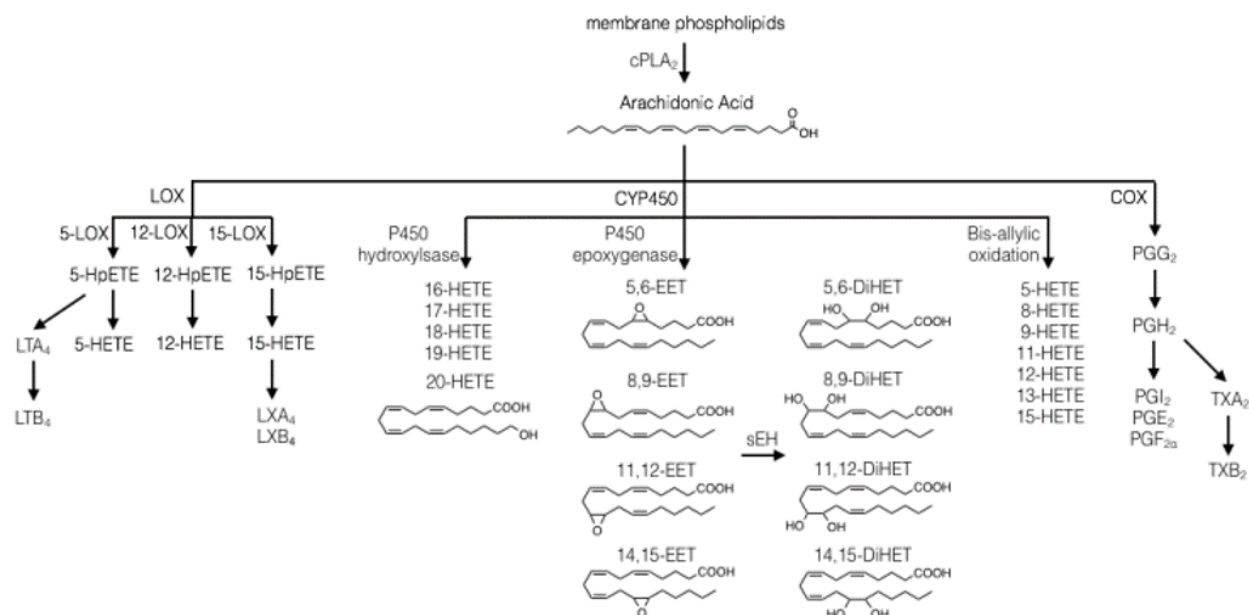


**Figure 1.1 Arachidonic acid metabolism pathways**

The stimulation of cytosolic phospholipid A2 (cPLA2) leads to arachidonic acid release from the membrane. Arachidonic acid can be metabolized into prostaglandins (PGG<sub>2</sub>, PGH<sub>2</sub>, PGE<sub>2</sub>, PGF<sub>2</sub>α), prostacyclin (PGI<sub>2</sub>), and thromboxanes (TXA<sub>2</sub> and TXB<sub>2</sub>) by lipoxygenase (LOX) and cyclooxygenase (COX). CYP450-mediated hydroxylation happens at the terminal and subterminal positions yield 16-, 17-, 18-, 19-, and 20-HETE. CYP450-mediated oxidation produces four regioisomers of cis-epoxyeicosatrienoic acid (EET): 5,6-, 8,9-, 11,12-, and 14,15-EET. They can be metabolized by soluble epoxide hydrolase (sEH) to DiHETs.

### 1.2.1 ω-hydroxylases and 20-HETE formation

CYP4 family plays a vital role in the ω-hydroxylation of arachidonic acid. 20-HETE is a vasoactive eicosanoid that elicits the vasoconstrictive effect in cerebral vasculatures (Poloyac et al. 2006). It is the hydroxylated product of arachidonic acid at the omega position (Lasker et al. 2000). CYP4A and CYP4F subfamilies are well-studied enzymes responsible for 20-HETE formation in rat and human species (Powell et al. 1998, Nguyen et al. 1999, Lasker et al. 2000).

The isozymes that are responsible for the majority of 20-HETE formation have long been a topic of debate. The enzymes that underlie 20-HETE formation rely on the protein level and catalytic activity. A summary of different CYP450 enzymes that are involved in 20-HETE formation is presented in Table 1.1. In humans, CYP4A11, CYP4F2, CYP4F3B, and CYP4F11 show catalytic activity to transform arachidonic acid into 20-HETE. These enzymes are mainly expressed in the liver, kidney, and small intestine (The Human Protein Atlas). A non-CYP4 enzyme, CYP2U1, that also catalyzes  $\omega$ -hydroxylation of arachidonic acid, was found in the thymus and cerebellum (Chuang et al. 2004). CYP4F2, 4F3B, and 4F11 share 74% amino acid sequence homology. And the only difference between CYP4F3A and CYP4F3B was the amino acid at residues 67 – 114 (Hirani et al. 2008). The high homology between these isoforms makes it challenging to quantify the amount of each enzyme with antibodies. Immunoquantitation of CYP4F2 using anti-CYP4F2 IgG revealed high variability of CYP4F2 expression in the liver and kidney with an average amount of  $16.4 \pm 18.6$  and  $3.9 \pm 3.8$  pmol/mg microsomal protein, respectively (Hirani et al. 2008). To the best of our knowledge, the protein levels of CYP4F3B and CYP4F11 are still unknown.

The contributing enzymes for 20-HETE formation in human species were first reported in 1999 by Powell's group. By applying antibodies of CYP4F2 and CYP4A11, the 20-HETE formation was inhibited by  $93.4 \pm 6\%$  and  $13.0 \pm 9\%$  in human liver microsomes, respectively (Powell et al. 1998). Enzyme kinetics was also reported in the same study. The apparent  $K_m$  of CYP4F2 for arachidonic acid (AA) is  $24 \mu\text{M}$ , which is nearly 10-fold lower than that of CYP4A11 of  $228 \mu\text{M}$  (Powell et al. 1998). This suggested that CYP4F2 has a high affinity for arachidonic acid and requires a lower concentration of arachidonic acid to achieve maximum hydroxylation reaction. The predominant role of CYP4F2 was also found in the kidney. Antibodies of CYP4F2

and CYP4F11 inhibited by 20-HETE formation by  $65.9 \pm 17\%$  and  $32.5 \pm 14\%$ , respectively (Lasker et al. 2000). The limitation in these studies is that the antibodies could not distinguish CYP4F2 from CYP4F3B, which shares high sequence identity with CYP4F2. CYP4F3B isoform also shows a high affinity to arachidonic acid. It has a  $K_m$  value of  $22 \mu\text{M}$  in the recombinant CYP4F3 microsomes (Christmas et al. 2001). Later, Mayde Fer et al. compared the catalytic activity of purified CYP4A11, CYP4F2, CYP4F3A, and CYP4F3B in hydroxylating arachidonic acid. CYP4F3B exhibited the highest hydroxylation rate, followed by CYP4F3A, CYP4F2, and CYP4A11 (Fer et al. 2008). One thing worth noting in this study is that 20-carboxy arachidonic acid (20-COOH-AA), a metabolite of 20-HETE, was measured. Therefore, the hydroxylation rate should not be generalized to compare the activity in forming 20-HETE. In a recent study of identifying selective CYP4 inhibitors, 1,2,3,4,5- $^{13}\text{C}$  AA was incubated in human kidney microsomes, CYP4A11, CYP4F2, and CYP4FB recombinant enzymes. The intrinsic clearance values for 1,2,3,4,5- $^{13}\text{C}$  AA were 9.5, 0.02, 0.9 and  $10.1 \mu\text{L}/\text{min}/\text{pmol}$ , respectively. Together, these results, in conjunction with the protein abundance, suggesting that CYP4F2 is more efficient in hydroxylating arachidonic acid because of the lower  $K_m$  ( $24 \mu\text{M}$ ) value, higher maximum 20-HETE formation rate, and greater reduction in 20-HETE formation in the immunoinhibition study in human liver microsomes. The quantification of enzyme abundance with specific antibodies will provide additional insight into the enzymatic pathways in 20-HETE biosynthesis.

In rats, CYP4A1, 4A2, 4A3, 4F1, and 4F4 can generate 20-HETE. CYP4A1, 4A2, 4A3, and 4A8 share 66-98% homology (Uniprot). CYP4A1 is mainly expressed in the liver. The four CYP4A isoforms were also expressed in the kidney, but there was a sex-dependent expression difference. The mRNA expression level was similar for CYP4A1, 4A3, and 4A8 in females, whereas CYP4A2 mRNA was four-fold greater in the kidney of males compared to females

(Sundseth et al. 1992). A recent study localized the expression of CYP4A enzymes in hippocampal and hypothalamic neurons, pial and penetrating arterioles in the brain (Gonzalez-Fernandez et al. 2019). CYP4F1 and CYP4F2 were found to express in the kidney and liver in a sex-dependent manner in contrast to CYP4A, where the protein expression was higher in females compared to males (Kalsotra et al. 2002). The protein levels studied in a western blot analysis showed that CYP4A and CYP4F subfamilies had similar protein expression in the liver (El-Sherbeni et al. 2013). The quantification of the absolute abundance of the isoforms will require specific antibodies.

In baculovirus-Sf9-expressed CYP4A isoforms, the  $K_m$  for arachidonic acid was 10  $\mu$ M, 19  $\mu$ M, and 41  $\mu$ M for CYP4A1, 4A2, and 4A3. The intrinsic clearance was 947, 72, and 22 nM/min, respectively (Nguyen et al. 1999). This evidence in the purified system suggested that CYP4A1 was more 10-times more efficient in generating 20-HETE compared to CYP4A2 and 4A3. CYP4A2 and 4A3 also act as epoxxygenases in forming 11,12-EET. Among the CYP4F subfamilies, CYP4F1 and CYP4F2 were the major catalysts of 20-HETE formation. Although CYP4F4 has higher hydroxylase activity, the relatively low expression compared to CYP4F1 in the kidney precludes its major role in 20-HETE synthesis (Xu et al. 2004). In an immunoinhibition study, anti-CYP4A1/2/3 antibody inhibited arachidonic acid hydroxylation by 71.5% in the liver, suggesting the primary role of CYP4A1/2 in 20-HETE formation in the liver.

**Table 1.1 Summary of CYP isoforms that catalyze 20-HETE formation**

Species	Isoform	Tissues	K <sub>m</sub> (μM)	V <sub>max</sub> (nmol/pmol of P450/min)	reference
Rat	CYP4A1	K, L, B	10	6.3 <sup>a</sup>	(Nguyen et al. 1999)
Rat	CYP4A2	K, L, B, V	19	1.1 <sup>a</sup>	
Rat	CYP4A3	K, L, B, V	0.92	0.7 <sup>a</sup>	
Rat	CYP4F1	K, L, LG	-	9 <sup>a</sup>	
Rat	CYP4F4	K, L, LG	-	11 <sup>a</sup>	
Human	CYP4A11	L, K	228	15.6	(Powell et al. 1998)
	CYP4F2		24	6.8	
Human	CYP4F2 wild type	L, K, SI	287	0.220	
	CYP4F2 V433M		-	-	(Yi et al. 2017)
Human	CYP4F3B	L, K	22	0.0133	(Christmas et al. 2001)
	CYP4F11 wild type		301	0.124	(Yi et al. 2017)
	CYP4F11 C276R		293	0.119	
Human	CYP4F11 D315N	L, K, SI	379	0.106	
	CYP4F11 D374Y		312	0.122	
	CYP4F11 D446N		293	0.124	
Human	CYP2U1	B	2.7	-	(Chuang et al. 2004)

<sup>a</sup> The turnover rate in rat was expressed in min<sup>-1</sup>.

L: liver; B: brain; K: kidney; V: vasculature; LG: lung; SI: small intestine.

“-”: unknown.

### 1.2.2 Epoxygenases and EETs formation

A variety of CYP enzymes can produce EETs, including CYP1A, 2B, 2C, 2D, 2E, 2J, and 4A subfamilies. The CYP epoxigenases add an epoxide group to the double bonds in arachidonic acid and produce four regioisomeric EETs, including 5,6-, 8,9-, 11,12-, and 14,15-EET (Fig 1.1). In humans, CYP1A2, 2B6, 2C8, 2C9, 2C19, and 2J2 have been reported to catalyze EETs formation (Roman 2002). CYP2C8, 2C9, and 2J2 were identified as primary enzymes for EETs formation. In the presence of CYP2C9 inhibitor sulfaphenazole, the epoxigenase activity was inhibited by 50% compared to a 32% reduction with CYP1A2 inhibitor alpha-naphthoflavone, indicating the primary role of CYP2C9 in EETs formation (Rifkind et al. 1995). In an immunoinhibition study, CYP2C8 antibody inhibited EETs formation by 85-90% (Zeldin et al. 1996). Although the expression of CYP2J2 in the liver is low, it has a significant role in catalyzing EETs in extrahepatic tissue such as the heart and pancreas (Xu et al. 2011).

In rats, isoforms including CYP1A2, 2B1, 2B2, 2C11, 2C12, 2C23, 2C24, 2D18, 2J3, 2J4, and 2J10 produce EETs (Roman 2002). The predominant epoxigenases showed a tissue-dependent manner. In an immunoinhibition study, CYP2C11, 2B1, 2C23, and CYP2C11/2C23 were found to be predominant epoxigenases in the heart, lung, kidney, and liver, respectively (El-Sherbeni et al. 2013). Specifically, anti-CYP2C11 and anti-CYP2C23 antibodies inhibited the epoxigenase activity by  $88.5 \pm 26.5\%$  and  $62.6 \pm 28\%$  in the liver microsomes, respectively.

### 1.3 Biological actions of 20-HETE

Many of the biological activities of 20-HETE and EETs are opposite. For example, 20-HETE inhibits large-conductance  $K^+$  channels and activates L-type  $Ca^{2+}$  channels in vascular smooth muscle cells to induce intracellular  $Ca^{2+}$  concentration and vasoconstriction. While EETs activate large-conductance  $K^+$  channels that lead to vasodilation. Through soluble epoxide hydrolase (sEH) metabolism, EETs are transformed to less bioactive metabolites DiHETs. Pharmacological inhibition of 20-HETE formation elicits beneficial effects in various therapeutic areas such as cardiac arrest, ischemic stroke, hemorrhagic stroke, and cancer (Poloyac et al. 2006, Williams et al. 2010, Alexanian et al. 2012, Donnelly et al. 2015, Shaik et al. 2015, Shekhar et al. 2019). The following sections will introduce the biological roles of 20-HETE in the brain.

#### 1.3.1 20-HETE and vascular tone

20-HETE constricts cerebral arterioles. The role of eicosanoid on vascular tone was first discovered for EETs. 5,6-EET dose-dependently dilated rabbit and cat pial arterioles *in vivo* (Ellis et al. 1990). The mechanism of EETs dilatory effect was found to be related to increased frequency of channel opening, mean open time, and the open-state probability of a 98-pS  $K^+$  channel. (Gebremedhin et al. 1992). Later, the biological effect of 20-HETE on cat cerebral arterioles was studied by the same group. The homogenate of cat cerebral microvessels incubated with [ $^{14}C$ ]-arachidonic acid in the presence of NADPH produced a metabolite that coeluted with synthetic 20-HETE by reverse-phase high-pressure liquid chromatography (HPLC), with a mass-to-charge ratio of 391 m/z. The same value of the mass-to-charge ratio and 20-HETE molecular weight

suggested that 20-HETE was produced in the cat cerebral microvessels. The application of exogenous 20-HETE (0.1-10 nM) to isolated cat pial arteries (100-200  $\mu$ M) induced a concentration-dependent reduction in arterial diameter. The mechanism of 20-HETE induced cerebral microvessel constriction was related to inhibition of a 217-pS  $K^+$  channel and activation of L-type  $Ca^{2+}$  channel, leading to the elevation of intracellular  $Ca^{2+}$  concentration and constricting cerebral arterial muscle (Harder et al. 1994, Gebremedhin et al. 1998, Harder et al. 2011). These results demonstrated that 20-HETE constrict cerebral microvasculature.

### **1.3.2 20-HETE and cerebral blood flow autoregulation**

The endogenously formed 20-HETE plays a role in cerebral blood flow (CBF) autoregulation. 20-HETE was produced with cerebral arterial microsomes when incubated with [ $^{14}C$ ] arachidonic acid, suggesting the endogenous 20-HETE was formed in cerebral arteries. When increasing intravascular pressure from 20 to 140 mmHg on isolated cerebral arteries, a 6-fold increase in 20-HETE concentration was induced. And treatment with a CYP450 inhibitor DDMS (10 $\mu$ mol/L) or a 20-HETE antagonist 20-hydroxyeicosa-6(Z),15(Z)-dienoic acid (20-HEDE) blocked pressure-induced constriction and increased the diameter at 140 and 160 mmHg compared to control (Gebremedhin et al. 2000). Additionally, when applying 20-HETE antagonists, 15-HETE and 20-HEDE, the pressure-induced arterial constriction was also attenuated. This suggested that 20-HETE is recognized as a mediator of pressure-induced myogenic constriction of cerebral arteries *in vitro*.

The significance of 20-HETE in cerebral blood flow autoregulation was also demonstrated *in vivo*. When intracranial infused 50  $\mu$ M DDMS, the autoregulation of CBF was impaired between pressure from 70 to 150 mmHg in Sprague Dawley rats (Gebremedhin et al. 2000). The



autoregulatory index (percentage change in CBF/percentage change in mean arterial pressure) increased from 0.10 of control to 0.92 of the DDMS treated group, when an autoregulatory index of 0 suggests perfect autoregulation. Fan et al. generated CYP4A1 transgenic rats that had eight-fold higher CYP4A1 expression and produced six-fold higher 20-HETE in cerebral vessels compared to Dahl salt-sensitive (SS) rats (Fan et al. 2015). The myogenic response of the middle cerebral artery was impaired in SS rats with unaltered diameters when increasing perfusion pressure from 60 to 140 mmHg. When mean arterial pressure (MAP) increased from 100 to 160 mmHg, CBF increased by  $49.1 \pm 6\%$  in SS rats compared to  $18.6 \pm 2\%$  and  $25.9 \pm 5\%$  in CYP4A1 transgenic and SS-5<sup>BN</sup> rats. Together, these data suggested either pharmacologic or genetic inhibition of 20-HETE formation, the pressure-induced myogenic response was blocked, implying the critical role of 20-HETE in CBF autoregulation *in vivo*.

### **1.3.3 20-HETE and angiogenesis**

20-HETE can promote angiogenesis, the process of forming blood vessels. The role of 20-HETE in angiogenesis was first reported in skeletal muscle. An increase in 20-HETE formation after chronic electrical stimulation was observed in skeletal muscle, and pharmacological blockade of 20-HETE by HET0016 abolished the increase in vessel density in response to electrical stimulation (Amaral et al. 2003). Similarly, Chen et al. demonstrated the 20-HETE induced angiogenesis was able to be inhibited by HET0016 in rat cornea *in vivo* (Chen et al. 2005). The promotion of angiogenesis by 20-HETE was contributed by the upregulation of hypoxia-inducible factor (HIF-1), superoxide, and vascular endothelial growth factor (VEGF) to increase the proliferation of epithelial cells (Guo et al. 2007, Guo et al. 2009).

There is limited information on 20-HETE and physiological angiogenesis in cerebral arteries. However, several studies reported the role of 20-HETE in angiogenesis under pathological conditions. In ischemic stroke patients, there were significantly increased microvessels in the infarcted tissues compared to the contralateral normal hemisphere. The new vessel formation also correlated with longer survival time in the patients (Krupinski et al. 1994). In astrocytes exposed to oxygen-glucose deprivation, HET0016 or CYP4A siRNA inhibited tube formation and prevented accelerating endothelial migration in endothelial cells, suggesting the role of 20-HETE in mediating endothelial cell proliferation and angiogenesis *in vitro* (Liu et al. 2019). Interestingly, in a mouse focal cerebral ischemia model, both CYP4A siRNA and HET0016 treatment suppressed microvessel density in the peri-infarct cortex by day 14 post-stroke. The suppressed angiogenesis was consistent with the neurological and functional outcome, where improvement was seen up to day 7, but a worse outcome was seen at day 14 post-stroke (Liu et al. 2019). This study suggests although inhibition of 20-HETE at an early time period demonstrated neuroprotection, but prolonged inhibition may be detrimental considering the possible protective proangiogenic effect of 20-HETE at a later phase. More research is required to further study the mechanisms of 20-HETE regulation of angiogenesis of the cerebral vasculatures.

#### **1.4 Therapeutic areas for developing 20-HETE formation inhibitors**

20-HETE synthase inhibitors have been evaluated as a potential intervention for several CNS diseases such as cardiac arrest and stroke. Despite different causes of the blood supply impediment to the brain, cardiac arrest and stroke develop secondary brain injury after the initial

insult. The biological effect of 20-HETE in the brain prompted researchers to investigate the effect of 20-HETE inhibition under these pathophysiological conditions.

### **1.4.1 Cardiac arrest**

Cardiac arrest (CA) is the cessation of cardiac mechanical activity and is confirmed by the absence of signs of circulation. Whole-body ischemia during cardiac arrest and after the return of spontaneous circulation (ROSC) lead to a series of post-cardiac arrest syndrome, including post-cardiac arrest brain injury, post-cardiac arrest myocardial injury, systemic ischemia/reperfusion response, and persistent precipitating pathology. Among all the organs, the brain, particularly the cerebral cortex, is vulnerable to ischemic/reperfusion injury and post-resuscitation neurological dysfunction represents the major cause of mortality and morbidity (Nolan et al. 2008).

#### **1.4.1.1 Cerebral hypoperfusion after cardiac arrest**

Alterations of CBF after cardiac arrest can be assessed with the development of clinically relevant cardiac arrest animal models. Upon successful resuscitation, CBF alterations can be divided into three phases, including immediate phase (0-20 min), early phase (20 min-12 h), and intermediate phase (12-72 h) (Iordanova et al. 2017).

The benchmark of the immediate phase is early hyperemia that causes impaired cerebral autoregulation. Hyperemia was found in adult and pediatric rats, rabbits, and dogs cardiac arrest models (Blomqvist et al. 1985, Lee et al. 1989, Sterz et al. 1992, Manole et al. 2009). After 9 min asphyxial cardiac arrest in postnatal day 17 rats, subcortical areas were hyperperfused at 5 min and returned to baseline by 10 min. After 12 min asphyxial cardiac arrest, hyperemia was absent

(Manole et al. 2009). Researchers have debated whether hyperemia is beneficial as an indication of increased local metabolic rate or detrimental as it may enhance reperfusion injury (Iordanova et al. 2017). Antioxidants and transgenic rats with superoxide dismutase overexpression targeting early hyperemia have been shown to improve outcomes after cardiac arrest (Cerchiari et al. 1987, Xu et al. 2009).

During the hypoperfusion phase, the cerebral metabolic fate gradually recovers, but the CBF is severely reduced, which usually lasts from hours to days. The prolonged phase of hypoperfusion may induce secondary injury after the initial insult and is correlated to neurocognitive, behavioral, sensory, and motor function deficit, representing a therapeutic target after cardiac arrest (Mongardon et al. 2011). Multiple mechanisms have been proposed to contribute to the hypoperfusion phase, including damage of endothelial cells, disturbance in vasoconstrictors and vasodilators, increased cerebral vascular resistance, and impaired autoregulation (Buunk et al. 1996, Sundgreen et al. 2001, Shaik et al. 2015, Iordanova et al. 2017). Manole et al. reported cortical hypoperfusion after 9 min asphyxial cardiac arrest from 10 to 150 min and immediate hypoperfusion in the cortex and subcortical regions after 12 min insult (Manole et al. 2009). Li et al. reported the prominent microcirculatory disturbance during immediate and early phases that contributes to hypoperfusion. Among 59 cortical capillaries from 12 rats that underwent cardiac arrest injury, highly heterogeneous microcirculatory disturbances were found. 25.4% and 13.5% capillary branches displayed no-reflow phenomenon at 30 and 60 min post-CA, and the time required for plasma to travel from the pial arterioles through capillaries into the pial venules increased post-CA (Li et al. 2019).

CBF may return to normal, remain low, or increase during the intermittent phase. In a prospective observational study in resuscitated cardiac arrest patients, the mean flow velocity

(MFV) in the middle cerebral artery gradually increases toward normal values in survivors during the first 72 h (van den Brule et al. 2017). In non-survivors, the MFV significantly increased compared to the survivors' group, suggesting a decrease in cerebral vascular resistance in these patients (van den Brule et al. 2017).

#### **1.4.1.2 Beneficial effects of 20-HETE inhibition after cardiac arrest**

CBF disturbance is a potential target for therapeutic intervention for secondary brain injury after cardiac arrest. CYP450-derived arachidonic acid metabolites including 20-HETE and EETs constrict and dilate blood vessels, which provide a mechanism of regulating CBF. Interventions that inhibit 20-HETE formation were evaluated in cardiac arrest injury models. Shaik et al. studied 20-HETE inhibition in PND 17 rats subjected to 9min or 12 min asphyxia cardiac arrest. Cortical 20-HETE levels significantly increased at 5 min compared to sham after 9 min asphyxia, and 20-HETE levels were significantly higher at 5 and 120 min after 12 min asphyxia (Shaik et al. 2015). The brain 20-HETE levels were parallel with the temporal profile of hypoperfusion as described previously after CA insult in this pediatric asphyxia cardiac arrest model (Manole et al. 2009). The elevated cortical and subcortical 20-HETE was reduced significantly by a single dose of HET0016 (0.9 mg/kg) administered at resuscitation after 12 min CA, without affecting other AA metabolites. HET0016 decreased brain water content at 24 h, and improved cortical perfusion at 5 and 10min, but not at 30 min and 60min. HET0016 treatment (0.9 mg/kg, q6h) also improved short-term neurological outcomes at 3 h and 24 h measured by neurological deficit score and reduced neurodegeneration measured by cortical pyknotic neurons. These findings suggested that the beneficial effect of 20-HETE inhibition is multifactorial, including the direct improvement of perfusion on vascular smooth muscle, improved perfusion secondary to reduced brain edema, and direct neuronal protective effect.

Similarly, Yang et al. demonstrated the protective effect of 20-HETE inhibition in a global hypoxia-ischemia (HI) neonatal piglet model, which mimics neonatal HI injury. Administration of HET0016 1mg/kg or 10mg/kg at 5 min after reoxygenation significantly increased the density of viable neurons to  $52 \pm 20\%$  and  $62 \pm 15\%$ , respectively, compared to  $21 \pm 11\%$  in the vehicle group (Yang et al. 2012). The protective effect was mediated by reducing the HI induced phosphorylation at PKC-sensitive sites and limit the HI-induced decrease in  $\text{Na}^+$ ,  $\text{K}^+$ -ATPase activity, suggesting 20-HETE exhibit direct neuronal effect on proteins involved in neuronal excitotoxicity. The same group reported HET0016 1mg/kg treatment provided additional neuroprotection besides therapeutic hypothermia by increasing the density of viable neurons in the putamen, cortex, and thalamus in the same model (Zhu et al. 2015). Together, these studies suggested the role of 20-HETE in neuronal excitotoxicity, cerebral hypoperfusion, and neurodegeneration after cardiac arrest. And inhibition of 20-HETE is a promising strategy to improve neuroprotection and reduce neurodegeneration after cardiac arrest.

#### **1.4.2 Stroke**

Ischemic strokes are caused by an obstruction within a blood vessel that supplies blood to the brain, which accounts for 87% of all strokes (Virani et al. 2020). Hemorrhagic strokes such as intracerebral hemorrhage (ICH) and subarachnoid hemorrhage (SAH) are less common, accounting for 13% of all stroke cases (Virani et al. 2020). Post-stroke sequelae such as neurological deterioration, cognitive impairment, cerebral vasospasm, and delayed cerebral ischemia are common complications after ischemic or hemorrhage stroke (Balami et al. 2011, Macdonald 2014).

#### **1.4.2.1 Cerebral hypoperfusion after ischemic stroke**

The pathophysiology of ischemic stroke is complex and involves multiple mechanisms. Oxygen-rich vascular supply is disrupted during ischemic stroke. Ischemia causes brain damage by oxygen or glucose depletion, energy failure, and disturbance of subsequent energy-dependent processes. Depletion of cellular energy causes elevation of intracellular  $\text{Na}^+$ ,  $\text{Ca}^{2+}$ , and extracellular  $\text{K}^+$ , which will cause cytotoxic edema (Durukan et al. 2007). With energy depletion, glutamate is released, activating of glutamate receptors which leads to  $\text{Na}^+$ ,  $\text{Ca}^{2+}$  influx, exacerbating edema and toxicity (Durukan et al. 2007). Generation of oxygen-free radicals and reactive oxygen species can react with cellular components and trigger inflammation and apoptotic pathways (Deb et al. 2010). Inflammation molecules, free radicals, hypoxia damage, and destruction of basal lamina by matrix metalloproteinases could disrupt the blood-brain barrier (BBB) (Durukan et al. 2007). Increased expression of mRNA of angiogenesis genes and angiogenic protein was observed in the ischemic area; however, it is still unclear if angiogenesis response could lead to the development of functional new blood vessels and improve brain function after ischemic stroke (Ergul et al. 2012). The cascade of events leads to neuronal death and irreversible loss of neuronal function.

The inner core of the cerebral vascular tissue that undergoes ischemia is hypoperfused (18–20 ml/100 g/min) and is at risk of dying within hours. The penumbra perfused at 60 ml/100 g/min is less likely to die (Deb et al. 2010). Treatment strategies have been developed to restore cerebral blood flow. Pharmacological intervention or mechanical recanalization to restore blood flow at an early time point has proven to salvage neurons and glia cells from the inner core and the penumbra. Despite successful recanalization, some patients experienced reperfusion injury, cytotoxic or vasogenic edema, and intracranial hemorrhage after reperfusion (Pan et al. 2007).

Reactive hyperemia occurs after reperfusion, where there is an elevation of regional blood flow along with loss of cerebral autoregulation and increased BBB permeability (Sundt et al. 1971, Olsen et al. 1981, Khatri et al. 2012). The length of post-ischemic hyperemia is directly proportional to the duration of the ischemic phase (Gourley et al. 1984). Reactive hyperemia is attributed to the abnormal vasodilation in the ischemic region caused by lactic acidosis and the release of vasoactive mediators (Rehncrona et al. 1981, Silver et al. 1992, Moore et al. 1994). A secondary hypoperfusion phase occurs after post-ischemic hyperperfusion, which lasts for 18 to 96 hours. The hypoperfusion is attributed to elevated microvascular resistance, astrocytic end-feet swelling, cerebral metabolic depression, and formation of endothelial microvilli (Khatri et al. 2012, Xiang et al. 2016, Ng Felix et al. 2018). These changes contribute to increased paracellular permeability, which is associated with vasogenic edema that worsens reperfusion injury.

The basis for stroke treatment is to remove the blockade to relieve the brain damage caused by loss of oxygen and reduced blood flow. Recombinant tissue-type plasminogen activator (rt-PA) is the only FDA-approved treatment for ischemic stroke by its antithrombotic effect in dissolving clots to improve blood flow (Adams Harold et al. 2007). The limitation of intravenous rt-PA is the risk of causing symptomatic intracranial hemorrhage and a therapeutic window within 4.5 hours after stroke symptoms onset to elicit benefits (The 1997, Hacke et al. 2008, Kernan Walter et al. 2014). The DEFUSE study has shown that a perfusion-weighted imaging (PWI) and diffusion-weighted imaging (DWI) mismatch ratio of 2.6 provides the highest sensitivity and specificity to identify patients who will benefit from reperfusion treatment (Albers et al. 2006, Kakuda et al. 2008). Relying on MRI imaging, patients who displayed PWI/DWI mismatch may still benefit from rt-PA beyond the 4.5 h therapeutic window (Ebinger et al. 2012, Fisher et al. 2013, Bai et al. 2019, Yi et al. 2019). Therefore, developing treatments that prolong the perfusion diffusion



mismatch by improving collateral flow is a potential adjunctive therapy to increase patients' opportunity to be treated with rt-PA.

#### **1.4.2.2 Beneficial effect of 20-HETE inhibition after ischemic stroke**

Given the vasoconstrictive and proangiogenic effect of 20-HETE, experimental therapies were developed to test whether pharmacological inhibition of 20-HETE formation can induce a protective effect in ischemic stroke models. Several research groups utilized the temporal focal ischemia middle cerebral artery occlusion (MCAO) model in rats to study the effect of 20-HETE inhibition in ischemic stroke. Poloyac et al. used HET0016 (10 mg/kg i.p.), and Roman's group used TS-011 (0.01 – 1.0 mg/kg/h i.v.) to achieve either acute or long-term blockade of 20-HETE. Both groups reported favorable treatment outcomes, including decreased cortical 20-HETE levels, reduced lesion volume, attenuation of the decreased CBF, and improved neurological and functional outcomes up to 7 days after the injury (Miyata et al. 2005, Omura et al. 2006, Poloyac et al. 2006, Tanaka et al. 2007, Dunn et al. 2008, Renic et al. 2009). Conflicting results of TS-011 beneficial effect on CBF were reported. Renic et al. showed that TS-011 0.1 mg/kg IV infusion over 2h had no improvement on cerebral blood flow in the cerebral cortex after MCAO injury in rats (Renic et al. 2009). Marumo et al. showed that TS-011 0.3 mg/kg IV infusion over 1h administered every 6h maintained the blood flow velocities in microvessels at values equivalent to pre-occlusion (Marumo et al. 2010). The discrepancies may be due to differences in TS-011 dosing regimen and different locations of CBF being monitored in the two studies. Moreover, the effect of TS-011 was also tested in a thromboembolic stroke model in monkeys. TS-011 significantly reduced neurological deficit score at 24 hours after the stroke onset. The infarct volume showed a trend of reduction compared to control treatment. The combination of rt-PA and TS-011 provided additional protection compared to a single therapy, where monkeys treated with

the combination therapy had significantly lower neurological deficit scores and smaller infarct size (Omura et al. 2006). In these studies, treatment was given either pre-injury, immediately after the onset of reperfusion, or up to 4 hours post MCAO. The positive results suggested inhibiting 20-HETE could be employed over a wider therapeutic window compared to other treatments such as endothelin receptor antagonist S-0139(Zhang Rui et al. 2008). Future studies with later initiation of the 20-HETE inhibition could test if the treatment would produce any protective effect if initiated beyond 4.5 hours. The combinational therapies targeting two distinct mechanisms appear to be a promising research direction, given more data are needed on the safety and efficacy.

The mechanism by which 20-HETE formation inhibitors improve neurological outcomes was studied by different groups. HET0016 reduced brain edema and protected and restored BBB integrity through reducing ROS production, suppressing MMP-9 expression and JNK pathway, and restoring tight junction proteins Claudin-5 and ZO-1 after the MCAO in rats (Liu et al. 2014). Inhibition of 20-HETE also produces a direct neuronal protective effect in an organotypic hippocampal slice and cortical neuron cultures under oxygen-glucose deprivation. The reduced neuronal death is associated with a decrease in superoxide production and attenuation of the cell death pathway via caspase-3 (Renic et al. 2012, Zhang et al. 2017). Therefore, 20-HETE synthase inhibitors are proposed to improve neurological outcomes by improving blood flow and via a direct effect on neuronal survival.

Clinical findings of 20-HETE in ischemic stroke raise the importance of its role in pathogenesis and clinical outcome. Lee et al. measured multiple HETEs, including 20-HETE, after stroke and found elevated HETE levels in stroke patients compared to controls (Lee et al. 2008). Similarly, Ward et al. reported plasma 20-HETE, EETs, DiHETs, and F2-isoprostane levels significantly increased in acute ischemic stroke patients compared with healthy controls in a

retrospective study, and 20-HETE and EETs levels attenuated at 30 days post-ischemic stroke (Ward et al. 2011). The association of 20-HETE with lesion size and reduced functional outcome in ischemic patients supported and strengthened the preclinical findings (Ward et al. 2011). The relationship was also found in a prospective study in acute ischemic stroke patients. Yi et al. reported that elevated levels of 20-HETE in cerebrospinal fluid and plasma from patients are associated with poor prognosis (Yi et al. 2016). Additionally, genetic polymorphism of CYP4A11 and CYP4F2 have been reported to be related to stroke. Stec et al. first demonstrated that the CYP4F2 M433 allele is associated with a 50% reduction in 20-HETE production (Stec et al. 2007). CYP4F2 V433M has been found to be associated with ischemic stroke in different populations, including male Swedes, male Northern Chinese Han population (Fava et al. 2008, Deng et al. 2010). In a Japanese male population, CYP4F2 G allele of rs2108622 and CYP4A11 GG genotype was associated with cerebral infarction and the T–C–G haplotype could be a risk factor for cerebral infarction in male Japanese (Fu et al. 2008, Fu et al. 2008). Together, these clinical findings provide incentives to develop safe and efficacious 20-HETE synthase inhibitors to investigate the effect of 20-HETE inhibition on clinical outcomes.

#### **1.4.2.3 Cerebral hypoperfusion after SAH**

According to the temporal progression of brain injury, early brain injury (EBI) and delayed brain injury (DBI) are used to describe the pathophysiology changes after SAH (Chen et al. 2014). Early brain injury (EBI), the immediate brain injury within 72 h of SAH onset, is an emerging cause of morbidity and mortality after SAH. The intracranial pressure (ICP) elevation after SAH aneurysmal rupture leads to a reduction in cerebral perfusion pressure (CPP) and reduced CBF, causing global cerebral ischemia (Cahill et al. 2006). ICP elevation can be induced by volume increase secondary to SAH, vasoparalysis, and cerebral spinal fluid (CSF) drainage obstruction

(Cahill et al. 2006). Prolonged and ICP-independent hypoperfusion was found in the acute phase in SAH patients and experimental SAH, suggesting early vasospasm (Schubert et al. 2011). Vasoconstriction was seen as early as 10 min after SAH in rats attributed to decreased levels of NO metabolites and increased endothelin-1 levels (Sehba et al. 2000). Abnormal Cerebral pial microcirculation and reduced cerebral blood flow were found in SAH mice within 180 min, where the acute vasoconstriction occurred predominantly in the arterioles instead of the venules (Yang et al. 2018). Targeting vasoconstriction, administration of NO donor S-nitrosoglutathione preserved vascular structure, increased CBF, increased internal carotid artery diameter, and decreased extracellular glutamate levels (Sehba et al. 1999, Sehba et al. 2007). Administration of endothelin receptor antagonist, clazosentan, prevented continuous CBF reduction in SAH rats (Schubert et al. 2008).

After the first 3 days, angiographic cerebral vasospasm is a common complication after SAH that may contribute to delayed cerebral ischemia (DCI). Approximately 70% of patients were estimated to have angiographic vasospasm, and 25% of patients develop symptomatic cerebral vasospasm after aSAH (Carr et al. 2013). Cerebral vasospasm describes the narrowing of cerebral arteries that can be detected by angiography or sonography (Durrant et al. 2015). Vasospasm usually onset at 3 days after SAH, reaches maximum constriction on 5 to 14 days, and gradually resolves at 2 to 4 weeks (Durrant et al. 2015). Several factors have been shown to be involved in vasospasm, such as abnormal and prolonged vascular smooth muscle contraction, blood breakdown products, endothelial dysfunction, imbalance in arachidonic acid metabolites, and loss of autoregulation (Boullin et al. 1979, Macdonald et al. 1991, Rubanyi 1991, Eiichi et al. 2004, Roman et al. 2006, Otite et al. 2014). Cerebral vasospasm has been found to be associated with the reduction in rCBF in SAH patients. During cerebral vasospasm, luminal narrowing of the large

extraparenchymal arteries was observed, inducing significantly reduced rCBF (Ohkuma et al. 2000). Cerebral vasospasm also decreases cerebral perfusion, but regional hypoperfusion can happen without vasospasm. The association is supported by the fact that hypoperfusion was seen in 46 regions in SAH patients, but 66% of the regions were supplied by vessels with no significant vasospasm (Dhar et al. 2012). Approximately 30% of the patients who develop cerebral vasospasm will develop DCI. DCI is one of the most important causes of poor neurological outcomes in SAH patients. A meta-analysis showed that clazosentan treatment significantly reduced vasospasm and the risk of delayed ischemic neurologic deficit but did not alter vasospasm-related morbidity or outcome (Cho et al. 2019). Similarly, Dhar et al. found that delayed cerebral infarction could develop in brain regions without vasospasm and it accounts for >25% of infarct from DCI. This suggests that vasospasm is not the sole mechanism for causing DCI, and there is an association between cerebral vasospasm and multifactorial mechanisms for DCI development (Pluta et al. 2009, Dhar et al. 2012).

Early prevention and or treatment of cerebral vasospasm are important. Oral administration of nimodipine, a calcium channel blocker, is the only FDA-approved drug to treat vasospasm that improves outcomes after aSAH. In a British Aneurysm Nimodipine Trial, patients who had oral nimodipine demonstrated a 34% reduction in cerebral infarction and a 40% reduction in poor outcomes at three months (Pickard et al. 1989). Clazosentan reversed arterial narrowing and reduced angiographic vasospasm but failed to show any effect on long-term outcomes (Vajkoczy et al. 2005, Macdonald et al. 2012). Since the process of developing vasospasm is multifactorial, therefore, it is important to investigate new therapies that target other mechanisms, as well as developing combination therapies to manage cerebral vasospasm.

#### **1.4.2.4 Beneficial effect of 20-HETE inhibition after SAH**

SAH may also benefit from the intervention of 20-HETE formation. Kehl et al. studied the effect of 20-HETE on CBF in SAH rats by utilizing two different 20-HETE formation inhibitors, a non-selective inhibitor 17-octadecynoic acid (17-ODYA) and a selective 20-HETE formation inhibitor HET0016. The 30% drop of cerebral blood flow at 10 min after SAH induction was attenuated by 20-HETE formation inhibitors by around 40%, and CSF 20-HETE production was brought down to control level by HET0016 (10mg/kg i.v.) or 17-ODYA (1.5 nmol) (Kehl et al. 2002). Pretreatment of TS-011 0.01–0.1mg/kg i.v. prevented sustained fall in CBF in rats after induction of SAH (Kehl et al. 2002, Miyata et al. 2005). Rats received TS-011 (0.1 mg/kg i.v.) showed recovery of cerebral artery diameter, CBF returned to control values and reversion of delayed vasospasm (Takeuchi et al. 2005). Crago et al. reported that CSF 20-HETE concentrations were associated with delayed cerebral ischemia (DCI) and Hunt & Hess score in aSAH patients (Crago Elizabeth et al. 2011). This was the first clinical evidence that supported an association between 20-HETE CSF levels with poorer aSAH outcomes. Later, Donnelly et al. found that aSAH patients with moderate or high 20-HETE CSF concentrations were more likely to have unfavorable 3 and 12-months Modified Rankin Scale, quicker onset to develop clinical neurologic deterioration, and three-fold higher 3 and 12-month mortality (Donnelly et al. 2015).

To summarize, regardless of the different CNS insults, imbalance in eicosanoids was observed in animal models in cardiac arrest and stroke. Specifically, brain tissue and CSF 20-HETE levels were upregulated. Favorable neurological outcomes in animal models when inhibiting 20-HETE and the associations seen between 20-HETE and clinical outcomes are motivations to develop novel compounds that modulate CYP4 enzymes. This is a potential strategy in the development of new treatments for ischemia-reperfusion injury in the brain.

## **1.5 Medicinal chemistry efforts to develop 20-HETE formation inhibitors**

The appealing effect of inhibiting 20-HETE formation or antagonizing its effect based on previously mentioned biological rationales encouraged the discovery of 20-HETE formation inhibitors or epoxyeicosatrienoic acid mimics. Several pharmaceutical companies and academic institutions have reported 20-HETE formation inhibitors. Table 1.2 provides a summary of the known 20-HETE inhibitors and mimetics. Early assays to quantify AA metabolites were hindered by long assay duration, low sensitivity, and a limited number of metabolites. The development of highly sensitive UPLC-MS/MS measurement for lipophilic metabolites of endogenous substrate AA was an effective way to verify the activity of lead compounds as well as the selectivity of the compounds because of its ability to simultaneously measure HETEs, EETs, DiHETs, and prostanoids (Miller et al. 2009, Shaik et al. 2014).

### **1.5.1 Early 20-HETE formation inhibitors**

Most of the early compounds nonselectively inhibit  $\omega$ -hydroxylase and epoxygenase pathways of arachidonic acid metabolism.  $\beta$ -diethylaminoethyldiphenylpropylacetate (SKF-525A) inhibits EETs and 20-HETE formation by binding to the heme in CYP enzymes and reduces the availability of the heme to incorporate into CYP enzymes (Borrello et al. 1986, Roman 2002). Administration of SKF525A (100  $\mu$ M) to isolated dog renal arteries reversed the arachidonic acid-induced constriction (Kauser et al. 1991). 17-octadecynoic acid (17-ODYA) introduced by Ortiz de Montellano et al., is a fatty acid analog that inhibits 20-HETE formation avidly depending on the terminal acetylenic moiety as a suicide-substrate inhibitor (Ortiz de Montellano et al. 1981, Shak et al. 1985). However, 17-ODYA also inhibited epoxygenases effectively at the same

concentration (Zou et al. 1994). Compound 1-aminobenzotriazole (ABT) (50 mg/kg) administered intraperitoneally completely inhibited 20-HETE and EETs formation by disrupting the CYP450 function via the formation of a heme adduct (Ortiz de Montellano et al. 1981, Maier et al. 2000). In addition to these compounds, endogenous vasodilators, nitric oxide (NO) and carbon monoxide (CO), bind to the heme in the CYP enzymes and block 20-HETE and EETs formation simultaneously even though NO donor dose-dependently inhibited 20-HETE formation in renal microsomes (Sun et al. 1998).

### **1.5.2 Selective 20-HETE formation inhibitors**

The discovery of the first potent and selective 20-HETE formation inhibitor was reported in 2001 by the Taisho Pharmaceutical Co., Ltd. using high throughput screening. The potency of N-(4-Butyl-2-methylphenyl)-N'-hydroxyformamidinium (HET0016) in human and rat kidney microsome were  $8.9 \pm 2.7$  and  $35 \pm 4$  nM, respectively (Sato et al. 2001). The group reported the N-hydroxyformamidinium moiety and a substitution at para position larger than the methyl group is necessary for potency. HET0016 inhibited EETs in rat kidney microsome with  $IC_{50}$  value ( $2800 \pm 300$  nM) around 80-fold for  $IC_{50}$  of 20-HETE formation inhibition (Miyata et al. 2001). The compound was selective, exhibiting over 370-fold selectivity for the inhibition of 20-HETE formation vs. the inhibition for CYP2C9, 2D6, and 3A4 in the human kidney microsome. It also did not affect COX enzymes ( $IC_{50} = 2300$  nM). This compound was then used in various *in vitro* and *in vivo* disease models, including ischemic and hemorrhagic stroke, cardiac arrest, preventing the fall of cerebral perfusion and CBF (Kehl et al. 2002, Poloyac et al. 2006, Shaik et al. 2015).

Although HET0016 was potent and selective, it was plagued by low water solubility (3.7  $\mu$ g/ml), short half-life ( $39.6 \pm 20.0$  min), and instability under acidic environment (43.2%



remaining at pH 4.0) due to the formamidine moiety (Nakamura et al. 2003, Mu et al. 2008). The low water solubility and the rapid metabolism by CYP450 enzymes require frequent administration and limited the use of the compound in preclinical studies. To improve physicochemical properties, specifically solubility and PK properties, Taisho Pharmaceutical explored derivatives with acid-stable isosteric moieties and conducted extensive structure-activity relationship (SAR) studies. Different derivatives with imidazole, triazole, pyridine, oxazole, isoxazole, isothiazole, pyrazole, pyrazine, pyrimidine, pyrrole, and tetrazole were synthesized. The SAR study suggested the crucial role of the nitrogen at the 3'-position of the various heterocyclic rings for the potent 20-HETE formation inhibition activity and a low spatial tolerance around nitrogen at the 3'-position (Nakamura et al. 2003). Among these derivatives, isoxazole (**23**) and pyrazole (**24**) derivatives maintained the potency and selectivity with improved stability under an acidic environment (Fig 1.2) (Nakamura et al. 2003). Comparing to HET0016, although the potency of compound **24** decreased by 2-fold ( $IC_{50} = 23 \pm 12$  nM), its stability improved under an acidic environment (100% remaining at pH 4.0, 50 °C, 1 day). Imidazole derivative (**3a**) exhibited good potency, but it also inhibited other CYP drug metabolizing enzymes (DMEs), which may cause drug-drug interactions (DDI).

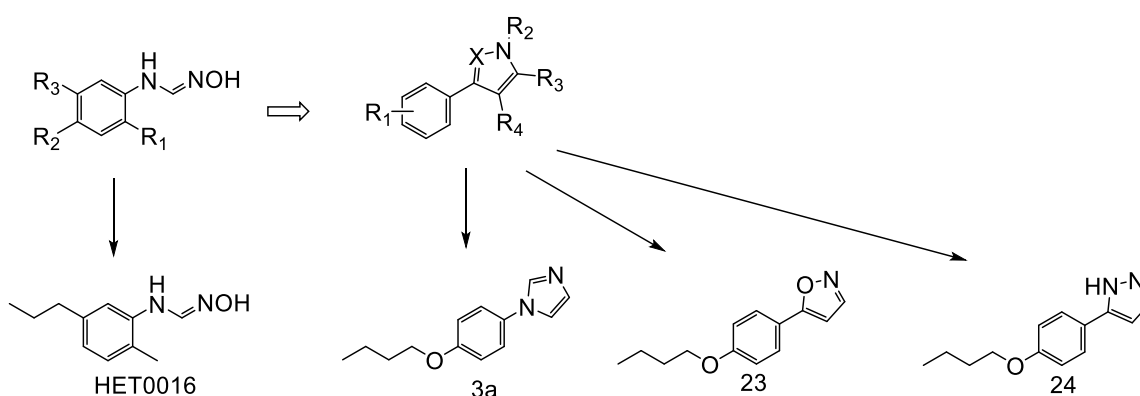


**Figure 1.2 Evolution of 20-HETE formation inhibitors and pharmacophores**

HET0016 was the first potent and selective 20-HETE formation inhibitor. Compound **3a**, **23**, and **24** were imidazole, isoxazole, and pyrazole derivatives of HET0016. The numbering of the compound follows the numbering from the referenced publication (Nakamura et al. 2003).

Multiple compounds showed 20-HETE formation inhibitory activity during the initial high throughput screening, including HET0016 and a phenylimidazole derivative (**1**) (Fig. 1.3). Compound **1** had a moderate potency ( $IC_{50} = 310$  nM). To further improve the activity of compound **1**, carboxyalkoxy moiety with 3-9 methylene groups was introduced to either 2'- or 4'-position of benzene of **1**. Derivatives with a side chain at 4'-position had improved the activity by 4- to 40-fold compared to compound **1** (e.g., **7c**,  $IC_{50} = 7.9$  nM), while derivatives with a side chain at 2'-position had reduced potency (Nakamura et al. 2004). The potency is also related to the length of the methylene group. An n of 5 for the methylene group for the carboxyalkoxy moiety at the 4'-position on benzene showed an optimum 40-fold increase of activity compared to compound **1**. The optimization also improved selectivity towards other DMEs.

The Taisho Pharmaceutical adopted multiple approaches to improve the properties of 20-HETE formation inhibitors. To decrease the affinity of **3a** to other DMEs, polar functional groups, such as amino groups, were introduced to the alkoxy side chain. Introduction of cyclic amino substituents maintained the activity against 20-HETE formation and reduced inhibition for other DMEs. Replacement of butoxy group with 2-dimethylaminohexyloxy derivative (**3g**) also yields a potent inhibitor with an  $IC_{50}$  value of 2.2 nM and an approximately 180- to 15,000-fold selectivity window toward CYP1A2, 2C9, 2C19, 2D6, and 3A4, suggesting the longer alkoxy side chain may be preferable for inhibition of 20-HETE formation (Fig. 1.3) (Nakamura et al. 2004). For the pyrazole derivatives, the introduction of polar substituents such as amino group or ether group on the side chain of compound **24** further improved the water solubility by around 100-fold. However, the increased solubility with acyclic aliphatic amino or cyclic aliphatic amino substituent was often

associated with a 10-fold loss of activity. Some piperazine derivatives with a rather bulky substitution at 4-position of the piperazine ring showed good activity, such as **3e** and **6b** (Fig. 1.3). Compound **3e** and **6b** also demonstrated attractive therapeutic potential in animal models of cerebrovascular disease (Nakamura et al. 2004). Unfortunately, there is no publicly available data regarding whether these derivatives have improved PK profiles. Our previous pharmacokinetic evaluation of HET0016 suggested that it has a high brain penetration with a brain to plasma ratio of 6 in adult rats (Mu et al. 2008). However, there were no publications reporting the brain penetration for the aforementioned derivatives. Therefore, without knowing the brain tissue concentrations of the derivatives, they might not be more optimal than HET0016 to be used as a 20-HETE formation inhibitor in preclinical cerebrovascular disease models.

N-(3-chloro-4-morpholin-4-yl) phenyl-N'-hydroxyimido formamide (TS-011) is a newer selective, potent 20-HETE formation inhibitor synthesized by Taisho Pharmaceutical, with an IC<sub>50</sub> range of 10-50 nM in human renal microsomes and recombinant CYP4A11, 4F2, 4F3B against 20-HETE formation and has > 8000-fold selectivity window against other DMEs (Fig. 1.3) (Miyata et al. 2005). TS-011 reduced CBF fall following SAH and reduced infarct size after ischemic stroke in rats. However, TS-011 has an extremely short half-life of 10 min in rats. TS-011 metabolic turnover in human liver microsomes or other *in vitro* human systems has not been disclosed, but the authors confirmed that its main metabolite did not show inhibitory effects against 20-HETE formation in human renal microsomes, suggesting the metabolite does not contribute to the pharmacological effect (Miyata et al. 2005). Therefore, the short half-life of TS-011 could be a challenge in compound development if the PD effect is driven by the compound's PK profile. Although TS-011 has a short biologic half-life in rats, the positive outcomes of TS-011-treatment in reducing infarct volume, improving CBF, and improving neurological outcomes in various

preclinical cerebrovascular disease models make it an exciting compound for structure optimization to generate novel molecules with improved PK and physicochemical properties that may also possess neuroprotective effects (Miyata et al. 2005, Tanaka et al. 2007, Renic et al. 2009, Marumo et al. 2010, Marumo et al. 2010).

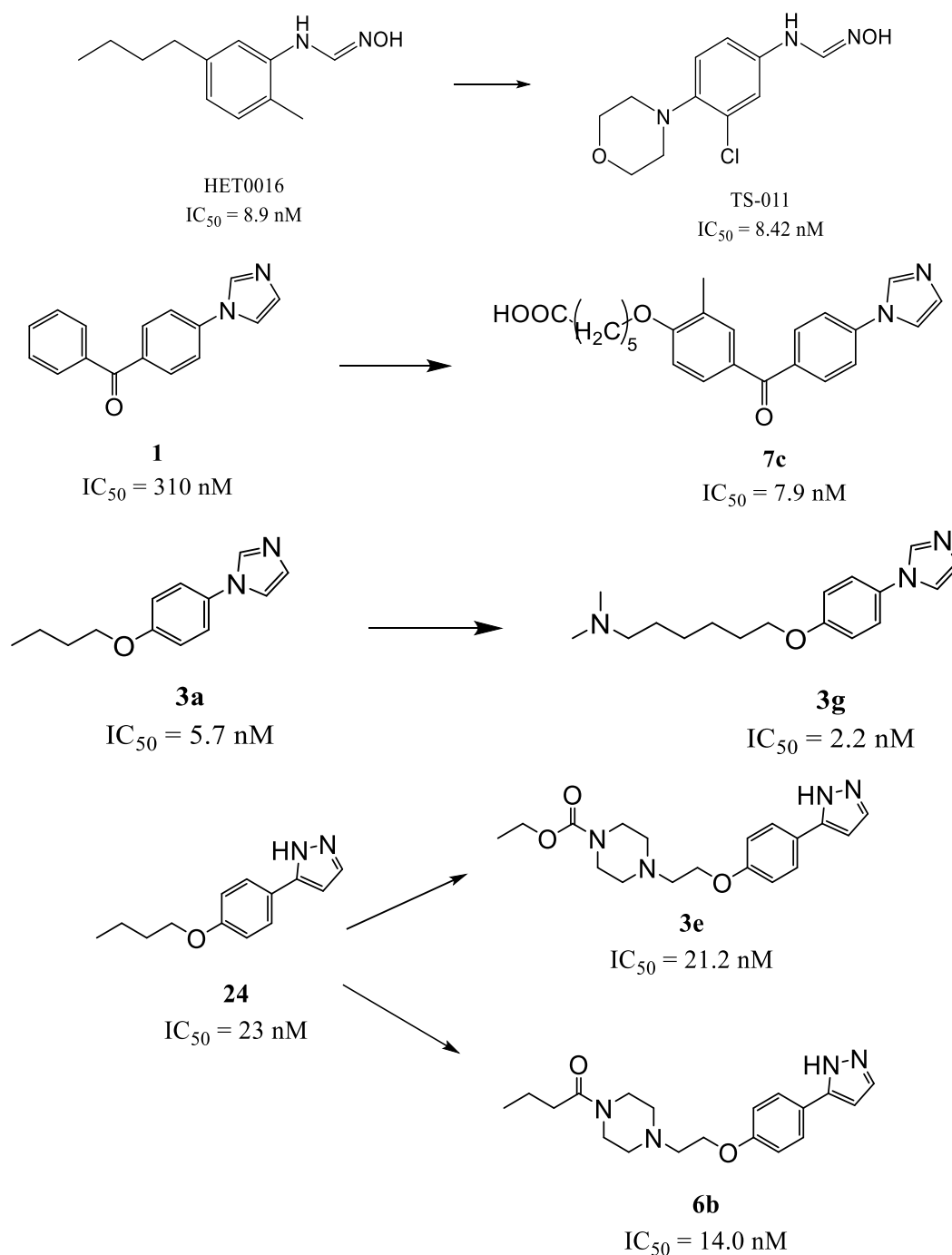


**Figure 1.3 Various 20-HETE formation inhibitors**

TS-011 is a newer 20-HETE formation inhibitor. Compound **1** was discovered together with HET0016 in high throughput screening. Compound **7c** is the derivative of compound **1** with side chain at 4'-position of benzene. Compound **3g** is a dimethylaminohexyloxy derivative of **3a** that showed decreased inhibition of DMEs. Compound **3e** and **6b** are derivatives of compound **24** with improved solubility and were tested in animal models of cerebrovascular disease. The numbering of the compounds follows the same numbers from the referenced papers (Nakamura et al. 2003, Nakamura et al. 2004, Nakamura et al. 2004, Nakamura et al. 2004).

### 1.5.3 20-HETE mimetics

Dr. John R Falck's group from The University of Texas Southwestern Medical Center reported multiple fatty acid analogs that have shown to be effective 20-HETE formation inhibitors. Four regioisomeric arachidonate isonitriles inhibited overall CYP450 arachidonic acid metabolism nonselectively with equipotency (Capdevila et al. 1988, Falck et al. 1990). At 5  $\mu$ M, 5,6-, 8,9-, 11,12-, and 14,15-NC regioisomers inhibited arachidonic acid metabolism by 51, 60, 66, and 73% (Fig. 1.4). 14,15-EET analog 14,15-EET aziridine exhibited similar potency compared to isonitriles, while the 14,15-thiirane analog was less potent.

12,12-dibromododec-11-enoic acid (DBDD) and its derivative N-methylsulfonyl-12,12-dibromododec-11-enamide (DDMS) and are dibromoolefinic fatty acids reported to selectively inhibit  $\omega$ -hydroxylation of AA with an  $IC_{50}$  of 2  $\mu$ M (Fig. 1.4) (Falck et al. 1997, Wang et al. 1998). Although the activity of both compounds is similar, DDMS was reported to have improved the resistance to  $\beta$ -oxidation. DDMS and DBDD inhibited the epoxxygenase pathway with an  $IC_{50}$  of 60  $\mu$ M and 51  $\mu$ M, respectively (Wang et al. 1998). DPMS was less potent than DDMS and DBDD, suggesting that a carboxylic acid or N-methyl sulfamide with 12 carbons may better fit the active site of CYP4A isoforms. One-hour intravenous infusion of DDMS (10 mg/kg) reduced rat renal 20-HETE formation by 70% (Alonso-Galicia et al. 1997). DDMS and DBDD had high  $IC_{50}$  values for 20-HETE formation inhibition and an approximately 25 – 30-fold selectivity window for the epoxxygenase pathway.

20-HETE effects on vascular tone are associated with activation of protein kinase C and mitogen-activated protein kinase signal transduction cascades, which suggests that the biological effect of 20-HETE is usually mediated by binding to a receptor. The 20-HETE receptor has long

been a mystery to be solved in the field. Before the discovery of the 20-HETE receptor, a series of synthetic 20-HETE analogs were developed to study whether vasoconstriction of 20-HETE can be mimicked or blocked by 20-HETE analogs (Fig. 1.5). A 19(S)-HETE analog 19-hydroxynonadecanoic acid (sC19 analog) at 1  $\mu$ M and 20-hydroxyeicosa-6(Z),15(Z)-dienoic acid [6(Z),15(Z)-20-HEDE] at 1  $\mu$ M eliminated the isolated perfused renal interlobular arteries' vasoconstrictor response to 20-HETE (Alonso-Galicia et al. 1999). In the presence of sC19 analog, the vasoconstrictor response reduced by about 50%. Similarly, the saturated derivative of 20-HETE (20-HE) displayed competitive antagonist activity (Fig. 1.5). Additional 20-HETE antagonists such as 2, 5, 8, 11, 14, 17-hexaoxanonadecan-19-yl 20-hydroxyeicosa-6(Z), 15(Z)-dienoate (20-SOLA) and N-disodium succinate-20-hydroxyeicosa-6(Z),15(Z)-diencarboxamide (**AAA**), more water-soluble 20-HETE antagonists, were disclosed. Administration of 20-SOLA (10 mg/kg/day) normalized the blood pressure in male hypertensive CYP4a14 KO mice (Garcia et al. 2015). Treatment of **AAA** in Cyp4a11 transgenic mice and Cyp1a1-Ren-2 transgenic rats induced with hypertension reduced systolic blood pressure (Savas et al. 2016, Sedláková et al. 2018).

Derivatives of endogenous 20-HETE antagonist, 19-HETE, were also explored (Fig 1.5). Appending azide to the terminal carbon of 19-HETE resulted in a 6-8 fold increased antagonism activity (compound **6**, **7**) compared to 19-HETE, which could be attributed to the increased hydrogen binding to the azide at the receptor binding site (Tchertanov 1999, Dakarapu et al. 2019). The addition of N-glycinates (**10**, **11**) led to improved potency and water solubility compared to **4**, **5** (**10** and **11**  $\approx$  0.5 mg/mL). N-aspartate derivative (**13**) also had improved activity but was not as potent as compound **11**. Intraperitoneal injection of compound **13** (10 mg/kg) to cyp4a14 (-/-) mice significantly decreased systolic blood pressure over a 10-day course.

In 2017, Garcia et al. used crosslinking analogs, click chemistry, and binding assays and identified G-protein receptor 75 (GPR75) as the 20-HETE receptor (Garcia et al. 2017). G protein-coupled receptors (GPCRs) are the largest family of transmembrane receptors that are involved in signal transduction, which mediates an array of intracellular responses (Howard et al. 2001). G protein-coupled receptor 75 (GPR75) is a 540 amino acid polypeptide, which maps to chromosome 2p16 and is identified as a novel human GPCR in 1999 by Emma E.T. et al. (Tarttelin et al. 1999). GPR75 is ubiquitously expressed in the human body, with the highest protein expression in the brain regions such as the cerebral cortex, basal ganglia, hippocampus, and amygdala (The Human Protein Atlas). The receptor has been shown to respond to stimulus through the chemokine CCL5/RANTES in a neuroprotective manner against amyloid B toxicity (Liu et al. , Ignatov et al. 2006). The identification of the 20-HETE receptor provided a new target and a new direction for novel compound development.



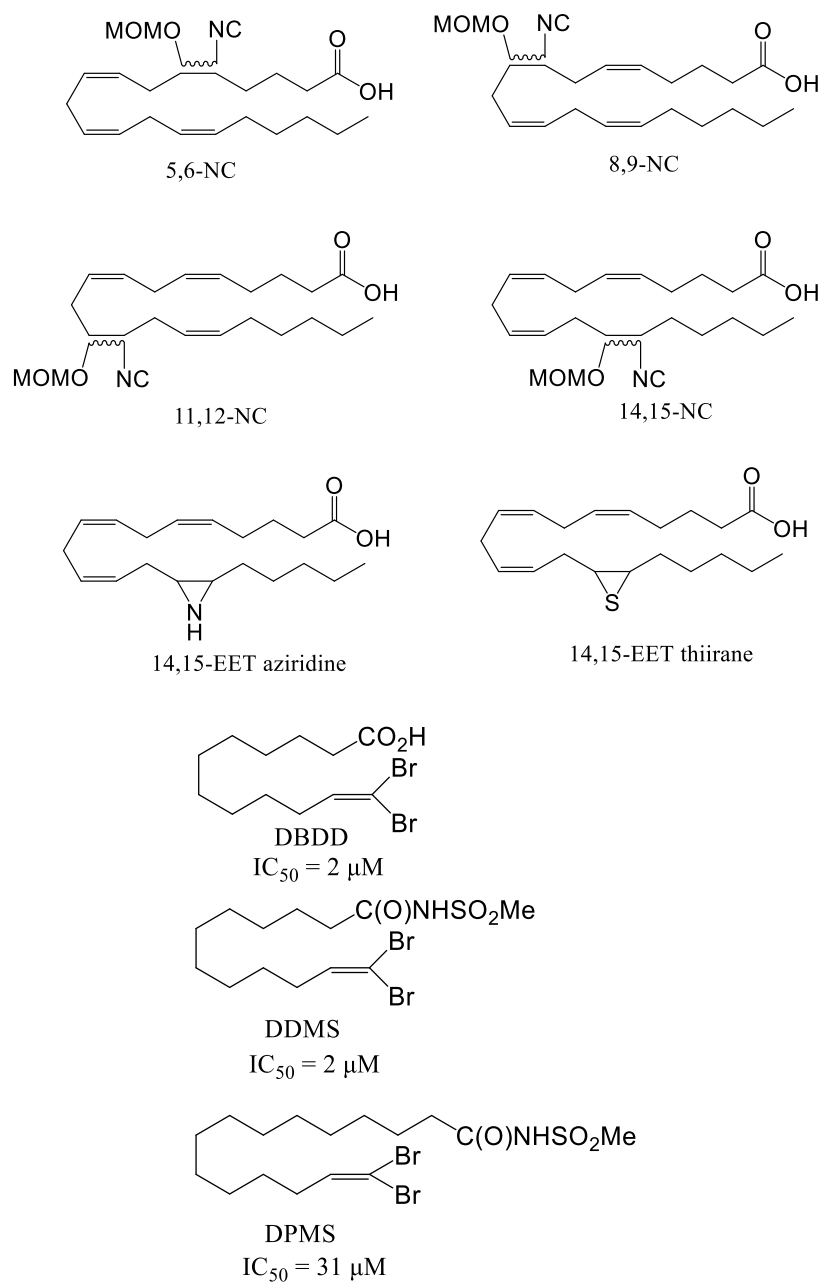
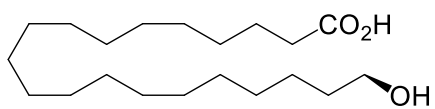
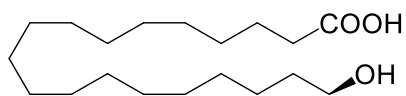


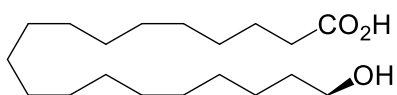
**Figure 1.4 Chemical structures of nonselective and selective arachidonic acid analogs that inhibit arachidonic acid metabolism.**



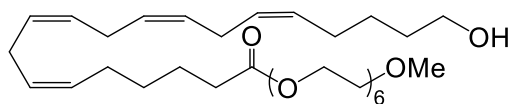
20-hydroxyeicosanoic acid (20-HE)



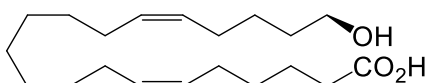
19-hydroxynonadecanoic acid



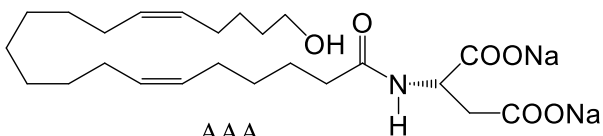
sC<sub>19</sub> analog



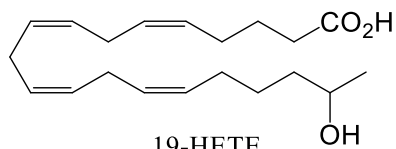
20-SOLA



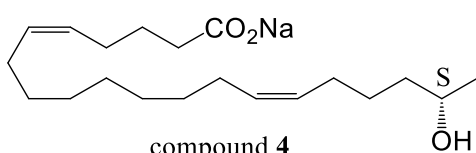
6(Z),15(Z)-20-HEDE



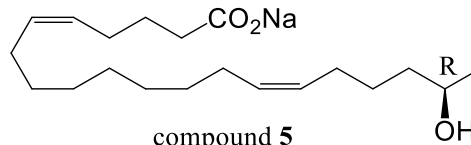
AAA



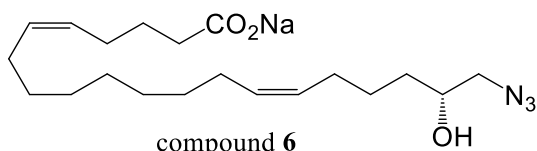
19-HETE



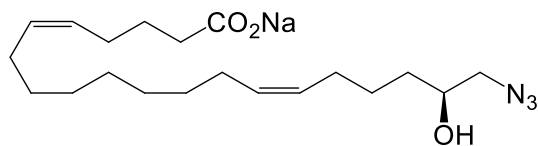
compound 4



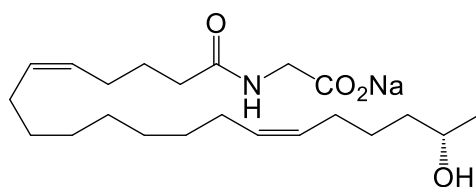
compound 5



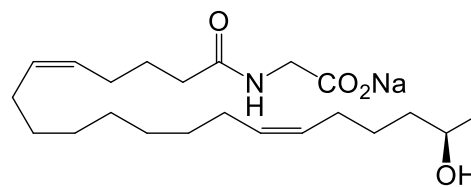
compound 6



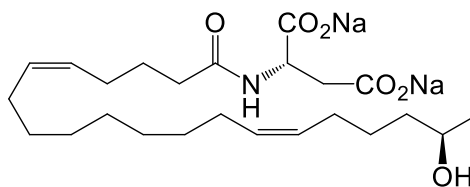
compound 7



compound 10



compound 11



compound 13

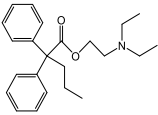
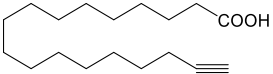
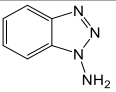
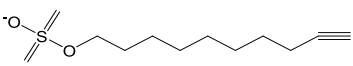
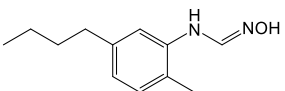
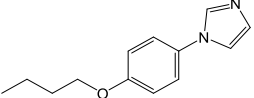
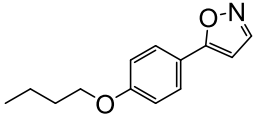
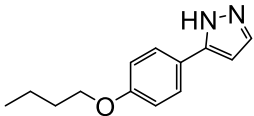
## Figure 1.5 Evolution of 20-HETE antagonists

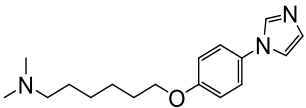
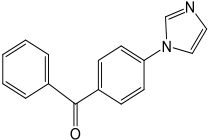
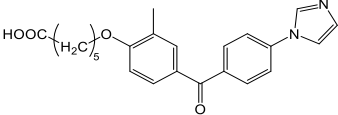
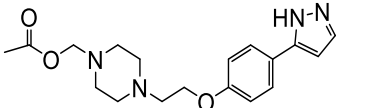
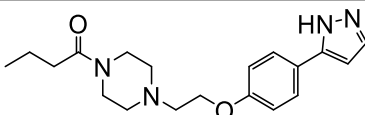
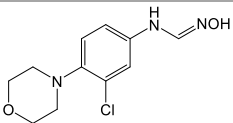
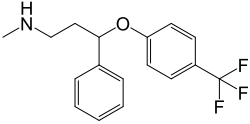
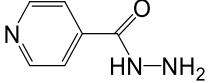
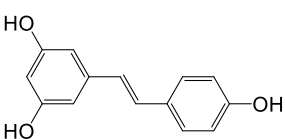
### 1.5.4 Repurposing drugs and supplements as 20-HETE formation inhibitors

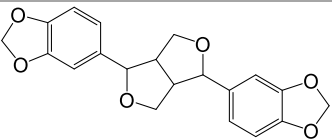
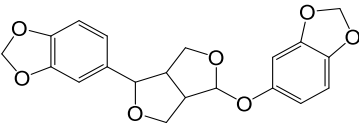
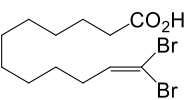
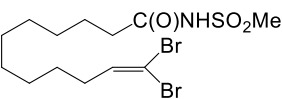
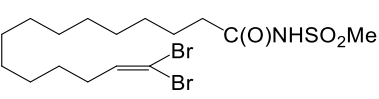
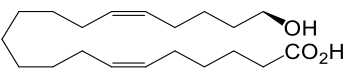
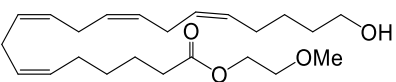
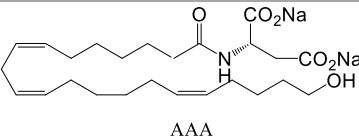
Several clinically approved drugs and supplements have been reported to inhibit 20-HETE formation. Fluoxetine has been proven to have protective effects by preventing BBB disruption in global ischemia-induced neuronal death (Lee et al. 2014). In a study done in neonatal mice, transient postnatal fluoxetine (10 mg/kg) exposure reduced brain 20-HETE concentration by 70.3%, suggesting the potential protective effect of fluoxetine in ischemic brain injury patients (Yuan et al. 2015). Isoniazid-treated male Sprague Dawley rats induced CYP2E1 protein and enzymatic function in liver and kidney, which led to increased 19-HETE levels, an endogenous 20-HETE antagonist. In isoniazid-treated animals, the 20-HETE tissue content in the liver and kidney was reduced by  $34\pm10\%$  and  $15.6\pm5.3\%$ . The 20-HETE formation rate in isolated kidney and liver tissues from isoniazid-treated rats also significantly decreased, which is in correspondence with reduced CYP4A protein expression (Poloyac et al. 2004). Similarly, in cardiac hypertrophy-induced rats treated with isoniazid (200mg/kg/day), there were increased cardiac 19-HETE levels by 20-fold and reduced 20-HETE levels by 98% (Elkhatali et al. 2015). *In vitro* incubation of arachidonic acid with resveratrol showed decreased 20-HETE formation rate, with  $IC_{50}$  values for CYP4F2, 4F3B, and 4A11 of 4  $\mu$ M, 109  $\mu$ M, and 90  $\mu$ M, respectively (El-Sherbeni et al. 2016). Using Monte Carlo simulation, the authors also predicted that 2.5g daily high and safe oral resveratrol would decrease 20-HETE levels by 16-35% in 90% of the human population (El-Sherbeni et al. 2016). Sesamin and sesamol are plant lignans derived from sesame seeds, which inhibited 20-HETE formation both *in vitro* and *in vivo* and inhibited epoxygenase

activity at  $IC_{50}$  of 50  $\mu$ M (Wu et al.). Recently, rubiarbonone C was identified as a selective CYP4F inhibitor (CYP4F2:  $IC_{50} = 4.2 \mu$ M; CYP4F3B:  $IC_{50} = 4.2 \mu$ M) among 50 natural compounds being tested. Its potency for CYP4A11 was greater than 50  $\mu$ M. The selectivity window was greater than 10-fold against CYP1, 2, and 3 families (Choi et al. 2018). Drugs or supplements identified through repurposing could potentially be evaluated for 20-HETE formation inhibitory effect in preclinical studies. These compounds could also be further optimized to explore the potency of derivatives.

**Table 1.2 20-HETE formation inhibitors and 20-HETE mimetics**

Compound	Structure	IC <sub>50</sub> (nM) in Human	IC <sub>50</sub> (nM) in Rat	Mechanism of inhibition	Reference
SKF525A		-	-	Mechanism-based	(Borrello et al. 1986, Roman 2002)
17-ODYA		-	<100 nM	Suicide substrate inhibitor, irreversible inhibition	(Zou et al. 1994, Sato et al. 2001, Edson et al. 2013)
1-ABT		μM range	-	Mechanism-based	(Sato et al. 2001, Sun et al. 2011)
10-SUYS		NA	10.1 ± 2.6	Mechanism-based	(CaJacob et al. 1986, Xu et al. 2002)
HET0016		8.9 ± 2.7 <sup>a</sup>	35.2 ± 4.4 (RKM)	Selective, non-competitive inhibitor	(Miyata et al. 2001, Sato et al. 2001, Seki et al. 2005)
3a		5.7 ± 1.0	-	-	(Nakamura et al. 2003)
23		38 ± 10	-	-	(Nakamura et al. 2003)
24		23 ± 12	-	-	(Nakamura et al. 2003)

3g		2.2	-	-	(Nakamura et al. 2004)
1		310	-	-	(Nakamura et al. 2004)
7c		7.9	-	-	(Nakamura et al. 2004)
3e		21.2	-	-	(Nakamura et al. 2004)
6b		14.0	-	-	(Nakamura et al. 2004)
TS-011		8.42 <sup>a</sup>	9.19 (RKM)	-	(Omura et al. 2006)
Fluoxetine		-	-	Alter CYP4A expression	(Yuan et al. , Ramadan et al. 2014)
Isoniazid		-	-	Alter CYP4A expression	(Poloyac et al. 2004)
Resveratrol		3 μM (HLM)		Alter CYP4A expression	(Chang et al. , Elbarbry et al. 2014, El-Sherbeni et al. 2016)

Sesamin		5.3 $\mu$ M (human)	-	-	(Wu et al.)
Sesamolin		3.4 $\mu$ M (human)	-	-	(Wu et al.)
DBDD		-	2 $\mu$ M (RKM)	Competitive inhibition, reversible	(Wang et al. 1998)
DDMS		-	2 $\mu$ M (RKM)	Competitive inhibition, reversible	(Wang et al. 1998)
DPMS		-	31 $\mu$ M (RKM)	Reversible	(Wang et al. 1998)
6(Z),15(Z)-20-HEDE		-	-	Antagonist	(Alonso-Galicia et al. 1999)
20-SOLA		-	-	Antagonist	(Garcia et al. 2015)
AAA		-	-	Antagonist	(Savas et al. , Sedláková et al. 2018)

“-”: data not available.

<sup>a</sup> IC<sub>50</sub> was measured in HKM.

### 1.5.5 Conclusions

In summary, the arachidonic acid metabolism pathways and 20-HETE play important roles in cerebral vascular tone, cerebral blood flow autoregulation, and angiogenesis. A number of preclinical studies suggested that 20-HETE formation inhibition or 20-HETE antagonism is a promising strategy to ameliorate secondary brain injury after ischemic stroke, hemorrhagic stroke, and cardiac arrest. At this time, the available 20-HETE formation inhibitors and 20-HETE antagonists are not suitable for clinical use. As such, the development of small molecules targeting either the production of 20-HETE or antagonize the 20-HETE effect is highly desirable given their potential to provide benefits in cerebrovascular diseases. We have been interested in the development of novel drug-like 20-HETE formation inhibitors. The development of bioanalytical assays and the preclinical evaluation of novel compounds to inhibit 20-HETE formation is presented in Chapters 2, 3, and 4.



## **2.0 Development of Bioanalytical Assays to Support Preclinical Evaluation of Novel 20-HETE Formation Inhibitors**

### **2.1 Introduction**

Drug discovery and development require a significant investment in both time and money. The median cost of getting a new drug into the market is 985 million, and it takes a minimum of ten years to complete the journey from initial discovery to the market (Mohs et al. 2017). The development time of the central nervous system (CNS) drugs, which requires an enormous multidisciplinary collaborative effort, takes up to 12 to 15 years (Grabowski et al. 2002).

The attrition rates of new chemical entities (NCEs) are high. Approximately 80-90% of the compounds fail before they get tested in humans. And among the drugs that enter the clinical trials, 95% failed (Seyhan 2019). The primary cause of failures includes lack of safety and efficacy in humans, suboptimal pharmacokinetics (PK) properties, nonclinical toxicity, commercial and regulatory reasons (Meanwell 2016, Fogel 2018). Twenty years ago, issues related to pharmacokinetics made up nearly 40% of drug development failures (Darvas et al. 2002). The attrition due to poor PK was around 10% when anti-infective compounds were excluded (Alavijeh et al. 2004). A more recent analysis of the 812 oral small molecule drug candidates that were developed within four major pharmaceutical companies between 2005 to 2010 showed a 5% failure due to pharmacokinetics and bioavailability (Waring et al. 2015). The decrease in suboptimal PK properties-induced failure implies the crucial knowledge that drug metabolism and pharmacokinetics (DMPK) could provide in drug development. Therefore, implementing DMPK screening during early drug development is essential to generate information for early stage drug

molecule design as well as late stage clinical study design. Developing reliable bioanalytical assays becomes an inseparable part of DMPK evaluation.

In this chapter, we reported the development of three in-house bioanalytical assays to facilitate the early profiling of novel chemical entities (NCEs). Metabolic stability (hepatic clearance) is recognized as one of the main determinants of drug concentrations. *In vitro* approaches have been extensively used to monitor metabolic stability and predict human clearance (Poloyac et al. 2020). Herein, we developed a metabolic stability assay by quantifying the depletion of the test compounds in the presence of human liver microsome using UPLC-MS/MS and derive the intrinsic clearance and half-life values. A potent CYP450 inhibitor may greatly inhibit the metabolism of a co-administered drug. Therefore, it is also essential to screen *in vitro* inhibition of major CYP450 isoforms for NCEs. We developed a UPLC-MS/MS assay that offers reliable quantification of the metabolites in the CYP cocktail assay. The observation of liabilities in these assays will provide an understanding of structural features that affect the developability of NCEs, which can be applied to guide drug design. We also developed an assay to measure a novel 20-HETE formation inhibitor in biological samples for subsequent pharmacokinetic analysis.

## **2.2 Materials and Methods**

### **2.2.1 Materials**

Acetaminophen, phenacetin, diclofenac, spectrophotometric grade dimethyl sulfoxide (DMSO), methanol (MeOH), ethyl ether, acetic acid, and other solvents were purchased from

Fisher Scientific (Pittsburgh, PA). (±)-Metoprolol (+)-tartrate, (±)-verapamil hydrochloride and warfarin were purchased from Sigma-Aldrich (St. Louis, MO). S-mephenytoin, 4'-hydroxydiclofenac, s-hydroxymephenytoin, dextromethorphan, dextrorphan, midazolam, 1'-hydroxymidazolam, and miconazole were purchased from Toronto Research Chemicals (Ontario, Canada). Acetaminophen-d4, dextrorphan-d3, 4'-hydroxymephenytoin-d4, midazolam-d4, and diclofenac-d3 were purchased from Cerilliant (Round Rock, TX). Human liver microsome (HLM), rat liver microsomes (RLM), and recombinant CYP4F2 (rCYP4F2) were purchased from Seikisui Xenotech (Lenexa, KS).

## **2.2.2 Methods**

### **2.2.2.1 Metabolic stability assay**

Microsomal incubates contained HLM (500 µg/ml), test compounds (1 µM), and NADPH (1.3 mM) in a 1 ml total volume of microsomal incubation buffer (0.12 M potassium phosphate buffer containing 5mM magnesium chloride). Each compound had three replications (n=3).

The reaction was started by adding NADPH to the incubates and was carried out at 37°C in a shaking water bath for 60 min. At 0, 15, 30, 45, 60 min, a 50 µl aliquot of incubates was removed and the reaction was stopped by adding aliquot into 200 µl ice-cold acetonitrile. After centrifugation at 14000×g for 5 min, 200 µl supernatant was used for UPLC-MS/MS analysis. Values at 0 min were used as corresponding control for test compounds. The disappearance of the parent compound over time was measured with the amount of drug at time zero as the reference. Verapamil, metoprolol, and warfarin, categorized as fast, moderate, and slow metabolized drugs, were used as positive controls. Incubates without NADPH group served as the negative control to reveal any chemical instability or non-NADPH dependent degradation. An incubation was also

performed in the boiled microsome to identify any unspecific binding. The substrate depletion method was used to calculate *in vitro* intrinsic clearance.

#### **2.2.2.2 CYP cocktail assay**

HLM was incubated with a substrates cocktail. Incubation mixtures (500  $\mu$ L) contained 0.1 M potassium phosphate buffer (pH 7.4), 3mM  $MgCl_2$ , 0.1 mg protein/ml of human liver microsomes, and NADPH (1 mM). Final concentrations of substrate cocktail listed in Table 2.2 are below their reported  $K_m$  values, i.e., 20, 2.0, 40, 5, and 2  $\mu$ M for phenacetin, diclofenac, S-mephenytoin, dextromethorphan, and midazolam, respectively. The reactions were initiated by adding NADPH to the incubation systems. The incubation was conducted at 37 °C for 10 min. The reaction was terminated by adding 12.5ul ice-cold internal standard mixtures. The samples were extracted with 1.5 ml diethyl ether, dried down under nitrogen gas, and reconstituted in 125  $\mu$ l 70:30 0.1% formic acid in  $H_2O$ : 0.1% formic acid in ACN for analysis.

#### **2.2.2.3 Biologic sample extraction for UPMP107 and 20-HETE**

**UPMP107**, a novel 20-HETE formation inhibitor, was identified as a preclinical candidate and is currently under *in vivo* evaluation in animals. A bioanalytical assay was developed to support the *in vivo* evaluation of **UPMP107**. **UPMP107** and 20-HETE concentrations were determined in brain tissue samples and plasma samples using solid phase extraction. Tissue samples were homogenized in a 0.12 M potassium phosphate buffer containing 5mM magnesium chloride and 0.113 mM butylated hydroxytoluene (BHT) and centrifuged for 30 minutes at 10,000 rpm. The supernatant was removed, 7.5ng of 20-HETE-d6 and 6.6 ng of N1-(4-butyl-2-methylphenyl) acetamide (SMIP004) (Maybridge, Cambridge, UK) were added as the internal standards. Supernatant was extracted using hydrophilic–lipophilic balance (HLB) solid phase

cartridges (Oasis, Waters, Milford, MA). Columns were washed with three 1 ml of 5% methanol and were eluted with 100% methanol. Extracts were dried under nitrogen gas at 37°C and reconstituted in 125 µl of 80:20 Methanol: deionized water. Plasma samples were added to 1ml of potassium phosphate buffer containing magnesium chloride and BHT for solid phase extraction. The eluent was processed the same as the brain samples.

#### **2.2.2.4 Chromatographic conditions**

Novel compound entities, CYP cocktail assay metabolites, and **UPMP107** separation were conducted using a UPLC BEH C18, 1.7 µm (2.1 × 100 mm) reversed-phase column (Waters, Milford, MA).

For metabolic stability assay, the column temperature was maintained at 50°C. Mobile phases consisted of 0.1% formic acid in deionized water (A) and acetonitrile (B) with a flow rate of 0.25 ml/min. The initial mixture of mobile phase was 80:20 of A and B. Mobile phase B increased from 20% to 95% at 0.5 minutes after injection in a linear gradient over 3 minutes and maintained for 0.5 minutes. This was followed by a linear return to initial conditions over 1.5 minutes. Total run time per sample was 5 minutes and all injection volumes were 7.5µl.

For the CYP cocktail assay, the column temperature was maintained at 50°C. Mobile phases consisted of 0.1% formic acid in deionized water (A) and 0.1% formic acid in acetonitrile (B) with a flow rate of 0.25 ml/min. The initial mixture of mobile phase was 70:30 of A and B. The percentage of B was increased linearly from 30 to 100% from 3 min to 4 min, then returned to 30% at 5min and maintained at 30% B for 1.5 min. Total run time per sample was 6.5 minutes and all injection volumes were 7.5µl.

For **UPMP107** separation, the column temperature was maintained at 55°C. Mobile phases consisted of 0.005% acetic acid, 5% acetonitrile in deionized water (A) and 0.005% acetic acid in

acetonitrile (B) with a flow rate of 0.5 ml/min. The initial mixture of mobile phase was 80:20 of A and B. The percentage of B was increased linearly from 20 to 70% from 2 min to 4 min and maintained at 70% B for 0.5 min. Total run time per sample was 5.5 minutes and all injection volumes were 7.5 $\mu$ l.

#### **2.2.2.5 Mass spectrometric conditions**

Mass spectrometric analysis for NCEs, CYP cocktail metabolites, and **UPMP107** was performed using a TSQ Quantum Ultra (Thermo Fisher Scientific, San Jose, CA) triple quadrupole mass spectrometer coupled with heated electrospray ionization (HESI) operated in positive selective reaction monitoring (SRM) mode with unit resolutions at both Q1 and Q3 set at 0.70 full width at half maximum.

For metabolic stability assay, the vaporizer temperature was 300 $^{\circ}$ C; spray voltage was set at 3000V; capillary temperature was set at 270  $^{\circ}$ C. Quantitation by SRM analysis on compounds was performed by monitoring their m/z transitions listed in Table 2.1.

For CYP cocktail assay, the vaporizer temperature was 314  $^{\circ}$ C; spray voltage was set at 3500V; capillary temperature was set at 202  $^{\circ}$ C. The MS conditions are presented in Table 2.2.

For **UPMP107**, the vaporizer temperature was 314  $^{\circ}$ C; spray voltage was set at 3500V; capillary temperature was set at 202  $^{\circ}$ C. To measure 20-HETE, the vaporizer temperature was 275 $^{\circ}$ C; spray voltage was set at 5000V; capillary temperature was set at 399  $^{\circ}$ C. The MS conditions for **UPMP107**, 20-HETE, and internal standards are presented in Table 2.3.

Quantitation by SRM analysis on compounds was performed by monitoring their m/z transitions. Scan time was set at 0.01 s and collision gas pressure was set at 1.2 mTorr. Analytical data were acquired and analyzed using Xcaliber 3.0 data system (ThermoFisher, San Jose, CA).

**Table 2.1 Analytical parameters for NCEs**

Compound	Precursor-product (m/z)	Collision energy (V)	Retention time (min)
Verapamil	455.3-165.0	27	2.68
Metoprolol	268.0-116.2	20	2.08
warfarin	309.1-163.3	20	3.41
<b>UPMP037</b>	286.3-254.3	18	2.87
<b>UPMP038</b>	286.1-254.2	18	2.29
<b>UPMP039</b>	286.2-254.4	20	2.91
<b>UPMP040</b>	286.3-254.3	20	2.32
<b>UPMP043</b>	244.1-150.3	26	2.42
<b>UPMP045</b>	286.2-126.2	14	2.44
<b>UPMP046</b>	242.1-96.2	26	3.20
<b>UPMP047</b>	242.2-150.2	20	2.51
<b>UPMP048</b>	320.1-227.4	31	1.69
<b>UPMP049</b>	320.2-227.3	31	2.49
<b>UPMP050</b>	259.2-122.2	21	0.96
<b>UPMP051</b>	272.1-96.2	33	2.81
<b>UPMP054</b>	272.2-96.2	32	2.17
<b>UPMP057</b>	260.1-96.2	26	2.72
<b>UPMP060</b>	299.0-150.0	21	1.06
<b>UPMP107</b>	325.0-251.0	27	1.38
<b>UPMP117</b>	276.0-150.1	20	1.65
<b>UPMP124</b>	311.3-150.2	21	2.13

**Table 2.2 Analytical parameters for the individual metabolites and internal standards**

	CYP1A2	CYP2C9	CYP2C19	CYP2D6	CYP3A4
Substrate	Phenacetin	Diclofenac	S-Mephenytoin	Dextromethorphan	Midazolam
Concentration	20 µM	2 µM	40 µM	5 µM	2 µM
Metabolite	Acetaminophen	4'-OH-diclofenac	4'-OH-mephenytoin	Dextrorphan	1'-OH-midazolam
Internal standard	Acetaminophen-d4	Diclofenac-d3	4'-OH-mephenytoin-d4	Dextrorphan-d3	Midazolam-d4
Retention time (min)	1.25	4.78	1.69	1.30	2.49
Ionization mode	+	+	+	+	+
Collision energy (V)	15	33	16	37	25
Precursor-product (m/z)	152.1-110.2	312.1-230.1	235.3-150.4	258.1-157.2	342.1-203.1
Linearity range (ng on column)	25-6000	25-3000	25-6000	25-6000	25-6000
QC high	1250	1250	1250	1250	1250
QC medium	450	450	450	450	450
QC low	75	75	75	75	75

**Table 2.3 Analytical parameters for UPMP107, 20-HETE and internal standards**

Analyte	UPMP107	20-HETE
Internal standard	SMIP004	20-HETE-d6
Retention time (min)	1.25	3.70
Ionization mode	+	-
Collision energy (V)	17	20
Precursor-product (m/z)	325.3-240.3	319.3-245.1,
Linearity range (ng on column)	12.5-1500	12.5-1500
QC high	900	900
QC medium	450	450
QC low	45	45



#### **2.2.2.6 Method validation**

Analysis on three separate days was performed to confirm the precision and accuracy of the LC-MS/MS method for the simultaneous quantification of six CYP-specific probe metabolites. Calibration curves were prepared at different concentration levels in microsomal incubation buffer. The deviation of the lower limit of quantification (LLOQ) should be within 20% and the accuracy of each concentration level should be within 85-115% according to the US Food and Drug Administration Bioanalytical Method Validation Guidance (2018). Quality control (QC) samples at three different concentrations were used to evaluate accuracy and precision. Intra-day precision and accuracy were determined by analyzing the QC samples on the same day. Inter-day precision was evaluated by analyzing the QC samples on three separate days. Precision and accuracy should not exceed  $\pm 15\%$ . The limit of detection (LOD) was defined as the signal-to-noise ratio = 3. LLOQ samples (n=5) were measured with precision ( $\pm 20\%$  RSD) and accuracy (80-120%). The lowest quantifiable concentration on the curve was the LLOQ.

### **2.3 Results**

#### **2.3.1 Validation of metabolic stability assay experimental system**

The primary purpose of developing the metabolic stability assay is to set up an in-house assay to determine *in vitro* metabolism and obtain estimates of *in vitro* intrinsic clearance for NCEs.

The assay conditions were determined based on literature reported values (Di et al. 2003). Test compounds concentration was set at 1  $\mu\text{M}$  to ensure the reaction is under a linear condition. The percentage of organic solvent was set at 0.5% to reduce the inhibitory effect on enzymatic activity. The protein concentration was 0.5 mg/ml to prevent non-specific binding. The amount of NADPH was 1.3 mM to ensure a saturated amount of cofactor in the system during a 1-hour incubation period. The peak area was used for each test compound as a surrogate for the amount. The assay was validated with verapamil, metoprolol, and warfarin known as fast, moderate, and slow metabolism positive controls in HLM (Fig. 2.1).

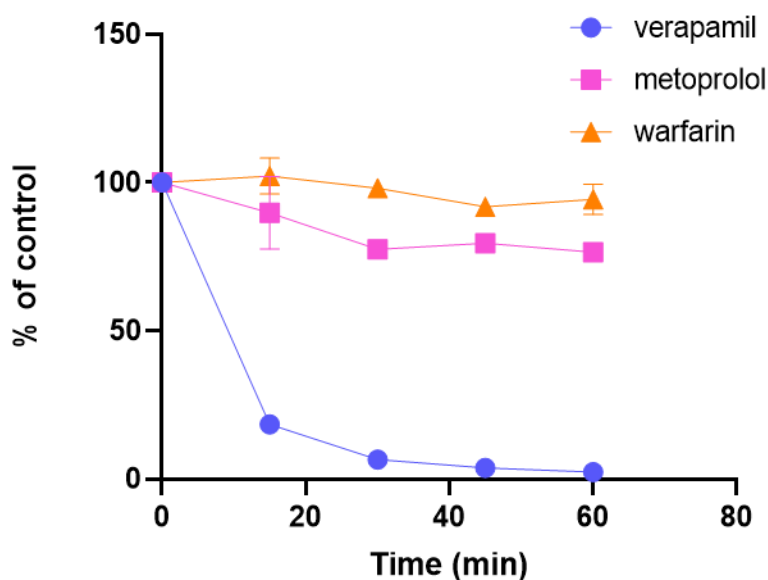


**Figure 2.1 Metabolic stability for verapamil, metoprolol, and warfarin**

The remaining percentage of verapamil, metoprolol, and warfarin was 98%, 77% and 6.5%, respectively.

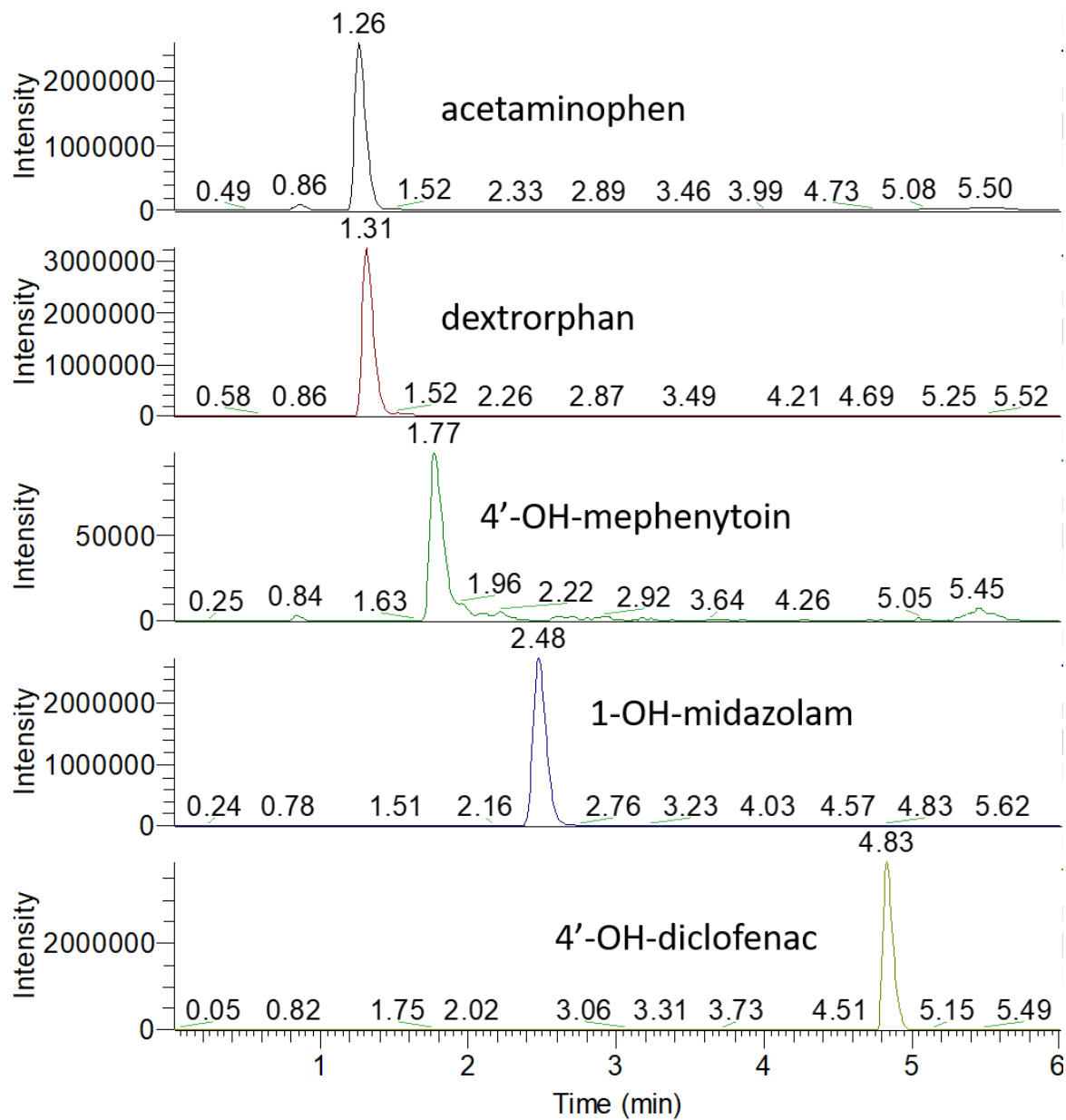
### **2.3.2 Chromatography and specificity for CYP probe metabolites**

The primary purpose of developing the CYP inhibition assay is to set up an in-house method to assess CYP-mediated inhibition for NCEs. The probe substrates used for the cocktail

assay included phenacetin (CYP1A2), diclofenac (CYP2C9), S-mephenytoin (CYP2C19), dextromethorphan (CYP2D6), and midazolam (CYP3A4). The substrates were selected based on the U.S. FDA recommendation. Internal standards include acetaminophen-d4, diclofenac-d3, 4'-OH-mephenytoin-d4, dextrorphan-d3, and midazolam-d4. The mixture of internal standards was added to the microsomal incubation system at the end of the reaction. All metabolites were eluted within 6 min. This saved time compared with previously published methods. The elution profiles of all metabolites and internal standards are shown in Fig. 2.2.

An incubation time of 10 minutes was used for the cocktail assay based on the reported literature where metabolite formation rates were linear during this incubation period (Li et al. 2015). Liquid-liquid extraction with diethyl ether was used as it showed the best sensitivity in detection.

A



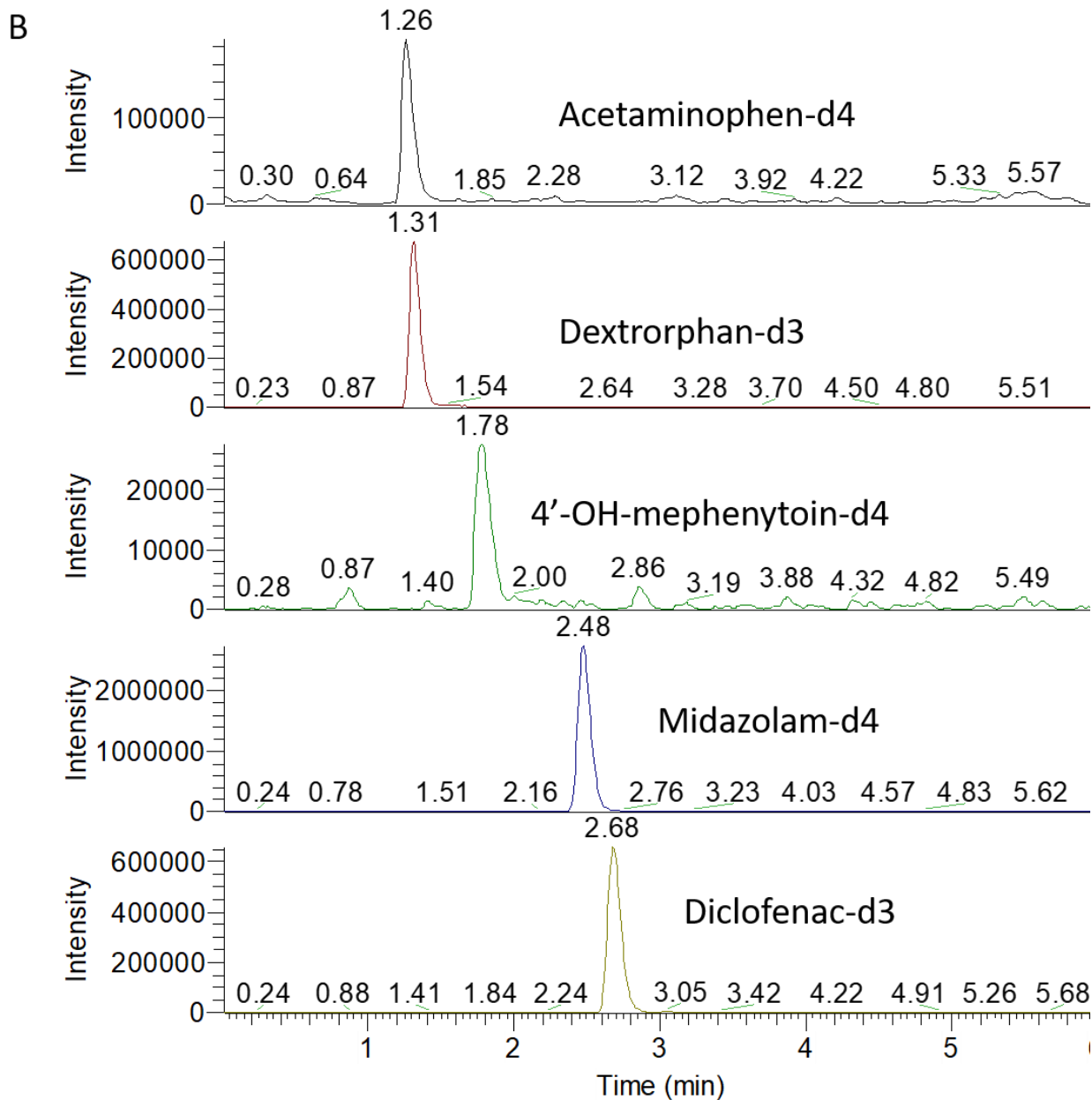


**Figure 2.2 Chromatograms of metabolites and internal standards**

(A) Metabolites for five CYP isoforms including acetaminophen, dextrorphan, 4'-OH-mephenytoin, 1-OH-midazolam, 4'-OH-diclofenac. (B) Internal standards including acetaminophen-d4, dextrorphan-d3, 4'-OH-mephenytoin-d4, midazolam-d4, and diclofenac-d4.

### 2.3.3 UPLC-MS/MS method validation for CYP inhibition assay

The concentration ranges of calibration curves and the QC samples are shown in Table 2.2. The calibration curves for each metabolite were:  $y = -0.0054 + 0.0109X$  for acetaminophen;  $y = -0.0104 + 0.0051X$  for dextrorphan;  $y = 0.0177 + 0.0031X$  for 4'-hydroxymephenytoin;  $y = -0.0171 + 0.0046X$  for 1'-hydroxymidazolam;  $y = -0.0688 + 0.0149X$  for 4'-hydroxydiclofenac;  $y$  represents the peak area ratio of metabolite vs corresponding internal standard. A weighting factor of  $1/y$  was placed on the calibration curve. The calibration curves showed good linearity in the concentration range for each metabolite ( $R^2 > 0.995$ ). The accuracy of each standard level in the calibration curve meets the recommended limits (85-115%) and LLOQ meets the 80-120% limit shown in Table 2.4.

The within-day and between-day precisions were below 10% and 16%, respectively. The precision for LLOQ was  $< 20\%$ , the accuracy obtained from LLOQs was within 80-120%.

**Table 2.4 Validation data: within-day precision, between-day precision and accuracy (n=5)**

		Acetaminophen	4'-Hydroxydiclofenac	4'-Hydroxymephenytoin	Dextrophan	1'-Hydroxymidazolam
Within-day Accuracy	HQC	-5.12%	8.57%	0.36%	-0.46%	2.83%
	MQC	3.06%	3.30%	2.62%	-4.04%	-4.84%
	LQC	-0.15%	-4.63%	-1.41%	-5.14%	3.45%
	LLOQ	1.24%	8.27%	4.61%	5.81%	16.0%
Between-day accuracy	HQC	4.59%	10.7%	2.12%	5.16%	7.61%
	MQC	0.43%	5.07%	0.57%	-2.95%	-1.19%
	LQC	-1.50%	-4.11%	-1.38%	-3.40%	1.06%
	LLOQ	-2.82%	11.5%	-4.34%	-3.56%	-2.62%
Within-day precision (%RSD)	HQC	8.02%	9.26%	7.02%	2.89%	4.36%
	MQC	4.60%	5.78%	3.80%	3.62%	5.16%
	LQC	5.60%	7.34%	6.09%	3.19%	7.75%
	LLOQ	10.5%	7.54%	10.3%	9.02%	7.47%
Between-day precision (RSD%)	HQC	10.7%	6.70%	6.40%	9.00%	6.10%
	MQC	6.40%	6.90%	5.90%	6.80%	6.10%
	LQC	6.70%	8.50%	9.20%	7.50%	9.30%
	LLOQ	12.0%	11.5%	16.6%	13.7%	16.0%

### 2.3.4 Validation of the CYP cocktail assay experimental system

Typically, a reliable *in vitro* CYP inhibition study should be conducted under a linear condition, where the formation of a metabolite is linearly correlated with the enzyme concentration and incubation time. High microsomal protein might complicate data interpretation, such as non-specific binding. Based on the FDA recommendation, the protein concentration should no more than 1mg/ml. Industrial scientists have suggested using a microsomal protein concentration as low as feasible (Obach 1997). We chose 0.1 mg protein/ml in our assay based on the reported values used in most of the literature.

We adopted the incubation conditions including protein amount, incubation time, substrate concentration from the most often reported values in the literature. The assay was partially validated by comparing the metabolite formation rates from our study to published literature values (Table 2.5). Broad inhibition with pan-inhibitor miconazole (3  $\mu$ M) was observed (Table 2.5). Our assay results were generally consistent with the published data (Liu et al. 2015, Chen et al. 2016).

**Table 2.5 Comparison of CYP activities between our data with published data**

Enzyme	Substrate	Enzymatic activity (pmol/min/mg protein) mean $\pm$ SD	Published value (pmol/min/mg protein) mean $\pm$ SD	Percentage of activity inhibited by miconazole
CYP1A2	Phenacetin	295 $\pm$ 20.0	162 $\pm$ 3.00	51.8 $\pm$ 2.95%
CYP2C9	Diclofenac	198 $\pm$ 37.0	155 $\pm$ 1.09	91.6 $\pm$ 1.05%
CYP2C19	S-Mephenytoin	11.1 $\pm$ 3.75	15.0 $\pm$ 0.70	99.6 $\pm$ 0.32 %
CYP2D6	Dextromethorphan	71.0 $\pm$ 14.6	87.8 $\pm$ 4.10	56.7 $\pm$ 1.43%
CYP3A4	Midazolam	249 $\pm$ 41.0	280 $\pm$ 1.32	95.5 $\pm$ 0.32 %



### 2.3.5 Chromatography and specificity for UPMP107 and 20-HETE

The goal of developing an analytical method for a novel 20-HETE formation inhibitor - **UPMP107** is to evaluate its amount in biological samples for subsequent pharmacokinetic or pharmacodynamic study. We evaluated the solid phase extraction sample processing method and developed a UPLC-MS/MS method to quantify **UPMP107**. The advantage of this assay is the application of the same mobile phase as AA metabolite quantification, which can improve the sample processing and quantification efficiency. Figure 2.3 displays typical chromatographs of **UPMP107** and 20-HETE along with the internal standards SMIP004 and 20-HETE-d6.

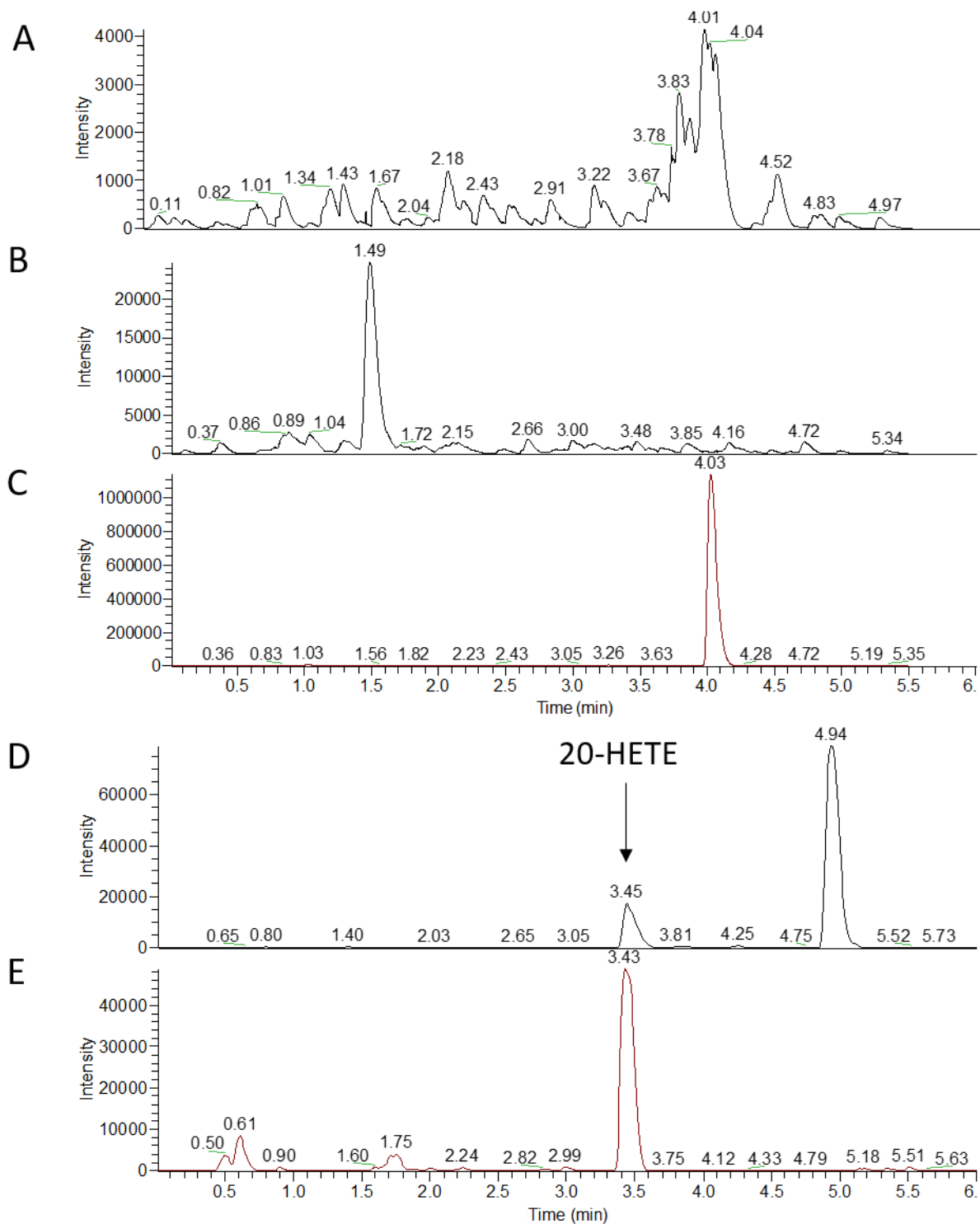


**Figure 2.3 Chromatograms of (A) blank, (B) UPMP107, (C) SMIP004, (D) 20-HETE, and (E) 20-HETE-d6 in plasma and brain samples**

### 2.3.6 UPLC-MS/MS method validation for UPMP107

The calibration standards ranged from 12.5 to 1500 pg on column. The QC levels are listed in Table 2.6. A weighting factor of 1/Y was placed on the calibration curve. The calibration curves showed good linearity in the concentration range for each metabolite ( $R^2 > 0.995$ ). The accuracy of each standard level in the calibration curve meets the recommended limits (85-115%) and LLOQ meet the 80-120% limit shown in Table 2.6.

The within-day and between-day precisions were below 14% and 18%. The precision for LLOQ was < 20%, the accuracy obtained from LLOQs was within 80-120%.

**Table 2.6 UPMP107 validation data: within-day precision, between-day precision and accuracy (n=5)**

		Levels	UPMP107	20-HETE
Within-day Accuracy	HQC	900	6.22%	-0.11%
	MQC	450	0.25%	-0.49%
	LQC	40	0.33%	-1.02%
	LLOQ	12.5	4.68%	-2.08%
Between-day accuracy	HQC	900	2.97%	-2.32%
	MQC	450	0.59%	-0.83%
	LQC	90	3.29%	-1.51%
	LLOQ	12.5	8.92%	7.74%
Within-day precision (%RSD)	HQC	900	4.71%	4.47%
	MQC	450	6.19%	2.24%
	LQC	90	4.46%	7.29%
	LLOQ	12.5	9.09%	13.7%
Between-day precision (RSD%)	HQC	900	8.88%	6.87%
	MQC	450	14.8%	2.45%
	LQC	90	10.2%	5.74%
	LLOQ	12.5	11.3%	17.5%

## 2.4 Discussion and conclusions

In this chapter, we developed three bioanalytical assays to support the early stage characterization and profiling of novel compounds. The employment of the assays will be used for metabolic stability evaluation, drug-drug interaction evaluation, and quantification of a preclinical candidate. These assays are integral parts of DMPK evaluation and can aid decision-making for NCEs advancement.

We developed a metabolic stability assay in HLM and UPLC-MS/MS method to enable fast screening of the *in vitro* clearance for NCEs. Drug metabolism can be classified as phase I and phase II, where phase I reactions like oxidation, reduction, and hydrolysis, which provide metabolites that may then get conjugated with glucuronic acid to increase water solubility during phase II reactions by enzymes, such as UDP-glucuronyl transferases (Sheweita 2000). Metabolic stability can be evaluated in liver microsomes or hepatocytes. Microsomes are commonly used systems for CYP-mediated phase I metabolism. Hepatocytes contain intact cell organelles that can be used to evaluate both phase I and phase II metabolism in a relatively more physiologically relevant system (Baranczewski et al. 2006). Regardless of the testing systems, the results generated from the assay include *in vitro* intrinsic clearance and *in vitro* half-life, which can be used to scale to *in vivo* intrinsic clearance using scaling factors (Bowman et al. 2019). The use of an *in vitro* drug metabolism approach to predict *in vivo* PK parameters has been widely practiced in the pharmaceutical industry. Compounds can be ranked based on their half-life or clearance values. Molecules demonstrating a low *in vitro* clearance and a prolonged *in vitro* half-life are favorable since they may be removed from the body slowly to ensure an adequate exposure for therapeutic effect. We acknowledge the limitation of using HLM as the testing system. However, in drug discovery, microsomes are more convenient for screening assays due to their commercial

availability and long storage time. Our metabolic stability assay obtains data at multiple time points throughout a 60-min incubation period. The data at multiple time points increased the predictability of *in vitro* half-life and the long incubation duration is able to differentiate stable compounds from unstable compounds. The limitation for a longer incubation duration is the lack of information to differentiate unstable compounds that may have half-lives shorter than 5 min (Di et al. 2004). Since our goal is to identify compounds with high metabolic stability, a 60-min incubation duration is deemed reasonable. The assay will be applied to test metabolic stability for novel molecules to ensure the selection of optimal compounds for further evaluation as well as guiding the design of compounds with improved metabolic stability properties.

We transferred an *in vitro* CYP cocktail assay in our lab and developed a UPLC-MS/MS method to assess the potential of drug-drug interaction for NCEs on five drug metabolizing CYP enzymes (CYP1A2, CYP2C9, CYP2C19, CYP2D6, and CYP3A4). Drug interactions can have a significant impact on the efficacy and safety of drugs. Polypharmacy is common in clinical practice and is more pronounced in critically ill patients, where there is a potential for drug-drug interactions (DDIs) (Dai et al. 2016). Therefore, evaluation of potential DDIs during early drug development can provide essential information on specific pathways to guide future clinical DDI studies (Tornio et al. 2019). HLM is a useful *in vitro* system to evaluate DDIs for molecules during early drug development (FDA 2017). Traditionally, DDI studies have been performed with individual CYP450 isoform. However, this approach is time-consuming and costly. A cocktail method by incubating several probe substrates simultaneously decreases the time and money costs. One of the major concerns in the cocktail assay is substrate interactions. CYP enzyme activities will be compromised as a result of potential substrate interactions. The probe substrate concentrations were selected below the reported  $K_m$  values to ensure the reaction falls within the

linear formation range. The lower concentrations of substrates also decrease the interactions in the cocktail assay (Spaggiari et al. 2014). We selected a 5-in-1 cocktail since CYP1A2, 2C9, 2C19, 2D6, and CYP3A4 account for the metabolism of approximately 90% of drugs (Lynch et al. 2007). Phenacetin was selected for CYP1A2 because of its specificity and it is the most often used substrate in other studies. Tolbutamide and diclofenac are frequently used probe substrates for CYP2C9. Bufuralol and dextromethorphan are commonly used probe substrates for CYP2D6. Although either probe substrate can be used, we selected diclofenac 4'-hydroxylation and dextromethorphan *O*-demethylation for CYP2C9 and 2D6 as these reactions were more frequently used in published papers (Spaggiari et al. 2014). For CYP2C19, we selected the FDA preferred probe substrate (*S*)-mephenytoin. For CYP3A4, we selected midazolam as recommended by the FDA (FDA 2020). The addition of chlorzoxazone doubled the run time due to its negative SRM mode for mass spectrometry quantification and unsatisfactory results with rapid polarity switching. Therefore, chlorzoxazone was not included in the cocktail. A limitation of the cocktail assay is that we did not conduct a full validation. An ideal full validation requires the determination of  $K_m$  values within the laboratory, testing the incubation conditions to ensure linear formation of the metabolites, and comparing cocktail formation rates with the individual incubation formation rates to validate the minimal interaction between substrates. In this method transfer between reported literature and our laboratory, we partially validated the assay by comparing the metabolite formation rates with published values. The overall less than 2-fold difference in enzymatic activity suggested the analytical method transfer was successful (Table 2.5). We also developed and validated a UPLC-MS/MS method to measure metabolites in the cocktail assay that meet the FDA recommendations. The quantification of metabolites was completed by a precise, sensitive, and

accurate UPLC-MS/MS method. The developed assay will be used to screen DDI potentials for novel molecules.

Herein, we reported the development and validation of a simple UPLC-MS/MS method for **UPMP107** and 20-HETE quantification with good linearity, sensitivity, accuracy, and precision. This is the first method for **UPMP107** quantification and will be applied to a pharmacokinetic study in Sprague-Dawley rats to measure **UPMP107** and 20-HETE concentrations in biological samples. In conclusion, we have developed three assays that would be employed to evaluate the preclinical profile of novel 20-HETE formation inhibitor compounds.

### **3.0 *In vitro* Evaluation of Novel Compounds: Discovery of UPMP107 as a Potent and Selective Inhibitor of 20-HETE Synthesizing Enzymes**

#### **3.1 Introduction**

Greater than 50% of survivors who were successfully resuscitated from cardiac arrest have neurological disabilities, which is the major limiting factor for full recovery (Iordanova et al. 2017). Alterations of cerebral blood flow (CBF) have been reported in both humans and various animal models after cardiac arrest. Post-cardiac arrest CBF disturbance can be classified into three stages. The initial stage is the absence of flow during cardiac arrest and cardiopulmonary resuscitation. The second stage is cerebral hyperemia that usually occurs at 5- 30 min after resuscitation following the return of spontaneous circulation. The last stage is cerebral hypoperfusion that occurs at 30 min – 6 h after hyperemia (Buunk et al. 2000). CBF-directed therapies have shown promising results in various animal species after cardiac arrest, encouraging the discovery and development of relevant molecules targeting specifically at the hypoperfusion phase of CBF alteration (Li 2019).

20-hydroxyeicosatetraenoic acid (20-HETE), a major metabolite of arachidonic acid (AA), plays a key role in CBF autoregulation by constricting brain arteries (Gebremedhin et al. 2000, Kehl et al. 2002). The formation of 20-HETE is catalyzed by cytochrome P450 (CYP) 4A and 4F enzymes in rats and humans (Ito et al. 1998, Powell et al. 1998). Elevations in 20-HETE concentrations contribute to the acute fall of CBF, neuronal toxicity, and delayed vasospasm after experimental ischemic stroke and subarachnoid hemorrhage (Kehl et al. 2002, Roman et al. 2006, Yang et al. 2012). The protective effect of 20-HETE inhibition is not only contributed by the



improvement in cerebral perfusion and cerebral blood flow, but also in the reduced brain edema, decreased blood-brain-barrier (BBB) leakage, and direct neuron protection (Poloyac et al. 2006, Lee et al. 2011, Renic et al. 2012, Shaik et al. 2015, Lu et al. 2018). Several studies in humans revealed the unfavorable role of 20-HETE where increased CSF 20-HETE levels are associated with delayed cerebral ischemia, poor neurological outcomes, and three-fold higher mortality in subarachnoid hemorrhage patients and plasma 20-HETE has found to be a predictor of neurological deterioration in acute minor ischemic stroke. (Crago Elizabeth et al. 2011, Donnelly et al. 2015, Yi et al. 2016). Therefore, developing therapies targeting 20-HETE formation is a promising approach to improve CBF after cardiac arrest.

Despite a number of efforts in medicinal chemistry, computational chemistry, and repurposing from natural products, no molecule that inhibits 20-HETE formation is in the clinical development stage. Figure 3.1 displays several currently available molecules that reported to inhibit 20-HETE formation in the literature. Available compounds have either unfavorable physicochemical properties or lack proper pharmacokinetic properties. Natural products like sesamin and resveratrol require large doses to inhibit 20-HETE (Wu Jason et al. 2009). Some arachidonic acid analogs like 17-ODYA nonselectively inhibit 20-HETE and EETs formation (Sato et al. 2001). Potent and selective inhibitors such as HET0016 and TS-011 are hampered by either fast metabolism or low water solubility (Mu et al. 2008). Therefore, there is a pressing need for the discovery and development of novel clinical viable 20-HETE formation inhibitors.

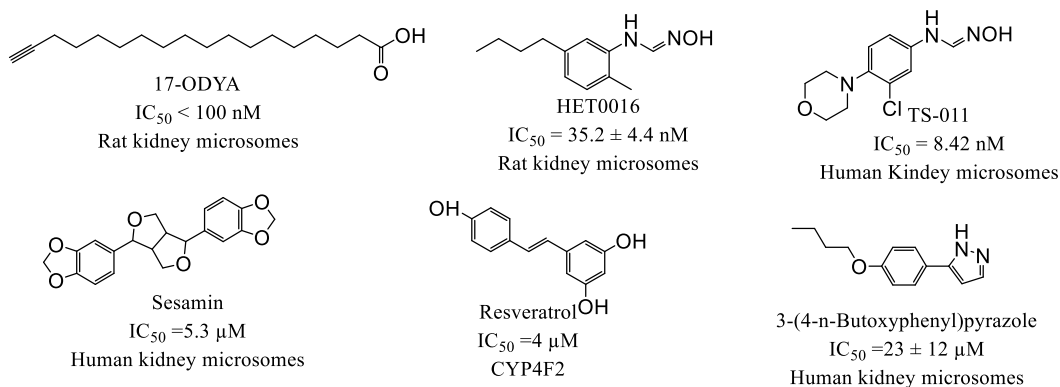


**Figure 3.1 Representative examples of 20-HETE formation inhibitors**

To identify compounds that overcome the disadvantages of previously reported molecules and identify preclinical candidates with improved physicochemical and pharmacokinetic characteristics, we proposed a tiered approach for screening and assessing novel compounds (Fig. 3.2). Tier 1 encompasses *in silico* assessment of physicochemical properties of designed compounds for being within a range seen in other central nervous system (CNS) acting drugs. Tier 2 involves the single concentration screening of synthesized compounds to evaluate their ability to inhibit 20-HETE formation in three types of microsomes. Tier 3 includes a more thorough *in vitro* evaluation, where compounds were subjected to various *in vitro* assays to assess potency, selectivity, solubility, metabolism, CYP inhibition, brain penetration, and *in vitro* toxicology. Successful compounds that met the criteria set for each of the steps in Tier1 to 3 would be considered as preclinical candidates. The evaluation from Tier 1 to Tier 3 is iterative. The best compounds that meet all criteria would be selected and be taken forward to Tier 4 *in vivo* pharmacokinetic and pharmacodynamic evaluation. Upon demonstration of good *in vivo* PK and target engagement in the brain, preclinical candidates would be assessed in a pediatric cardiac arrest injury model to test *in vivo* neuroprotective effects. Compounds would advance through tiers if they satisfy benchmarks in prior tiers. By applying this tiered evaluation approach, it ensures the efficient use of resources to select compounds. Specifically, in Tier 3, compounds that did not

meet the criteria for any single assay would be considered to be precluded from the preclinical candidate pool. Therefore, not every compound that entered Tier 3 was tested in all the proposed assays. With the data we obtained throughout the tiered evaluation, we present a decision tree in section 3.3.5 to illustrate the selection of a preclinical candidate to be advanced to *in vivo* evaluation.

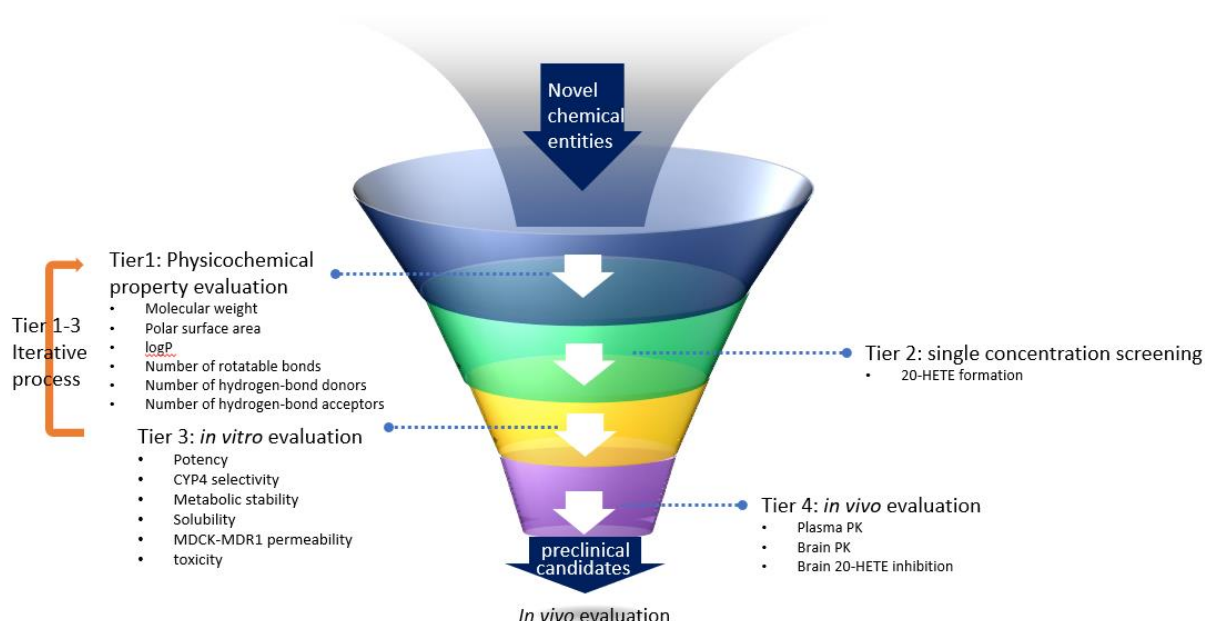


**Figure 3.2 A tiered approach to evaluate novel compounds**

The purpose of this study is to identify novel 20-HETE formation inhibitors with strong potency, CYP4 selectivity, improved physicochemical and pharmacokinetic properties compared to currently available molecules. The key objective is to identify a 20-HETE formation inhibitor that could have a high probability of advancement into clinical development as a neuroprotective agent. Here, we report the preclinical evaluation of a library of novel small molecules and the discovery of **UPMP107**, a novel 20-HETE formation inhibitor that fulfilled all criteria from Tier 1 to 3. This novel 20-HETE formation inhibitor is a promising preclinical candidate. It has (1) strong potency against 20-HETE formation; (2) high selectivity for CYP4 enzymes over CYP1A2,

2C9, 2C19, 2D6, 3A4, and epoxigenases; (3) low *in vitro* intrinsic clearance in human liver microsomes; (4) good *in vitro* BBB penetration in MDCK-MDR1 assay with (6) no safety flags when assessed at 10  $\mu$ M in the *in vitro* Cerep SafetyScreen44 panel.

## 3.2 Materials and methods

### 3.2.1 Materials

Novel compounds **UPMP001-143** were designed and synthesized in the lab of our collaborator Dr. Lee McDermott (School of Pharmacy, University of Pittsburgh). Stock standards of ( $\pm$ )5,6-dihydroxy-8Z,11Z,14Z-eicosatrienoic acid (5,6-DiHET), ( $\pm$ )8,9-dihydroxy-5Z,8Z,14Z-eicosatrienoic acid (8,9-DiHET), ( $\pm$ )11,12-dihydroxy-5Z,8Z,14Z-eicosatrienoic acid (11,12-DiHET), ( $\pm$ )14,15-dihydroxy-5Z,8Z,11Z-eicosatrienoic acid (14,15-DiHET), ( $\pm$ )8(9)-epoxy-5Z,11Z,14Z-eicosatrienoic acid (8,9-EET), ( $\pm$ )11(12)-epoxy-5Z,8Z,14Z-eicosatrienoic acid (11,12-EET), ( $\pm$ )14(15)-epoxy-5Z,8Z,11Z-eicosatrienoic acid (14,15-EET), 20-hydroxy-5Z,8Z,11Z,14Z-eicosatetraenoic acid (20-HETE), 20-hydroxy-5Z,8Z,11Z,14Z-eicosatetraenoic-16,16,17,17,18,18-d<sub>6</sub> acid (20-HETE-d<sub>6</sub>), 12S-hydroxy-5Z,8Z,10E,14Z-eicosatetraenoic acid (12-HETE), 15S-hydroxy-5Z,8Z,11Z,13E-eicosatetraenoic acid (15-HETE) and arachidonic acid (peroxide free) were purchased from Cayman Chemical (Ann Arbor, MI). Spectrophotometric grade dimethyl sulfoxide (DMSO) was purchased from Sigma-Aldrich (Milwaukee WI), high purity methanol (MeOH), ethyl ether, acetic acid, and other solvents were purchased from Fisher Scientific (Pittsburgh, PA). ( $\pm$ )-Metoprolol (+)-tartrate, ( $\pm$ )-verapamil hydrochloride and warfarin were purchased from Sigma-Aldrich (St. Louis, MO). Acetaminophen, phenacetin, and diclofenac

were purchased from Fisher Scientific (Pittsburgh, PA). S-mephenytoin, 4'-hydroxydiclofenac, s-hydroxymephenytoin, dextromethorphan, dextrorphan, midazolam, 1'-hydroxymidazolam, and miconazole were purchased from Toronto Research Chemicals (Ontario, Canada). Acetaminophen-d4, dextrorphan-d3, 4'-hydroxymephenytoin-d4, midazolam-d4, and diclofenac-d3 were purchased from Cerilliant (Round Rock, TX). Human liver microsome (HLM), rat liver microsomes (RLM), and recombinant CYP4F2 (rCYP4F2) were purchased from Sekisui Xenotech (Lenexa, KS).

### **3.2.2 Methods**

#### **3.2.2.1 *In vitro* screening: AA metabolism**

##### **3.2.2.1.1 Incubation conditions**

To screen the inhibitory effects against 20-HETE formation, compounds were tested in three different types of microsomes, including HLM, RLM, and rCYP4F2. Compounds were dissolved in DMSO to yield 10 mM stock solutions. Microsomal incubation conditions were previously optimized. Microsomal incubations contained HLM, RLM (300 µg/ml) or rCYP4F2 (25 pmol/ml), AA (100 µM), NADPH (1 mM) and test compounds at 500nM in a 1ml microsomal incubation buffer (0.12 M potassium phosphate buffer containing 5mM magnesium chloride). Each compound had three replications (n=3). Vehicle group was used as control to calculate the percentage of eicosanoids formation rates. HET0016 (250 nM) was the positive control. Incubates without NADPH were the negative control. Reaction was started by adding NADPH to the incubates and was carried out at 37°C in a shaking water bath for 20 min. Reaction was stopped by placing tubes on ice, followed by adding 12.5 µl 20-HETE-d6 as internal standard. Microsomal

incubations were extracted with 3 ml ethyl ether, dried down under nitrogen gas and reconstituted in 125 µl 80:20 methanol: deionized H<sub>2</sub>O for analysis. 20-HETE formation was quantified using a validated UPLC-MS/MS assay and normalized by vehicle group (Miller et al. 2009).

### 3.2.2.1.2 Chromatographic Analysis

An Acquity ultra performance LC autosampler (Waters, Milford, MA) was used to separate HETEs, EETs, and DiHETs on a UPLC BEH C18, 1.7 µm (2.1 × 100 mm) reversed-phase column (Waters, Milford, MA) protected by a guard column (2.1 × 5 mm; Waters, Milford, MA). Column temperature was maintained at 55° C. Mobile phases consisted of 0.005% acetic acid, 5% acetonitrile in deionized water (A) and 0.005% acetic acid in acetonitrile (B). The flow rate was 0.5 ml/min. The initial mixture of mobile phase was 65: 35 of A: B. Mobile phase B increased at 0.4 minutes after injection from 35% to 70% in a linear gradient over 4 minutes, and again increased to 95% over 0.5 minutes where it remained for 0.3 minutes. This was followed by a linear return to initial conditions over 0.1 minutes with a 1.5 minutes pre-equilibration period prior to the next sample run. Total run time was 6.4 minutes for each injection. Injection volumes were 7.5µl. Mass spectrometric analysis was carried out using a TSQ Quantum Ultra (Thermo Fisher Scientific, San Jose, CA) triple quadrupole mass spectrometer using heated electrospray ionization (HESI). Mass spectrometer was operated in negative selective reaction monitoring (SRM) mode. Quantitation of HETEs, EETs, and DiHETs by SRM was performed by monitoring their m/z transitions listed in Table 3.1. Analytical data were acquired and analyzed using Xcaliber 3.0 data system (ThermoFinnigan, San Jose, CA).

**Table 3.1 Analytical parameters of eicosanoids**

Compound	Precursor-product (m/z)	Collision energy (V)	Retention time (min)
20-HETE	455.3-165.0	27	2.68

15-HETE	268.0-116.2	20	2.08
12-HETE	309.1-163.3	20	3.41
8,9-EET	286.3-254.3	18	2.87
11,12-EET	286.1-254.2	18	2.29
14,15-EET	286.2-254.4	20	2.91
5,6-DiHET	286.3-254.3	20	2.32
8,9-DiHET	244.1-150.3	26	2.42
11,12-DiHET	286.2-126.2	14	2.44
14,15-DiHET	242.1-96.2	26	3.20
20-HETE-d6	242.2-150.2	20	2.51

### 3.2.2.1.3 Data analysis

Screening data were presented as % of control. No statistical test was performed.

### 3.2.2.2 Potency assessment

To test the *in vitro* potency, stock solution (10 mM) was serially diluted into 12 concentrations (0.1-50000 nM). Each concentration has three replicates. Incubations were performed with compounds of different concentrations in HLM or RLM (300 µg/ml) with AA (100 µM) and NADPH (1 mM). IC<sub>50</sub> values were derived from the concentration-response curve by fitting nonlinear regression  $Y=100/(1+10^{((\text{LogIC}_{50}-X)\times\text{HillSlope}))})$ .

### 3.2.2.3 Selectivity assessment

Other eicosanoids from AA metabolism pathways including 15-, 12-HETEs, 8,9-, 11,12-, 14,15-EETs, and 5,6-, 8,9-, 11,12-, 14,15-DiHETs were quantified by UPLC-MS/MS simultaneously (Table 3.1). Selectivity of CYP4 over EETs and DiHETs was presented as CYP450 activity by calculating the total formation rates of three EETs and four DiHETs and presented as % of control. IC<sub>50</sub> values for EETs and DiHETs formation were not obtained due to lack of inhibitory activity within the concentrations tested.

### 3.2.2.4 Metabolic stability assay

#### 3.2.2.4.1 Incubation conditions

Metabolic stability assays were conducted in HLM as previously described (Chapter 2). In brief, HLM (0.5 mg/ml), test compounds (1  $\mu$ M), and NADPH (1.3 mM) were incubated in microsomal incubation buffer. Reaction was started by adding NADPH and was carried out at 37°C in a shaking water bath for 60 min. A 50  $\mu$ l aliquot of incubates was removed at 0, 15, 30, 45, 60 min and reaction was stopped by adding aliquot into 200  $\mu$ l ice-cold acetonitrile. After centrifugation at 14000 $\times$ g for 5 min, 200  $\mu$ l supernatant was removed for UPLC-MS/MS analysis.

#### 3.2.2.4.2 Chromatographic analysis

Detailed information on chromatographic analysis is presented in Chapter 2. The liquid chromatographic analysis can be found in section 2.2.2.4. The transitions for mass spectrometric analysis are listed in section 2.2.2.5, Table 2.1.

#### 3.2.2.4.3 Data analysis

Using the  $t = 0$  peak area as 100%, the percentage remaining at each time point was calculated. *In vitro* half-life is calculated based on the assumption of compound metabolism following first-order kinetics. The log percentage remaining verses incubation time was plotted, and the slope was calculated (Equation 3.1.1). The half-life was calculated according to Equation 3.1.2. The equation for *in vitro* intrinsic clearance is shown in equation (3.1.3-3.1.4). Estimates of *in vivo* PK parameters can be obtained by *in vitro-in vivo* extrapolation (IVIVE) by equation (3.1.5-3.1.6). MPPGL is a scaling factor that represents the microsomal protein per gram of liver (40 mg/g). Liver weight is 20 g/kg of body weight.



Elimination rate constant ( $k$ ) =  $-slope$  (Equation 3.1.1)

$$\text{Half-life } (T_{1/2}) = \frac{0.693}{k} \text{ (Equation 3.1.2)}$$

$$V \left( \frac{\mu\text{l}}{\text{mg}} \right) = \frac{\text{volume of incubation } (\mu\text{l})}{\text{protein in the incubation } (\text{mg})} \text{ (Equation 3.1.3)}$$

$$\text{In vitro intrinsic clearance } (CL_{in\ vitro,int}) \left( \frac{\mu\text{l}/\text{min}}{\text{mg protein}} \right) = \frac{V \times 0.693}{T_{1/2}} \text{ (Equation 3.1.4)}$$

$$\text{In vivo intrinsic clearance } (CL_{in\ vivo,int}) = CL_{in\ vitro,int} \times MPPGL \times \text{liver weight} \text{ (Equation 3.1.5)}$$

$$\text{hepatic clearance } (CL_H) = \frac{CL_{in\ vivo,int} \times Q_H \times f_u}{CL_{in\ vivo,int} + f_u \times Q_H} \text{ (Equation 3.1.6)}$$

### 3.2.2.5 CYP inhibition assay

#### 3.2.2.5.1 Incubation conditions

CYP cocktail assay was performed as described in Chapter 2. In brief, incubations contained 20, 2.0, 40, 5, and 2  $\mu\text{M}$  of phenacetin, diclofenac, S-mephenytoin, dextromethorphan, and midazolam, respectively; 0.1 mg protein/ml of human liver microsomes; and 1 mM NADPH in 500  $\mu\text{l}$  potassium phosphate buffer (pH 7.4, 3 mM  $\text{MgCl}_2$ ). The incubation was performed at 37  $^{\circ}\text{C}$  for 10 min. The reactions were terminated by adding 12.5  $\mu\text{l}$  ice-cold internal standard mixtures (Table 2.2). The samples were extracted with 1.5 ml diethyl ether, dried down under nitrogen gas, and reconstituted in 125  $\mu\text{l}$  mobile phase for analysis.

### **3.2.2.5.2 Chromatographic analysis**

Chromatographic analysis was performed according to the method developed in Chapter 2. Detailed liquid chromatography method is provided in section 2.2.2.4. The mass spectrometric conditions for metabolites quantification are presented in section 2.2.2.5, Table 2.2.

### **3.2.2.5.3 Data analysis**

DMSO was used as vehicle control. Formation rates were presented as % of vehicle control.

### **3.2.2.6 Solubility assay**

Aqueous solubility was measured by Dr. Lawrence Verneti at Drug Discovery Institute, University of Pittsburgh. A stock DMSO solution of the test compound was serially diluted to produce a range of concentrations. The final solutions were incubated in 0.01 M phosphate buffered saline (pH 7.4) for 2 hr at 37 °C. The absorbance at 620 nm was read for each sample at the end of the incubation period. Data are presented as mean  $\pm$  std.

### **3.2.2.7 MDCK-MDR1 assay**

Madin-Darby Canine Kidney (MDCK)-MDR1 assay was performed by Absorption Systems (Exton, PA) (Absorption Systems 2020). In brief, MDCK-MDR1 cells were grown to confluence on microporous membranes. Compound (5  $\mu$ M) was added to the apical side to measure the apical to basolateral (A to B) transport or to basolateral well to measure basolateral to apical (B to A) transport and incubated at 37°C with 5% CO<sub>2</sub> in a humidified incubator. Samples were collected from both apical and basolateral wells at 120 min (n=3) and then analyzed using

LC-MS. The apparent permeability (Papp) was calculated as  $Papp = \frac{dQ/dt}{C_0 \times A}$ , where  $dQ/dt$  is the rate of permeability,  $C_0$  is the initial concentration in the donor compartment, and A is the surface area. The efflux ratio (ER) was calculated as  $ER = \frac{Papp_{B-A}}{Papp_{A-B}}$ . A  $Papp_{A-B} \geq 3.0 \times 10^{-6}$  cm/s and  $ER < 3.0$  is classified as high BBB penetration potential. A  $Papp_{A-B} \geq 3.0 \times 10^{-6}$  cm/s and  $3.0 \leq ER < 10$  is classified as moderate BBB penetration potential. A  $Papp_{A-B} \geq 3.0 \times 10^{-6}$  cm/s and  $ER \geq 10$  or  $Papp_{A-B} < 3.0 \times 10^{-6}$  cm/s is classified as low BBB penetration potential.

### 3.2.2.8 *In vitro* safety pharmacology profiling

*In vitro* safety pharmacology evaluation was conducted by Eurofins Discovery in a SafetyScreen44, Cerep Panel (Celle-Lévescault, France) (Eurofins Discovery 2020). In brief, compound (10  $\mu$ M) was tested for 38 binding assays including receptors, ion channels, transporters and six enzyme inhibition and uptake assays. The targets are primarily associated with well-described cardiovascular, CNS side effects, and arachidonic acid metabolic enzymes COX1, COX2, etc. Compound binding was calculated as a % inhibition of the binding of a radioactively labeled ligand specific for each target. Compound enzyme inhibition was calculated as % of inhibition of control enzyme activity. An inhibition or stimulation greater than 50% is considered a significant effect for the test compound. An inhibition or stimulation between 25% - 50% is considered as a weak to moderate effect. An inhibition or stimulation of less than 25% is not considered significant (Eurofins Discovery 2020).

### 3.2.2.9 Statistical analysis

Data analysis for each assay is provided within each method section. One-way ANOVA was carried out and corrected with Bonferroni as post-hoc test. Values that are statistically significant are designated by asterisks (\*,  $p < 0.05$ ).

## 3.3 Results

### 3.3.1 Physicochemical property evaluation

Several physicochemical properties are important for CNS drug design. Lipophilicity, calculated as the logarithm of octanol/water partition coefficient (clogP); number of rotatable bonds (NRB); number of hydrogen-bond donors (HBD); number of hydrogen-bond acceptors (HBA); polar surface area (PSA) and molecular weight (MW) are important attributes for small molecules (Rankovic 2015). Compounds with physicochemical properties of  $MW \leq 450$ ,  $\log P \leq 3.5$ ,  $PSA \leq 70$ ,  $HBD \leq 3$ ,  $HBA \leq 7$ ,  $NRB \leq 5$  are more likely to penetrate BBB (Pajouhesh et al. 2005). All compounds evaluated were designed to have physicochemical properties within the range seen in CNS drugs, suggesting compounds may have a high probability of BBB penetration via passive diffusion (Pajouhesh et al. 2005).

### 3.3.2 Hit identification through *in vitro* screening

The initial goal was to identify novel scaffolds that exhibit 20-HETE formation inhibitory activity in HLM by screening a small library of compounds. Pyrazole derivative, 5-(4-

butoxyphenyl)-1H-pyrazole (compound **24**, Fig 1.2) was reported as a 20-HETE formation inhibitor in 2003. This compound has an  $IC_{50}$  value of 23 nM against 20-HETE formation in human kidney microsomes, good selectivity against other CYP enzymes and improved stability in an acidic environment compared to HET0016 (Nakamura et al. 2003). The replacement of the N-hydroxyformamidine by the pyrazole led to a more stable compound without affecting the potency. Therefore, 5-(4-butoxyphenyl)-1H-pyrazole (compound **24**) was viewed as a good starting point for novel compound development. The structure of compound **24** can be segmented into three sections, the right-hand side pyrazole, the middle section benzene ring, and the left-hand side butane chain (Fig. 3.3). Compound **24** is a potent 20-HETE formation inhibitor and has three possible sections for structure changes to generate new compounds.

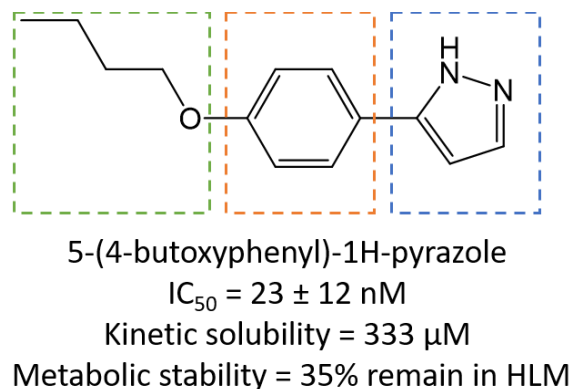


**Figure 3.3 Compound 24 and possible positions for structure changes**

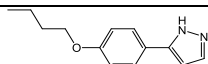
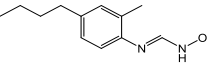
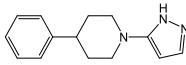
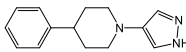
We screened a small early exploratory library of 20 novel compounds designed with various and diverse moieties as replacements for the moieties seen in the three possible positions of compound **24** that could be altered. Compounds were screened for 20-HETE formation inhibition at 250 nM in HLM, rCYP4F2, and RLM (Tang 2016). Our early objective was to identify potent leads quickly. Therefore, a concentration of 250 nM, 7-fold higher than the  $IC_{50}$  of HET0016 in HKM (35 nM), would seem like a reasonable starting point to achieve this objective. The amount of 20-HETE formation was used as a surrogate for compound activity. Ideal

compounds should display 20-HETE inhibition in HLM and exhibit inhibition in rCYP4F2, which confirms the target engagement of CYP4F2. Compounds that showed the greatest inhibition in 20-HETE formation in HLM were selected as compounds of interest for further evaluation.

Through the initial screen, we identified **UPMP010** and **UPMP019** as hit compounds (Tang 2016). Both **UPMP010** and **UPMP019** showed the greatest 20-HETE inhibition in HLM during screening at 250 nM (Table 3.2). They also demonstrated that the inhibitory effect was mediated by the inhibition of CYP4F2 in the rCYP4F2 microsomal system. Both compounds showed good *in vitro* potency in HLM (**UPMP010**: IC<sub>50</sub> = 443 nM; **UPMP019**, IC<sub>50</sub> = 187 nM).

The difference between **UPMP010** and **UPMP019** was the link position of the pyrazole group with the phenyl pyridine moiety present in these compounds. Based on the potency in HLM, linking the phenyl piperidine moiety at the 4-position of the pyrazole appeared to lead to a 2-fold improvement in the inhibition of 20-HETE formation.

**Table 3.2 *In vitro* screening and potency evaluation of UPMP010 and UPMP019**

Compound	Structure	% of control in rCYP4F2	% of control in HLM	% of control in RLM	IC <sub>50</sub> (nM) in HLM
<b>24</b>		- <sup>b</sup>	-	-	23 ± 12 <sup>a</sup>
HET0016		7.80 ± 2.72	1.70 ± 0.37	9.50 ± 2.60	8.9 ± 2.7 <sup>a</sup>
<b>UPMP010</b>		46.4 ± 5.93	69.6 ± 3.15	86.5 ± 1.92	443
<b>UPMP019</b>		18.7 ± 2.00	44.3 ± 1.22	-	187

Number of replicate = 3/compound

<sup>a</sup> The IC<sub>50</sub> value was obtained from human kidney microsome.

<sup>b</sup> “-” represents data not available.

### 3.3.3 Characterization of properties for hit compounds

Properties including solubility, selectivity, and metabolic stability were assessed for **UPMP010** and **UPMP019**. Both compounds displayed strong inhibition against the  $\omega$ -hydroxylase pathway (Fig. 3.4). There was a dose-dependent inhibition towards 20-HETE formation in HLM. Both compounds did not show inhibition towards the epoxigenase pathway in HLM within the range of concentrations tested. The estimated IC<sub>50</sub> values for EETs/DiHETs formation were greater than 10 and 50  $\mu$ M for **UPMP010** and **UPMP019**, respectively.

Both compounds had reasonable solubility. **UPMP010** had kinetic solubility > 600  $\mu$ M, and **UPMP019** had solubility of 121  $\mu$ M (Table 3.3). Both compounds were slowly metabolized in HLM. **UPMP010** had 91.6% parent compound remaining at 30 min. **UPMP019** did not show disappearance of the parent compound at 30 min (Fig. 3.5).

**Table 3.3 Property comparison for compound 24, HET0016, UPMP010 and UPMP019**

Compound	20-HETE inhibition IC <sub>50</sub> (nM) in HLM	% compound remain in HLM at 30 min	Solubility ( $\mu$ M)	EETs inhibition IC <sub>50</sub> ( $\mu$ M)
<b>24</b>	23 <sup>a</sup>	35	333	-
HET0016	11.5	4.0	163	2.8 $\mu$ M
<b>UPMP010</b>	443	91	> 600	> 50 $\mu$ M
<b>UPMP019</b>	187	100	121	> 10 $\mu$ M

<sup>a</sup> The IC<sub>50</sub> of compound **24** was measured in human kidney microsome.

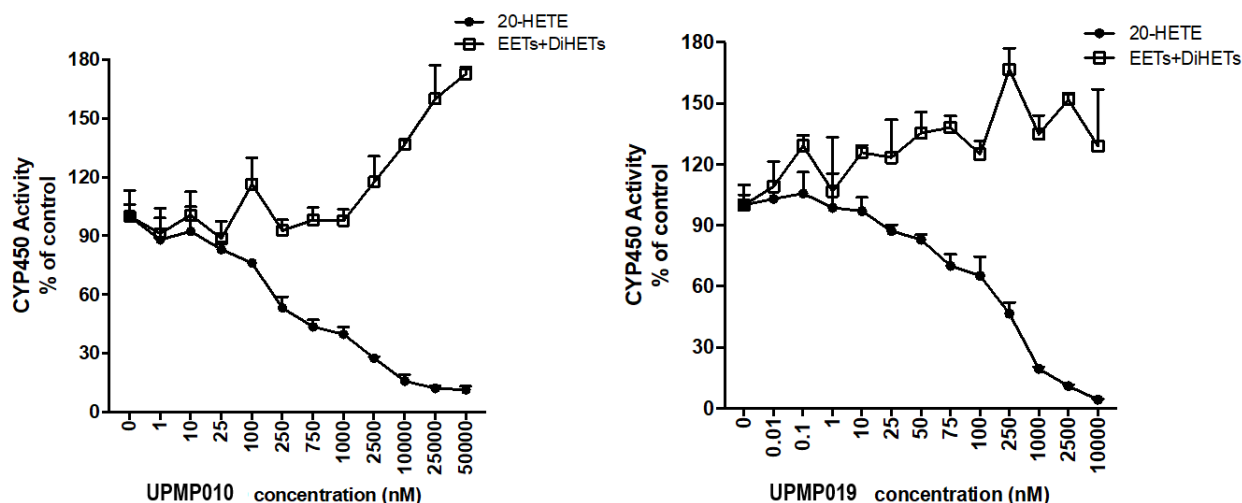


**Figure 3.4 Selectivity of 20-HETE formation inhibition versus EETs/DiHETs formation inhibition for UPMP010 and UPMP019**

The formation rates of 20-HETE, EETs and DiHETs were used to represent CYP450 activity. The formation rates are presented as percent of the control of the vehicle group. **UPMP010** and **UPMP019** inhibit 20-HETE formation in a concentration-dependent manner. Both compounds did not inhibit EETs and DiHETs formation.

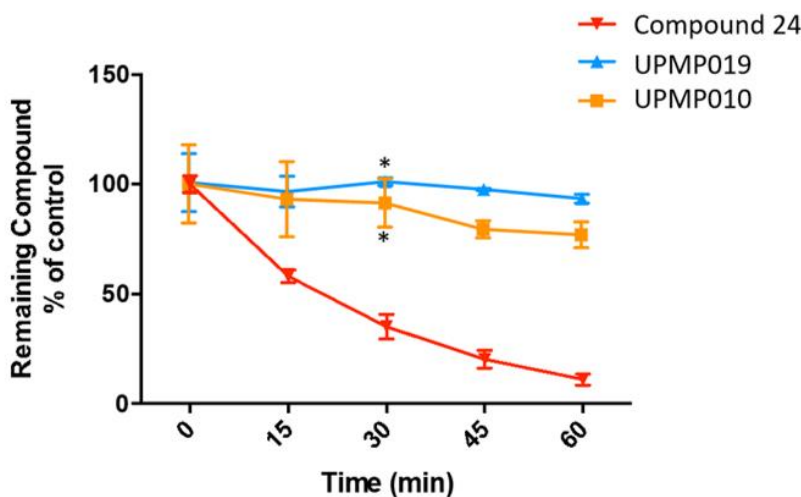


**Figure 3.5 Metabolic stability for compound 24, UPMP010, and UPMP019**

**UPMP010** and **UPMP019** were slowly metabolized in HLM. HLM incubation of **UPMP010** and **UPMP019** had  $91.4 \pm 11.0\%$  and  $100 \pm 1.73\%$  remaining at 30 min, respectively. One-way ANOVA was performed to compare the remaining parent compound at 30 min between



**UPMP010**, **UPMP019** and compound **24**. The remaining compound of **UPMP010** and **UPMP019** was significantly greater than compound **24** of  $35.1 \pm 5.66\%$ .

To summarize, in the initial screening, we identified two compounds **UPMP010** and **UPMP019**, with good 20-HETE inhibitory activity, large selectivity window against the epoxigenase pathway, good solubility, and low phase I metabolism. Therefore, **UPMP010** and **UPMP019** were chosen as hit compounds for further optimization to generate more analogs.

An updated screening concentration was set at 500 nM. This concentration would increase the potential candidate pool, allowing us to select and study structurally different compounds to understand the structural need for 20-HETE formation inhibition. For the evaluation and advancement of novel **UPMP010** and **UPMP019** derivatives, the criteria for Tier 2 - *in vitro* screening were a greater than 50% inhibition of 20-HETE formation ( $< 50\%$  20-HETE remaining) in HLM and a greater than or equal to 40% inhibition of 20-HETE formation ( $\leq 60\%$  20-HETE remaining) in RLM. The criteria were set for both HLM and RLM, which would allow us to develop molecules in a preclinical animal model in rats. Compounds that meet both HLM and RLM criteria would be advanced to Tier 3 selected assays to generate data that could help understand how structure changes could affect selected properties. In Tier 3, the criteria for potency, solubility, selectivity, metabolic stability, BBB permeability, and *in vitro* safety pharmacology for derivatives are presented in Table 3.4. The potency should be less than or equal to 100 nM in HLM. Although an  $IC_{50}$  less than compound **24** is desired, we viewed that compounds with good biopharmaceutical and drug-like properties with a slightly higher  $IC_{50}$  would also be attractive for *in vivo* development. Thus, a 100 nM for potency was deemed an acceptable cut-off value. The solubility for compounds to advance should be greater than or equal to 400  $\mu$ M. A high solubility would allow the flexibility in designing dosage form and the dosage required to achieve

desired concentration in the systemic circulation. The selectivity of 20-HETE versus EETs, or the selectivity of CYP4 inhibition versus other drug-metabolizing CYP isoforms should be greater than 100-fold. This would allow a wide therapeutic window, where increasing the dose of the inhibitor will not affect EETs formation or affect drug metabolism by other CYP isoforms. For metabolic stability, the remaining parent compound at 30 min should be greater than or equal to 80%. This cut-off value was chosen to identify stable compounds ( $T_{1/2} > 90$  min) with a low *in vitro* clearance. For BBB permeability assessed in MDCK-MDR1 cell lines, the PappA-B should be greater than  $3 \times 10^{-6}$  cm/s, and ER should be less than 10. Compounds that meet these criteria are predicted to have moderate to high brain penetration. Lastly, the *in vitro* safety pharmacology criteria were inhibition or stimulation less than 50% at 10  $\mu$ M in the transporters, ion channels, and enzymes tested in the Cerep Safetyscreen44 Panel. This cut-off value would identify compounds that may have effect on receptors, ion channels, or enzymes that could potentially lead to undesired side effects. A greater than 50% inhibition or stimulation would require further investigation for IC<sub>50</sub> determination for that specific target.

**Table 3.4 Criteria for Tier 1-3 to evaluate compound**

Drug-like property	Criteria
Physicochemical properties	MW $\leq$ 450, cLogP $\leq$ 3.5, TPSA $\leq$ 70, HBD $\leq$ 3, HBA $\leq$ 7, NRB $\leq$ 5
Screening	% of inhibition $>$ 50% in HLM, % of inhibition $>$ 40% in RLM
Solubility	$\geq$ 400 $\mu$ M
Potency	IC <sub>50</sub> $\leq$ 100 nM in HLM
Selectivity	IC <sub>50</sub> for EETs/DiHETs $\geq$ 100-fold IC <sub>50</sub> for 20-HETE
Metabolic stability	HLM stability $\geq$ 80% at 30 min
CYP inhibition	IC <sub>50</sub> for CYP isoforms $\geq$ 100-fold IC <sub>50</sub> for 20-HETE; Or IC <sub>50</sub> for CYP isoforms $\geq$ 1000 nM
BBB permeability	PappA-B $>$ $3 \times 10^{-6}$ cm/s, ER $<$ 3 or 3 $<$ ER $<$ 10
<i>In vitro</i> safety pharmacology (CEREP panel)	Inhibition (or stimulation) $<$ 50% at 10 $\mu$ M


### 3.3.4 Lead optimization

#### 3.3.4.1 Potency evaluation of UPMP010 and UPMP019 derivatives

After confirmation of the selectivity, metabolic stability, and solubility of **UPMP010** and **UPMP019**, we conducted *in vitro* evaluation for synthesized derivatives of both compounds.

In a small subset of derivatives in which the phenyl is directly linked to piperidine and when there is a single simple non-halogen substitution on the phenyl group, we observed a trend that seems to suggest that linking the piperidine moiety at the 4-position of the pyrazole increases 20-HETE formation inhibition compared to linking at the 5-position (Table 3.5). This trend seemed to be consistent with the finding that **UPMP019** had a stronger inhibitory activity than **UPMP010**.

**Table 3.5 CYP4 inhibition of analogs with single substitution on benzene**



Compd (UPMP)	R <sub>1</sub>	IC <sub>50</sub> (nM) in HLM	Compd (UPMP)	R <sub>2</sub>	IC <sub>50</sub> (nM) in HLM
<b>010</b>	-	443	<b>019</b>	-	187
<b>027</b>	4-OMe	143	<b>031</b>	4-OMe	73.4
<b>028</b>	3-OMe	194	<b>029</b>	3-OMe	169
<b>041</b>	2-OMe	>500 <sup>a</sup>	<b>042</b>	2-OMe	>500
<b>037</b>	4-COOMe	>500	<b>038</b>	4-COOMe	>500
<b>039</b>	3-COOMe	>500	<b>040</b>	3-COOMe	>500
<b>046</b>	4-Me	111	<b>047</b>	4-Me	78.8
<b>081</b>	3-Me	177.8	<b>077</b>	3-Me	111.5
<b>080</b>	2-Me	>500	<b>078</b>	2-Me	647
<b>049</b>	4-ethylsulfonyl	107	<b>048</b>	4-ethylsulfonyl	80.3
<b>051</b>	4-MeOCH <sub>2</sub>	280	<b>054</b>	4-MeOCH <sub>2</sub>	195
<b>061</b>	4-N-methylacetamide	>500	<b>060</b>	4-N-methylacetamide	101
<b>062</b>	4-acetamide	173	<b>072</b>	4-acetamide	45.8

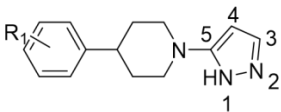
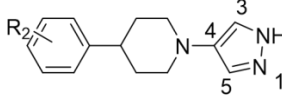
<sup>a</sup> A > 500 nM was assigned to compounds that inhibited 20-HETE less than 50% in HLM.

The data presented in Table 3.5 for simple non-halogen derivatives of **UPMP010** and **UPMP019** suggested that the 4-methoxy derivatives (**UPMP027**,  $IC_{50} = 143$  nM; **UPMP031**,  $IC_{50} = 73.4$  nM) were ~3 and ~2.5-fold more potent compared to **UPMP010** and **UPMP019**. Moving methoxy to 3-position on the phenyl (**UPMP028**,  $IC_{50} = 194$  nM; **UPMP029**,  $IC_{50} = 169$  nM) led to ~1.4 to ~2.3-fold less active compounds compared to 4-methoxyl derivatives, but they had improved activities compared to hit compounds **UPMP010** and **UPMP019**. When the methoxy group was at the 2-position on the phenyl, this led to **UPMP041** and **UPMP042** that were markedly less active ( $IC_{50} > 500$  nM). We found 4-methyl derivatives (**UPMP046**,  $IC_{50} = 111$  nM; **UPMP047**,  $IC_{50} = 73.4$  nM) to have comparable activity to **UPMP027** and **UPMP031**. A similar trend of decrease in activity was seen when moving methyl group from 4- to 3-, and 2-position on benzene (**UPMP081**, **UPMP077** and **UPMP080**, **UPMP078**). An interesting result was that substitution with methyl acetate moiety (**UPMP037**, **UPMP039**, **UPMP038**, and **UPMP040**) negated CYP4 inhibitory activity in HLM. *In vitro* screening in rCYP4F2 suggested **UPMP037**, **UPMP039**, **UPMP038**, and **UPMP040** have inhibitory activity in rCYP4F2 and followed the trend of 4-position > 3-position (data not shown here). The loss of activity in HLM could be attributed to the hydrolysis of methyl acetate by esterase in the HLM, whereas rCYP4F2 is a purified system with no esterase in presence, leaving compounds intact. In this small set of derivatives of **UPMP010** and **UPMP019**, we found that *para*- substitution induced the greatest activity improvement followed by *meta*-, whereas *ortho*- substitution was less tolerated. Other derivatives with substituents at 4-position such as ethylsulfonyl (**UPMP049**,  $IC_{50} = 107$  nM; **UPMP048**,  $IC_{50} = 80.3$  nM) and acetamide (**UPMP062**,  $IC_{50} = 107$  nM; **UPMP072**,  $IC_{50} = 45.8$  nM) resulted in a more than ~1.8- to ~2.5-fold improved activity. Methoxymethyl (**UPMP051** and

**UPMP054**) and N-methylacetamide (**UPMP061** and **UPMP060**) substitutions did not result in a clear improvement in potency. In this set of derivatives, the potency data seemed to suggest that 4-phenyl-1-(1*H*-pyrazole-4-yl)piperidine derivatives had better 20-HETE formation inhibition compared to 4-phenyl-1-(1*H*-pyrazol-5-yl)piperidine derivatives. Small simple substitutions at 4- and 3-position on the phenyl group are tolerated compared to 2-position. Among these derivatives, the acetamide derivative (**UPMP072**) demonstrated the strongest inhibition against CYP4 enzymes.

Evaluation of compounds with halogen modifications on the benzene ring of **UPMP010** and **UPMP019** is shown in Table 3.6. In this subset of compounds, based on the screening data, halogen substitution appeared to be tolerated. Fluorine at the *ortho*- position did not seem to affect the inhibitory activity. 2-F derivative **UPMP083** ( $IC_{50} = 235$  nM) has a comparable activity to **UPMP019** ( $IC_{50} = 187$  nM). Derivatives with chloro substitution at 4- and 3- position showed similar percent of 20-HETE formation inhibition compared to derivatives with fluoro substitution at 2-, 3- and 4- position. In this subset of halogen-monosubstituted derivatives, based on the screening data, it appeared that the 4-phenyl-1-(1*H*-pyrazol-4-yl)piperidine derivatives were more potent.

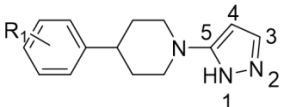
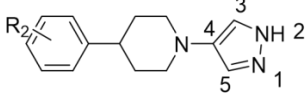
**Table 3.6 CYP4 inhibition of analogs with simple halogen substitution**

					
Compd (UPMP)	R <sub>1</sub>	% of inhibition in HLM <sup>a</sup>	Compd (UPMP)	R <sub>2</sub>	% of inhibition in HLM
<b>071</b>	4-F	66	<b>070</b>	4-F	80
<b>074</b>	3-F	67	<b>075</b>	3-F	80
<b>079</b>	2-F	47	<b>083</b>	2-F	77
<b>085</b>	4-Cl	60	<b>086</b>	4-Cl	74
-	-	-	<b>084</b>	3-Cl	77

<sup>a</sup> Screening results were used for the comparison of inhibitory activity.

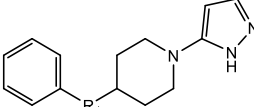
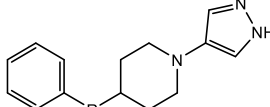
We also evaluated derivatives with double substitution on the phenyl group of **UPMP010** and **UPMP019** (Table 3.7). The 3-F, 4-OMe derivative (**UPMP068**,  $IC_{50}$  = 49.5 nM) showed a ~1.5-fold improvement in activity compared to 4-OMe derivative (**UPMP031**,  $IC_{50}$  = 73.4 nM). The 2-F, 4-OMe derivative (**UPMP073**,  $IC_{50}$  = 82.1 nM) had comparable activity to **UPMP031**. In this subset of derivatives with two substitutions on the phenyl group, the screening data suggested that the 4-phenyl-1-(1H-pyrazol-4-yl)piperidine derivatives and the 4-phenyl-1-(1H-pyrazol-5-yl)piperidine derivatives had comparable activity against 20-HETE formation.

**Table 3.7 CYP4 inhibition of analogs with double substitutions**

					
Compd (UPMP)	R <sub>1</sub>	% of inhibition in HLM <sup>a</sup>	Compd (UPMP)	R <sub>2</sub>	% of inhibition in HLM
<b>076</b>	3-F,4-OMe	92	<b>068</b>	3-F, 4-OMe	95
<b>082</b>	2-F, 4-OMe	88	<b>073</b>	2-F, 4-OMe	92
<b>097</b>	3-F, 5-OMe	61	<b>096</b>	3-F, 5-OMe	77
<b>098</b>	3-OMe, 4-F	55	<b>099</b>	3-OMe, 4-F	61
<b>091</b>	3-Cl, 4-OMe	83	<b>088</b>	3-Cl, 4-OMe	88
<b>090</b>	2-Cl, 4-OMe	58	<b>089</b>	2-Cl, 4-OMe	56
<b>095</b>	2-F, 4-N-methylacetamide	82	<b>093</b>	2-F, 4-N-methylacetamide	86

<sup>a</sup> Screening results were used for the comparison of inhibitory activity.

**Table 3.8 CYP4 inhibition of analogs with extended linker**

					
Compd (UPMP)	R <sub>1</sub>	$IC_{50}$ (nM) in HLM	Compd (UPMP)	R <sub>2</sub>	$IC_{50}$ (nM) in HLM
<b>010</b>	-	443	<b>019</b>	-	187
<b>021</b>	R <sub>1</sub> = CH <sub>2</sub>	149	<b>022</b>	R <sub>2</sub> = CH <sub>2</sub>	49.6
<b>013</b>	R <sub>1</sub> = O	>500 <sup>a</sup>	<b>043</b>	R <sub>2</sub> = O	215

<b>056</b>	R <sub>1</sub> = S	>500	<b>057</b>	R <sub>2</sub> = S	98.1
<b>059</b>	R <sub>1</sub> = O=S=O	>500	<b>058</b>	R <sub>2</sub> = O=S=O	>500

<sup>a</sup> A > 500 nM was assigned to compounds that showed less than 50% inhibition in HLM.

Evaluation of compounds with a linker between the piperidine and benzene moieties is presented in Table 3.8. When the phenyl group in **UPMP010** and **UPMP019** was extended by a methylene group, an improved potency was observed (**UPMP021**, IC<sub>50</sub> = 149 nM; **UPMP022**, IC<sub>50</sub> = 49.6 nM). In this small set of derivatives shown in Table 3.8, we observed that when the linker was -S- (**UPMP056**), -O- (**UPMP013**), or -O=S=O (**UPMP059**) on derivatives with 1H-pyrazol-5-yl-piperidine core, there was a loss of activity compared to hit **UPMP010**. Comparing derivatives with 1H-pyrazol-4-yl-piperidine core, it appeared that the potency showed a trend of -C- > -O- > -S- > -O=S=O (**UPMP022**, IC<sub>50</sub> = 49.6 nM; **UPMP057**, IC<sub>50</sub> = 98.1 nM; **UPMP043**, IC<sub>50</sub> = 215 nM; **UPMP058**, IC<sub>50</sub> > 500 nM).

So far, after potency evaluation, several compounds with great 20-HETE formation inhibition were identified, including **UPMP072** (IC<sub>50</sub> = 45.8 nM), **UPMP068** (IC<sub>50</sub> = 49.5 nM), and **UPMP022** (IC<sub>50</sub> = 49.6 nM).

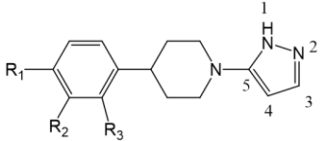
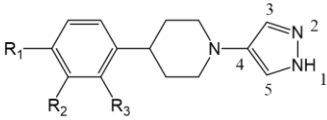
**UPMP072** contains an amide group that we suspected might subject to hydrolysis. Although active, **UPMP072** had low metabolic stability in HLM (section 3.3.5.3). Derivatives of **UPMP072** with amide groups and amide isosteres that might have reduced tendency for hydrolysis were synthesized and evaluated for potency to test whether these analogs could maintain the strong inhibitory activity of **UPMP072**. The microsomal stability was also evaluated to see if analogs exhibited slow turnover in HLM (section 3.3.5.3).

Comparison of **UPMP124** to **UPMP072** suggested that introducing a cyclic amide ring (**UPMP124**, IC<sub>50</sub> = 53.6 nM) led to a compound with similar potency of **UPMP072** (Table 3.9). Based on screening results, **UPMP101**, **UPMP102**, and **UPMP125** all showed similar percent of

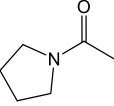
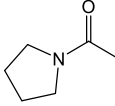
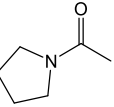
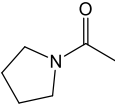
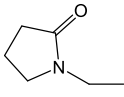
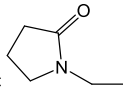
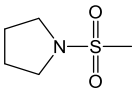
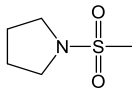
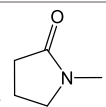
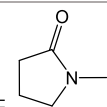
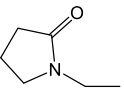
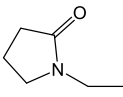
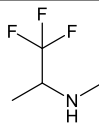
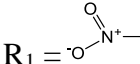
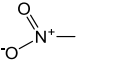
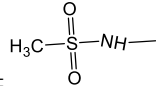
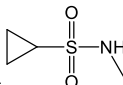
inhibition compared to **UPMP072**. Extending the distance between benzene and the cyclic amide group substituent of **UPMP124** led to **UPMP107** ( $IC_{50} = 54.2$  nM) with comparable activity to **UPMP072**. Comparing **UPMP105**, **UPMP106** to **UPMP101**, **UPMP102**, the addition of fluoro at 3-position of benzene did not seem to provide an improvement in activity. Similarly, when comparing **UPMP135**, **UPMP136** to **UPMP107**, **UPMP108**, the addition of fluoro at 2-position of benzene did not show improvement in 20-HETE percent of inhibition in HLM. Based on the screening results, 1,1,1-trifluoropropan-2-amine (**UPMP130**) seemed to maintain the 20-HETE formation inhibitory activity, and 4-cyclopropyl sulfonamide (**UPMP140**) seemed to have less activity in HLM. We also evaluated the hypothesized active moiety of **UPMP072**, 4-NH<sub>2</sub> (**UPMP131**), which showed a slight reduction in inhibition of 20-HETE formation. Additionally, we also evaluated nitro derivatives **UPMP137** and **UPMP138**, the methanesulfonamide and pyrrolidinesulfonamide derivatives (**UPMP139**, **UPMP109**, and **UPMP120**) (Table 3.9). Except for **UPMP120**, these derivatives appeared to show less inhibition of 20-HETE formation compared to **UPMP072**.

For derivatives with a sulfone moiety, it appears that the sulfone position and if the sulfone is a part of a ring, affects the inhibitory activity (**UPMP113**, **UPMP126**, and **UPMP134**) (Table 3.10). Further potency evaluation is needed to reach a solid conclusion.

**Table 3.9 CYP4 inhibition of analogs of amide derivatives**

					
Compd <sup>a</sup> (UPMP)	Substituents <sup>b</sup>	% of inhibition in HLM	Compd (UPMP)	Substituents	% of inhibition in HLM
<b>062</b>	$R_1 = \text{NH-C(=O)-CH}_3$	60.0	<b>072</b>	$R_1 = \text{NH-C(=O)-CH}_3$	86.0

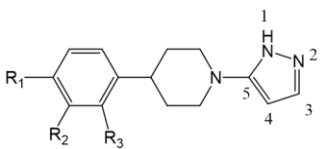
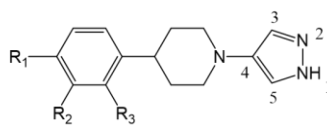


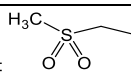
<b>102</b>	$R_1 = $ 	82.6	<b>101</b>	$R_1 = $ 	83.6
<b>106</b>	$R_1 = $  , $R_3 = F$	74.5	<b>105</b>	$R_1 = $  , $R_3 = F$	83.1
<b>108</b>	$R_1 = $ 	79.4	<b>107</b>	$R_1 = $ 	91.6
<b>120</b>	$R_1 = $ 	63.1	<b>109</b>	$R_1 = $ 	81.3
<b>125</b>	$R_1 = $ 	79.0	<b>124</b>	$R_1 = $ 	76.1
<b>136</b>	$R_1 = $  , $R_2 = F$	80.4	<b>135</b>	$R_1 = $  , $R_2 = F$	90.3
-	-	-	<b>130</b>	$R_1 = $ 	86.1
-	-	-	<b>131</b>	$R_1 = NH_2$	67.3
<b>138</b>	$R_1 = $ 	21.9	<b>137</b>	$R_1 = $ 	43.5
-	-	-	<b>139</b>	$R_1 = $ 	30.5
-	-	-	<b>140</b>	$R_1 = $ 	68.7

<sup>a</sup> Not all compounds with 4-phenyl-1-(1H-pyrazol-5-yl)piperidine core were synthesized.

<sup>b</sup>  $R_2 = H$  and  $R_3 = H$  when  $R_2$  and  $R_3$  are not defined in the table.

**Table 3.10 CYP4 inhibition analogs UPMP113, UPMP134, UPMP139**

Compd <sup>a</sup> (UPMP)	Substituents <sup>b</sup>	% of inhibition in HLM	Compd (UPMP)	Substituents	% of inhibition in HLM
-	-	-	<b>113</b>	R <sub>1</sub> = 	34.8
-	-	-	<b>134</b>	R <sub>1</sub> , R <sub>2</sub> = 1,3-dihydro[ <i>c</i> ]thiophene 2,2-dioxide	90.0
-	-	-	<b>126</b>	R <sub>1</sub> , R <sub>2</sub> = 2,3-dihydro[ <i>b</i> ]thiophene 1,1-dioxide	27.9

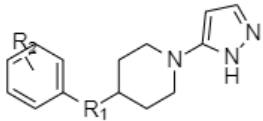
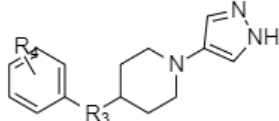
<sup>a</sup> Not all compounds with 4-phenyl-1-(1H-pyrazol-5-yl)piperidine core were synthesized.

<sup>b</sup> R<sub>2</sub> = H and R<sub>3</sub> = H when R<sub>2</sub> and R<sub>3</sub> are not defined in the table.

Evaluation of derivatives with a linker between piperidine and substituted benzene moieties is presented in Table 3.11. Derivatives with 3-OMe (**UPMP069**), or 4-pyrrolidone (**UPMP133**), while keeping the CH<sub>2</sub> linker had comparable percent of inhibition for 20-HETE formation in HLM compared to **UPMP022**. Derivative (**UPMP103**) with 4-OMe seemed to be less active compared to **UPMP022**. When using -S- as the linker, introducing R<sub>4</sub> substituents (**UPMP094**, **UPMP100**, **UPMP104**, **UPMP106**) seemed to maintain the inhibition of 20-HETE formation compared to **UPMP022**. In this set of derivatives, 4-Cl derivative (**UPMP117**, IC<sub>50</sub> = 17.3 nM) and 4-CH<sub>3</sub> derivative (**UPMP142**, IC<sub>50</sub> = 24.0 nM) led to a 2.8- and 2- fold increase in potency

compare to the top activities (e.g. **UPMP072**, IC<sub>50</sub> = 45.8 nM; **UPMP022**, IC<sub>50</sub> = 49.6 nM), respectively.

**Table 3.11 CYP4 inhibition of UPMP021 and UPMP022 derivatives**

					
Compd <sup>a</sup> (UPMP)	R <sub>1</sub> , R <sub>2</sub> <sup>b</sup>	% of inhibition in HLM <sup>b</sup>	Compd (UPMP)	R <sub>3</sub> , R <sub>4</sub>	% of inhibition in HLM
<b>021</b>	R <sub>1</sub> = CH <sub>2</sub>		<b>022</b>	R <sub>3</sub> = CH <sub>2</sub>	77.3
-	-	-	<b>103</b>	R <sub>3</sub> = CH <sub>2</sub> , R <sub>4</sub> = 4-OMe	59.8
-	-	-	<b>069</b>	R <sub>3</sub> = CH <sub>2</sub> , R <sub>4</sub> = 3-OMe	71.0
-	-	-	<b>142</b>	R <sub>3</sub> = CH <sub>2</sub> , R <sub>4</sub> = 4-CH <sub>3</sub>	86.4
<b>121</b>	R <sub>1</sub> = CH <sub>2</sub> , R <sub>2</sub> = 3-CH <sub>3</sub>	35.3	<b>118</b>	R <sub>3</sub> = CH <sub>2</sub> , R <sub>4</sub> = 3-CH <sub>3</sub>	61.3
-	-	-	<b>117</b>	R <sub>3</sub> = CH <sub>2</sub> , R <sub>4</sub> = 4-Cl	93.0
<b>115</b>	R <sub>1</sub> = CH <sub>2</sub> , R <sub>2</sub> = 3-Cl	40.4	<b>114</b>	R <sub>3</sub> = CH <sub>2</sub> , R <sub>4</sub> = 3-Cl	67.0
-	-	-	<b>133</b>	R <sub>3</sub> = CH <sub>2</sub> , R <sub>4</sub> = 4-pyrrolidone	78.9
<b>092</b>	R <sub>1</sub> = S, R <sub>2</sub> = 4-OMe	48	-	-	-
-	-	-	<b>100</b>	R <sub>3</sub> = S, R <sub>4</sub> = 3-OMe	84.4
-	-	-	<b>104</b>	R <sub>3</sub> = S, R <sub>4</sub> = 4-OMe	85.7
-	-	-	<b>094</b>	R <sub>3</sub> = S, R <sub>4</sub> = 4-F	84.8
-	-	-	<b>116</b>	R <sub>3</sub> = S, R <sub>4</sub> = 2-F	77.3

<sup>a</sup> Not all compounds with 4-phenyl-1-(1H-pyrazol-5-yl)piperidine core were synthesized.

<sup>b</sup> R<sub>2</sub> = H when R<sub>2</sub> is not defined in the table.

### 3.3.4.2 Species difference in inhibitory activity

Given the species difference in enzymes responsible for 20-HETE formation between rodents and humans, we also assessed CYP4 inhibitory activity in RLM. Based on the screening data, we observed large differences in 20-HETE formation inhibition between HLM and RLM (Appendix A Table 1 - 6). Based on the screening data, small single non-halogen substituents on benzene such as 3-OMe (**UPMP029**), 3-Me (**UPMP077**), 3-COOMe (**UPMP040**) appeared to have better inhibitory activity when compared to derivatives with the same substitutions on 4-position (**UPMP031**, **UPMP047**, **UPMP038**) (Appendix Table 1). It appeared that double substitutions with -OMe, -F, or -Cl (**UPMP068**, **UPMP073**, **UPMP099**, **UPMP088**) showed a trend of improvement in the 20-HETE formation inhibition when comparing to single non-halogen small substitution (Appendix Table 3). When extending the phenyl group, **UPMP022** did not seem to improve 20-HETE inhibitory activity in RLM compared to **UPMP019** (Appendix Table 4). However, the 4-methyl derivative (**UPMP142**) and 4-chloro derivative (**UPMP117**) showed increased 20-HETE formation inhibition in RLM. The above findings are interim and preliminary based on screening data. IC<sub>50</sub> evaluation in RLM may provide a better understanding of structural requirements for compounds' potency improvement.

Among some of the potent compounds presented in Table 3.12, there was an approximately 5- to 14-fold difference in potency between different species. For example, **UPMP107** was 13-fold less potent in RLM compared to HLM (IC<sub>50</sub> =54.2 nM in HLM; IC<sub>50</sub> =723 nM in RLM). **UPMP072** was ~ 5-fold less potent in RLM than in HLM. To summarize, in Tier 2 single concentration screening, we screened 143 compounds in three microsomal systems. Among these compounds, 76 compounds showed greater than 50% 20-HETE formation inhibition in HLM, 28 compounds showed greater than 40% 20-HETE formation inhibition in RLM. These compounds

of interest would be advanced to Tier 3 *in vitro* evaluation. We evaluated the potency for 40 novel molecules and obtained preliminary SAR traits. Based on the available data, it appeared that (1) the (1*H*-pyrazole-4-yl)piperidine core seemed to provide improved 20-HETE formation inhibitory activity compared to (1*H*-pyrazole-5-yl)piperidine core when single small substitution is present at the phenyl group that directly attached to the piperidine group; (2) Double substitutions on phenyl group seems to induce an improvement in 20-HETE formation inhibition when the phenyl group directly connected to the piperidine group; (3) Single substitution on the phenyl group on *para*- position and *meta*- position were tolerated in a small subset of derivatives. When fluorine was at the *ortho*- position, the activity seemed to be preserved comparing to other substitution at *ortho*-position in compounds with benzene moiety directly attached to the piperidine group; (4) Extending the piperidine connection of the phenyl group via a methylene or a S link may provide additional active compounds for development. A portion of the SAR traits was based on single concentration screening and a small amount of IC<sub>50</sub> data. Generation of additional IC<sub>50</sub> values for compounds of interest will help further evaluate the SAR to support lead optimization.

Based on the potency in HLM, a list of 14 compounds that met the criteria of IC<sub>50</sub> ≤ 100 nM in HLM were identified. Based on the potency in HLM, a ranking of novel chemical entities was derived (Table 3.12). The fourteen compounds were ranked as top compounds to be assessed in the other *in vitro* assays.

**Table 3.12 Top ranked novel compounds based on IC<sub>50</sub> in HLM**

Compound (UPMP)	IC <sub>50</sub> (nM) in HLM	IC <sub>50</sub> (nM) in RLM
<b>117</b>	17.3	120
<b>142</b>	24.0	-
<b>072</b>	45.8	240
<b>105</b>	47.4	>500
<b>068</b>	49.5	337
<b>022</b>	49.6	>500

<b>124</b>	53.6	570
<b>107</b>	54.2	723
<b>031</b>	73.4	>500
<b>047</b>	78.8	>500
<b>048</b>	80.3	>500
<b>073</b>	82.1	-
<b>057</b>	98.1	>500
<b>060</b>	101	-

---

### 3.3.5 Characterization of properties for top ranked compounds

#### 3.3.5.1 Selectivity

Through the tiered screening and potency evaluation, compounds with IC<sub>50</sub> as low as 17.3 nM against CYP4 enzymes were identified. The selectivity of 20-HETE versus EETs and DiHETs was studied next. The UPLC-MS/MS method allowed us to quantify 8,9-, 11,12-, 14,15- EET; 5,6-, 8,9-, 11,12-, 14,15-DiHET and 20-HETE simultaneously. The formation of EETs and DiHETs was used as a surrogate index for epoxygenase activity. As compound concentration increased, compounds inhibited 20-HETE formation in a concentration-dependent manner. Formation of EETs and DiHETs were not affected until reaching high concentrations (Fig.3.6). Therefore, all the top compounds that were evaluated had IC<sub>50</sub> for EETs and DiHETs > 10,000 nM, which were ≥ 100-fold IC<sub>50</sub> for 20-HETE inhibition, meeting the selectivity criteria.

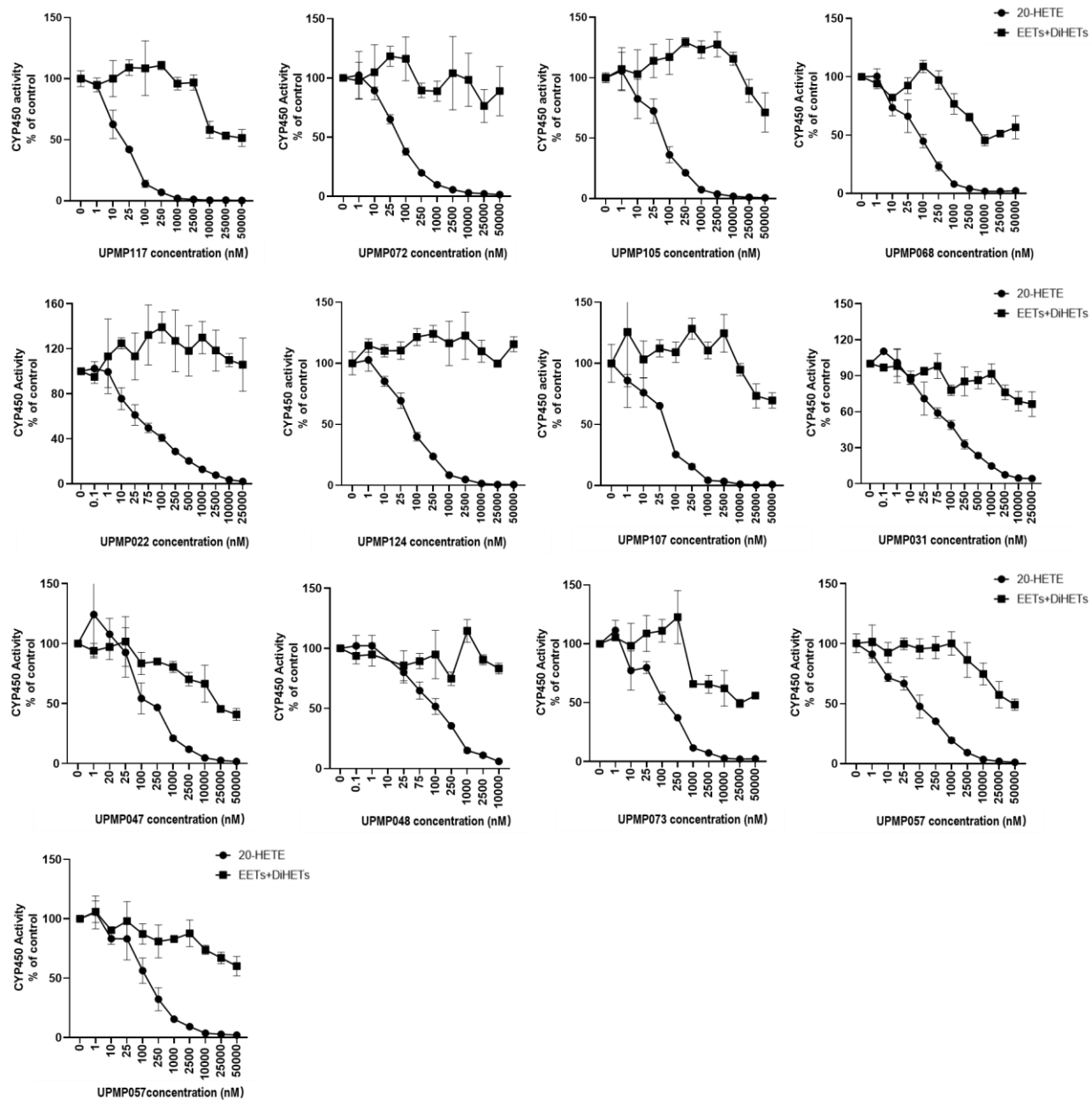


**Figure 3.6 Selectivity of 20-HETE versus EETs and DiHETs for top ranked compounds**

Effects of novel top ranked compounds on the formation of 20-HETE versus EETs and DiHETs in HLM. Results are expressed as percent of control and are mean  $\pm$  std (n=3). Compounds inhibited 20-HETE concentration-dependently. Compounds either did not show inhibition for epoxigenases or inhibited EETs and DiHETs with IC<sub>50</sub> values greater than 100-fold of IC<sub>50</sub> values for 20-HETE.

### 3.3.5.2 Solubility

Kinetic solubility was evaluated for the top ranked compounds (Table 3.13). Compound **UPMP072**, **UPMP022**, **UPMP107**, and **UPMP060** met the solubility criteria of  $> 400 \mu\text{M}$ . **UPMP068** had a solubility of  $35.4 \mu\text{M}$ , which is approximately 700-fold higher than its  $\text{IC}_{50}$  in HLM. The rest of the compounds had solubilities that were 1000-fold higher than their respective  $\text{IC}_{50}$  values for 20-HETE inhibition in HLM, giving a wide window to increase the dose without insolubility concern if they were to be prepared as an IV formulation to be evaluated in animal studies.

### 3.3.5.3 Metabolic stability and preliminary prediction of human clearance

Metabolic stability of compounds was evaluated in HLM at a concentration of  $1 \mu\text{M}$ . Time-courses of substrate disappearance is shown in Fig 3.7. *In vitro*  $t_{1/2}$  and *in vitro* intrinsic clearance ( $\text{CL}_{\text{int, in vitro}}$ ) were derived from the natural logarithmic transformed data by fitting linear regression. Most of the top ranked compounds were slowly metabolized throughout the 60-min incubation period comparing to benchmark compound **24**. We found that the novel compounds had prolonged *in vitro*  $t_{1/2}$  compared to positive controls (HET0016,  $t_{1/2} = 6.10 \text{ min}$ ; compound **24**,  $t_{1/2} = 19.6 \text{ min}$ ) (Table 3.13). Novel 20-HETE formation inhibitors had 5.2- to 130-fold prolonged  $t_{1/2}$ . Among the novel compounds, approximately 100% of **UPMP048** and **UPMP068** remained after incubation with HLM over 60 min test period. The  $t_{1/2}$  values were not estimated due to slow metabolism (Table 3.13). **UPMP060** and **UPMP072** were quickly metabolized and did not meet the metabolic stability criteria. The fast metabolism of **UPMP060** and **UPMP072** might be attributed to the hydrolysis of the amide group as disappearance of compounds in NADPH-free incubation in HLM was observed (Table 3.14). Human *in vivo* intrinsic clearance ( $\text{CL}_{\text{int, in vivo}}$ ) was calculated according to Equation 3.1.5 and presented in Table 3.13. Hepatic clearance was not predicted due



to unknown plasma protein binding. Among the 12 evaluated top ranked compounds, all met metabolic stability criteria except **UPMP060** and **UPMP072**.

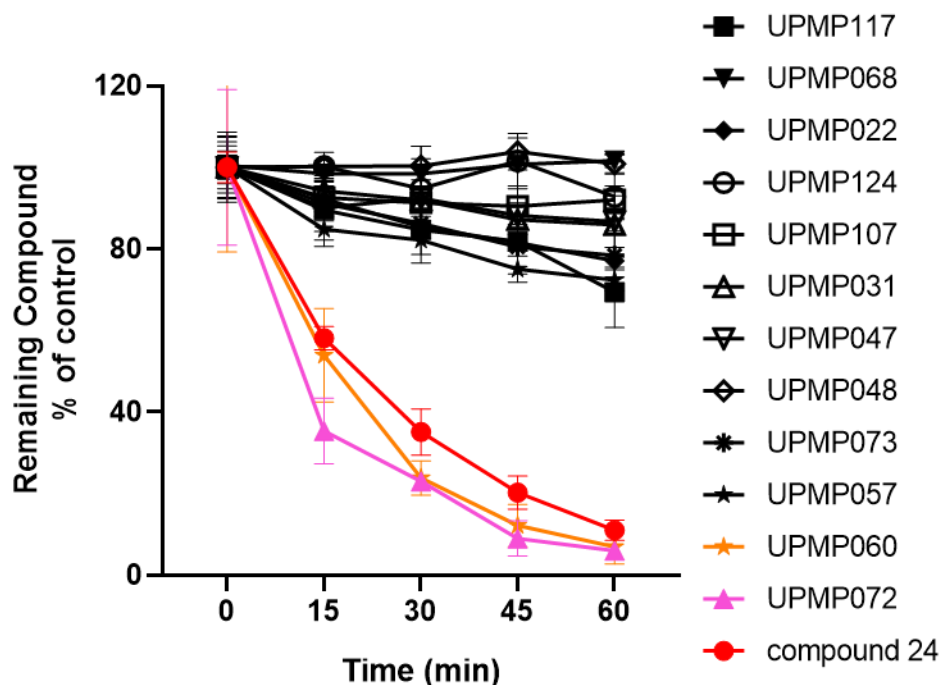


**Figure 3.7 Metabolic stability of top ranked compounds in HLM.**

Compounds were incubated in HLM, data are presented as percent of control and are mean  $\pm$  std. Compound **24** (red) was metabolized quickly in HLM ( $t_{1/2} = 19.5$  min). There was 35.1% remaining compound at 30 min. **UPMP060** (orange) and **UPMP072** (pink) were quickly metabolized in HLM. The remaining amounts were 23.8 and 23.0%, respectively. Other top ranked compounds (black) had greater than 80% remaining compounds at 30 min.

**Table 3.13 Evaluation of clearance, solubility, and MDCK-MDR1 permeability of top ranked compounds**

Compd	Kinetic Solubility ( $\mu$ M)	IVIVE of clearance			MDCK-MDR1		ER
		<i>In vitro</i> t <sub>1/2</sub> (min)	CL <sub>int, in vitro</sub> ( $\mu$ l/min/mg protein)	CL <sub>int, in vivo</sub> (ml/min/kg)	Papp <sub>A-B</sub> (10 <sup>-6</sup> cm/s)	Papp <sub>B-A</sub> (10 <sup>-6</sup> cm/s)	
HET0016	163	6.10	227	182	-	-	-
<b>24</b>	333	19.5	71.1	56.8	-	-	-
<b>UPMP117</b>	117	200	5.19	6.94	44.3	40.0	0.902
<b>UPMP142</b>	71	-	-	-	77.4	70.3	0.908
<b>UPMP072</b>	482	9.99 <sup>a</sup>	139	111	-	-	-
<b>UPMP105</b>	353	-	-	-	-	-	-
<b>UPMP068</b>	35.4	NM <sup>a</sup>	NM	-	-	-	-
<b>UPMP022</b>	505	152	9.09	7.27	62.8	60.1	0.957
<b>UPMP124</b>	74	796	1.74	1.74	22.2	46.9	2.12
<b>UPMP107</b>	>600	267	6.94	5.19	5.16	41.6	8.06
<b>UPMP031</b>	35	226	6.12	4.90	32.0	25.7	0.803
<b>UPMP047</b>	85	248	5.60	4.48	-	-	-
<b>UPMP048</b>	244	NM	NM	-	-	-	-
<b>UPMP073</b>	-	144	9.64	7.71	47.8	32.1	0.672
<b>UPMP057</b>	96	109	12.8	10.2	-	-	-
<b>UPMP060</b>	>600	14.8 <sup>b</sup>	93.6	74.9	18.4	40.2	2.18

<sup>a</sup> Not metabolized in HLM for the duration of 60 min.

<sup>b</sup> The compound was assumed to be hydrolyzed in incubation without NADPH.

**Table 3.14 Metabolic stability of UPMP060 and UPMP072 in the presence and absence of NADPH**

Time (min)	Metabolic stability (% of control)					
	NADPH-dependent		NADPH-free		Boiled microsome	
	UPMP060	UPMP072	UPMP060	UPMP072	UPMP060	UPMP072
0	100	100	100	100.0	100	100
15	53.9	35.3	39.2	44.1	159	97
30	23.8	23	16.9	24.0	106	101
45	12.2	9	6.93	5.83	103	-
60	6.92	6	11.3	4.27	106	105
CL <sub>int, in vitro</sub> ( $\mu$ l/min/mg protein)	119	139	79.0	125	-	-

#### 3.3.5.4 MDCK-MDR1 and BBB permeability

To our knowledge, previous reports on 20-HETE formation inhibitors did not disclose BBB permeability. To develop 20-HETE formation inhibitors as neuroprotective agents that work in the brain, early *in vitro* evaluation of BBB penetration is of critical importance. Among the compounds that were evaluated for MDCK-MDR1 permeability, Papp<sub>A-B</sub> varied from 5.16 to  $77.4 \times 10^{-6}$  cm/s, suggesting high apical to basolateral passive permeability and brain uptake potential (Table 3.13). The ratio of Papp<sub>A-B</sub>/Papp<sub>B-A</sub> (ER) was used as an index of P-gp mediated efflux across MDCK cells transfected with the human *mdr1* gene that expresses P-gp. The ER for the compounds ranged between 0.803 – 8.06. Overall, among top ranked compounds that were tested, they all exhibited moderate to high BBB penetration in the MDCK-MDR1 assay. These compounds might have good BBB permeability *in vivo*.

### 3.3.5.5 CYP inhibition and DDI potential

We also tested the analogs for inhibition against five drug metabolizing CYP enzymes. A greater than 50% percent of control suggests an IC<sub>50</sub> for a CYP isoform > 100-fold of IC<sub>50</sub> for 20-HETE formation, yielding at least a 100-fold selectivity window. **UPMP117** abolished CYP2C19 activity at 2000nM (Table 3.15). **UPMP068** inhibited CYP2C19 activity by 89% at 1000 nM. Inhibition of CYP enzymes was less than 50% for **UPMP107** and **UPMP124**. Therefore, **UPMP107** and **UPMP124** met the CYP inhibition criteria.

**Table 3.15 CYP inhibition for NCEs**

compound <sup>a</sup>	% of control				
	CYP1A2	CYP2C9	CYP2C19	CYP2D6	CYP3A4
<b>UPMP117</b>	102±16.7	74.8±14.6	1.05±0.34	56.3±11.6	121±8.06
<b>UPMP068</b>	94.2±7.65	49.4±2.13	11.2±2.78	98.5±3.47	119±12.5
<b>UPMP022</b>	85.4±25.1	102±6.75	44.4±43.1	65.7±10.2	111±6.07
<b>UPMP124</b>	101±8.50	70.6±4.98	71.3±8.01	97.2±3.71	94.2±6.37
<b>UPMP107</b>	82.0±9.57	51.3±6.70	83.4±6.76	106±15.5	92.3±5.56

<sup>a</sup> Compound were tested at concentrations of **UPMP117**: 2000 nM; **UPMP068**: 1000nM; **UPMP022**:5000nM; **UPMP107**: 5000 nM; **UPMP124**: 5000 nM.

### 3.3.5.6 *In vitro* safety pharmacology

The use of *in vitro* safety pharmacology profiling is an important tool to identify potential adverse effects and reduce safety-related attrition early in drug discovery. A panel of 44 known human pharmacological targets was used to evaluate **UPMP107** and **UPMP124** at 10 µM (Table 3.16). The targets included well-described cardiovascular or CNS targets such as 5-HT receptors, hERG, ion channels, and enzymes such as COX. **UPMP107** did not show a greater than 50% inhibition or stimulation on GPCRs, kinases, ion channels, transporters or enzymes in the panel. Initial safety pharmacology evaluation suggested that **UPMP124** had a 78% inhibition on the L-type Ca<sup>2+</sup> channel. A followed-up IC<sub>50</sub> evaluation showed a lack of dose-dependent inhibition,

suggesting a lack of inhibition on the L-type  $\text{Ca}^{2+}$  channel (Table 3.17). Therefore, **UPMP107** and **UPMP124** met the *in vitro* safety pharmacology criteria of <50% inhibition at 10  $\mu\text{M}$ .

**Table 3.16 *In vitro* safety pharmacology results of UPMP107 and UPMP124**

Assay	% Inhibition of control specific binding	
	UPMP107	UPMP124
A2A (h) (agonist radioligand)	-9	1
alpha 1A (h) (antagonist radioligand)	24	-3
alpha 2A (h) (antagonist radioligand)	-5	2
beta 1 (h) (agonist radioligand)	-3	-3
beta 2 (h) (antagonist radioligand)	-6	-2
BZD (central) (agonist radioligand)	-10	-22
CB1 (h) (agonist radioligand)	-12	1
CB2 (h) (agonist radioligand)	-4	-6
CCK1 (CCKA) (h) (agonist radioligand)	-16	2
D1 (h) (antagonist radioligand)	2	2
D2S (h) (agonist radioligand)	3	-7
ETA (h) (agonist radioligand)	5	-2
NMDA (antagonist radioligand)	0	-3
H1 (h) (antagonist radioligand)	-6	2
H2 (h) (antagonist radioligand)	-21	-10
MAO-A (antagonist radioligand)	6	14
M1 (h) (antagonist radioligand)	10	2
M2 (h) (antagonist radioligand)	21	-6
M3 (h) (antagonist radioligand)	-2	-10
N neuronal alpha 4beta 2 (h) (agonist radioligand)	10	9
delta (DOP) (h) (agonist radioligand)	-2	0
kappa (h) (KOP) (agonist radioligand)	2	-4
mu (MOP) (h) (agonist radioligand)	2	1
5-HT1A (h) (agonist radioligand)	-8	-3
5-HT1B (h) (antagonist radioligand)	-6	-4
5-HT2A (h) (agonist radioligand)	-7	-4
5-HT2B (h) (agonist radioligand)	-21	20
5-HT3 (h) (antagonist radioligand)	-4	7
GR (h) (agonist radioligand)	2	5
AR (agonist radioligand)	2	4
V1a (vh) (agonist radioligand)	9	-3

Ca <sup>2+</sup> channel (L, dihydropyridine site) (antagonist radioligand)	-15	78
Potassium Channel hERG (human)- [3H] Dofetilide	-3	0
KV channel (antagonist radioligand)	1	-5
Na <sup>+</sup> channel (site 2) (antagonist radioligand)	17	16
norepinephrine transporter (h) (antagonist radioligand)	-4	-1
dopamine transporter (h) (antagonist radioligand)	-2	0
5-HT transporter (h) (antagonist radioligand)	6	-8

Assay	% Inhibition of control values	
COX1(h)	8	-29
COX2(h)	28	25
PDE3A (h)	1	-3
PDE4D2 (h)	-15	-8
Lck kinase (h)	1	-13
acetylcholinesterase (h)	-7	5

**Table 3.17 UPMP124 binding to Ca<sup>2+</sup> channel**

Test concentration (M)	% inhibition of control specific binding	% of control specific binding (mean)
$1.37 \times 10^{-8}$	6	93.5
$4.12 \times 10^{-8}$	3	97.1
$1.23 \times 10^{-7}$	-7	106.9
$3.70 \times 10^{-7}$	1	99.4
$1.11 \times 10^{-6}$	4	96.4
$3.33 \times 10^{-6}$	1	99.1
$1.00 \times 10^{-5}$	-3	102.7
$3.00 \times 10^{-5}$	11	88.5
$1.37 \times 10^{-8}$	8	91.5
$4.12 \times 10^{-8}$	-6	106.2
$1.23 \times 10^{-7}$	-1	101.1
$3.70 \times 10^{-7}$	3	97.4
$1.11 \times 10^{-6}$	29	71.1
$3.33 \times 10^{-6}$	-1	100.7
$1.00 \times 10^{-5}$	-5	104.5
$3.00 \times 10^{-5}$	10	89.7

It should be noted that while other compounds with more potent 20-HETE formation inhibition were identified (e.g. **UPMP117**,  $IC_{50} = 17.3$  nM; **UPMP072**,  $IC_{50} = 45.8$  nM; **UPMP068**,  $IC_{50} = 49.5$  nM; **UPMP022**,  $IC_{50} = 49.6$  nM), each possessed unfavorable attributes compared to **UPMP107**. Specifically, **UPMP117**, **UPMP068**, and **UPMP022** had liability in CYP inhibition. **UPMP072** was markedly less stable in HLM, with a  $t_{1/2}$  value of 9.99 min. Additionally, hydrolysis of **UPMP072** will produce an aniline group which may be subject to chemical oxidation reactions (Bruns et al. 2012).

The decision process of selecting **UPMP107** as the preclinical candidate is presented in Fig.3.8. In Tier 2, we screened 143 compounds. Among these compounds, 76 of them displayed  $\geq 50\%$  inhibition in HLM that would be advanced for potency evaluation. We completed potency evaluation for 40 compounds in HLM. Among them, 14 compounds had  $IC_{50} \leq 100$  nM in HLM. The 14 compounds are the top ranked compounds presented in Table 3.12. Since we would like to evaluate the efficacy of novel molecules in rats that express different 20-HETE formation enzymes, compounds with good 20-HETE formation inhibition in RLM would be preferable. Of the 14 compounds, 7 compounds (**UPMP072**, **UPMP105**, **UPMP022**, **UPMP031**, **UPMP047**, **UPMP048**, and **UPMP057**) were excluded from the preclinical candidate pool because of low 20-HETE inhibition in RLM in the single concentration screening assay. Among the seven compounds remained, **UPMP117**, **UPMP142**, **UPMP068**, **UPMP124**, and **UPMP073** had solubility less than 400  $\mu$ M and were excluded from further consideration. This led to two compounds for further evaluation. The quick metabolism of **UPMP060** in HLM made it an unfavorable candidate. Among all the compounds evaluated, **UPMP107** met all prespecified *in vitro* property criteria and therefore became the preclinical candidate that would be advanced to *in vivo* evaluation.

To summarize, by following the multi-tiered evaluation approach of evaluating potency and other characteristics including solubility, selectivity, metabolic stability, BBB permeability, CYP inhibition, and *in vitro* safety pharmacology, we reported the identification of **UPMP107** as a novel preclinical candidate that target CYP4 enzymes to inhibit 20-HETE formation. This novel compound was selected to be evaluated in animal studies.

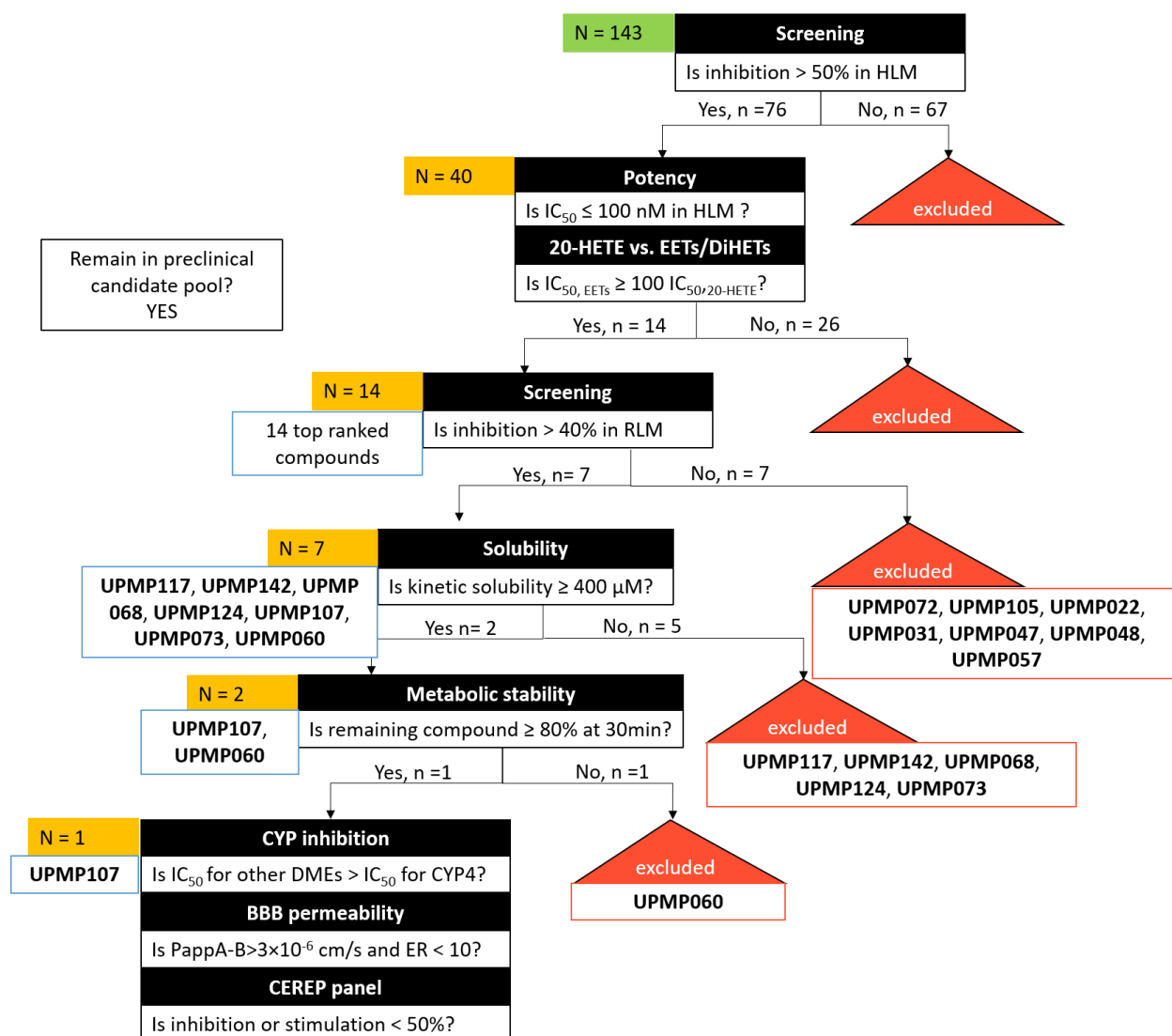


**Figure 3.8** Decision tree to narrow down the preclinical candidate pool



The decision tree illustrates the process of **UPMP107** being selected as a preclinical candidate. In Tier 2, 143 compounds were screened. 76 compounds inhibited 20-HETE formation  $\geq 50\%$  in HLM and were advanced for potency evaluation. Among the 76 compounds, we tested  $IC_{50}$  for 40 compounds in HLM, 14 compounds showed  $IC_{50} \leq 100$  nM. They were the 14 top ranked compounds present in Table 3.12. Among them, 7 compounds showed poor 20-HETE formation inhibition in RLM in screening assay and were excluded from the preclinical candidate pool. Among the 7 compounds that were evaluated for solubility, **UPMP107** and **UPMP060** had  $\geq 400$   $\mu$ M kinetic solubility. **UPMP107** also met metabolic stability, CYP inhibition, BBB permeability, and Cerep *in vitro* safety pharmacology criteria. Therefore, **UPMP107** was selected as the preclinical candidate for *in vivo* evaluation.

### 3.4 Discussion and conclusions

The CYP4 enzymes, responsible for the activation of numerous eicosanoids signaling pathways, represent an important therapeutic target in multiple disease areas, such as hypertension, stroke, and cancers. However, exploiting CYP4 as a drug target is yet to be achieved. In this study, we showed that **UPMP107** is a novel CYP4 inhibitor with strong potency against 20-HETE formation in both human and rat liver microsomes and good physicochemical properties. **UPMP107** was selective, with a greater than 900-fold selectivity window for 20-HETE formation inhibition vs. EETs and DiHETs formation inhibition. **UPMP107** was highly soluble. Furthermore, in contrast to the rapid *in vitro* metabolism of HET0016, **UPMP107** was metabolically stable in HLM. **UPMP107** was further characterized as having a low potential for DDIs and good BBB penetration potential.

One of the challenges for structure-based drug design for 20-HETE formation inhibitors is the absence of CYP4F2 or CYP4A11 protein structural information. Computational protein 3D structure prediction such as homology modeling has been frequently applied in drug discovery projects to determine protein structure from amino acid sequence based on a template (Cavasotto

et al. 2009). CYP4 enzymes catalyze fatty acid hydroxylation at terminal  $\omega$ -carbon or internal sites (Fer et al. 2008). The unique feature of CYP4 structure is the presence of an ester bond between the heme and the carboxyl group of glutamic acid in helix I (LeBrun et al. 2002, Joyce et al. 2004, Hsu et al. 2017). Hydroxylation of endogenous CYP4F2 substrate vitamin K1 was investigated by a CYP4F2 homology model and shed light on the active residues including Phe124, Phe327, Glu328, Val368, and Leu504 in vitamin K1 binding to the inner pocket of CYP4F2 (Li et al. 2018). CYP4B1 has also been successfully utilized to generate CYP4Z1, CYP4A22 homology models (Xu et al. 2017, Durairaj et al. 2019). Considering rat CYP4B1 has 45% sequence identity with human CYP4F2 and specifically  $\omega$ -hydroxylate short-chain saturate alkanes, the structural inferences that can be made about CYP4F2 are limited (Fisher et al. 1998). Nonetheless, the availability of a homology model may provide insight on the active sites to help design compounds and study the binding of the compounds.

We observed a large species difference in CYP4 inhibitory activity across the compounds that had been screened. Among the 143 screened compounds, 76 met the screening criteria of > 50% inhibition in HLM and 26 met the screening criteria of > 40% inhibition in RLM. The large interspecies difference is not unexpected but poses a challenge in developing novel 20-HETE formation inhibitors. The difference in compound activity could be due to (1) different isoforms catalyze the formation of 20-HETE in rats and humans. CYP4A1, 4A2, 4A3, 4A8, 4F1, and 4F4 in rats; CYP4A11, 4F2, 4F3B in human are 20-HETE-synthesizing enzymes (Powell et al. 1998, Nguyen et al. 1999, Hoch et al. 2000, Kalsotra et al. 2002); (2) even if the isoforms are same across species, the differences in CYP protein primary sequence will lead to different substrate specificity; and (3) CYP isoform expression levels may be different in rodents and humans (Boobis et al. 1990, Eagling et al. 1998, Martignoni et al. 2006).

Novel compounds showed either greater inhibition in HLM compared to rCYP4F2 or greater inhibition in rCYP4F2. This could likely be explained by that CYP4F2 is not the sole enzyme for 20-HETE synthesis and the expression and function of the isoforms are unknown. To date, CYP4A11 and CYP4F2 are still considered two major enzymes that underlie 20-HETE formation. CYP4A11 has the strongest catalytic activity of 15.6 nmol/min/nmol P450, but the affinity for arachidonic acid is relatively low with  $K_m$  value of 228  $\mu$ M. Although CYP4F2 has a lower 20-HETE formation rate of 6.8 nmol/min/nmol P450, it has a high affinity to arachidonic acid ( $K_m=24$   $\mu$ M) (Powell et al. 1998). Several other CYP isoforms also possess 20-HETE formation activity, including CYP4F3B, CYP4F11, and CYP2U1 (Lasker et al. 2000, Chuang et al. 2004, Fer et al. 2008, Tang et al. 2010). CYP4F3B also has a high affinity to the substrate ( $K_m = 22$   $\mu$ M) (Christmas et al. 2001). The total amount of CYP4F protein level has a large variability in human liver microsomes, as estimated to be 18 – 128 pmol/mg liver microsomal protein (Tang et al. 2010). Due to the high homology of CYP4F2, CYP4F3B, CYP4F11 and CYP4F12, the absolute amount of each enzyme in the liver is unknown (Edson et al. 2013). The expression, catalytic activity of enzymes responsible for 20-HETE formation may vary in HLM from batch to batch. The affinity of enzymes and compounds is unknown. Compounds that showed greater inhibition in HLM than CYP4F2 might bind to several enzymes that can form 20-HETE in HLM.

We observed induction in 20-HETE formation for several compounds such as **UPMP13** and **UPMP132**. The induction of 20-HETE could be an artifact and should be confirmed with repeated potency tests. Another explanation might be related to CYP enzyme activation. CYP3A4 has been studied extensively with respect to enzyme activation with different substrates, such as CYP3A4-catalyzed phenanthrene in the presence of 7,8-benzoflavone. In the presence of CYP3A4 substrate 7,8-benzoflavone, phenanthrene metabolism showed an increased  $V_{max}$  without affecting

$K_m$ , and phenanthrene didn't increase  $K_m$  of 7,8- benzoflavone metabolism, while decreasing its  $V_{max}$ , indicating more than one molecule could bind to CYP3A4 active sites simultaneously. Phenanthrene and 7,8- benzoflavone serve as each other's effector of metabolism. 7,8- benzoflavone stimulates phenanthrene metabolism by 15.7-fold, while phenanthrene is a partial inhibitor of 7,8-benzoflavone metabolism. The unchanged  $K_m$  values suggested that phenanthrene and 7,8-benzoflavone could not displace each other from the active site (Korzekwa et al. 1998). There are at least two or possibly three active sites within CYP3A4 (Hosea et al. 2000). This atypical kinetics was also observed for other CYP enzymes and substrates such as dapsone activation of CYP2C9-mediated metabolism (Korzekwa et al. 1998, Matthew Hutzler et al. 2003, Blobaum et al. 2013). When coincubating dapsone with flurbiprofen, the CYP2C9-mediated flurbiprofen 4'-hydroxylation had a decrease in  $K_m$  and an increase in  $V_{max}$ . The decreased spectral binding constant from 14.1 to 2.1  $\mu M$  also suggested that the presence of dapsone increased the affinity of flurbiprofen for CYP2C9.(Matthew Hutzler et al. 2003). This kinetic evidence suggested that both effector (dapsone) and substrate (flurbiprofen) may be present in the active site simultaneously, supporting a two-site binding model of CYP450-mediated metabolism (Hutzler et al. 2001). By studying dapsone and its nine analogs, a sulfone group in direct association with two benzene rings with para- electron-donating groups were found to be the structural requirements to be an efficient activator of CYP2C9 (Hutzler et al. 2002). The increase in 20-HETE formation in the presence of a test compound could suggest a possibility of arachidonic acid binding to the CYP4F2 active site in the presence of a test compound. The test compound might cause arachidonic acid to bind more efficiently or in a more productive orientation that leads to increased catalytic activity of 20-HETE formation. Incubation needs to be repeated to confirm the finding of compounds that exhibited an increase in 20-HETE formation.

Additional experiments to obtain  $V_{\max}$  and  $K_m$  of arachidonic acid  $\omega$ -hydroxylation by coincubating arachidonic acid and compound of interest at various concentrations and analysis of Eadie-Hofstee plots would support the effect of compound on CYP4F2-mediated arachidonic acid activation.

The human brain is a sophisticated organ with the protection of blood-brain barrier (BBB), enabling selective access of molecules. Designing compounds that can penetrate the protection system to achieve optimal exposure at the site of action is an utmost challenge in CNS drug development. Physicochemical properties such as lipophilicity, hydrogen bonding potential, and size have been identified as important requirements for penetrating the BBB (Janicka et al. 2020). Lipophilicity is an important property that is related to permeability, solubility, and protein binding. Higher lipophilicity (LogP) is usually associated with increased plasma and tissue binding, and increased passive permeability for molecules containing ionizable groups (Gleeson 2008, Reichel 2009). An analysis of 3000 diverse GlaxoSmithKline compounds found a negative correlation between LogP and fraction of unbound in the brain ( $f_{u,b}$ ), suggesting higher free drug concentrations in the brain might be obtained by lowering LogP to achieve higher efficacy (Gleeson 2008). Based on the free-drug assumption that only unbound drugs are able to cross the BBB to produce a therapeutic effect, compounds with higher lipophilicity are not favorable as they might be highly protein bound and are less likely to penetrate the BBB. However, drugs that are highly protein bound such as imipramine and desimipramine have high concentrations in the brain (Lin et al. 1987). In fact, 15 most prescribed CNS drugs have  $f_{u,b} < 5\%$  (Liu et al. 2014). The possible mechanisms include 1) conformational change of protein when interacting with capillary walls may free the drug molecule from a drug-protein complex; 2) binding with protein may induce protein-mediated transport to enhance BBB penetration; and 3) capillary endothelium in some

regions is more permeable (Wanat 2020). The calculated LogP for **107** is 1.90, within the optimal cLogP range of 1 – 3 that provides a balance between the hydrophilicity and lipophilicity and to reduce the chances of poor solubility, high metabolism and increases the possibility of passive permeation across BBB. Hydrogen bond descriptors were also found to be critical CNS differentiators. Increased H-bonding potential is associated with lower passive permeability (Veber et al. 2002). Marketed CNS drugs have 2.12 hydrogen bond acceptors and 1.5 hydrogen bond donors on average (Pajouhesh et al. 2005). **UPMP107** has 1 hydrogen bond donor and 2 hydrogen bond acceptors, meeting the physicochemical properties seen in CNS positive drugs.

BBB permeability and active transport are recognized determinants of drug exposure in the brain. Currently, high-throughput permeability assays are generally employed in human colon carcinoma (Caco-2), MDCK, or human bladder carcinoma (ECV304)) cell lines (Morofuji et al. 2020). Although these cells are not derived from the brain, the tight junctions enable *in vitro in vivo* permeability correlation (Puscas et al. 2019). The ABC efflux transporter P-gp, encoded by *MDR1*, is a key transporter that recognizes a wide array of structural types of compounds and actively transport drugs out of brain capillary endothelial cells. MDCK-MDR1, a canine renal epithelial model transfected with the human *MDR1* gene, is generally used as a cell-based surrogate for BBB penetration (Hellinger et al. 2012). In addition to P-gp, other efflux transporters such as breast cancer resistance protein (BCRP), multidrug resistance proteins (MRPs) are also expressed at the BBB. A recent study of BBB transporter protein abundance in 30 postmortem adults showed a ranking of BCRP > P-gp for efflux transporters (Billington et al. 2019). Although compounds found to be P-gp substrates in rodents are also likely to be substrates in higher species, there is a more than two-fold difference in protein abundance such as P-gp and MRP4 between humans and Sprague-Dawley rats (Syvanen et al. 2009, Hoshi et al. 2013). Therefore, when

interpreting the result from the MDCK-MDR1 assay, the lack of expression of other relevant BBB transport proteins and species difference should be considered. Nonetheless, **UPMP107** has  $P_{appA-B}$  of  $5.16 \times 10^{-6}$  cm/s and an ER of 8.06, suggesting that **UPMP107** might have good brain penetration *in vivo*.

*In vitro* metabolic stability is routinely examined to exclude compounds with potentially high clearance. We utilized substrate depletion method to determine *in vitro* metabolism in human liver microsomes as it provides the most convenient and affordable way to study CYP-mediated metabolism and is not confounded by other metabolic processes or transporter uptakes (Jia et al. 2007). Phase II metabolism can be tested by addition of UDP-glucuronyltransferases to microsomes. There could be an underprediction of clearance when using human liver microsomes to measure phase I metabolism given that microsomes do not contain organelles or transporters like hepatocytes and phase II metabolism not being studied. An average 9-fold underprediction of *in vivo* clearance was reported when using HLM (Chiba et al. 2009). Efforts have been made to reduce the systemic underprediction via applying a multiplicative correction factor (Poulin et al. 2013). *In vitro-in vivo* extrapolation is commonly used to estimate human hepatic clearance. Microsomes can be used to determine an *in vitro* intrinsic clearance ( $CL_{int, in vitro}$ ) and then scaled by microsomal protein content and liver weight to an *in vivo* intrinsic clearance ( $CL_{int, in vivo}$ ) that can be used to calculate hepatic clearance using a well-stirred model (Houston 1994, Riley et al. 2005, Obach 2011). Our attempt to predict human hepatic clearance is preliminary. The calculation of  $CL_{int, in vitro}$  did not account for the fraction of unbound in the incubation ( $f_{u,inc}$ ). Hepatic clearance was not estimated due to a lack of information in plasma protein binding. As promising leads are discovered, obtaining information on metabolism and elimination pathways is critical. Clearance in multiple animal species is also required to perform human clearance prediction with

high confidence (Caldwell et al. 2004, Lombardo et al. 2013). We observed several compounds such as **UPMP048** and **UPMP068** exhibited low turnovers in HLM. Although achieving a low clearance is commonly the goal when designing new compounds, the low clearance in HLM also presents a challenge in predicting accurate *in vivo* clearance. A couple of methodologies were proposed to overcome the challenge of low clearance including measuring metabolite formation, coculture hepatocyte systems, and hepatocyte relay method to improve the accuracy of *in vitro* clearance measurement (Di et al. 2015).

Inhibition of a CYP enzyme can cause potential drug-drug interaction that may lead to failure in clinical development due to serious side effects. Among all CYP isoforms, CYP1A2, 2C9, 2C19, 2D6, and 3A4 take up 8.9%, 12.8%, 6.8%, 20%, and 30.2% of the total CYP450 in the liver, but are responsible for the metabolism of 95% marketed drugs (Zanger et al. 2013, Spaggiari et al. 2014). *In vitro* DDI studies using human liver microsomes indicated a lack of potential of **UPMP107** to directly inhibit CYP1A2, 2C19, 2D6, 2C8, and 3A4 at a concentration of 5000 nM, but **UPMP107** inhibited CYP2C9 activity by 48.7%, barely passing the prespecified CYP inhibition selectivity criteria. This fast screening results at a single concentration serve as preliminary information to preclude compounds that have CYP inhibition liabilities. Further study is needed to obtain an  $IC_{50}$  value for each isoform to draw a solid conclusion.

Our study has several limitations that are worth noting. First, some of the SAR findings were derived from screening data. The SAR exploration is interim and preliminary and warrants additional  $IC_{50}$  evaluation for pairs of compounds to extract well-defined patterns. Second, we did not test compound activity in human brain microsomes due to the commercial unavailability of the materials and the need for large quantities of microsomes for screening and  $IC_{50}$  determination. Third, prediction of human clearance is an initial attempt, more information on the metabolism



mechanism, metabolism pathways, protein binding is needed to improve the prediction accuracy. Fourth, we did not obtain IC<sub>50</sub> values for compounds that showed inhibition of drug metabolizing CYP activities, considering the goal was to exclude compounds with liabilities at this stage. And finally, a P-gp inhibitor in the MDCK-MDR1 assay would confirm the role of P-gp in transporting **UPMP107**. Ideally, a comprehensive evaluation should be performed for all promising compounds so that from a medicinal chemistry perspective, lead compounds can be optimized based on selectivity, stability, permeability, or toxicology results. Nonetheless, the goal of identifying a preclinical candidate with favorable attributes is completed in this body of work.

In conclusion, this study is the first to report the discovery of a novel CYP4 inhibitor, **UPMP107**, that reduce 20-HETE formation *in vitro*. The advantages of this novel compound include high metabolic stability, low *in vitro* clearance, strong potency, wide selectivity window, and *in vitro* BBB penetration. These favorable characteristics are intended to improve the druggability of **UPMP107** to support its development as a highly promising preclinical candidate to be proceeded to *in vivo* evaluation.

## **4.0 Pharmacokinetics and Pharmacodynamics of a Novel 20-HETE Formation Inhibitor**

### **UPMP107 in Pediatric Rats**

#### **4.1 Introduction**

Out-of-hospital cardiac arrest (OHCA) remains an unresolved public health emergency. The estimated number of children that experience OHCA is more than 5000 each year in the United States (Topjian Alexis et al. 2019). Although cardiopulmonary resuscitation (CPR) and prompt defibrillation are two effective treatments, the reported survival to hospital discharge in children of 6.4% to 10.2% from 2005 – 2013 is low (Atkins et al. 2009, Perkins et al. 2015, Fink et al. 2016). Post-cardiac arrest brain injury remains the main cause of morbidity and mortality in children after admission to ICU following OHCA (Topjian Alexis et al. 2019). Neurological sequelae associated with hypoxic-ischemic brain injury (HIBI) after cardiac arrest impede pediatric OHCA survivors to return to daily living and school performance due to high risk of physical, cognitive, and emotional disabilities (Chiota et al. 2011).

Cerebral perfusion after cardiac arrest was identified by the International Committee on Resuscitation as an important target to prevent secondary brain injury (Nolan et al. 2008). A recent literature review suggested that flow promotion and vasodilatory therapies are the two promising classes of agents for improving cerebral perfusion to increase cerebral blood flow (CBF) (Li 2019). Although multiple experimental treatments are available and several therapies have been tested in clinical studies, no therapies other than therapeutic hypothermia have been reported to show beneficial effects on neurological outcomes. (Geocadin et al. 2008). Therefore, there is a critical

need to discover and develop novel compounds as CBF-directed treatment to ameliorate secondary brain injury after cardiac arrest.

20-hydroxyeicosatetraenoic acid (20-HETE) is an important vasoconstrictive mediator in regulating CBF (Attwell et al. 2010). 20-HETE is produced by cytochrome P450 family 4 (CYP4) enzymes. Specifically, CYP4A11, 4F2, and 4F3B have been recognized to transform arachidonic acid (AA) into 20-HETE in humans (Powell et al. 1998, Harmon et al. 2006). Growing evidence has implicated the role of 20-HETE in the pathogenesis of post-cardiac arrest HIBI. Preclinical animal studies support the beneficial effect of inhibition of 20-HETE formation on CBF and neurological outcomes in pediatric rat and piglet cardiac arrest models (Shaik et al. 2015, Zhu et al. 2015). Despite the therapeutic potential in 20-HETE formation inhibition, developing chemical inhibitors of CYP4 enzymes to inhibit 20-HETE formation has been discouraged by potency, physicochemical properties, or pharmacokinetic (PK) liabilities.

N-Hydroxy-N'-(4-n-butyl-2-methylphenyl)formamidinium (HET0016) is a potent inhibitor of 20-HETE formation enzymes. It has been widely employed in preclinical studies as a pharmacologic agent to study the role of 20-HETE formation in various disease models such as cardiac arrest and ischemic stroke (Poloyac et al. 2006, Shaik et al. 2015). Limitations of HET0016 including poor aqueous solubility, instability under an acidic environment, rapid metabolism, and a narrow selectivity window have rendered it an undesirable preclinical compound for clinical development and have complicated the interpretation of its dose-response relationship in preclinical studies (Mu et al. 2008). Therefore, developing novel inhibitors that can prevail in these aspects is in crucial need.

Ongoing efforts have focused on overcoming the challenges mentioned above for developing CNS-targeted 20-HETE formation inhibitors. Cheminformatics, medicinal chemistry,

and sensitive bioanalytical methods were utilized to set up tiers of evaluation to facilitate the discovery of novel derivatives of a new series of 20-HETE formation inhibitors. **UPMP107** has been identified as a novel potent CYP4 inhibitor through a battery of *in vitro* evaluation. Previous studies have shown that **UPMP107** exhibits a high degree of selectivity in 20-HETE formation inhibition. The IC<sub>50</sub> values for 20-HETE formation inhibition in human liver microsome (HLM) and rat liver microsome (RLM) are 0.0542 µM and 0.723 µM, respectively. The IC<sub>50</sub> values for epoxyeicosatrienoic acids (EETs) and dihydroxyeicosatrienoic acid (DiHETs) formation are > 50 µM in HLM. The inhibition towards CYP1A2, 2C9, 2C19, 2D6, and 3A4 had IC<sub>50</sub> values > 5 µM. Additionally, **UPMP107** *in vitro* intrinsic clearance (Cl<sub>int,in vitro</sub> = 5.19 µl/min/mg protein) in HLM is 43 fold lower compared to HET0016 (227 µl/min/mg protein). **UPMP107** has a kinetic solubility > 600 µM and a PappA-B =  $5.16 \times 10^{-6}$  cm/s, ER = 8.06 in MDCK-MDR1 assay, suggesting a good BBB penetration potential. **UPMP107** met the key drug-like characteristics and warrant further *in vivo* studies for assessment of pharmacokinetics and central target engagement.

On the strength of the favorable attributes of **UPMP107** observed from the *in vitro* studies, the goal of this study was to evaluate the pharmacokinetics and pharmacodynamics of **UPMP107** *in vivo*. The purpose includes (1) study the pharmacologic effect of 20-HETE inhibition of **UPMP107**; (2) evaluate **UPMP107** plasma PK; and (3) evaluate **UPMP107** brain PK. In this present study, we used a developed and validated UPLC-MS/MS method to quantify **UPMP107** and 20-HETE concentrations in the plasma and brain. The results from this study will provide a foundation to help design future animal studies.

## **4.2 Materials and Methods**

### **4.2.1 Materials**

Arachidonic acid, 20-HETE, 20-HETE-d6, and HET0016 were purchased from Cayman Chemicals (Ann Arbor, MI). N-(4-Butyl-2-methylphenyl)acetamide (SMIP004) was purchased from Millipore Sigma (Burlington, MA). Organic solvents including acetonitrile, methanol, and acetic acid were purchased from ThermoFisher Scientific Co. (Pittsburgh, PA).

### **4.2.2 Animals**

Postnatal day (PND) 16-18 Sprague-Dawley male rats (bodyweight 28-42g) were obtained from Envigo (Denver, PA). Upon arrival, the animals were maintained on a 12-hour light/dark cycle and were given free access to pellets and water. All animal procedures were approved by the Institutional Animal Care and Use Committee of the University of Pittsburgh.

### **4.2.3 Chemicals and formulation**

**UPMP107** was designed and synthesized in the laboratory of Dr. Lee McDermott (School of Pharmacy, University of Pittsburgh). **UPMP107** was formulated in hydroxypropyl- $\beta$ -cyclodextrin (HP $\beta$ CD) (Mu et al. 2008). Briefly, 1.5mg of **UPMP107** powder was added to 1ml of 15% HP $\beta$ CD. The solution was agitated at 450 rpm under room temperature for 48 hours on a Titer Plate Shaker (Lab – Line Instruments, Inc., Melrose Park, IL). At the end of the agitation, the samples were aliquoted and lyophilized to complete dryness with a Freezone 6 Lyophilizer.

(Labcono Inc., Kansas City, MO). Samples were reconstituted on the day of animal experiments with phosphate-buffered saline (PBS) and filtered using Millipore 0.45  $\mu$ m, 13 mm PVDF Syringe Filters (Fisher Scientific, Pittsburgh, PA) before intravenous administration to animals.

#### 4.2.4 Single dose pharmacokinetic study

This study was an open, parallel-group experimental design. Rats were randomly assigned to the vehicle or **UPMP107** groups. Rats were anesthetized with 3% isoflurane in conjunction with 50/50 N<sub>2</sub>O/O<sub>2</sub> in a Plexiglas chamber until unconscious. Femoral artery and venous catheters were placed with a 50-gauge connected to 10-gauge polyethylene tubing. Mean arterial blood pressure (MAP) and heart rate were monitored through the arterial catheter. Arterial blood gases were measured at baseline. Rectal temperature was continuously monitored and maintained at 37°C by a heated water blanket system. **UPMP107** was administered as a single intravenous (IV) dose. A single IV bolus of **UPMP107** at either 5, 10, and 20 mg/kg was administered (n=8/group). The doses were selected to achieve plasma concentrations of 50-, 100-, and 200-fold of IC<sub>50</sub> of **UPMP107** based on previous plasma concentrations observed in postnatal day 17 rats. Plasma sampling time points were at 0, 5, 30, 60, 120, 240, 360, and 480 min after dosing (Table 4.1). The sampling scheme is considered long enough to capture the entire time course of **UPMP107** based on pilot *in vivo* study in postnatal day 17 rats, where we observed the half-life was approximately 60 min. A blood volume of 50  $\mu$ l was collected at each time point. Blood samples were collected via the arterial line for time points before 60 min and collected through the tail vein for time points after 60 min. The last blood sample was collected through cardiac puncture right before perfusing the brain. Blood samples were collected in heparinized Eppendorf tubes. Within 5min of blood collection, plasma was collected by centrifuging at 1000g for 10 min. Rats were euthanized by

exsanguination during brain perfusion after the last blood sample at 480 min. Mixed brain tissue (whole left or right hemisphere) was harvested at 480 min. Plasma and brain samples were stored at -80°C until analysis.

**Table 4.1 Blood collection scheme for UPMP107 IV PK study at dose levels of 5, 10, and 20**

Rat	mg/kg							
	Time (min)							
	0	5	30	60	120	240	360	480
1	x	x	x	x				x
2		x			x	x	x	x
3	x	x	x	x				x
4		x			x	x	x	x
5	x	x	x	x				x
6		x			x	x	x	x
7	x	x	x	x				x
8		x			x	x	x	x

#### 4.2.5 Brain distribution study

A separate cohort of animals received **UPMP107** 3 mg/kg and 20 mg/kg single IV injection. Animals were sacrificed at multiple time-points at 60, 180, 360, 540, or 720 min to collect blood and mixed brain tissues (n= 4/time point). The selection of sampling time points was exploratory. We hypothesized the PK of **UPMP107** drives the PD effect, and a prolonged 20-HETE formation inhibitory effect is expected due to its relatively long *in vitro*  $t_{1/2}$  of 267 min. The first time point 60 min would capture the early distribution of **UPMP107** into the brain. The last time point was at 720 min for 3 mg/kg. The last time point was updated to 540 min for 20 mg/kg

based on the emerged plasma PK data from 3 mg/kg. A detailed sampling scheme is presented in Table 4.2.

**Table 4.2 Blood and brain samples collection scheme for UPMP107 brain distribution study at dose level of 3 and 20 mg/kg**

Rat	Time (min)			
	60	180	360	540 or 720
1	x	x	x	x
2	x	x	x	x
3	x	x	x	x
4	x	x	x	x

#### 4.2.6 Plasma and brain sample preparation

20-HETE and **UPMP107** concentrations were determined using solid phase extraction as previously described. Briefly, brain tissue samples were homogenized in 0.12 M potassium phosphate buffer containing 5mM magnesium chloride and 0.113 mM butylated hydroxytoluene (BHT) and centrifuged at 10,000 rpm for 30 min. The supernatant was collected, 7.5 ng of 20-HETE-d6 and 7.5 ng of SMIP004 were added to the supernatant as internal standards. The samples were extracted using HLB solid phase extraction cartridges (Oasis, Waters, Milford, MA). Similarly, plasma samples were added to 1ml of the buffer, and internal standards were added to the solution for extraction. Columns were washed with three 1ml of 5% methanol and were eluted with 100% methanol. The eluent was dried down under nitrogen gas at 37°C and reconstituted in 125ul of 80:20 methanol: deionized water.



#### 4.2.7 Quantification of UPMP107 and 20-HETE

Plasma and brain concentrations of **UPMP107** and 20-HETE were determined using a validated UPLC-MS/MS method described in Chapter 2. Briefly, analysis of 20-HETE was carried out using a UPLC BEH C18, 1.7  $\mu\text{m}$  ( $2.1 \times 100$  mm) reversed-phase column (Waters, Milford, MA). Mobile phase consisted of 0.005% acetic acid, 5% acetonitrile in deionized water (A) and 0.005% acetic acid in acetonitrile (B). The flow rate for mobile phases was 0.5 ml/min. The initial mixture of mobile phase was 65:35 of A and B. Mobile phase B increased at 0.4 minutes after injection from 35% to 70% in a linear gradient over 4 minutes, and again increased to 95% over 0.5 minutes where it remained for 0.3 minutes. This was followed by a linear return to initial conditions over 0.1 minutes with a 1.5 minutes pre-equilibration period prior to the next sample run. The total run time was 6.4 minutes for each injection. Injection volumes were 7.5  $\mu\text{l}$ .

Separation of **UPMP107** was conducted using the above methods with a slight modification in the gradient. The initial mixture of mobile phase was 80:20 of A: B. Mobile phase B increased at 2 min from 20% to 70% in a linear gradient over 2 min and maintained at this condition for 1.5 min. This is followed by a 1.5 minutes pre-equilibration before the next injection. Total run time was 5.5 min and injection volumes were 7.5  $\mu\text{l}$ .

Mass spectrometric analysis detail can be found in Table 2.3. In brief, the analysis was performed using a TSQ Quantum Ultra (Thermo Fisher Scientific, San Jose, CA, USA) triple quadrupole mass spectrometer coupled with heated electrospray ionization operated in negative selective reaction monitoring mode for 20-HETE and positive selective reaction monitoring mode for **UPMP107**. Unit resolutions at both Q1 and Q3 were set at 0.70 full-width at half-maximum. Quantitation by selective reaction monitoring analysis on 20-HETE and **UPMP107** was performed by monitoring their  $m/z$  transitions (20-HETE:  $m/z$  325.3  $\rightarrow$  251, collision energy: 20 V;

**UPMP107**:  $m/z$  325.3  $\rightarrow$  240.3, collision energy: 17 V). Scan time was set at 0.01 seconds and collision gas pressure was set at 1.3 mTorr. Analytical data were acquired and analyzed using Xcalibur software version 2.0.6 (Thermo Finnigan, San Jose, CA, USA). The linearity range for **UPMP107** was 12.5 – 1500 pg on column, and the linearity range for 20-HETE was 6.25 – 10,000 pg on column.

#### 4.2.8 Pharmacokinetic analysis

PK parameters were analyzed by two methods. Noncompartmental analysis (NCA) was performed for naïve pooled data on the average plasma concentrations using R 4.0.3 (package: PKNCA). Briefly, the terminal phase of the plasma concentration-time curve was fitted by linear regression of data points to obtain the slope of the terminal phase ( $\lambda_z$ ). The area under the concentration-time curve from time zero to infinity ( $AUC_{0-\infty}$ ) was determined using the trapezoidal method plus the extrapolated area. The extrapolated area was determined by dividing the last measurable concentration at 480 min by  $\lambda_z$ . Other pharmacokinetic parameters included elimination half-life ( $T_{1/2}$ ), the observed maximum concentration ( $C_{max}$ ), the mean residence time (MRT), total body clearance ( $CL = \text{dose}/AUC_{0-\infty}$ ), and volume of distribution at steady state ( $V_{ss} = \text{MRT} \times CL$ ).

An animal population PK model was developed using the nonlinear mixed effect modeling software NONMEM 7.4.3 (ICON Development Solutions, Ellicott City, MD, USA). R 4.0.3 was used for dataset preparation and graphical display. One- or two-compartment structural model with linear or nonlinear elimination were evaluated to describe **UPMP107** plasma concentrations. Initial parameter estimates were obtained from NCA results. Individual PK parameters were assumed to follow a log-normal distribution with the mean ( $\theta$ : typical value) and variance ( $\omega^2$ :

interindividual variability). Additive, constant coefficient of variation (CCV), and additive plus CCV residual error models were tested. The first-order conditional estimation with interaction (FOCE-I) algorithm was used throughout model development process. Model selection and comparison was based on successful convergence of the minimization process, Akaike information criterion (AIC), and goodness-of-fit plots (GOF) including observed concentrations versus individual predicted concentrations (IPRED), observed concentrations versus population predicted concentrations (PRED), individual conditional weighted residuals (IWRES) versus IPRED, and conditional weighted residuals (CWRES) versus time. The predictive performance was also evaluated by visual predictive checks (VPC). VPC was performed with 500 runs. For the final model, nonparametric bootstrapping ( $n = 1,000$ ) was performed to check model stability and to obtain the confidence intervals (CI) for the model parameters.

#### **4.2.9 Statistical analysis**

Animal baseline physiology parameters were summarized by descriptive statistics and expressed as mean and standard deviation (SD). The Welch-Satterthwaite t-test was used to compare the differences between the control group and the treated group. NCA obtained PK parameters were summarized as population means for different dosage groups. No statistical analysis was performed due to the naïve pooling method. Dose proportionality was evaluated by two methods. An analysis of variance (ANOVA) was performed on dose normalized  $C_{\max}$  to evaluate the dose proportionality between different dosage groups. The test was performed at a level of  $\alpha$  equals 0.05. The p-value of the ANOVA test was interpreted in only an exploratory manner. No post-hoc test was conducted. A p-value  $> 0.05$  suggests the acceptance of dose proportionality. Dose proportionality was also assessed using a power model expressed in

Equation 4.1.1, which transformed to linear regression (Equation 4.1.2) after taking natural logarithm transformation. Dose proportionality is measured by the estimate and confidence interval of  $\beta$  (Equation 4.1.3). A  $\beta$  equals 1 indicates perfect dose proportionality, suggesting doubling the dose equals doubling the exposure. If  $\beta$  equals 0, it implies the response is independent of the dose. Dose proportionality was accepted when the 90% CI for  $\beta$  lies completely within the critical region defined in Equation 4.1.3, where  $r$  is the ratio of the highest to the lowest administered dose,  $\theta_L = 0.8$  and  $\theta_H = 1.25$  (Smith et al. 2000).

$$y = e^a \times dose^\beta \times e^\varepsilon \text{ (Equation 4.1.1)}$$

$$\ln(PK \text{ parameter}) = a + \beta \times \ln(dose) + \varepsilon \text{ (Equation 4.1.2)}$$

$$1 + \frac{\ln \theta_L}{\ln r} \leq \beta \leq 1 + \frac{\ln \theta_H}{\ln r} \text{ (Equation 4.1.3)}$$

## 4.3 Results

### 4.3.1 Animal baseline physiology

Sixty-eight PND17 male rats were included in the study, with a mean weight of 35.1 g (28 – 44.7g). In the brain distribution study, 16 rats were dosed at 3 mg/kg **UPMP107**, 16 rats were dosed for 20 mg/kg **UPMP107**, each time point comprised of 4 rats. Four rats were treated with vehicle. In the single dose pharmacokinetic study, 8 rats were dosed with **UPMP107** for each dosage group, and 8 rats were administered with vehicle. No adverse effects were observed in animals treated with **UPMP107**. A summary of blood gases at 5 min after **UPMP107** IV injection and physiological parameters are listed in Table 4.3 for rats in the single dose pharmacokinetic

study. At 5 min after compound injection, all physiological parameters were within normal range. No differences were observed between **UPMP107** and the vehicle group.

**Table 4.3 Baseline physiological variables and blood gas of animals**

	<b>UPMP107</b> (Mean $\pm$ SD)	Vehicle (Mean $\pm$ SD)
Weight (g)	35.1 $\pm$ 4.64	38.3 $\pm$ 2.83
Temperature ( $^{\circ}$ C)	37.0 $\pm$ 0.23	37.2 $\pm$ 0.01
Heart rate (bpm)	364 $\pm$ 74.9	375 $\pm$ 21.2
MAP (mmHg)	48.7 $\pm$ 5.41	47.5 $\pm$ 10.6
pH	7.36 $\pm$ 0.07	7.36 $\pm$ 0.07
pCO <sub>2</sub> (mmHg)	42.6 $\pm$ 6.68	43.1 $\pm$ 3.39
pO <sub>2</sub> (mmHg)	215 $\pm$ 28.2	259 $\pm$ 10.7
HCO <sub>3</sub> <sup>-</sup> (mmol/L)	23.9 $\pm$ 1.79	22.7 $\pm$ 1.56
Actual base excess	-1.47 $\pm$ 2.25	-2.65 $\pm$ 2.47

#### 4.3.2 Analytical results

Chromatographs of **UPMP107**, 20-HETE, and internal standards are displayed in Figure 4.1. The R<sup>2</sup> of standard curves was  $\geq 0.99$ . The linearity ranged from 12.5 to 1500 pg on column. The predicted QC deviation was  $\leq 13.3\%$  of the nominal values. Based on the performance of standard curves and QC samples, the assay of **UPMP107** was accurate, precise, and reproducible. Formulated **UPMP107** was dissolved in PBS and the concentration was measured by UPLC-MS/MS method before animal experiments to ensure the correct amount was administered.

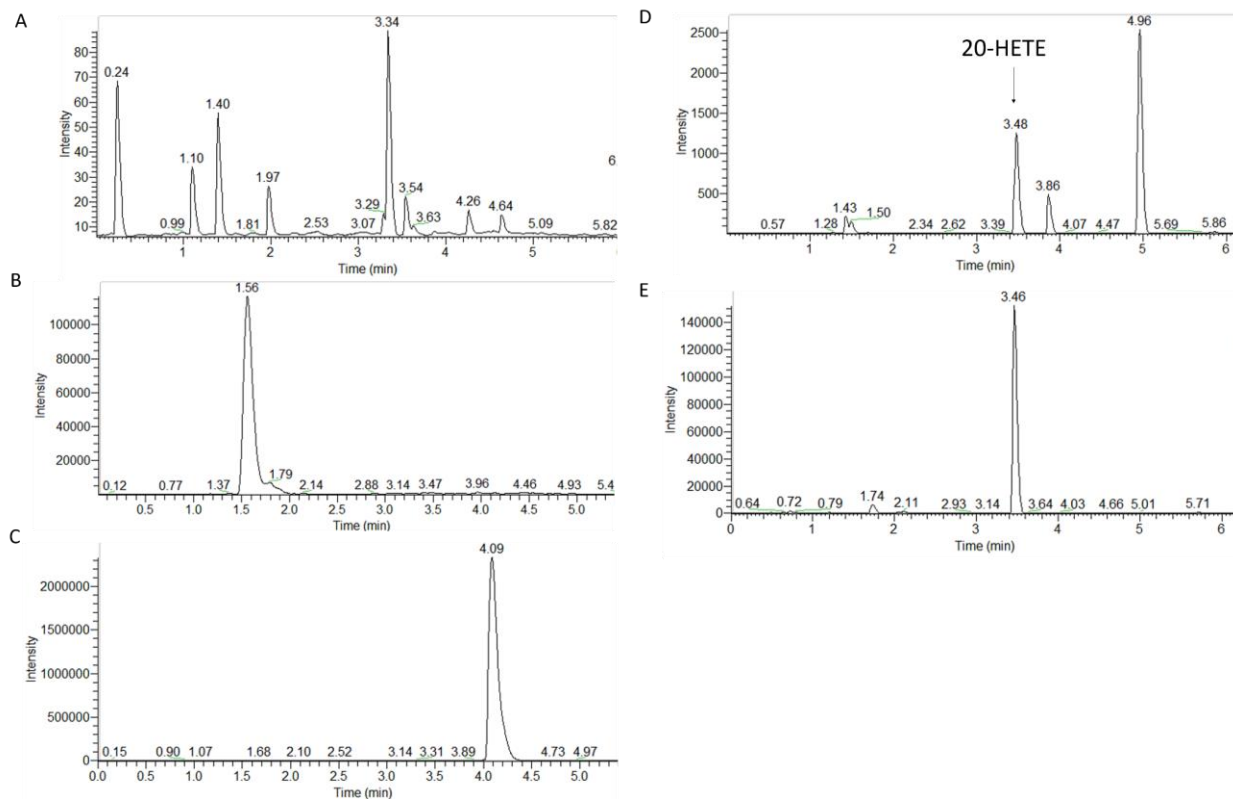


**Figure 4.1 Chromatograms in plasma samples**

The chromatograms are (A) blank, (B) **UPMP107**, (C) SMIP004, (D) 20-HETE, and (E) 20-HETE-d6. Tissues and plasma samples underwent solid-phase extraction followed by UPLC-MS/MS analysis for 20-HETE and **UPMP107** as described in the Materials and methods section. The UPLC-MS/MS method allows for subsequent analysis of 20-HETE and **UPMP107**.

#### 4.3.3 Noncompartmental analysis results

Concentration-time profiles of **UPMP107** following IV administration of 5, 10, and 20 mg/kg (n=8/group) are illustrated in Fig. 4.2. Mean (S.E.) plasma concentrations were presented in Table 4.4. Plasma concentrations were detectable up to 8 hours post-injection.

NCA was performed on mean plasma concentrations for each dosage group. The PK parameters determined by NCA are summarized in Table 4.5. Following IV administration of **UPMP107**, plasma concentrations declined rapidly in a biexponential fashion indicating

**UPMP107** was rapidly distributed upon dosing. Within 30 min after cessation of intravenous administration, plasma levels of **UPMP107** declined 74-89% from  $C_{max}$ .

The systemic clearance (CL) values for **UPMP107** ranged from 13.7 to 20.1 ml/min/kg. As the dose increased from 5 to 10 mg/kg, CL values decreased by approximately 32%. As the dose increased from 10 to 20 mg/kg, CL values maintained relatively the same with a slight 3% increase.

The volume of distribution ranged from 415 – 734 ml/kg. The  $V_{ss}$  values for **UPMP107** were approximately 6-11 fold greater than the plasma volume and are similar to the total body water in rats. Similar to CL,  $V_{ss}$  showed a 43% decrease when the dose increased from 5 to 10 mg/kg and a 17% increase from 10 to 20 mg/kg.

Elimination half-life and mean residence time were short. The  $t_{1/2}$  and MRT were relatively consistent across different dose levels. Elimination half-life ranged from 21.1 to 25.3 min and MRT ranged from 30.4 to 36.5 min.

Since NCA was performed on mean plasma concentrations, therefore, the individual concentrations did not contribute to the interpretation of **UPMP107** pharmacokinetics. Hence, NCA might not accurately analyze the PK parameters, and there was a need to use a population approach to incorporate all individual concentrations that would adequately describe **UPMP107** PK in plasma.

**Table 4.4 UPMP107 mean plasma concentrations after IV administration at 5, 10, and 20**

<b>mg/kg</b>						
Time	Mean plasma concentrations (pg/ $\mu$ l)					
	5 mg/kg		10 mg/kg		20mg/kg	
	Mean	SE	Mean	SE	Mean	SE
0	25446	2919	36054	994	61604	23776
5	5048	466	21039	2714	33319	5027

30	1906	366	9036	2587	16280	2652
60	1095	83.3	2188	116	8572	2116
120	102	14.2	479	92.6	795	230
240	29.9	8.72	41.4	11.0	70.2	48.2
360	28.4	17.8	14.5	2.54	24.8	21.3
480	10.7	2.86	5.95	1.41	9.03	3.46

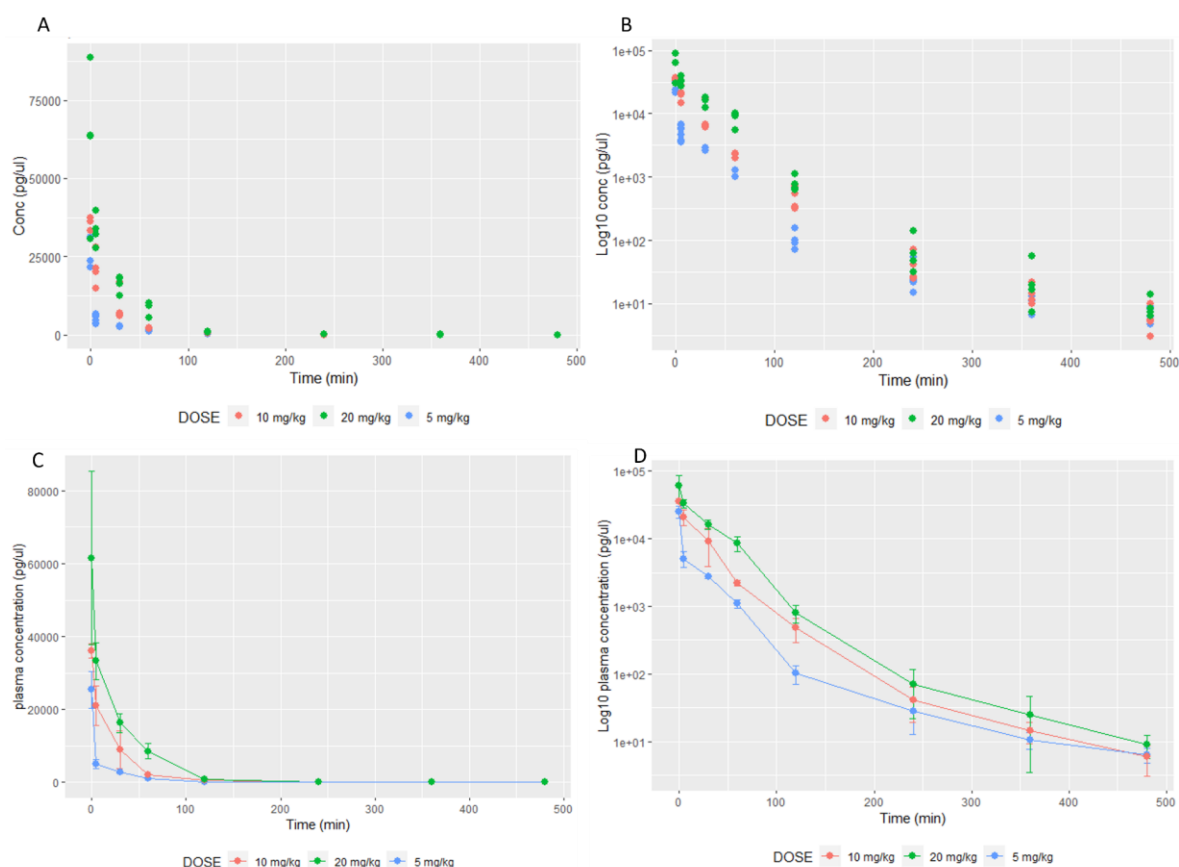


**Figure 4.2 Plasma concentration-time profile following UPMP107 IV administration of 5, 10, and 20 mg/kg**

Data are presented as individual concentrations in (A) cartesian and (B) semilogarithmic scale, and as mean concentrations in (C) cartesian and (D) semilogarithmic scale

**Table 4.5 NCA results of UPMP107 following a single IV administration at dose of 5, 10, and 20 mg/kg**

PK parameter <sup>a</sup>	5mg/kg	10mg/kg	20mg/kg
---------------------------	--------	---------	---------



	(n = 8)	(n = 8)	(n = 8)
AUCinf (ng*min/ul)	248.4	732.5	1,425
AUMCinf (ng*min <sup>2</sup> /ul)	9,056	22,279	49,179
MRTinf (min)	36.46	30.41	34.52
Kel (min <sup>-1</sup> )	0.02742	0.03288	0.02897
T <sub>1/2</sub> (min)	25.27	21.08	23.92
CL (ml/min/kg)	20.13	13.65	14.04
Vss (ml/kg)	734.1	415.2	484.6

<sup>a</sup> Standard deviation are not reported since PK parameters calculation was based on mean plasma concentrations.

#### 4.3.4 Dose proportionality

The dose-proportionality following a single dose of **UPMP107** was evaluated for C<sub>max</sub> and AUC<sub>0-∞</sub>. C<sub>max</sub> increased in a proportion less than the increment in dose. As the dose increase in a ratio of 1: 2: 4, C<sub>max</sub> increased in the ratio of 1: 1.4: 2.4. On the contrary, AUC<sub>0-∞</sub> increased in a proportion greater than the increment in dose. As dose increased, AUC<sub>0-∞</sub> increased in a ratio of 1: 2.9: 5.7.

One-way ANOVA was performed to evaluate dose proportionality on dose normalized C<sub>max</sub>. After IV administration, there was a borderline significant (p = 0.049) dose effect for C<sub>max</sub>, indicating C<sub>max</sub> increase in a dose-dependent manner. Since p-value is less than 0.05, the null hypothesis was not rejected, suggesting a lack of dose proportionality in C<sub>max</sub>. One-way ANOVA was not performed on AUC<sub>0-∞</sub> due to limited sample size.

In addition, dose proportionality was evaluated by the power model. The linear regressions of individual ln(C<sub>max</sub>) versus ln(dose) and ln(AUC<sub>0-∞</sub>) versus ln(dose) with 90% confidence interval (90% CI) are presented in Fig. 4.3. The slopes (90% CI) for C<sub>max</sub> and AUC<sub>0-∞</sub> were 0.60 (0.32 - 0.88) and 1.26 (0.17 - 2.35), respectively. The slope for AUC exhibited a wide 90%CI, suggesting a high variability. The β values for AUC and C<sub>max</sub> did not fall within the equivalent

limit of (0.84, 1.16) calculated by Equation 4.1.3 using  $r = 20/5$ ,  $\theta_L = 0.8$  and  $\theta_H = 1.25$ . Based on the results of  $\beta$  estimates, **UPMP107**  $AUC_{0-\infty}$  increased more than expected by dose proportionality, while  $C_{max}$  increased less than expected by dose proportionality. A two-fold increase in dose leads to a 0.6-fold increase in  $C_{max}$  and a 1.26-fold increase in  $AUC_{0-\infty}$ , respectively. The results of the power model analysis are presented in Table 4.6. The results from the power model analysis are consistent with the one-way ANOVA analysis on dose-normalized PK parameters, suggesting a lack of dose proportionality for  $C_{max}$ .

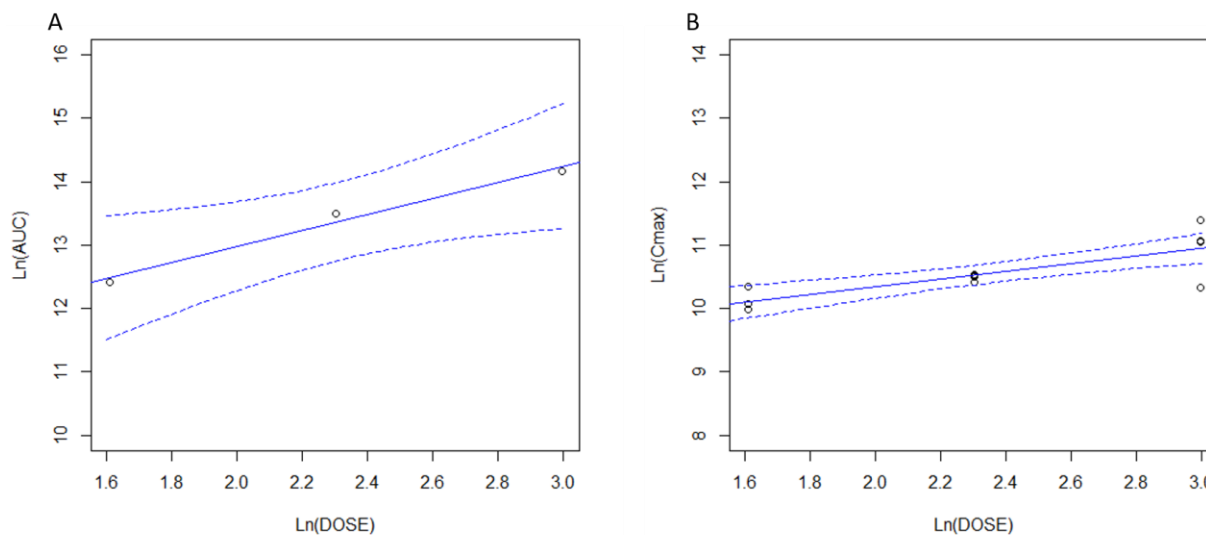


**Figure 4.3 Regression plots of UPMP107 for (A)  $AUC_{0-\infty}$  and (B)  $C_{max}$**

The circles are observed  $AUC_{0-\infty}$  and  $C_{max}$  values. The solid lines are the fitted line based on the power model. The dashed lines are the 90% CI.

**Table 4.6 Dose proportionality results for  $C_{max}$  and  $AUC_{0-\infty}$  based on power model**

Parameters	$\beta$	90% CI	Acceptance range
$C_{max}$	0.6016	(0.3222, 0.8811)	(0.8390, 1.1610)
$AUC_{0-\infty}$	1.2595	(0.1685, 2.3505)	(0.8390, 1.1610)

#### 4.3.5 Brain distribution and pharmacological effect on brain 20-HETE

A total number of 36 rats were included in the experiment, 32 rats were treated with **UPMP107**, 4 rats were treated with vehicle. Brain concentrations of **UPMP107** and 20-HETE were measured at 60, 180, 360, 540, or 720 minutes after **UPMP107** single IV administration (n = 4 per time point). As shown in Fig. 4.4, **UPMP107** was able to penetrate BBB rapidly and exhibited the same biphasic decline as plasma concentrations. The B/P ratios at each time point are presented in Table 4.7. The B:P ratios in both dosage groups showed high variability. At 3 mg/kg, B/P ratios ranged from 0.7 – 2.2 within the experiment duration. The B/P ratios increased as the time increased from 60 min to 720 min, suggesting it may take longer than 180 min to reach equilibrium between brain and plasma. At 20 mg/kg, B/P ratios were lower, ranging from 0.1 – 0.8. The B/P ratios also increased in a similar trend, suggesting B/P ratios after 180 min might be more representative of steady-state B/P ratios.

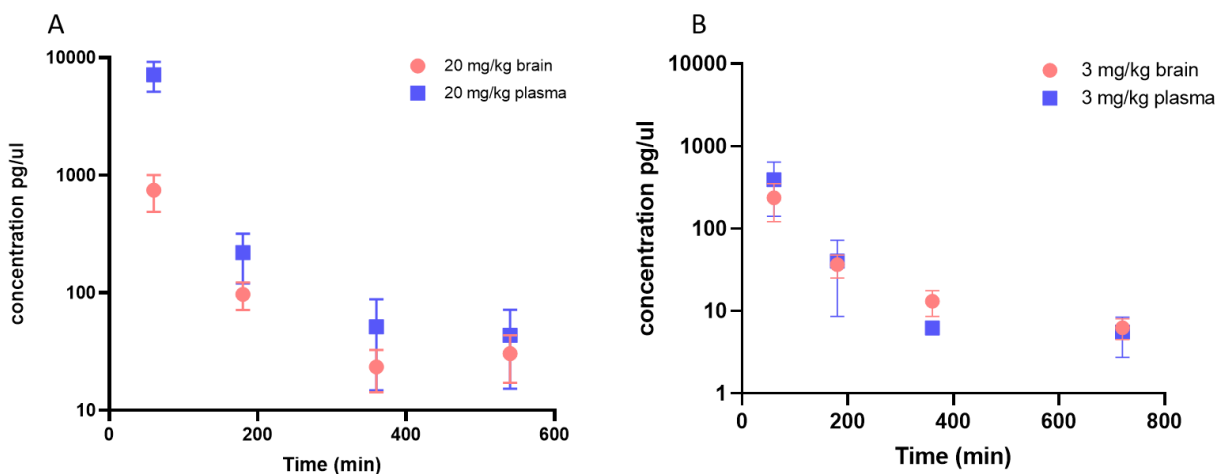


**Figure 4.4 Plasma and brain concentration-time profiles of UPMP107 following IV administration**

A single dose of (A) 20 mg/kg and (B) 3 mg/kg of **UPMP107** was administered to male PND17 SD rats. Symbols and error bars represent means and standard deviation (n =4 per time point).

To explore the response-time courses of 20-HETE inhibition, the drug effect was plotted against time for the two dosage groups. At 3 mg/kg, there was an initial 84% reduction of brain 20-HETE levels at 60 min, the inhibitory effect gradually declined and 20-HETE returned to baseline level at 360 min. In the 20 mg/kg group, there was an initial 76% reduction in brain 20-HETE levels at 60 min and the inhibition effect maintained at 60% until 540 min.

**Table 4.7 Brain to plasma ratio of UPMP107 following IV administration**

		B/P ratio			
3 mg/kg	Time (min)	60	180	360	720
	Mean $\pm$ SD	0.70 $\pm$ 0.33	1.13 $\pm$ 0.47	2.20 $\pm$ 1.02	1.55 $\pm$ 1.13
20 mg/kg	Time (min)	60	180	360	540
	Mean $\pm$ SD	0.10 $\pm$ 0.02	0.51 $\pm$ 0.26	0.53 $\pm$ 0.17	0.78 $\pm$ 0.26

n = 4/time point

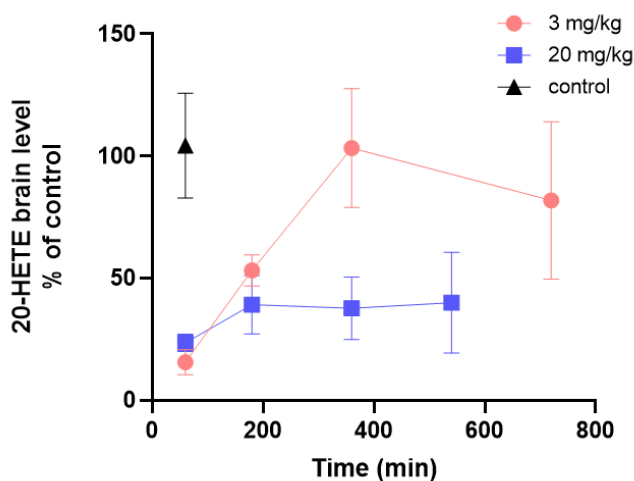


**Figure 4.5 Brain 20-HETE levels after UPMP107 administration at 3 and 20 mg/kg**

Brain 20-HETE concentrations are expressed in % of control. Intravenous administration of 3 mg/kg **UPMP107** inhibited 20-HETE for a short duration. The brain 20-HETE levels returned to control value at 360min. A higher dose at 20 mg/kg maintained the 20-HETE inhibitory effect throughout the experiment duration.

#### 4.3.6 Population PK model

A total of 27 rats with 117 observations were included to build the pop PK model. Several linear and nonlinear compartmental PK models were evaluated to describe **UPMP107** plasma concentrations. Based on the AIC and GOF plots, a two-compartment model with nonlinear elimination and a combined residual error model was selected as the final model that best described the data. The system comprised compartment 1 (central compartment) and compartment 2 (peripheral compartment). The differential equations describing the system are given in Equations 4.2.1 – 4.2.2.  $X_1$ ,  $X_2$  are the drug amount in the central and peripheral compartments, and  $k_{12}$ ,  $k_{21}$  are the first-order distribution rate constants.  $V_{\max}$  is the maximum enzyme catalytic velocity;  $K_m$  is the concentration of substrate that reaches half  $V_{\max}$ .

$$\frac{dX_1}{dt} = -k_{12}X_1 + k_{21}X_2 - \frac{V_{\max} \times X_1}{K_M \times V_1 + X_1} \text{ (Equation 4.2.1)}$$

$$\frac{dX_2}{dt} = -k_{21}X_2 + k_{12}X_1 \text{ (Equation 4.2.2)}$$

The GOF plots and the results of visual predictive checks (VPC) are displayed in Fig 4.6 and 4.7, respectively. The predicted and observed concentrations are overall in good agreement. The individual fitted plots of observed versus predicted values are presented in Appendix A Figure 1. The model underestimated the observed concentration at later time points and overestimated concentrations at earlier time points (Fig. 4.6D). The VPC results suggest the model adequately predicts the observed concentrations with regards to the median and the spread of the data (Fig. 4.7).

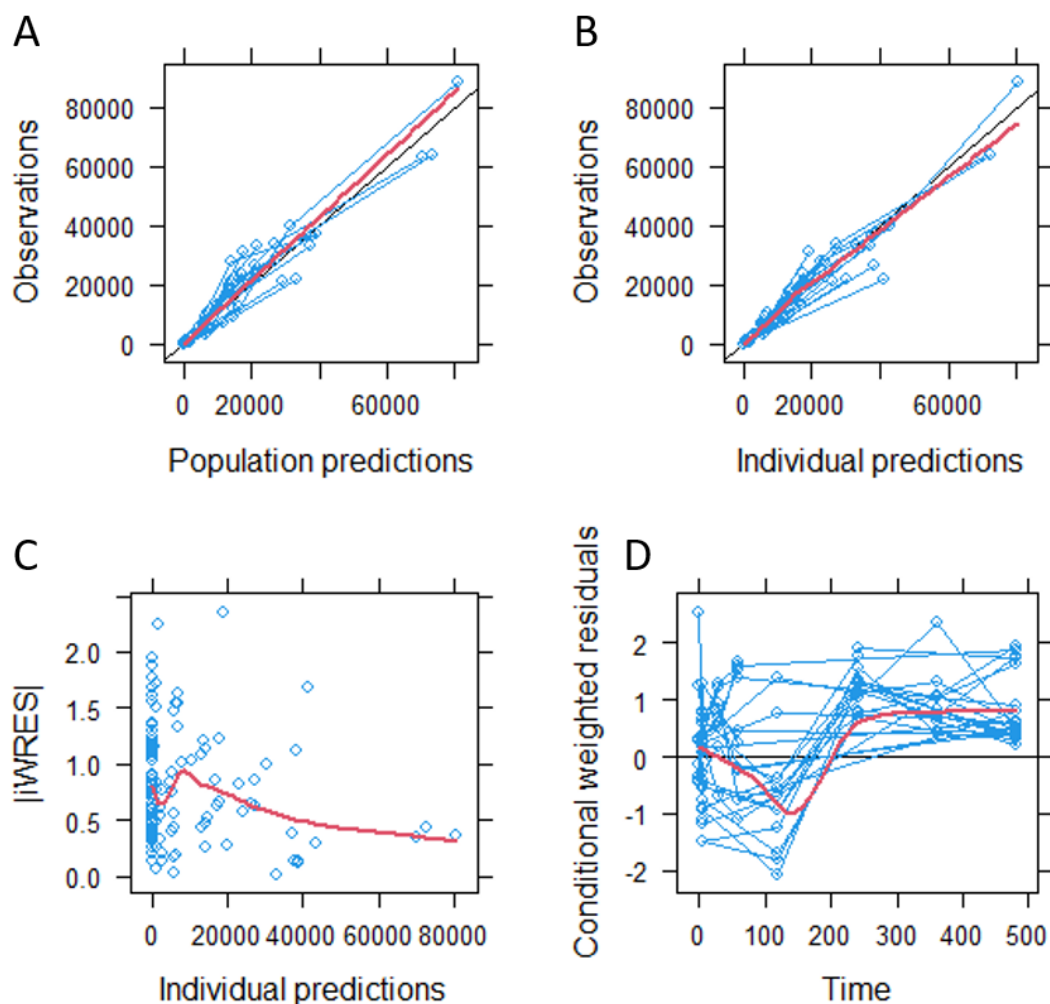


**Figure 4.6 Goodness-of-fit plots of the final model**

In the (A) observed concentration versus population predicted concentration and (B) observed concentration versus individual predicted concentration, the data were evenly distributed around the line of identity. The red lines indicate the linear regression fit and the black line represent the line of identity. In the (C) individual weighted residuals (IWRES) versus individual predicted concentrations and the (D) conditional weighted residuals (CWRES) versus time, the data are mostly within -2 and 2. The red lines represent the trend line.

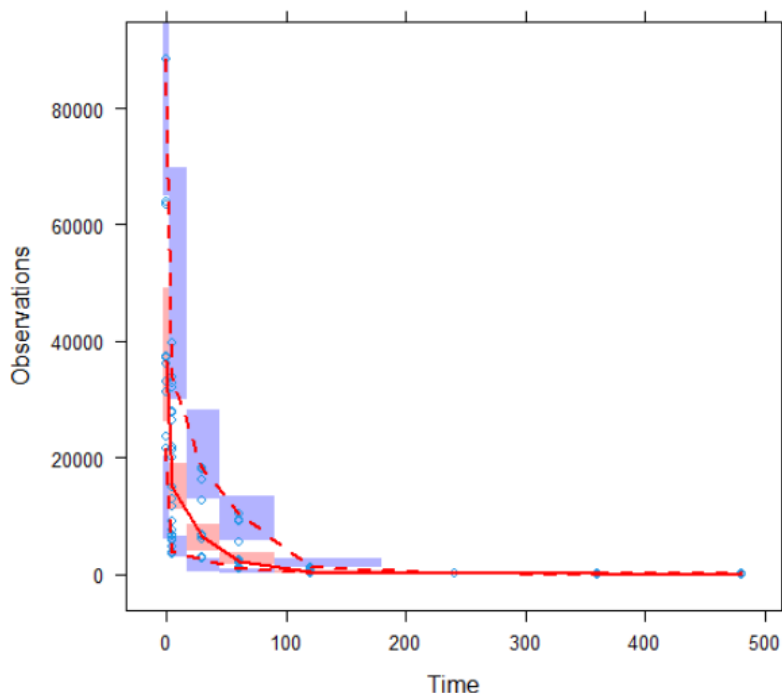


**Figure 4.7 Visual predictive check of UPMP107 plasma concentrations versus time**

The blue circles indicate the observations. The solid red line represents the median of the simulations, the red dashed lines represent the 5<sup>th</sup> and 95<sup>th</sup> percentiles of the observed data. The shaded regions represent the 95% confidence intervals of the 5<sup>th</sup>, 50<sup>th</sup>, and 95<sup>th</sup> percentiles from the predicted data. Overall, the plot demonstrates that the model predictions captures much of the observed **UPMP107** concentrations within the 5<sup>th</sup> and 95<sup>th</sup> percentiles of the simulated values ( $n = 500$ ).

The point estimates for the model parameters of the final model, the nonparametric bootstrap median and confidence interval for the model parameters are listed in Table 4.8. Overall, the estimated  $V_{\max}$  is 0.0212 mg/min,  $K_m$  is 21.6 mg/L,  $V_1$  is 0.00994 L for the volume of distribution for the central compartment,  $V_2$  is 0.0166 L for the peripheral compartment, and  $Q$  is 0.0027 L/min for intercompartment clearance. The interindividual variability (IIV) could only be estimated for  $V_1$  and  $Q$  and were dropped for the other PK parameters. No covariates were evaluated for the animal popPK model. The bootstrap results from 1000 runs confirmed the stability of the final model and 51.4% of the bootstrapping runs were minimized successfully. The

median values were close to the parameter estimates from the original dataset with low relative biases.



**Table 4.8 Parameter estimates of the final popPK model from the original dataset and from 1000 bootstrap replicates**

Parameter	Unit	Estimate	RSE (%)	Shrinkage (%)	Nonparametric bootstrap	
					Bootstrap median (2.5 <sup>th</sup> – 97.5 <sup>th</sup> PT <sup>a</sup> )	Relative bias (%)
V1	L	0.00994	8.97		0.009808 (0.008423 – 0.01125)	-1.33
Km	mg/L	21.6	28.0		20.8 (11.3 – 69.5)	-3.58
Vmax	mg/min	0.0212	21.1		0.0206 (0.0132 – 0.0581)	-2.70
V2	L	0.0166	11.0		0.0168 (0.0143 – 0.0197)	1.40
Q	L/min	0.0027	33.6		0.0026 (0.00155 – 0.00516)	-3.86
Interindividual variability						
IIV (V1)	CV%	7.77	254	76.2	9.8 (0.155 – 24.4)	11.7
IIV (Q)	CV%	234	48.1	31.0	129 (78.0 - 549)	28.7
Residual variability						
Proportional	CV%	27.7	21.3	6.63	26.1 (20.3 – 31.8)	-5.69
Additive	mg/L	15.6	24.5	6.63	15.4 (12.8 – 18.5)	-1.39

<sup>a</sup>PT: percentile.

<sup>b</sup>Relative bias: = (bootstrap median -final model estimate)/final model estimate × 100.

#### 4.4 Discussion and conclusions

We report for the first time that that **UPMP107** penetrates the blood-brain barrier and exhibits a quick onset of brain 20-HETE inhibition in pediatric rats. We observe a biphasic decline of plasma and brain concentrations after **UPMP107** intravenous administration. This study is the first attempt to investigate **UPMP107** plasma pharmacokinetics, brain pharmacokinetics, and efficacy. The findings will provide knowledge for designing future PK and PD studies in animals.

**UPMP107** showed rapid brain penetration. After IV administration, **UPMP107** quickly distributes throughout the body, evidenced by the fast decline of plasma concentrations (Fig. 4.2). Maximum brain concentrations were observed at 1 hour after administration (Fig. 4.4). A shorter brain  $T_{\max}$  could not be precluded due to the first brain sample being collected at 1 hour post-injection. The chemical properties for **UPMP107**, including molecular weight  $< 350$ ,  $\text{clogP} \leq 5$ , number of H-bond donor  $< 3$ , number of H-bond acceptor  $< 7$ , are favorable attributes seen in marketed drugs with passive CNS penetration (Pajouhesh et al. 2005). Previous *in vitro* MDCK-MDR1 BBB permeability assay showed that **UPMP107** has high permeability from apical to basolateral. We observed an influence of dose on the brain-to-plasma ratio (B/P). A higher B/P ratio under a lower dose of 3 mg/kg and a lower B/P ratio in the 20 mg/kg group at different time points was found. The decreasing B/P ratios with dose might be a sign of dose-dependent brain penetration. Since the B/P ratios were calculated by single-point ratios of brain and plasma concentrations, this finding should be validated by additional studies and the B/P ratios should be calculated by ratios of  $\text{AUC}_{\text{brain}}/\text{AUC}_{\text{plasma}}$ . The role of P-glycoprotein in **UPMP107** brain penetration should also be investigated as it is of great significance in further development.

Despite the short plasma half-life of **UPMP107**, inhibition of brain 20-HETE concentrations remained for a prolonged duration. The onset of 20-HETE inhibition was fast. The response was the strongest at 1 h post-injection in both dosage groups. Unlike the gradual decline of the 20-HETE inhibition observed in the 3 mg/kg group, a saturation of the response was observed at 20 mg/kg (Fig. 4.5). The absence of post-peak decline of the inhibitory response in the 20 mg/kg group may be explained by the sampling time not being long enough to capture the entire time course of the PD response. From a pharmacodynamic perspective, the short half-life does not necessarily require a continuous infusion to maintain the 20-HETE inhibitory activity. In-depth knowledge of the compound transfer to and from the CYP4 enzymes, the affinity for CYP4, and target turnover are important information to help study the onset, intensity, and duration of the pharmacological response of 20-HETE inhibition (Gabrielsson et al. 2019). The dose-response-time data from this study and data generated from future studies can be used together with the application of mathematical models for dose-response-time analysis to elucidate the possible mechanisms of pharmacodynamic responses.

A good correlation between the estimated plasma PK parameters by NCA and popPK analysis was observed. PopPK predicted volume of distribution ( $V_d$ ) and NCA estimated  $V_d$  is in close agreement. NCA derived  $V_{ss}$  ranged from 415 – 734 ml/kg. The  $V_1$  and  $V_2$  obtained from popPK analysis were 9.94 ml and 16.6 ml, respectively (Table 4.8). For a two-compartment IV bolus model,  $V_{ss}$  can be calculated using Equation 4.3. A  $V_{ss}$  value of 664 ml/kg was obtained after normalizing the body weight, which is consistent with the NCA results. For Sprague-Dawley rats, the blood volume is 64 ml/kg and the total body water volume is 668 ml/kg (Davies et al. 1993). The  $V_{ss}$  of **UPMP107** is approximately equal to the volume of total body water. **UPMP107** is distributed to the peripheral compartment as evidenced by the rapid brain distribution (Fig. 4.4)

and high intercompartment clearance ( $Q = 67.5$  ml/min/kg). The popPK estimated intrinsic clearance ( $CL_{int}$ ) can be calculated from Equation 4.4. The  $CL_{int}$  value of 24.5 ml/min/kg is slightly higher than the clearance calculated from NCA (13.7 – 20.1 ml/min/kg). Nevertheless, **UPMP107** has a low clearance as the value is lower than the hepatic blood flow of 55.0 ml/min/kg in rats (De Buck et al. 2007).

$$V_{ss} = V_1 + V_2 \text{ (Equation 4.3)}$$

$$CL_{int} = \frac{V_{max}}{K_M} \text{ (Equation 4.4)}$$

**UPMP107** has a short biological half-life of  $21.7 \pm 1.97$  minutes. Prior *in vitro* study suggested **UPMP107** has a low *in vitro* intrinsic clearance of 5.19  $\mu$ l/min/mg of protein in human liver microsomes (HLM). Comparing to **UPMP107**, HET0016 has a 44-fold higher *in vitro*  $CL_{int}$  of 227  $\mu$ l/min/mg of protein in HLM. The short biological half-life was somewhat unexpected considering the low *in vitro*  $CL_{int}$  of **UPMP107**. The underestimation of *in vivo* clearance has several explanations. First, conventional *in vitro* - *in vivo* extrapolation (IVIVE) could lead to a  $\geq$  10-fold underestimation of hepatic  $CL_{int}$  (Chiba et al. 2009). Next, the investigation of **UPMP107** metabolism pathways are insufficient. The measurement of *in vitro* metabolic stability was carried out in HLM, where there could be species difference in enzyme affinity and activity in metabolizing **UPMP107** between human and rodents. Metabolic stability in HLM system using co-factor NADPH overlooked phase II metabolism by UDP-glucuronosyltransferases (UGT). To study if phase II enzymes are involved in metabolizing **UPMP107**, uridine-5'-diphospho- $\alpha$ -D-glucuronic acid (UDPGA) could be used as the co-factor in HLM. Recently, we studied 107 phase II metabolism in both human and rat S9 fraction., and **UPMP107** was not metabolized throughout the incubation period, suggesting phase II metabolism is likely not involved in the elimination of **UPMP107**. Finally, there could be extrahepatic metabolism in tissues such as kidney, or renal

elimination that could contribute to the clearance of **UPMP107**. Nevertheless, *in vivo* results should always take precedence over *in vitro* results (Jia et al. 2007).

Previous pharmacokinetic study in adult Sprague-Dawley rats showed that HET0016 has a half-life of  $39.6 \pm 20.0$  minutes, with a clearance of  $57.4 \pm 14.8$  ml/min/kg and a volume of distribution of 2400 ml/kg (Mu, Klamerus et al. 2008). To amend the difference in PK due to age and body size, we studied HET0016 PK in PND17 rats (data not shown here). The HET0016 CL and  $V_{ss}$  in pediatric rats were lower compared to adult rats with values of 7.21 ml/min/kg and 444 ml/kg, respectively. The half-life was similar to that in adults with a value of  $42.7 \pm 2.4$  minutes. **UPMP107** has a higher CL and a similar  $V_{ss}$  compared to HET0016 in PND17 rats. Although the half-lives of HET0016 and **UPMP107** are similar, the advantages of **UPMP107** over HET0016 is a higher solubility and a wider selectivity window that enables a large window for dose increment.

We were unable to conclude a dose-linearity for **UPMP107** in the range of 5 – 20 mg/kg using various statistical methods. Dose linearity is an important PK assessment during drug development. A linear PK suggests dose proportionality, indicating the PK parameters such as  $T_{max}$ ,  $T_{1/2}$ , CL,  $V_{ss}$ , and MRT should remain constant regardless of the dose levels. If dose proportionality is not seen, an escalation to higher dose levels may saturate a metabolic or elimination pathway that would lead to an upswing of concentrations or exposures (Walker 2004). We observed that **UPMP107**  $AUC_{0-\infty}$  exhibited a more than dose-proportional increase as dose increases, and  $C_{max}$  exhibited a less than dose-proportional increase. In the ANOVA analysis, the p-value for  $C_{max}$  was at borderline significance. The slope of  $C_{max}$  and AUC did not fall in the acceptance range. The nonlinear elimination resulted a better fit evidenced by a 3-unit drop in AIC value. In future studies, serial plasma sampling would allow AUC calculation for each animals to

increase the sample size for statistical analysis and to further evaluate the dose-linearity of **UPMP107**.

The current study had some limitations that are worth mentioning. First, the failure to conclude dose-linearity was based on a small number of dose levels. Studies are needed with more dose levels and full serial plasma sampling in order to collect adequate information to evaluate the dose proportionality. Next, we did not measure drug concentration in different brain regions due to the limited amount of brain samples that could be harvested from a pediatric rat. Drug distribution into and within the brain is governed by multiple factors such as plasma protein binding, uptake and efflux transporters, and blood flow; and compounds do not distribute evenly across different brain regions (Alavijeh et al. 2005). The target of the action, CYP4 enzymes, are expressed in the neocortex, entorhinal cortex, hippocampus, thalamus, and hypothalamus. CYP4 is also expressed in cerebral vasculature such as endothelial cells, vascular smooth muscle cells, and glial limiting membrane of pial arteries and penetrating arterioles (Gonzalez-Fernandez et al. 2020). Future studies of measuring protein-unbound drug concentrations in different brain regions are needed to bring light to the pharmacokinetics and pharmacodynamics of 20-HETE inhibitors in the central nervous system.

In summary, CNS drug development has long been hindered by the inadequate consideration of CNS pharmacokinetics and pharmacodynamics. Understanding the plasma PK, neuro PK, and neuro PD are of great importance to help inform CNS drug discovery and development. This study generated important pharmacokinetic and pharmacodynamic information for **UPMP107**. **UPMP107** exhibited a biphasic plasma concentration-time profile after IV administration. It has a low clearance and an intermediate volume of distribution with a relatively short half-life. We reported for the first time that **UPMP107** has a rapid distribution into brain

tissues and exhibited brain target engagement where brain 20-HETE levels were reduced. These data are of great importance for future preclinical PK/PD study design.

## 5.0 Population Pharmacokinetics of Propofol in ICU patients

### 5.1 Introduction

Patients in intensive care units (ICU) often require sedatives and analgesics to manage pain, reduce stress, improve mechanical ventilation synchronization, and keep them comfortable but rousable (Sessler et al. 2008, Hughes et al. 2012, Reade et al. 2014). Propofol and benzodiazepines are commonly used for ICU sedation. Benzodiazepine sedatives are associated with longer duration of the first episode of delirium, longer duration on mechanical ventilation, longer ICU and hospital stay, increased risk of delirium, and increased mortality (Pisani et al. 2009, Fraser et al. 2013, Lonardo et al. 2014, Zaal et al. 2015). In the current guideline, it is recommended to avoid benzodiazepines for sedation in the ICU, and propofol is recommended over benzodiazepines for mechanically ventilated patients (Devlin et al. 2018).

Propofol (2,6-diisopropylphenol) is a short-acting anesthetic frequently used for induction and maintenance of general anesthesia or sedation. Propofol has a large volume of distribution of 5.8 L/kg due to its high lipophilicity, a high clearance of 3.2 L/h/kg. The terminal half-life ranges from 4 - 7 h, and may increase up to 1 – 3 days after a 10-day infusion (FDA 2017, Folino. 2020). . Due to its rapid onset of action and quick recovery, it is usually given by an i.v. injection of a bolus dose followed by continuous infusion. Several population pharmacokinetic (popPK) and pharmacodynamic (PD) models have been developed to describe propofol in different populations such as children, burnt, underweight, obese or ICU (Barr et al. 2001, Yamashita et al. 2010, Park et al. 2018). Usually, propofol pharmacokinetics (PK) can be best described with two-or three-compartment models. Some popPK models have been programmed in target-controlled infusion



(TCI) devices to achieve user-defined plasma or effect-site concentration for optimum effectiveness and safety (Eleveld et al. 2018, García Guzzo et al. 2020).

Critical illness such as sepsis can have a significant influence on physiology and organ function such as sepsis-induced liver hypoperfusion and increase in  $\alpha$ -1 glycoprotein that will affect drug disposition (De Paepe et al. 2002). The PK of propofol in ICU patients differs significantly from the PK of propofol in healthy subjects (Schüttler et al. 1985, Shafer et al. 1988). Furthermore, there is a large variability in the time to emergence and extubation in ICU patients that were given propofol (Barr et al. 2001). Therefore, propofol PK and PD in ICU patients needs further investigation.

The purpose of this study is to characterize the pharmacokinetics of propofol and identify covariates that significantly influence the PK parameters in a diverse ICU population available to us. The characterization of the PK profile and identification of potential factors can be used to better individualize the propofol doses to meet the sedation needs in the critically ill patients.

## **5.2 Methods**

### **5.2.1 Analysis population**

The population for this analysis consisted of propofol-treated ICU patients. Detailed information on study conduct, including analytical methodology can be found in the paper published by Masica et al. (Masica et al. 2007). In brief, adult patients who required the use of propofol were included in the analysis. Propofol dosing was managed according to clinical guidelines. Nurses adjusted doses based on physician-ordered clinical sedation targets to reach

these goals. Doses were adjusted by titrating propofol infusion rates and based on patient weight (propofol:  $\mu\text{g/kg/min}$ ). Drug doses were recorded each morning. Sedation levels were measured twice daily by study personnel using Richmond Agitation-Sedation Scale (RASS). Blood samples (~5 ml) were collected twice daily concurrent with RASS measurements according to the protocol. The exact date and time were recorded and were used for the analysis. Blood samples were collected up to 48 hr after the cessation of the infusion.

### **5.2.2 Bioanalytical assay**

Blood samples were collected in EDTA tubes. Samples were centrifuged and plasma were collected and stored in  $-80^{\circ}\text{C}$  freezer until analyzed for propofol using a validated HPLC assay with fluorescence detection (Plummer 1987). In brief, The linearity range for the calibration curve was 10-1000 ng/ml (Masica et al. 2007).

### **5.2.3 Data handling**

A time-ordered dataset of doses and concentrations was constructed from raw data. The data were checked for inaccuracies by investigating any observations that did not reasonably agree with the dosing records. Inaccuracies were identified and corrected when possible. Start and end times for the infusions were only available for the dose around which plasma samples were drawn. According to the protocol, propofol dose entry was recorded every 1 hour. When a dose entry had both dose and infusion start time, we assumed the dose was infused at the entered time and used the actual start and end time for infusion duration calculation. When an entry had infusion start time  $< 1$  h from the previous infusion, but no dose was recorded, we assumed there was no dose

infused at that start time. When an entry had infusion start time  $> 1$  h from the previous infusion and had a dose recorded, we calculated the actual infusion duration based on the entered time. For dose entries before the last measured plasma concentrations that was recorded as 0, but followed with non-zero dose, we assumed the dose was stopped for 1 h. For doses entries before the last measured plasma concentrations that was recorded as 0, and followed with zero doses, we assumed the propofol treatment was stopped for that subject. All other infusions were assumed to have been infused for 1h.

For propofol concentrations, suspected outliers were tested and excluded. Concentrations were initially fitted with one compartment model, observations with  $|CWRES| > 6.0$  or  $|WRES| > 6.0$  were considered as influential samples (Quartino et al. 2016, Li et al. 2020). Cook's distance  $> 4/n$  were also used to identify suspected outliers. Data for each subject were fit with and without the suspected outlier. If the PK profile was altered significantly ( $>20\%$  change in the PK parameter estimate) and an improvement in the fit was seen in the remaining samples for that patient, the observation was determined as a significant outlier and was excluded from the analysis.

#### **5.2.4 Statistical methods**

All data preparation and presentation were performed using R 4.0.3. The data were analyzed using nonlinear mixed effect modeling software NONMEM 7.4.3 (ICON Development Solutions, Ellicott City, MD, USA). First order conditional estimation with interaction method (FOCE-I) was used throughout the model building process.

Selection of non-nested models was based on Akaike information criterion (AIC) and goodness-of-fit (GOF) plots. A lower number in AIC would support the selection of a model. To compared nested models, a minimum value of objective function value (OFV;  $-2 \times \log\text{-likelihood}$ )

was pursued. The change in OFV follows an asymptotical  $\chi^2$  distribution. A greater than 3.84 decrease in OFV was considered a statistically significant improvement ( $\alpha = 0.05$ , degrees of freedom  $[df] = 1$ ).

The model was assessed by examination of the following: (1) scatterplot of measured concentrations versus population predicted concentrations; (2) scatterplot of measured concentrations versus individual predicted concentrations; (3) scatterplot of individual weighted residuals versus individual predicted concentrations; (4) scatterplot of conditional weighted residuals versus time since last dose; (5) changes in the estimates of interindividual and residual variability; and (4) the precision of the parameter estimates measured by the percent standard error of the mean ( $RSE\% = \text{standard error}/\text{parameter estimate} \times 100\%$ )

### **5.2.5 Population pharmacokinetic analysis**

The procedure for popPK model development follows structural model development, error model evaluation, covariate evaluation, model refinement, and final model evaluation.

#### **5.2.5.1 Structural model development**

##### **5.2.5.1.1 Compartmental model**

Original plasma concentrations or natural logarithmic transformed concentrations were fitted with either one-, two-, and three compartmental models with zero order input and first order elimination from the central compartment.

#### 5.2.5.1.2 Interindividual variability

Interindividual variability (IIV) of PK parameters were assumed to be log-normal distributed and were modeled using an exponential error model given by equation 5.1 where  $X_j$  is the true value of the  $X$  parameter in the  $j$ th individual,  $\tilde{X}_j$  is the typical value of parameter  $X$  in the  $j$ th individual, and  $\eta_j^x$  is the variability that is normally distributed with a mean of 0 and a variance of  $\omega^2$  ( $\eta \sim (0, \omega^2)$ ). The estimates are presented as percent coefficient of variation (%CV). For IIV, several forms of variance-covariance matrix structure were explored.

$$X_j = \tilde{X}_j \times e^{\eta_j^x} \quad (5.1)$$

#### 5.2.5.1.3 Residual variability

Residual variability was described using an additive model (Equation 5.2.1), constant coefficient of variation (CCV) model (Equation 5.2.2), additive plus CCV model (Equation 5.2.3), or log error model (Equation 5.2.4).  $Cp_{ij}$  represents the measured  $i$ th concentration in the  $j$ th subject,  $\hat{Cp}_{ij}$  represents the predicted  $i$ th concentration in the  $j$ th subject,  $\varepsilon_{ij}$  is the random variable which represents the difference between the measured and the predicted  $i$ th serum concentration in the  $j$ th subject.  $\varepsilon_{ij}$  is normally distributed with a mean of 0 and variance of  $\sigma^2$  and represents additive, proportional, additive and proportional, and log error in equations 5.2.1-5.2.4, respectively.

$$Cp_{ij} = \hat{Cp}_{ij} + \varepsilon_{ij} \quad (5.2.1)$$

$$Cp_{ij} = \hat{Cp}_{ij} \times (1 + \varepsilon_{ij}) \quad (5.2.2)$$

$$Cp_{ij} = \hat{Cp}_{ij} \times (1 + \varepsilon_{1ij}) + \varepsilon_{2ij} \quad (5.2.3)$$

$$\log Cp_{ij} = \log \hat{Cp}_{ij} + \varepsilon_{ij} \quad (5.2.4)$$

### 5.2.5.2 Covariate model development

After an adequate structural model was identified, individual Bayesian estimates of the PK parameters were generated. Diagnostic plots of parameters versus covariates were generated and evaluated for observable trends. If large numbers of patients had missing values for a covariate, the covariate was not evaluated.

The covariates were prespecified based on clinical significance and literature reports. For continuous covariates such as age and body weight, the relationship between the typical value of a parameter and a continuous covariate was evaluated either linear, exponential or power model in equations 5.3.1 – 5.3.3. For dichotomous and categorical covariates, the relationship between the typical value of a parameter and a covariate was evaluated with either additive or proportional model in equations 5.3.4 – 5.3.5.

$$\text{Linear: } \tilde{X}_j = \theta_X^{int} + \theta_X^{COV} \times (COV_j - \overline{COV}) \quad (5.3.1)$$

$$\text{Exponential: } \tilde{X}_j = \theta_X^{int} \times e^{\theta_X^{COV} \cdot (COV_j - \overline{COV})} \quad (5.3.2)$$

$$\text{Power: } \tilde{X}_j = \theta_X^{int} \times (COV_j / \overline{COV})^{\theta_X^{COV}} \quad (5.3.3)$$

$$\text{Additive: } \tilde{X}_j = \theta_X + \theta_X^{COV} \times COV_j \quad (5.3.4)$$

$$\text{Proportional: } \tilde{X}_j = \theta_X \times (1 + \theta_X^{COV} \times COV_j) \quad (5.3.5)$$

Where:

$\tilde{X}_j$  : estimated typical parameter value in the  $j$ th subject;

$COV_j$ : measured value of a covariate in the  $j$ th subject;

$\overline{COV}$ : median value of a covariate in the  $j$ th subject;

$\theta_X^{int}$ : estimated parameter population mean for subjects with the median value of a covariate

$\theta_X^{COV}$ : linear: change in parameter value per unit change in a covariate

exponential: change in log parameter value per unit change in a covariate

power: change in log parameter value per unit change in log covariate

proportional: the increase or decrease in  $\theta_x$  for subjects with  $COV_j = 1$

$\theta_x$ : estimated parameter population mean for subjects with  $COV_j = 0$

Stepwise forward inclusion and backward elimination was used for covariate model development. At least a 3.84 decrease in OFV ( $\alpha = 0.05$ ,  $df = 1$ ) needed to be achieved for covariates to be considered significant. The covariate that contributes to the most significant reduction in OFV was added to the structural model. The forward inclusion was repeated until no further covariates produce additional significant changes in the OFV. This model was considered the full model. Each covariate was then removed from the model using backward elimination method. A covariate was considered significant if it contributed at least a 10.84 increase in the OFV ( $\alpha = 0.001$ ,  $df = 1$ ) when removed from the model. This process was repeated until all remaining covariates were significant.

The final model including all significant covariate was then evaluated by visual predictive check (VPC) and bootstrap, where patients were randomly sampled with replacement, and the parameter estimates from actual analysis and bootstrap results were compared to evaluate the robustness of the model.

## 5.3 Results

### 5.3.1 Patient characteristics

A total of 119 subjects were included in the analysis. The demographic profiles of subjects are summarized in Table 5.1 and 5.2. Frequency distribution histograms for the continuous demographic characteristics are provided in Fig. 5.1. These plots demonstrated that there was a wide distribution of baseline demographic characters. The overall population used to develop the population PK model had a slightly larger number of males than females. Most patients were White (87.4%). The median age was 54 years and ranged from 19 to 91 years. The median weight was 87.9 kg and ranged from 34.5 to 272 kg.

**Table 5.1 Demographic characteristics of the analysis population (continuous variables)**

Demographics	Mean	Median (min – max)
Age (yr)	53	54 (19 - 91)
Weight (kg)	94.2	87.9 (34.50 - 272)
Height (cm)	172.1	172.7 (142.2 – 205.7)
BMI (kg/m <sup>2</sup> )	31.6	28.4 (12.3 - 84.3)
Bilirubin (mg/dl)	2.31	1.20 (0.3 – 39.3)
Creatinine (mg/dl)	1.79	1.30 (0.38 – 9.36)

**Table 5.2 Demographic characteristics of the analysis population (catogorical variables)**

	Number of individuals	Percent (%)
Sex		
Male	68	57.1
Female	51	42.9
Race		
White	104	87.4
Black	15	12.6
Hepatic SOFA score		
0	81	68.1



1	15	12.6
2	17	14.3
3	5	4.20
4	1	0.840
Cardiovascular SOFA score		
0	27	22.7
1	47	39.5
2	3	2.52
3	22	18.5
4	20	16.8
ICU type		
Medical	79	66.4
Surgical	40	33.6

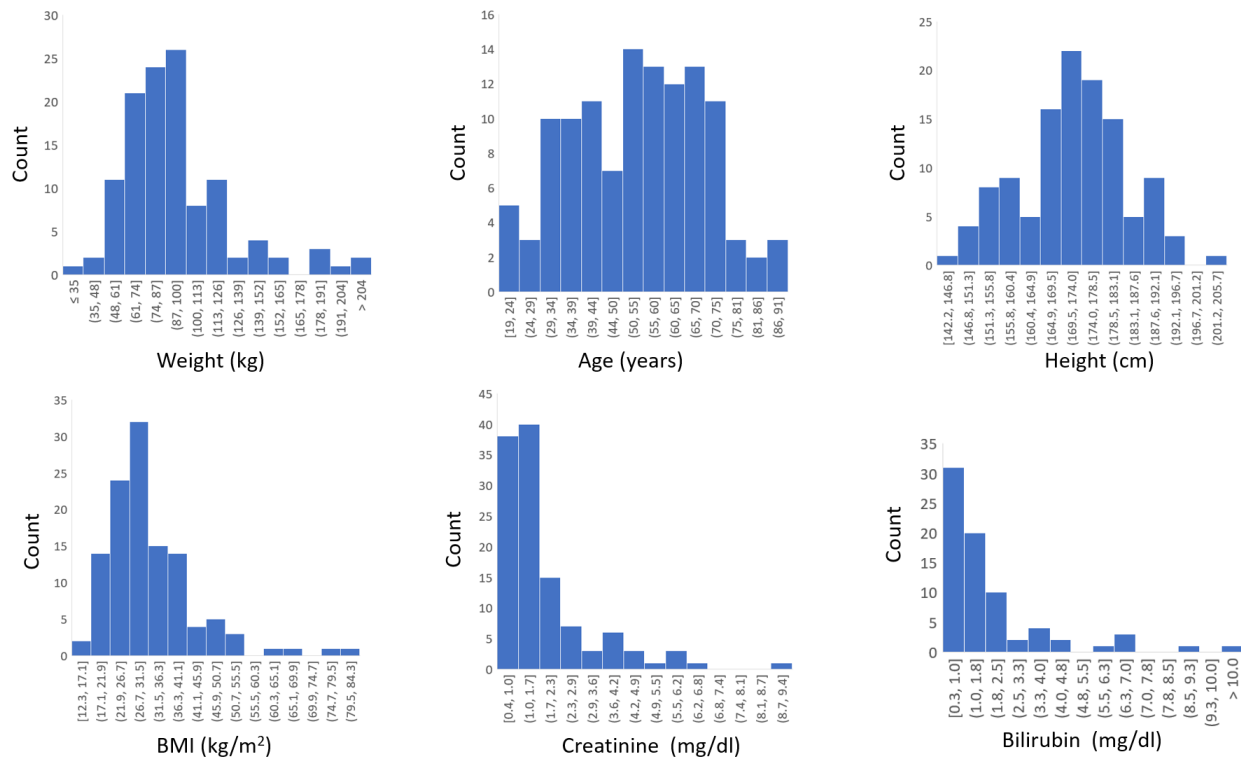


**Figure 5.1** Frequency distribution histograms of continuous demographics variables for the analysis population

Histograms show a wide distribution in baseline weight, age, height, BMI, creatinine and bilirubin levels among included subjects.

### 5.3.2 Sample description and outlier analysis

A total of 253 PK samples were available from 119 subjects before removing the outliers. The observed plasma concentration (DV) versus time since last dose (TSLD) was presented in Fig. 5.2. An iterative process was taken to identify outliers in the initial structural model. Individual fit was examined for each patient with and without the outlier. A total of 19 observation records were deleted from the population PK analysis for the following reasons: patients with missing dosing histories ( $n = 2$ ); unreasonable concentrations that exceed the upper limit of propofol plasma concentration usually observed in the literature (10,000 ng/ml) ( $n = 3$ ); relatively high propofol concentrations based on individual dosing profiles and concentration-time trajectories that are not plausible ( $n = 14$ ) (Table 5.3). Following the deletion of these data, a total of 234 propofol concentrations from 116 subjects were available for the development of the population PK model. Most of the PK samples were sparse. Number of samples per patient and distribution of sampling time are presented in Table 5.4 and Figure 5.3.

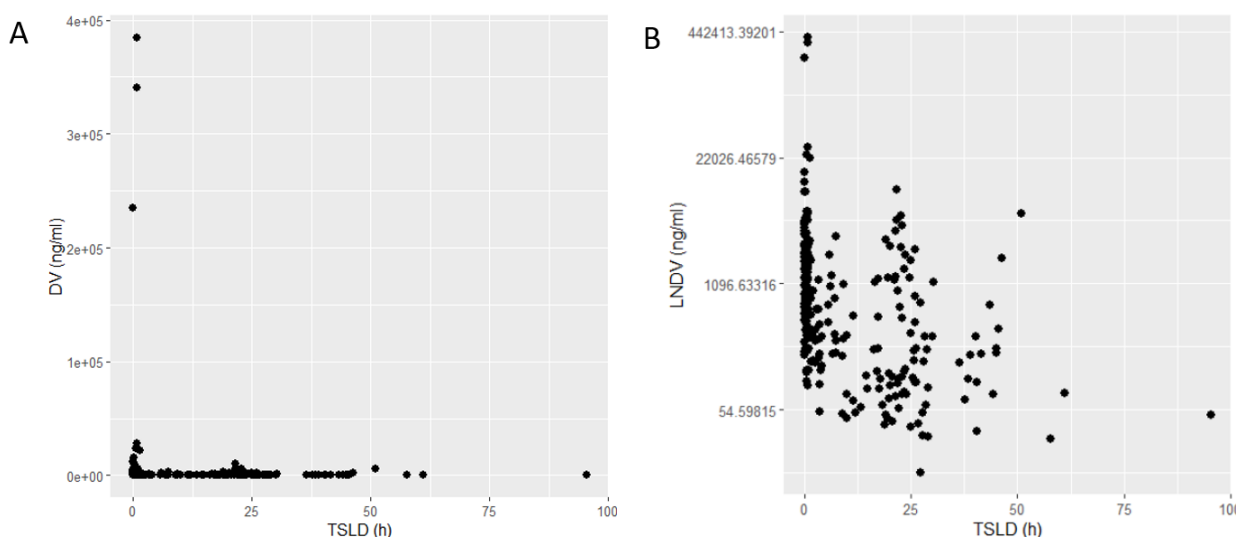
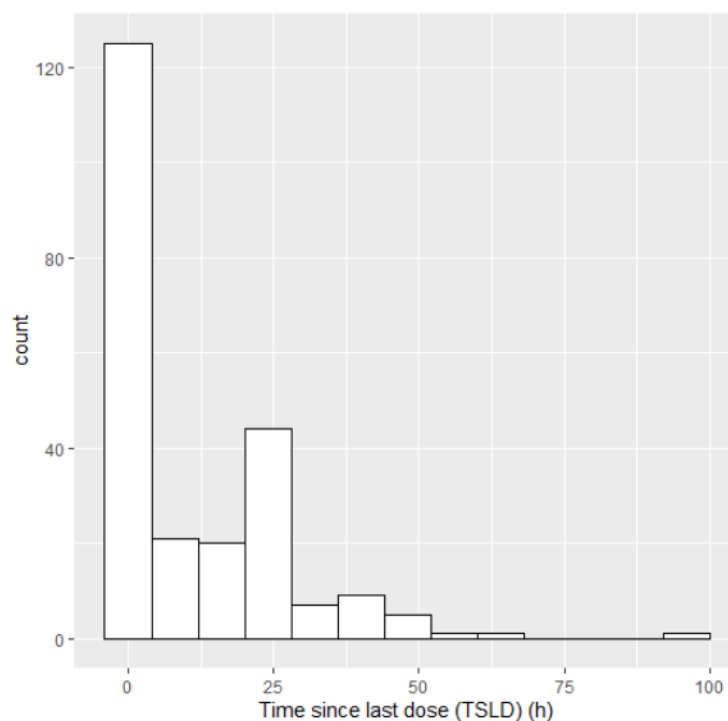


Figure 5.2 DV versus TSLD

(A) Observed concentration (DV) versus time since last dose (TSLD) and (B) natural logarithm transformed DV versus TSLD. Three concentrations were greater than 20-fold than the reported upper limit (10,000 ng/ml) of propofol plasma concentration.

**Table 5.3 Summary of outliers that were removed from the dataset**

Samples excluded	Patients excluded	Reason for exclusion
3	0	Extremely high concentration values > 200,000 ng/ml
2	1	No dosing information
14	2	Relatively high concentration values that were not plausible based on the dosing information



**Figure 5.3 Frequency distribution histogram of time since last dose (TSLD) for all concentrations**

**Table 5.4 Distribution of the number of PK samples per patient**

Number of samples per patient	Number of patients	Percent (%)
1	41	35.3
2	47	40.5
3	17	14.7
4	7	6.03

### 5.3.3 Structural pharmacokinetic model

A two-compartment model with zero-order intravenous infusion and first-order linear elimination was fit to the sparse PK data. The model parameters contained CL, V1, Q, and V2. Interindividual variability of CL, V1, Q, and V2 was described using an exponential error model. A combined additive and CCV error model was used to describe the residual variability.

The results indicated that the model was able to support the estimation of all parameters except the interindividual variability (IIV) of the central volume of distribution (V1). Specifically, the variance for V1 interindividual variability was close to zero (0.00198) with a precision (%RSE) of 5707%. The removal of IIV(V1) improved the parameter estimation for CL, V1, and Q typical values where the %RSE changed from 35%, 156%, and 27% to 24%, 32%, and 17% respectively. Therefore, the IIV of V1 was removed and the model was re-evaluated. Population parameter estimates and precisions (%RSE) are provided in Table 5.5 for the structural model. The model parameters were within reasonable precision (%RSE < 50%) except for V1 and additive component of the residual error. The GOF plots suggested that there was a slight underprediction for high concentrations and at early time points (Fig. 5.4). One or three-compartment models were also tested to see if there were improvements in the model fit. One compartment model underpredicted concentrations to a larger degree and the sparse data were not able to support a more complex three compartment model. The covariances were also estimated in NONMEM to improve the fit of the model. There was a high degree of correlation between CL and Q as shown

in Table 5.6. The process of structural model development and model selection are presented in Appendix B Table 8.

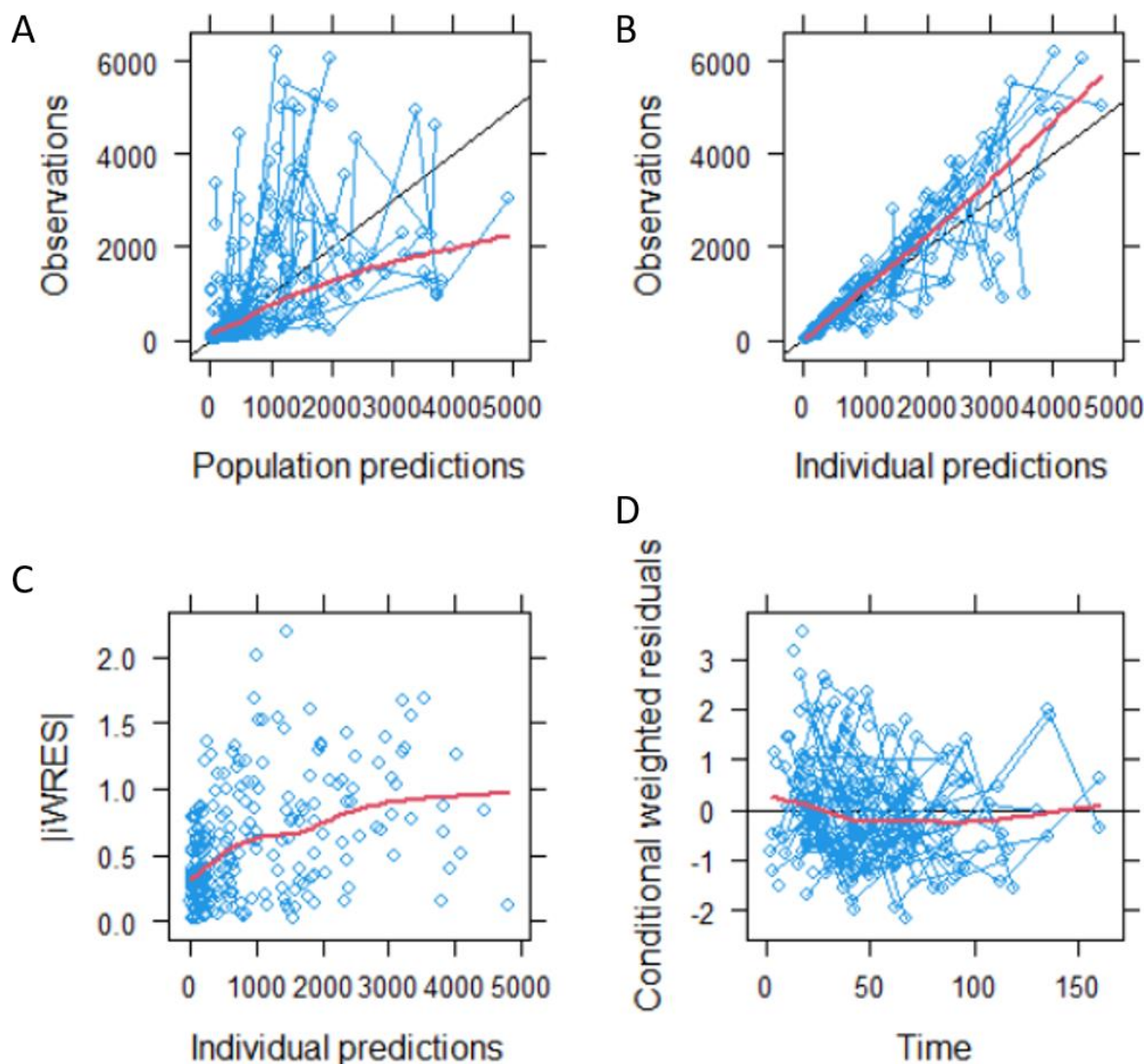


**Figure 5.4 Goodness-of-fit plots for the structural model**

(A) Observed propofol concentration (DV) vs. population predicted concentration (PRED); (B) Observed propofol concentration vs. individual predicted concentration (IPRED); (C) Conditional weighted residuals (CWRES) vs. population predictions and (D) conditional weighted residuals vs. time. The black lines in (A) and (B) represent the line of unity. The solid black lines in (C) and (D) represent  $y = 0$ . The red line is the smoothing line.

**Table 5.5 Parameter estimates of the base structural model**

Parameter	Unit	Estimate	RSE (%)	Shrinkage (%)
-----------	------	----------	---------	---------------

CL	L/h	53.7	20.5	
V1	L	32.2	53.1	
Q	L/h	240	20.6	
V2	L	6860	17.8	
Interindividual variability				
IIV (CL)	CV%	208	26.0	50.8
IIV (Q)	CV%	112	43.4	34.6
IIV (V2)	CV%	214	17.4	44.0
Residual variability				
Proportional	CV%	42.8	14.8	29.3
Additive	mg/L	14.3	101	29.3

RSE: relative standard error; V1: volume of distribution of central compartment; Q: intercompartment clearance; V2: volume of distribution of peripheral compartment; IIV: interindividual variability.

**Table 5.6 Correlation matrix for the PK parameter estimates from the structural model**

	CL	Q	V2
CL	1.00		
Q	0.753	1.00	
V2	0	0	1.00

### 5.3.4 Forward selection of covariates

There were 234 records from 116 subjects in the dataset used for the covariate modeling development. Univariate linear regression was performed to explore the relationship between PK parameters and covariates. The univariate plots of CL versus covariates, V2 versus covariates, and Q versus covariates are provided in Fig. 5.5-5.7. The significant relationship based on univariate regression were sex with CL; weight, BMI, and hepatic SOFA score with V2; weight and sex with Q. Age, and creatinine were reported to be significant covariates in the literature, so we tested the statistical significance for the addition of these covariates as well. Since more than 10% of the subjects were missing bilirubin measurement, it was not included in the covariate assessment.

The abovementioned covariates were included by forward selection. During the first step of forward selection, the most significant relationship was between sex and CL and was therefore added to the base model. During the second step of forward selection, the effect hepatic SOFA score at enrollment on V2 was most significant and was therefore added to the model. During the third step of forward selection, the most significant covariate from this step was the relationship between BMI and V2 and was therefore added to the model. During the fourth step, there was no significant covariate that demonstrated a relationship with PK parameters. Summaries of covariates being tested during each step, the functional form, and the statistical significance are provided in Table 5.7-5.10.

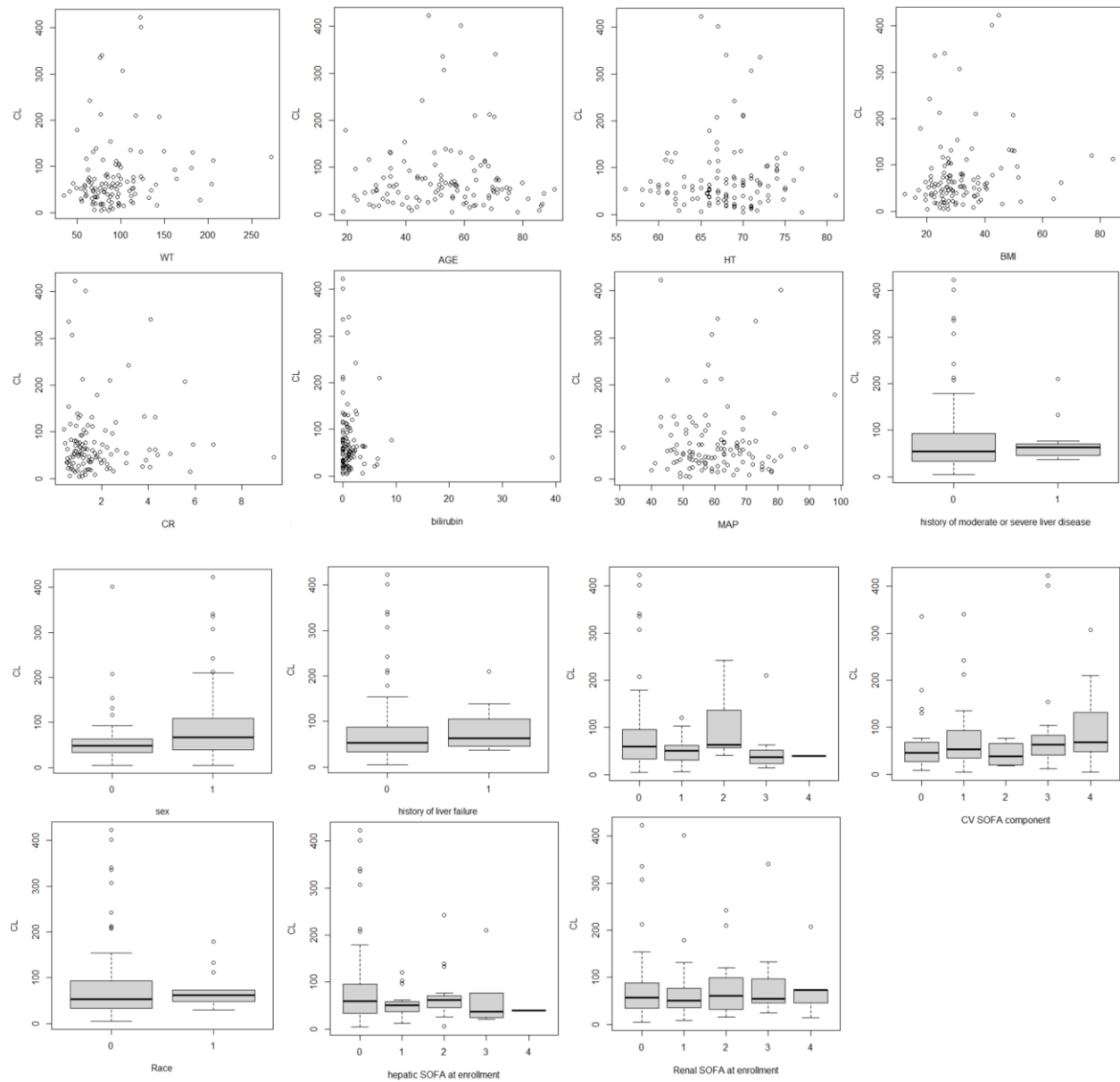


**Figure 5.5 Univariate plots of various covariates versus propofol CL**

The line inside the boxplots represents the median, the upper and lower limits of the box are the 75<sup>th</sup> and 25<sup>th</sup> percentiles. The upper and lower error bars indicate the 95<sup>th</sup> and 5<sup>th</sup> percentiles. The points outside the error bars represent data outside the 5<sup>th</sup> and 95<sup>th</sup> percentiles.



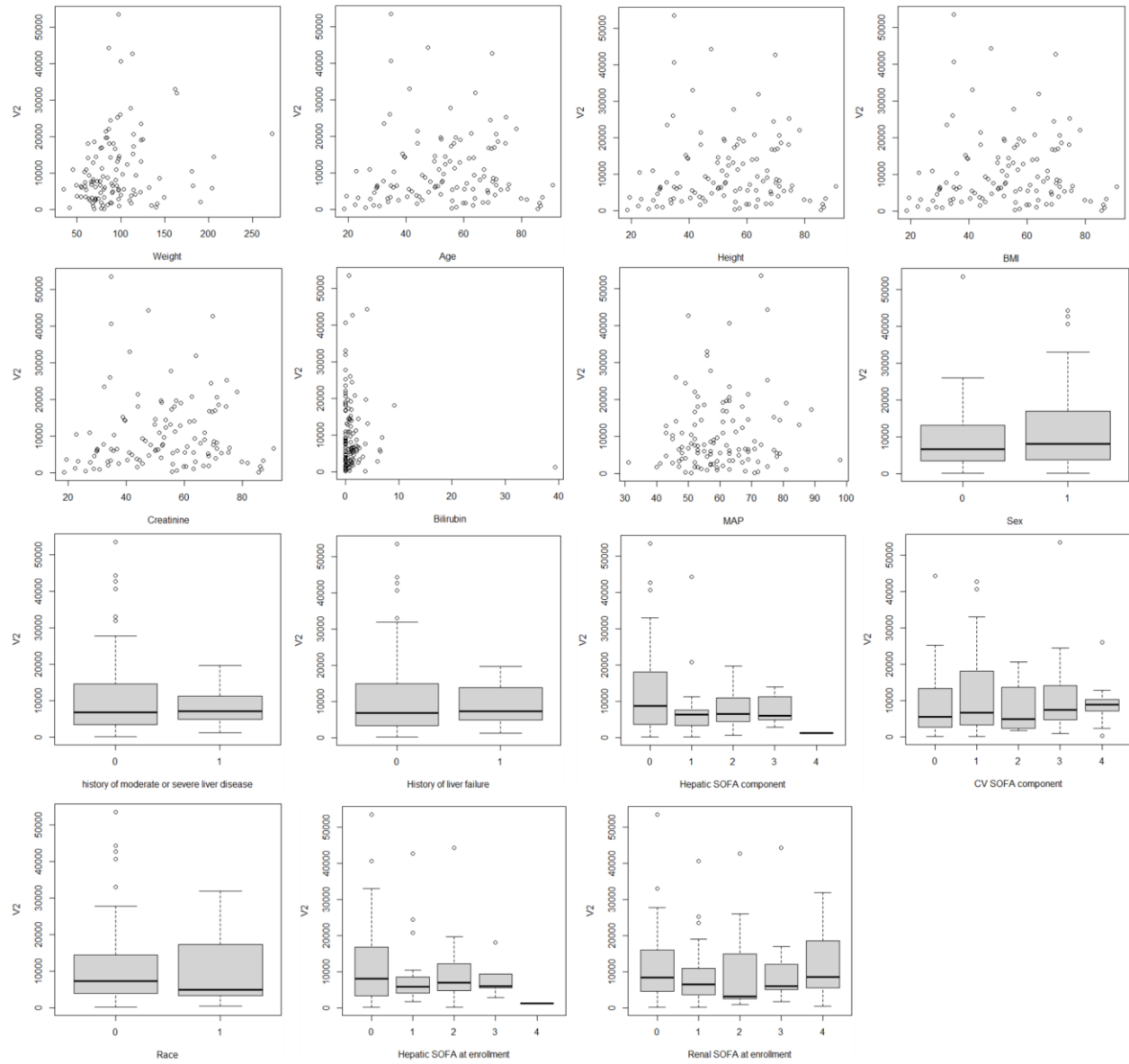


**Figure 5.6 Univariate plots of various covariates versus propofol V2**

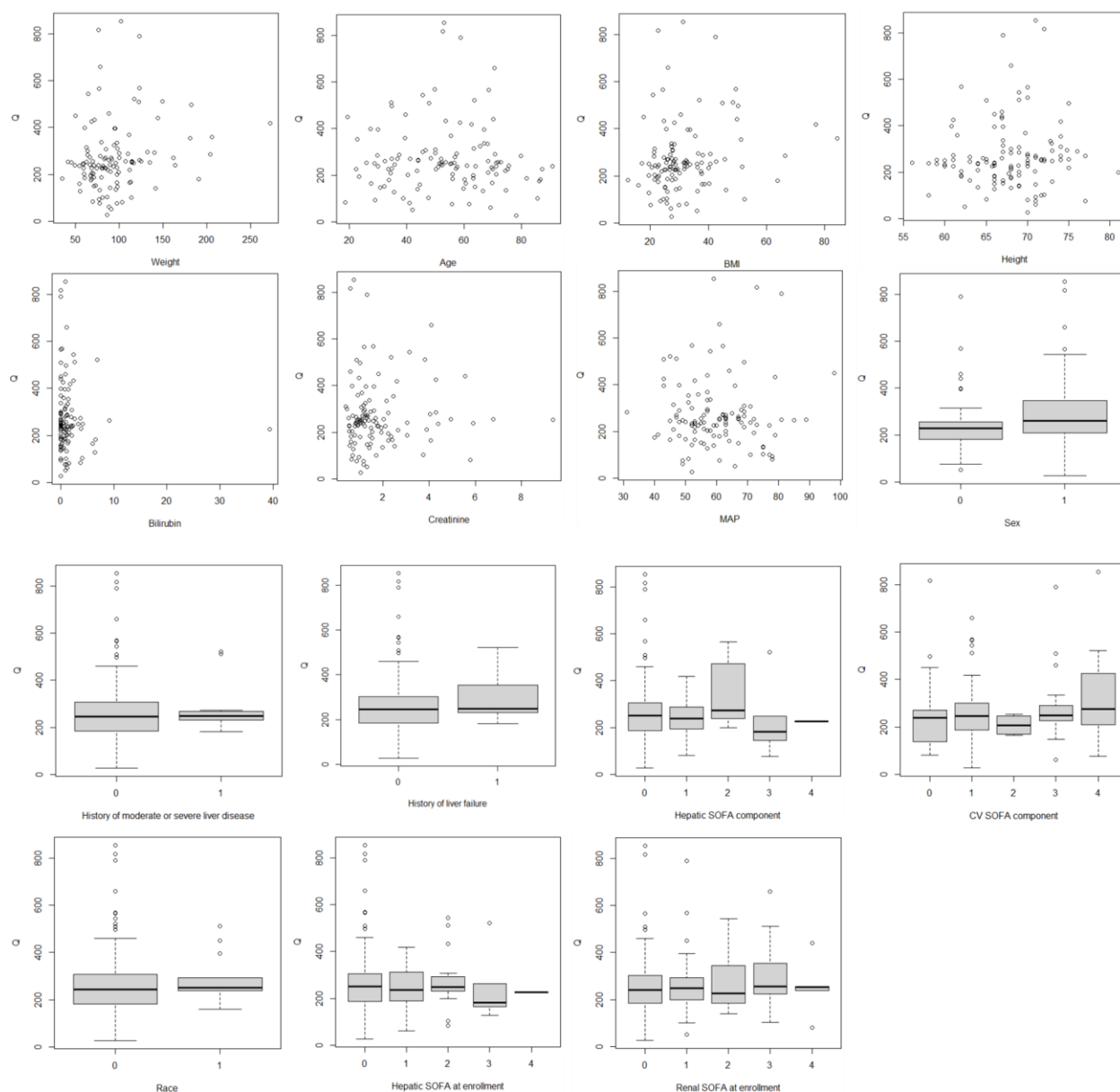


**Figure 5.7 Univariate plots of various covariates versus propofol Q**

**Table 5.7 Step one covariate selection for CL, V2, and Q**

Model	Parameter added	Functional form	$\Delta$ OFV
Base			0
1a	Sex on CL <sup>a</sup>	Exponential	-6.82
1b	Age on CL	Power	-3.25
1c	Weight on CL	Exponential	-5.09
1d	BMI on CL	Exponential	-2.78

1f	Creatinine on CL	Additive	-0.49
1g	SOFA liver on CL	Proportional	-3.07
1h	Sex on V2	Exponential	-3.66
1i	Age on V2	Additive	-1.70
1j	Weight on V2	Power	-6.02
1k	BMI on V2	Exponential	-6.16
1l	Creatinine on V2	Additive	-1.94
1m	SOFA liver on V2	additive	-4.99
1n	Sex on Q	Additive	-2.42
1o	Age on Q	Power	0
1p	Weight on Q	Exponential	-5.62
1q	BMI on Q	Exponential	-4.70
1r	Creatinine on Q	Additive	0
1s	SOFA liver on Q	Additive	-0.61

<sup>a</sup> The grey shaded covariate is the most significant covariate found in the step

**Table 5.8 Step two covariate selection for CL, V2, and Q**

Model	Parameter added	Functional form	ΔOFV
Base	Sex on CL		0
2a	Age on CL	Additive	2.32
2b	Weight on CL	Power	-0.13
2c	BMI on CL	Power	-1.64
2d	Creatinine on CL	Additive	0.03
2f	SOFA liver on CL	Additive	-0.22
2g	Sex on V2	Exponential	0.87
2h	Age on V2	Additive	-0.53
2i	Weight on V2	Exponential	-2.12
2j	BMI on V2	Power	-4.58
2k	Creatinine on V2	Additive	0.37
2l	SOFA liver on V2	additive	-5.67
2m	Sex on Q	Exponential	0.93
2n	Age on Q	Additive	0.02
2o	Weight on Q	Exponential	-1.40
2p	BMI on Q	Exponential	-1.48
2q	Creatinine on Q	Additive	-0.01
2r	SOFA liver on Q	Additive	3.68

**Table 5.9 Step three covariate selection for CL, V2, and Q**

Model	Parameter added	Functional form	$\Delta$ OFV
Base	Sex on CL, SOFA on V2		0
3a	Age on CL	Power	2.65
3b	Weight on CL	Power	-0.20
3c	BMI on CL	Power	-0.36
3d	Creatinine on CL	Additive	0.15
3e	SOFA liver on CL	Additive	-0.66
3f	Sex on V2	Exponential	-0.21
3g	Age on V2	Exponential	-0.03
3h	Weight on V2	Power	-1.70
3i	BMI on V2	Power	-3.88
3j	Creatinine on V2	Additive	-0.13
3k	Sex on Q	Exponential	-0.03
3l	Age on Q	Additive	-0.01
3m	Weight on Q	Power	-0.73
3n	BMI on Q	Exponential	-1.57
3o	Creatinine on Q	Additive	0.24
3p	SOFA liver on Q	Proportional	0.08

**Table 5.10 Step four covariate selection for CL, V2, and Q**

Model	Parameter added	Functional form	$\Delta$ OFV
Base	Sex on CL, SOFA on V2, BMI on V2		0
4a	Age on CL	Additive	0
4b	Weight on CL	Power	-0.20
4c	BMI on CL	Power	-0.36
4d	Creatinine on CL	Additive	-0.33
4e	SOFA liver on CL	Additive	-0.22
4f	Sex on V2	Exponential	0
4g	Age on V2	Exponential	-0.05
4h	Weight on V2	Power	-0.98
4i	Creatinine on V2	Additive	0
4j	Sex on Q	Exponential	-0.11
4k	Age on Q	Additive	0
4l	Weight on Q	Exponential	-3.14
4m	BMI on Q	Exponential	1.29
4n	Creatinine on Q	Additive	0
4o	SOFA liver on Q	Proportional	-0.12

In summary, after forward selection, the covariate sex, hepatic SOFA score, and BMI were found to be significant predictors for propofol CL and V2. The equations for CL and V2 are provided in Equations 5.4.1-5.4.3.

$$TVCL_j \text{ (L/h)} = 20.6 \times e^{1.08 \times SEX} \quad (5.4.1)$$

$$\text{If SOFA} \leq 3, TVV2_j \text{ (L)} = 8150 \times (BMI/29.27)^{0.984} \quad (5.4.2)$$

$$\text{If SOFA} \geq 4, TVV2_j \text{ (L)} = 8150 \times (BMI/29.27)^{0.984} - 1630 \times SOFA \quad (5.4.3)$$

$TVX_j$  = the typical value of the  $X^{th}$  parameter for the  $j^{th}$  subject.

SEX = indicator variable in the  $j^{th}$  subject with a value of 1 for male and 0 for female.

SOFA = hepatic SOFA score ranged from 0 – 4.

BMI = body mass index calculated as body weight in kilograms divided by height in meters.

### 5.3.5 Evaluation of the full model

Population mean parameter estimates and precision from the full model are provided in Table 5.11. The addition of covariates decreased interindividual variability on CL and V2. The addition of SEX explained CL variability by 45%. The addition of hepatic SOFA score and BMI explained V2 variability by 8%. Figure 5.8 shows the GOF plots for the full model. There was a slightly better agreement between the population predicted and individual predicted concentrations versus observed concentrations than previously observed with the base structural model. Further attempts were made to estimate the IIV for V1, however, the data could not support the estimation of this parameter. The plot of individual weighted residual error versus individual predicted concentrations did not reveal observable biases across the predicted concentrations.

The results of the full model showed that the precision of V1 was large (RSE % = 282). The effect of sex, hepatic SOFA, and BMI on CL and V2 was reasonably estimated with RSE% ranging

from 45% to 54%. The additive residual error also estimated with large uncertainty ( $RSE\% = 119\%$ ).

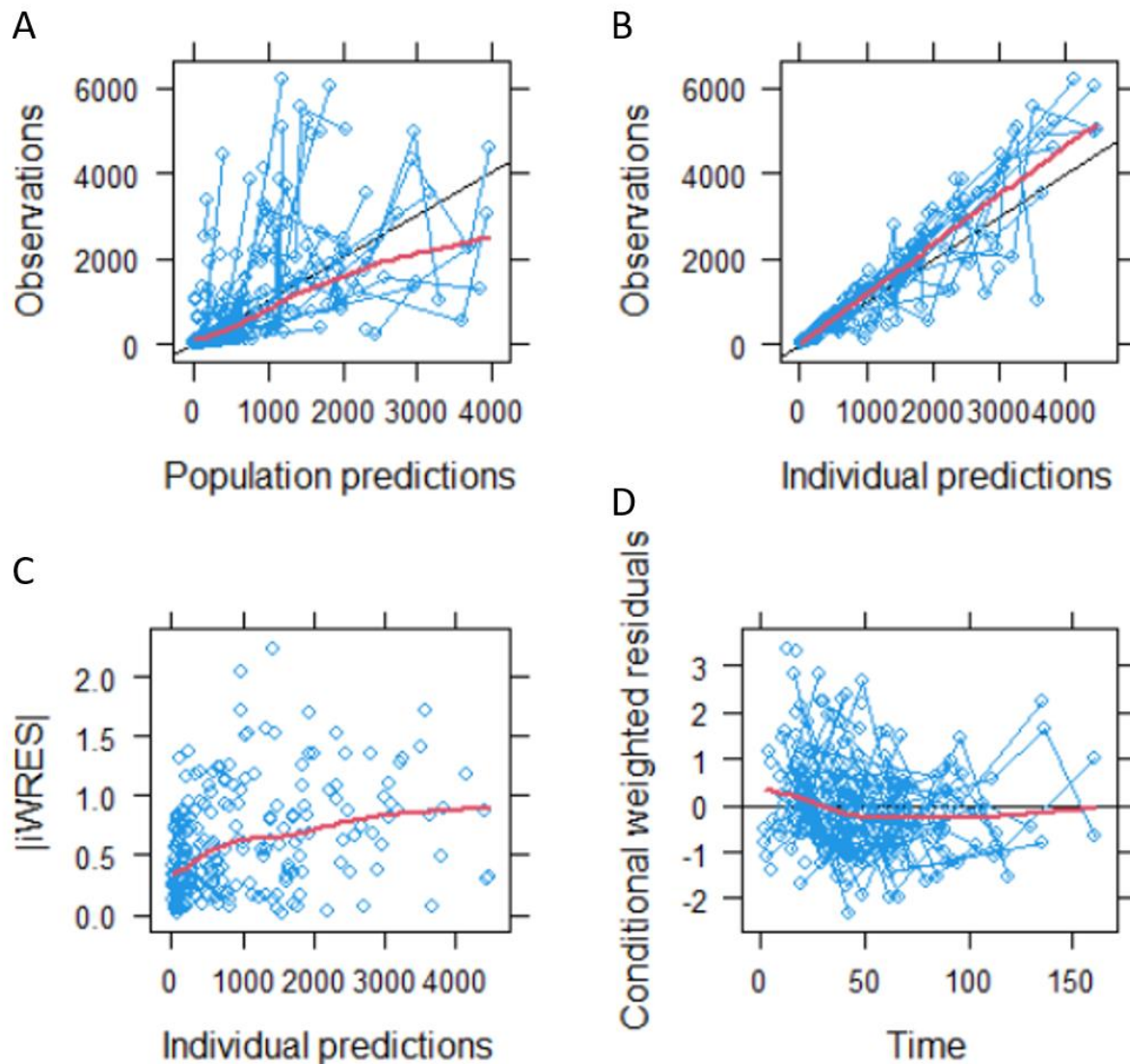


**Figure 5.8 Goodness-of-fit plots for the full model**

(A) Observed propofol concentration (DV) vs. population predicted concentration (PRED); (B) Observed propofol concentration vs. individual predicted concentration (IPRED); (C) Conditional weighted residuals (CWRES) vs. population predictions and (D) conditional weighted residuals vs. time. The black lines in (A) and (B) represent the line of unity. The solid black lines in (C) and (D) represent  $y = 0$ . The red line is the smoothing line.

**Table 5.11 Parameter estimates of the full popPK model replicates**

Parameter	Unit	Estimate	RSE (%)	Shrinkage (%)
CL	L/h	20.7	59.9	
V1	L	27.4	282	
Q	L/h	280	53.2	
V2	L	8160	38.2	
SEX on CL		1.08	44.9	
SOFA on V2		-1640	46.4	
BMI on V2		0.984	54.2	
Interindividual variability				
IIV (CL)	CV%	163	95.4	39.3
IIV (Q)	CV%	120	36.4	39.7
IIV (V2)	CV%	206	23.6	13.5
Residual variability				
Proportional	CV%	41.8	16.1	27.1
Additive	mg/L	13.7	119	27.1

### 5.3.6 Backward elimination of covariates

Stepwise backward elimination was performed. The effects of BMI on V2, hepatic SOFA on V2, and sex on CL were removed from the model in a stepwise fashion. Details of each step of backward elimination process are provided in Table 5.12. The covariate of BMI on V2, hepatic SOFA score at enrollment on V2, and sex on CL were removed from the full multivariate model ( $p > 0.01$ ).

**Table 5.12 Backward elimination of covariates**

Model	Parameter added	$\Delta$ OFV	p-value
Full	Sex on CL, SOFA on V2, BMI on V2	0	
5a	-BMI on V2	3.75	0.053
5b	-SOFA on V2	4.85	0.028
5c	-Sex on CL	3.66	0.056
5d	-Sex on CL, -BMI on V2	3.85	0.050

5e	-Sex on CL, -SOFA on V2	4.89	0.027
5f	-Sex on CL, -BMI on V2, -SOFA on V2	7.30	0.0069

### 5.3.7 Final model

The population mean parameter estimates and precisions of the final model are provided in Table 5.13. The precision for V1 and additive residual error were greater than 50%, but the remaining parameters were estimated with acceptable precision. Given the lack of covariates identified through the backward elimination, this is the best model that was fitted to the sparse data.

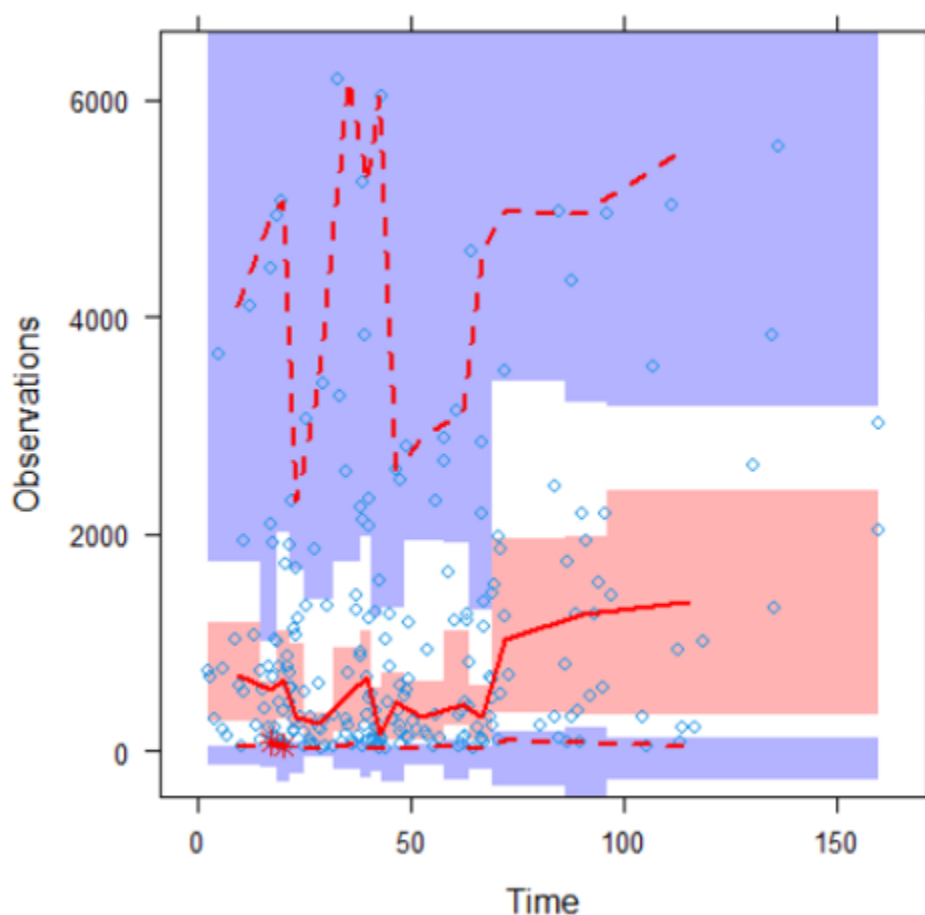


**Figure 5.9 Visual predictive check of the final model**



The blue dots represent the observed data. The solid red line indicates the 50th percentile of the simulated data. The red dashed lines indicate the 5th and 95th percentiles of the observed data. The shaded areas represent 95% confidence intervals of the simulated 50th percentile and 5th and 95th percentiles. Overall, the plot demonstrates that the model predictions captures much of the observed concentrations within the 5<sup>th</sup> and 95<sup>th</sup> percentiles of the simulated values (n = 500).

No model misspecification was detected from the VPC (Fig.5.9). The bootstrap results from 1000 runs confirmed the stability of the final model and 79.7% of the bootstrapping runs were minimized successfully. Median values of the parameters obtained from bootstrap datasets (n=1000) are displayed in Table 5.13. For CL, Q, and V2 the mean estimates from the original dataset are close to the median value of estimates from the bootstrap analysis, suggesting the mean estimates from the final model are relatively unbiased. The relative biases for V1 was high (-28.3%), suggesting the mean estimate of V1 is somewhat biased. The frequency histograms of the mean PK parameter estimate distribution histograms from the bootstrap analyses are shown in Appendix Fig 2.

**Table 5.13 Parameter estimates of the final popPK model from the original dataset and from 1000 bootstrap replicates**

Parameter	Unit	Estimate	RSE (%)	Shrinkage (%)	Nonparametric bootstrap	
					Bootstrap median (2.5 <sup>th</sup> – 97.5 <sup>th</sup> PT <sup>a</sup> )	Relative bias (%)
CL	L/h	53.7	20.5		44.8 (26.1 – 80.1)	-16.6
V1	L	32.2	53.1		23.1 (11.3 – 68.7)	-28.3
Q	L/h	240	20.6		262 (117– 372)	9.17
V2	L	6860	17.8		8102 (3846 – 10382)	18.1
Interindividual variability						
IIV (CL)	CV%	208	26.0	50.8	172 (58.6 – 350)	-20.9
IIV (Q)	CV%	112	43.4	34.6	119 (56.4 – 224)	5.88
IIV (V2)	CV%	214	17.4	44.0	211 (123 – 313)	-1.42
Residual variability						
Proportional	CV%	42.8	14.8	29.3	41.5 (35.5 – 47.0)	-3.13
Additive	mg/L	14.3	101	29.3	14.0 (4.87 – 23.1)	-2.14

<sup>a</sup>PT: percentile.

<sup>b</sup>Relative bias: = (bootstrap median -final model estimate)/final model estimate × 100.

## 5.4 Discussion and conclusions

The objective of this project was to develop a population pharmacokinetic model to describe the pharmacokinetics of propofol in a heterogeneous ICU population. The final model that best fit the data was a two-compartment model with zero-order infusion and linear elimination. There was high degree of variability in CL, V2, and Q in this ICU population. Further development of the model was performed to understand the influence of demographics, covariates on the pharmacokinetics of propofol in this target population. Hepatic SOFA score was a significant covariate on V2.

The population mean clearance was estimated to be 53.7 L/h. This value is smaller than previously reported values in ICU patients that underwent long-term sedation (87.6 L/h, 12.4 %CV) (Smuszkiewicz et al. 2016). In a multicenter popPK analysis, where 256 out of 270 subjects underwent surgery, the authors reported a CL of 86.4 L/h, 37.4 %CV (Schuttler et al. 2000). . Distributive clearance (240 L/h) is larger compared to reported values in ICU patients ranging from 69 to 111 L/h (Smuszkiewicz et al. 2016, Blussé van Oud-Alblas et al. 2019). The population mean for central volume of distribution (V1) was 32.2 L and the estimated value for peripheral volume of distribution (V2) was quite large (6860 L). The large volume of distribution reported in critically ill patients ranged from 499 to 4850 L (Bailie et al. 1992, Frenkel et al. 1995, Barr et al. 2001). The differences in clearance and volume of distribution seen in the current analysis compared to reported values have several explanations. First, the sparse samples in our dataset pose a challenge in estimating clearance and volume of distribution for multi-compartmental drugs. For patients included in the study, their plasma samples were collected twice daily

concurrent with sedation level measurements up to 48 hr after the cessation of the infusion. The design of the sampling time points was not optimal for clearance or volume of distribution estimation. Among the 234 available samples, 143 samples (59%) were collected during the infusion, which provides limited information for propofol elimination. The limited absolute number of samples per patient and the inconsistent sampling time could cause difficulty in predicting precise parameter values. The referenced studies contain rich PK data. Smuszkiewicz et al. included 393 propofol concentrations from 29 subjects and the multicenter popPK analysis by Schuttler et al. included 4112 concentrations from 270 subjects. (Schuttler et al. 2000, Smuszkiewicz et al. 2016). With limited sampling strategies, optimization of sampling times are of particular importance (Sylvie Retout n.d.). Second, the less controlled study used in this analysis may preclude the ability to obtain accurate estimates as evidenced by the relatively large RSE% seen in V1. The effect of sample size and sampling time on variability in propofol PK parameters had been reported. There was an as large as 25-fold difference in central volume of distribution and a 2-fold difference in clearance between three studies when different numbers of samples and different sampling time points were used to derive the propofol pharmacokinetics (Reed 1999). In addition, the uncertainty in infusion duration may contribute to the large proportional residual error.

A secondary objective of this analysis was to study if any patient factors could help explain the interindividual variability in propofol pharmacokinetic parameters. The current analysis did not identify significant covariates for PK parameters. Common covariates that explain parameter variability usually include body weight and age for CL; body weight or BMI for volume of distribution (Sahinovic et al. 2018). In our analysis, we did not identify any covariates that significantly explained the variability in PK parameters. The lack of significant covariates on

propofol clearance and volume of distribution has also been reported in an ICU population that underwent long-term sedation (Smuszkiewicz et al. 2016). In the three-compartment model, the interindividual variability for V1, Q1, and V2 were not able to be estimated. The interindividual variability for CL, V1, and Q2 was 52.0%, 90.1%, and 249%, respectively. And, the authors reported none of the covariates were significant. The inability to identify covariates when there was a large variability in the parameter distribution could be contributed by the relatively large shrinkage values ( $> 30\%$ ). The possible relationships between covariates and parameters may be masked or falsely presented (Savic et al. 2009). Another explanation is the aforementioned difficulty in obtaining accurate parameter estimates, which could be due to the sampling scheme or data inaccuracies secondary to the study design.

In conclusion, a population pharmacokinetic model was developed to describe propofol concentrations in a heterogeneous ICU population. A two-compartment model with zero-order infusion and first-order elimination best described the data. No covariates were found significant. The large interindividual variability within ICU patients requires individualized dosing based on the degree of sedation. Future studies with serial PK collections in this population would help to inform the model and improve parameter precision.

## 6.0 Summary and Future Directions

The main objective of this thesis dissertation was to develop novel compounds that inhibit 20-HETE formation, which aimed to improve cerebral blood flow to ameliorate secondary brain injury. This was achieved by 1) development and validation of bioanalytical assays to assist the evaluation of metabolic stability, CYP inhibition, and quantification of preclinical candidate of interest; 2) *in vitro* screening of over 140 compounds and evaluation of compounds by a multi-tiered approach to select preclinical candidate **UPMP107** that has best drug-like properties; and 3) *in vivo* efficacy and pharmacokinetics evaluation of **UPMP107** in healthy pediatric rats. The secondary objective of this dissertation was to characterize the pharmacokinetics of propofol in a heterogeneous ICU population. This was achieved by 1) development of a structural population pharmacokinetic model and 2) exploration of covariates that could potentially explain to the variability of the propofol pharmacokinetic parameters. The key findings, clinical implications, and future directions are discussed in the following sections.

### 6.1 Key research findings

#### 6.1.1 Development and validation of bioanalytical assays

The development and validation of UPLC-MS/MS methods for metabolic stability, CYP inhibition, and quantification of **UPMP107** are described in Chapter 2. The development of these

assays facilitated the evaluation of drug-like properties and measurement of preclinical candidate in biological samples.

In the metabolic stability assay, we utilized the substrate disappearance method to evaluate *in vitro* metabolic stability in HLM. The substrate concentration was 1  $\mu$ M to ensure linear reaction. The protein concentration was 0.5 mg/ml to minimize nonspecific binding. The incubation duration was 1 hour. This assay enables the assessment of *in vitro* clearance for novel compounds. The sample processing was simple and time efficient. The UPLC-MS/MS method developed for each compound had a short run time and was specific. This assay was developed to specifically support the work described in Chapter 3.

To evaluate the *in vitro* drug-drug interaction, a CYP cocktail assay was developed. Phenacetin, diclofenac, S-mephenytoin, dextromethorphan, and midazolam were probe substrates for CYP1A2, 2C9, 2C19, 2D6, and 3A4, respectively. The protein concentration was 0.1 mg/ml. The concentrations of probe substrates were below their corresponding  $K_m$  values to ensure the linear formation of metabolites. A UPLC-MS/MS method was developed to simultaneously quantify the five metabolites. The method had a short run-time and passed FDA bioanalytical method validation recommendations (FDA 2018). The method was developed to support the work in Chapter 3.

We also reported the first UPLC-MS/MS method for the quantification of novel 20-HETE formation inhibitor **UPMP107**. The method was validated according to the FDA bioanalytical method validation guidance. The UPLC-MS/MS assay supported the quantification of **UPMP107** and 20-HETE under the same LC method, which improves the efficiency of sample processing and sample quantification. The method was developed to support the work described in Chapter 4.

### 6.1.2 *In vitro* evaluation of novel 20-HETE formation inhibitors

The objective of this chapter was to identify preclinical candidate that inhibit 20-HETE formation through preclinical evaluation of drug-like properties and other characteristics including potency, solubility, selectivity, metabolic stability, *in vitro* BBB permeability, CYP inhibition, and *in vitro* toxicity. The screening of entire library of compounds was carried out in three types of microsomes: HLM, RLM, and rCYP4F2. The formation rate of 20-HETE was used as an indicator to identify active compounds. The potency and selectivity of 20-HETE over EETs/DiHETs was evaluated in HLM. Quantification of an arachidonic acid metabolite panel including 10 metabolites were used to derive IC<sub>50</sub> values for 20-HETE formation inhibition and selectivity of  $\omega$ -hydroxylase versus epoxigenase. *In vitro* metabolic stability was evaluated by the previously developed metabolic stability assay. The calculated *in vitro* intrinsic clearance was used to derive human *in vivo* intrinsic clearance by IVIVE. Compounds were evaluated for *in vitro* drug-drug interaction based on the disappearance of the metabolites in the CYP cocktail assay. The solubility, BBB permeability, and *in vitro* safety pharmacology was also evaluated for selected compounds. Using the prespecified criteria for drug-like properties, 143 novel compounds were screened and evaluated according to the multi-tiered evaluation funnel (Fig. 3.2). The potential preclinical candidates were narrowed down based on whether the compound was able to fulfill the criteria. We reported that **UPMP107** was found to be the preclinical candidate as a 20-HETE synthase inhibitor. It has a strong inhibitory activity (IC<sub>50</sub> = 54.2 nM in HLM) and a greater than 100-fold selectivity window for CYP4 over other drug metabolizing enzymes. **UPMP107** has a low *in vitro* intrinsic clearance of 6.94  $\mu$ l/min/mg protein and is highly soluble (kinetic solubility > 600  $\mu$ M). It has a good brain penetration in MDCK-MDR1 assay ( $Papp_{A-B}$  =  $5.16 \times 10^{-6}$  cm/s, ER = 8.06).



And **UPMP107** did not show > 50% inhibition or stimulation for a panel of 44 ion channels, enzymes, or transporters in the *in vitro* safety pharmacology evaluation.

### 6.1.3 *In vivo* evaluation of novel 20-HETE formation inhibitor: **UPMP107**

The novel finding of previous chapter that **UPMP107** possesses strong potency and favorable drug-like properties prompted us to continue its *in vivo* development. The main objective of Chapter 4 was to investigate whether the previously selected preclinical candidate, compound **UPMP107**, can reduce brain 20-HETE levels in healthy pediatric rats. The secondary objective of this chapter was to study the plasma and brain pharmacokinetics of **UPMP107**. The main objective was achieved by assessing the levels of **UPMP107** and 20-HETE in brain tissue after a single IV bolus dose. Compound and 20-HETE levels were measured by previously developed UPLC-MS/MS method. We reported for the first time that **UPMP107** penetrated into the brain and inhibited brain 20-HETE levels. The distribution of **UPMP107** was rapid, and the brain concentrations decline in a biphasic pattern. The brain to blood ratios ranged from 0.7 to 2.2 for 3 mg/kg group and 0.1 to 0.8 for 20 mg/kg group. At 20 mg/kg, the 20-HETE inhibitory effect lasted for 9 hr post-injection. In the single dose pharmacokinetics study, we observed **UPMP107** exhibited a biexponential decay of the pharmacokinetics profile after IV injection. It has a total clearance ranging from 13.7 – 20.1 ml/min/kg, a steady state volume of distribution ranging from 415 - 734 ml/kg, and a half-life of  $21.7 \pm 1.97$  min. This is the first *in vivo* study that demonstrated **UPMP107** penetrated into brain tissue and produced a prolonged 20-HETE inhibitory effect in the Sprague Dawley rat brain. It is also the first *in vivo* study that showed **UPMP107** has a low clearance, a volume of distribution that equals total body water, and a short half-life. The PK information can help dose regimen estimation in the future **UPMP107** pharmacokinetic study in

pediatric cardiac arrest rats. The nominal concentration-time data can be incorporated with future concentration time data from injured rats to study from how disease (cardiac arrest) or physiological parameter (body temperature) change induce a change in the pharmacokinetic of **UPMP107**.

#### **6.1.4 Population pharmacokinetics of propofol in ICU patients**

The objective of chapter 5 was to study the population pharmacokinetics of propofol in ICU patients and explore potential covariates that could explain the variability of propofol pharmacokinetic parameters. A population pharmacokinetics approach was used to evaluate propofol sparse concentrations. First-order conditional estimation with interaction method was used throughout the model development process. Structural model was compared by AIC and diagnostic plots. Stepwise forward selection and backward elimination were applied to evaluate the statistical significance of prespecified continuous and categorical covariates including age, body weight, BMI, height, creatinine, MAP, sex, race, hepatic SOFA score, renal SOFA score, cardiovascular SOFA score, history of liver failure, and history of moderate or severe liver disease. Final model was evaluated by visual predictive check (VPC) and bootstrap. A final model of two compartment, zero-order input, first-order elimination with a combined residual error model was found to best describe the data. For a lipophilic drug, typically total body weight is a significant covariate on volume. The failure to identify covariates on CL or V is somewhat unexpected due to the large inter-individual variability. The typical value of propofol clearance is 53.7 L/h and the typical values for volume of distribution are 32.2 L and 6860 L for central and peripheral compartment, respectively. The results suggested the population pharmacokinetic model was developed to describe the sparse propofol concentrations in a heterogeneous ICU population and

we did not find any covariates that could explain the interindividual variability in PK parameters. In the future, collection of serial plasma samples from this population would help improve the parameter estimate precision.

## 6.2 Clinical implications

The project of preclinical evaluation of novel 20-HETE formation inhibitors has a major strength in which studies were designed and performed to improve the translational success of novel compound to be developed as a treatment for secondary brain injury. Translational approaches were taken to help accelerate the move of basic research findings into therapeutics in the clinical research environment.

The development of metabolic stability assay, CYP inhibition assay, and quantification for **UPMP107** are essential for this drug development project. The LC-MS/MS methods are sensitive, specific, robust, and reproducible. These assays allowed us to measure *in vitro* intrinsic clearance, evaluate drug-drug interaction, and quantify the amount of preclinical candidate **UPMP107** in biological samples presented in Chapter 3 and 4. These methods are the groundwork that allows the continuous support of lead optimization and *in vivo* testing of preclinical candidates.

The identification of the preclinical candidate **UPMP107** is a novel finding in this discovery and early development project. The advance of the project is in accordance with the drug development process, where a number of streamlined assessments were applied to identify molecules that would possess suitable characteristics for future drug development (Fig. 6.1). The target, 20-HETE has been identified as a potential therapeutic target as described in Chapter 1. Bioanalytical assays have been developed and validated as described in Chapter 2. Rigorous

advancement criteria as stated in Chapter 3 were prespecified for the hit generation, lead generation and optimization stages where compounds that meet the “Go” criteria were advanced to decrease the late stage failure rate in drug development. Hits (**UPMP010** and **UPMP019**) were confirmed by repeated potency evaluation, assays confirmed the specificity and selectivity, druggability evaluation including solubility, stability, and BBB permeability was also confirmed. During lead optimization, preliminary SAR was explored, druggability was evaluated for compounds to ensure the selection of the optimized preclinical candidate (**UPMP107**). The wide selectivity window of compounds provides a favorable clinical implication. A wide therapeutic window, where increasing the dose will lead to greater efficacy of 20-HETE inhibition with minimum inhibitory effect for EETs enables a wide dose range selection. *In vitro* intrinsic clearance is also one of the important “Go” and “No Go” decisions for compound development. Specifically, we applied a translational approach of IVIVE to project human pharmacokinetic parameters from *in vitro* data. Although additional experiments are required to improve the accuracy of human PK parameter predictions, important human PK information was obtained for the first time, which could support first-in-human studies. The evaluation of BBB permeability at early drug development stage also has great clinical significance. The moderate brain penetration of **UPMP107** from BBB permeability assay may be of clinical importance given that drug efflux by P-gp can reduce brain concentrations, and for drugs that have central activities, it may induce a treatment failure (Loscher et al. 2005). Therefore, it is vital to conduct further experiments to confirm if **UPMP107** is a substrate of human P-gp thereby facilitating the design or interpretation of future clinical studies. In addition, the *in vitro* safety profiling of new chemical entities during early stages of drug development is an essential tool to predict clinical adverse effects. Collectively, the plausible mechanism of action of 20-HETE inhibition in recombinant CYP4F2 microsomes was validated;

a multi-tiered *in vitro* evaluation approach was implemented to evaluate drug-like properties and select compounds according to the prespecified rigorous criteria at early drug development, which enables the discovery of compounds that might have high probability of clinical success.

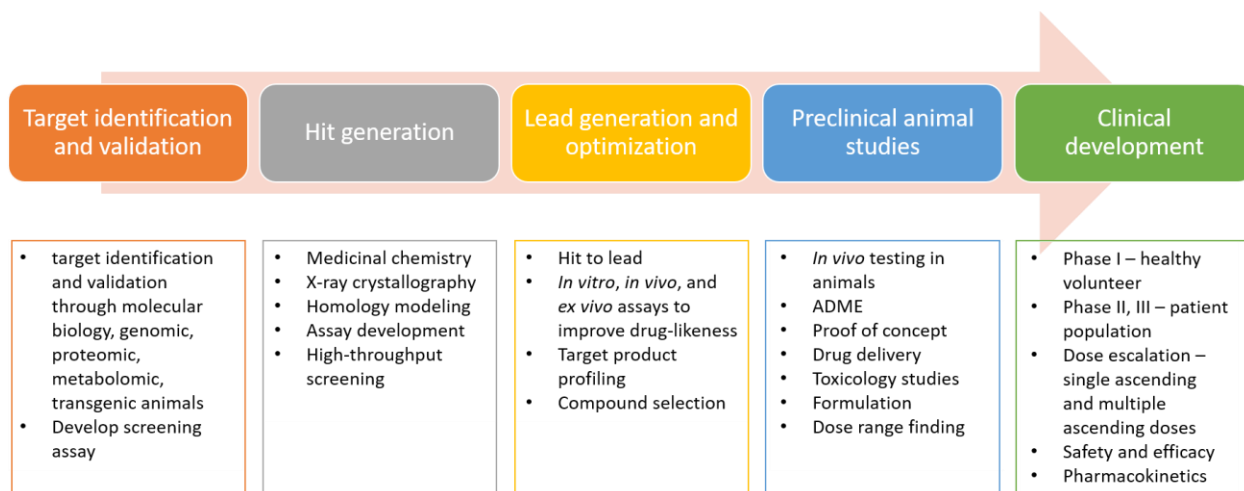


**Figure 6.1 Steps for early drug development**

Figure is adapted from Nature Review by Knowles et al. (Knowles et al. 2003).

Preclinical pharmacokinetic evaluation can facilitate the early termination of weak candidates and can help identify lead candidates with favorable pharmacokinetics that are more likely to be efficacious and safe. The *in vivo* studies in this project provide preliminary evidence of pharmacokinetics and efficacy of **UPMP107** in pediatric rats. The pharmacokinetic data from animals can be used to predict human pharmacokinetics. The prediction of human pharmacokinetics from animal pharmacokinetics or toxicokinetics data is of great clinical importance as the information such as no-observed-adverse-effect level (NOAEL) is useful in the design of the first-in-human study for a drug development program. Besides the naïve pooling approach to analyze the **UPMP107** pharmacokinetic data by noncompartmental analysis, we also applied population pharmacokinetics principles and techniques to analyze the **UPMP107** pharmacokinetic data to facilitate the early drug development and translational research. The model is subject to continuous refinement and optimization as more data is collected to provide

insight in designing future animal studies, such as incorporating an effect-site compartment to assist the prediction of effect-site concentration (brain) under a specific dose. The developed model is also of great translational value when making the transition from nonclinical studies to first-in-human clinical trials in facilitating allometric scaling across species, predict human exposure, and provide between-subject variabilities.

In addition to new drug discovery, we also studied the PK of propofol in an ICU population. The goal was to develop a popPK/PD model and explore if there are any covariates that could explain the PK variability. The ultimate goal was to perform model-based simulation to study the association of various dosing regimens and sedation level in this population. The application of the population PK model to guide dose titrations to achieve required sedation levels has been reported. Population pharmacokinetic models have been programmed in target-controlled infusion (TCI) systems to help calculate required infusion rates to achieve desired plasma concentrations (Marsh et al. 1991, Schnider et al. 1998). We also observed large interindividual variability of propofol pharmacokinetics in ICU patients. However, no significant covariate for PK parameters was found. In our analysis, propofol peripheral volume of distribution was large, suggesting significant drug accumulation and saturation in the peripheral tissues.

### **6.3 Future directions**

In this dissertation, we identified a preclinical candidate **UPMP107** through a tiered screening and evaluation approach that showed good brain penetration and brain 20-HETE inhibition. We also developed a population pharmacokinetic model for propofol to describe propofol PK in ICU patients.

As the development of novel chemical entities is still at an early stage, a large body of additional work and analysis could to be performed in order to achieve the ultimate goal of developing a clinically relevant neuroprotective agent. We will primarily discuss the work that can contribute to this project from drug metabolism and pharmacokinetics perspective.

### **6.3.1 Future work related to *in vitro* evaluation for novel compounds**

There are several enzymes that contribute to 20-HETE formation such as CYP4F2, CYP4A11, and CYP4F3B. As introduced previously, CYP4A11 has the highest catalytic activity for arachidonic acid, followed by CYP4F2, and CYP4F3B. The affinity of arachidonic acid to these enzymes were ranked as CYP4F2 > CYP4F3B > CYP4A11. CYP4F2 was recognized as the predominant enzyme for 20-HETE formation in an immunochemical analysis, where CYP4F2 antibodies inhibited 93.4% of 20-HETE formation in hepatic microsomes. The specificity of novel compounds was evidenced by the inhibition of 20-HETE formation in recombinant CYP4F2 microsomes. In the screening assay, we observed compounds that showed greater inhibition in HLM than in rCYP4F2, implying the potential involvement other CYP isoforms in forming 20-HETE. Testing the inhibition of 20-HETE in recombinant CYP4A11 or CYP4F3B microsomes will elucidate the potential enzyme targets for novel compounds.

As mentioned in Chapter 3, there are several limitations in the assays to evaluate the drug-like properties. First, the metabolic stability assay can be tested in hepatocytes to measure the clearance contributed by both phase I, II enzymes, and transporters. Inhibition of other drug metabolizing CYP enzymes should be further confirmed by obtaining IC<sub>50</sub> values. The role of P-gp in **UPMP107** brain penetration could be tested in the presence of a known P-gp inhibitor in the MDCK-MDR1 assay.

The inhibition mechanism and metabolism pathways for **UPMP107** are unknown currently. The inhibition mechanism can be studied by performing incubation in three groups, including 1) 0 min pre-incubation group; 2) 30 min pre-incubation in the presence of NADPH; and 3) 30 min pre-incubation in the absence of NADPH prior to the addition of substrate arachidonic acid. A  $\geq 1.5$ -fold shift in the  $IC_{50}$  values between group 2 and 3 would suggest the compound is a time-dependent inhibitor (Grimm et al. 2009). A lack of  $IC_{50}$  difference between group 1, 2, and 3 would suggest the compound is a reversible inhibitor. The identification of enzymes involved in metabolizing the molecule is of equal importance because elucidating the metabolism pathway helps predict the possible drug-drug interactions in humans. The enzymes involved in the metabolism of a novel molecule can be studied by CYP phenotyping in human liver microsomes or hepatocytes in the presence and absence of selective inhibitors for a specific CYP isoform (Jia et al. 2007). To improve the accuracy of human PK parameters projection, microsomal protein binding, blood to plasma ratio, and plasma protein binding are also important information that can be collected during *in vitro* evaluation.

To continue finding compounds that are more potent and with better properties, it is important to evaluate a larger number of compounds in the *in vitro* assays. The trend observed not only in potency, but also in other properties such as metabolic stability and BBB permeability could provide information on optimizing novel compound structure.

Aside from continuing evaluation of novel compounds' properties, research interest also lies in elucidating the molecular mechanisms of novel compounds. Hippocampal slices subjected to oxygen-glucose deprivation could be treated with either novel compound or control. The cell viability, reactive oxygen species (ROS), and caspase-3 activity could be tested. If a higher neuronal survival, a decreased ROS, and lower caspase-3 activity were to be observed, a direct



neuronal protective effect would be positive finding in addition to the proposed effect of attenuating the fall of CBF caused by microvascular vasoconstriction.

### **6.3.2 Future work related to *in vivo* evaluation of preclinical candidate: UPMP107**

Although the *in vitro* metabolic stability study suggested **UPMP107** is slowly metabolized, the pharmacokinetic study of **UPMP107** in pediatric rats suggested it has a short *in vivo* half-life. The short biological half-life of **UPMP107** observed *in vivo* have several explanations including instability in plasma or extrahepatic metabolism. Compounds with functional groups such as esters, amides, lactones, lactams, carbamides, sulfonamides, and peptic mimetics are prone to hydrolysis in plasma (Di et al. 2005). Plasma instability can cause low levels of a compound in the systemic circulation. To test whether **UPMP107** gets degraded in plasma, the disappearance of parent compound in rat or human plasma at different time points could be measured. Extrahepatic metabolism can be tested by incubating the compound in tissues such as the kidney microsomes and measure the disappearance of the parent compound. In addition, non-hepatic clearance in organs such as kidney could be one of the elimination pathways, which can be tested by measuring the amount of compound excreted in the urine samples.

CYP4A enzyme expressions were found in various regions in the brain including neocortex, hippocampus, thalamus, hypothalamus, striatum and amygdala (Gonzalez-Fernandez et al. 2020). These regions were consistent with previous reported brain regions that are susceptible to hypoxia after cardiac arrest (Neumann et al. 2013). It is important to study how the compound distribute within different regions in the brain to see if the compounds reached desired concentration or exposure at the site of action.

To ensure the administered dose can achieve desired brain concentrations in pediatric cardiac arrest rats. PK and PD studies are required to be performed in injured animals to obtain information in clearance, volume of distribution, brain to plasma ratio, and brain 20-HETE inhibition. The PK parameters and PD endpoint and the relationship between dose and brain 20-HETE could be used as a guide to support dose regimen that will be used in the following animal efficacy studies. Furthermore, the addition of the PK data under disease state can contribute to the development and refinement of animal popPK model, which can study whether disease, temperature, or gender would alter the PK of **UPMP107**.

The experiment of great interest would be to test whether **UPMP107** could produce neuroprotective effect in the pediatric cardiac arrest injury model. We are interested in evaluating the treatment effect on cortical perfusion, neuron viability, brain edema, BBB integrity, and functional outcomes in injured animals. The result of decreased brain 20-HETE concentrations without affecting EETs and DiHETs, improvement in the cortical perfusion, reduction in brain water content and lower neurological deficit score in the treated group will reaffirm the important role of CYP-derived eicosanoids in cerebral blood flow and neurodegeneration in cardiac arrest. It will also provide the first evidence of novel **UPMP107** being effective in ameliorating secondary brain injury after cardiac arrest.

To envision advancing to clinical development of the **UPMP107**, obtaining no observed adverse effect level (NOAEL) from nonclinical safety studies in the most appropriate animal species would inform the first-in-human dose. Due to the complexity of pathophysiological mechanisms of brain injury after cardiac arrest or other critical illness, single agent might not be adequate to achieve treatment success. The hope of improved neurological outcomes may lie in a

combination of the novel compound with other medications targeting at different mechanisms of the pathophysiology of secondary brain injury.

### **6.3.3 Future work related to propofol model development**

It would be ideal to collect serial plasma samples to inform the model development. Using published plasma concentrations from literature could potentially help refine the model. Another approach is to adopt a PRIOR subroutine in NONMEM with parameter estimate from previous models. Development of a PD model that characterizes the level of sedation and establishment of a relationship between the PD and population PK model would be of great interest. The PD model could be developed using sedation scores such as Bispectral Index (BIS) or Richmond Agitation Sedation Scale (RASS). The observed or measured sedation scores could be modeled using a sigmoidal  $E_{\max}$  model and link to effect site concentrations. If a population PK/PD could be developed, the model would potentially allow the exploration of the relationship between propofol exposure and sedation depth. Various dosing regimens could be simulated to evaluate if the dosing regimen might achieve a preset sedation level in this ICU population.

## **6.4 Conclusions**

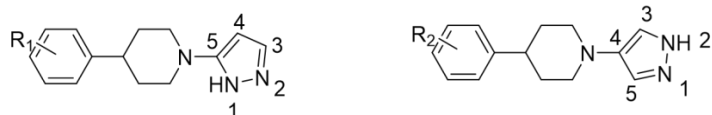
In this dissertation, we focused on two projects related to CNS drugs. First, we developed and validated several bioanalytical assays that are sensitive, accurate, and robust to facilitate the discovery, development, and evaluation of novel 20-HETE formation inhibitors. Next, we applied a multi-tiered approach to facilitate the evaluation of novel chemical entities. We identified

multiple novel molecules that are specific and selective 20-HETE formation inhibitors. Of these novel molecules, we selected **UPMP107** as a preclinical candidate that is highly soluble, potent, selective, metabolically stable, brain penetrable, and did not show toxicity at 10  $\mu$ M in *in vitro* Safetyscreen44Panel. Based on the favorable characteristics, **UPMP107** was advanced to the preclinical *in vivo* evaluation in pediatric rats. We demonstrated for the first time that **UPMP107** crossed the blood-brain barrier, worked centrally to inhibit brain 20-HETE, and obtained plasma pharmacokinetics of **UPMP107**. In the second project, we used a modelling approach to characterize the PK of propofol, a widely used sedative in patients with brain injury, in an ICU population. A two-compartment model with zero-order infusion and linear elimination best described the sparse plasma concentrations. There was a large interindividual variability of propofol PK in this population. No significant covariate that explain the variability of PK parameters was found.

To summarize, 20-HETE has been identified as an important modifiable mediator in various cerebrovascular disease. 20-HETE is a quantifiable biomarker that relates to compounds' potency. 20-HETE is found to be associated with clinical outcomes in ischemic stroke and subarachnoid hemorrhage patients. Developing novel therapies targeting 20-HETE formation to ameliorate secondary brain injury is an interesting and exciting research direction which requires continuous and collaborative efforts from researchers and scientists across different fields.

Appendix A **Supplementary data for Chapter 3 - *In vitro* evaluation of 20-HETE formation inhibitors**

**Appendix Table 1 CYP4 inhibition of analogs with single substitution on benzene in RLM**

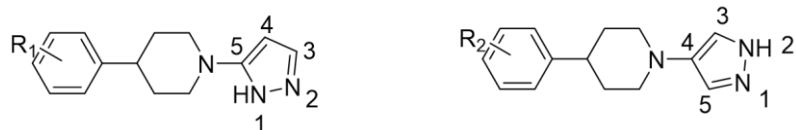


Compd (UPMP)	R <sub>1</sub>	% inhibition in RLM <sup>a</sup>	Compd (UPMP)	R <sub>2</sub>	% inhibition in RLM
<b>010</b>	-	13.5 <sup>b</sup>	<b>019</b>	-	
<b>027</b>	4-OMe	31.8	<b>031</b>	4-OMe	25.9
<b>028</b>	3-OMe	42.5	<b>029</b>	3-OMe	45.6
<b>041</b>	2-OMe	0	<b>042</b>	2-OMe	0
<b>037</b>	4-COOMe	3.60	<b>038</b>	4-COOMe	18.3
<b>039</b>	3-COOMe	0	<b>040</b>	3-COOMe	43.0
<b>046</b>	4-Me	0	<b>047</b>	4-Me	16.3
<b>081</b>	3-Me	12.0	<b>077</b>	3-Me	44.0
<b>080</b>	2-Me	0	<b>078</b>	2-Me	0
<b>049</b>	4-ethylsulfonyl	0	<b>048</b>	4-ethylsulfonyl	13.4
<b>051</b>	4-MeOMe	22.3	<b>054</b>	4-MeOMe	27.8
<b>061</b>	4-N- methylacetamide	8.00	<b>060</b>	4-N- methylacetamide	52.0
<b>062</b>	4-acetamide	38.0	<b>072</b>	4-acetamide	27.0

<sup>a</sup> Data were obtained from screening results in RLM.

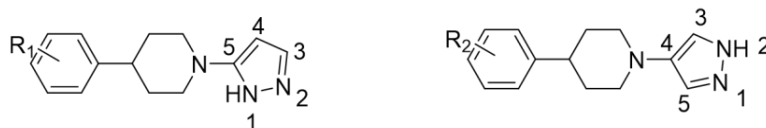
<sup>b</sup> Screening of compound 10 was conducted at 250 nM

**Appendix Table 2 CYP4 inhibition of analogs with simple halogen substitution in RLM**



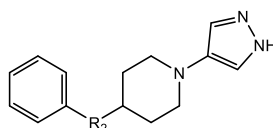
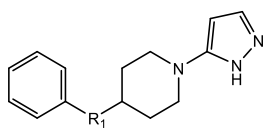
Compd (UPMP)	R <sub>1</sub>	% inhibition in RLM	Compd (UPMP)	R <sub>2</sub>	% of inhibition in RLM
<b>071</b>	4-F	41.0	<b>070</b>	4-F	57.0
<b>074</b>	3-F	0	<b>075</b>	3-F	31.0
<b>079</b>	2-F	26.0	<b>083</b>	2-F	53.0
<b>085</b>	4-Cl	0	<b>086</b>	4-Cl	21.3
-	-	-	<b>084</b>	3-Cl	61.0

**Appendix Table 3 CYP4 inhibition in RLM for analogs with double substitutions**



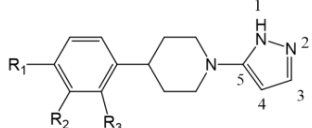
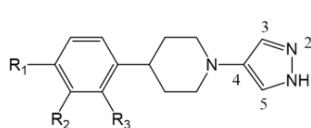
Compd (UPMP)	R <sub>1</sub>	% of inhibition in RLM	Compd (UPMP)	R <sub>2</sub>	% of inhibition in RLM
<b>076</b>	3-F,4-OMe	27.0	<b>068</b>	3-F, 4-OMe	42.0
<b>082</b>	2-F, 4-OMe	46.0	<b>073</b>	2-F, 4-OMe	63.0
<b>097</b>	3-F, 5-OMe	61	<b>096</b>	3-F, 5-OMe	11.1
<b>098</b>	3-OMe, 4-F	55	<b>099</b>	3-OMe, 4-F	61
<b>091</b>	3-Cl, 4-OMe	30.2	<b>088</b>	3-Cl, 4-OMe	49.0
<b>090</b>	2-Cl, 4-OMe	0	<b>089</b>	2-Cl, 4-OMe	0
<b>095</b>	2-F, 4-N- methylacetamide	25.0	<b>093</b>	2-F, 4-N- methylacetamide	27.3

**Appendix Table 4 CYP4 inhibition in RLM for analogs with extended linker**

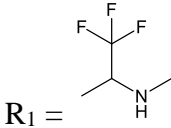
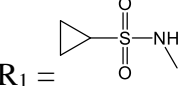


Compd	R <sub>1</sub>	% of inhibition in RLM	Compd	R <sub>2</sub>	% of inhibition in RLM
<b>10</b>	-	13.5	<b>19</b>	-	-
<b>21</b>	R <sub>1</sub> = C	0	<b>22</b>	R <sub>3</sub> = C	2.49
<b>12</b>	R <sub>1</sub> = O	0	<b>43</b>	R <sub>3</sub> = O	0
<b>56</b>	R <sub>1</sub> = S	0	<b>57</b>	R <sub>3</sub> = S	7.80
<b>59</b>	R <sub>1</sub> = O=S=O	0	<b>58</b>	R <sub>3</sub> = O=S=O	0

Appendix Table 5 CYP4 inhibition in RLM for analogs UPMP101 - 140

<div style="display: flex; justify-content: space-around; align-items: center;"> <div style="text-align: center;">  </div> <div style="text-align: center;">  </div> </div>					
Compd <sup>a</sup> (UPMP)	Substituents <sup>b</sup>	% of inhibition in RLM <sup>b</sup>	Compd (UPMP)	Substituents	% of inhibition in RLM
<b>062</b>	$R_1 = \text{NH-C(=O)-CH}_3$		<b>072</b>	$R_1 = \text{NH-C(=O)-CH}_3$	
<b>102</b>	$R_1 = \text{N-C(=O)-CH}_3$	0	<b>101</b>	$R_1 = \text{N-C(=O)-CH}_3$	13.8
<b>106</b>	$R_1 = \text{N-C(=O)-CH}_3$ , $R_3 = \text{F}$	2.30	<b>105</b>	$R_1 = \text{N-C(=O)-CH}_3$ , $R_3 = \text{F}$	19.3
<b>108</b>	$R_1 = \text{N-C(=O)-CH}_2\text{CH}_3$	42.7	<b>107</b>	$R_1 = \text{N-C(=O)-CH}_2\text{CH}_3$	49.6
<b>120</b>	$R_1 = \text{N-SO}_2\text{CH}_3$	0	<b>109</b>	$R_1 = \text{N-SO}_2\text{CH}_3$	0
<b>125</b>	$R_1 = \text{N-CH}_3$	48.7	<b>124</b>	$R_1 = \text{N-CH}_3$	42.9
<b>136</b>	$R_1 = \text{N-CH}_2\text{CH}_3$ , $R_2 = \text{F}$	63.6	<b>135</b>	$R_1 = \text{N-CH}_2\text{CH}_3$ , $R_2 = \text{F}$	62.7
-	-	-	<b>131</b>	$R_1 = \text{NH}_2$	27.0
-	-	-	<b>113</b>	$R_1 = \text{SO}_2\text{CH}_3$	0
<b>138</b>	$R_1 = \text{O}_2\text{N-CH}_2\text{CH}_3$	21.9	<b>137</b>	$R_1 = \text{O}_2\text{N-CH}_2\text{CH}_3$	22.3
-	-	-	<b>139</b>	$R_1 = \text{SO}_2\text{NH-CH}_2\text{CH}_3$	24.3
-	-	-	<b>134</b>	$R_1, R_2 = 1,3\text{-dihydro}[c]\text{thiophene } 2,2\text{-dioxide}$	41.7

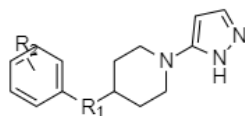
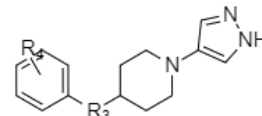


-	-	-	<b>126</b>	R <sub>1</sub> , R <sub>2</sub> = 2,3-dihydro[ <i>b</i> ]thiophene 1,1-dioxide	0
-	-	-	<b>130</b>	 R <sub>1</sub> =	36.0
-	-	-	<b>140</b>	 R <sub>1</sub> =	26.7

<sup>a</sup> Not all compounds with 4-phenyl-1-(1H-pyrazol-5-yl)piperidine core were synthesized.

<sup>b</sup> R<sub>2</sub> = H and R<sub>3</sub> = H when R<sub>2</sub> and R<sub>3</sub> are not defined in the table.

**Appendix Table 6 CYP4 inhibition in RLM for derivatives of UPMP021 and 022**

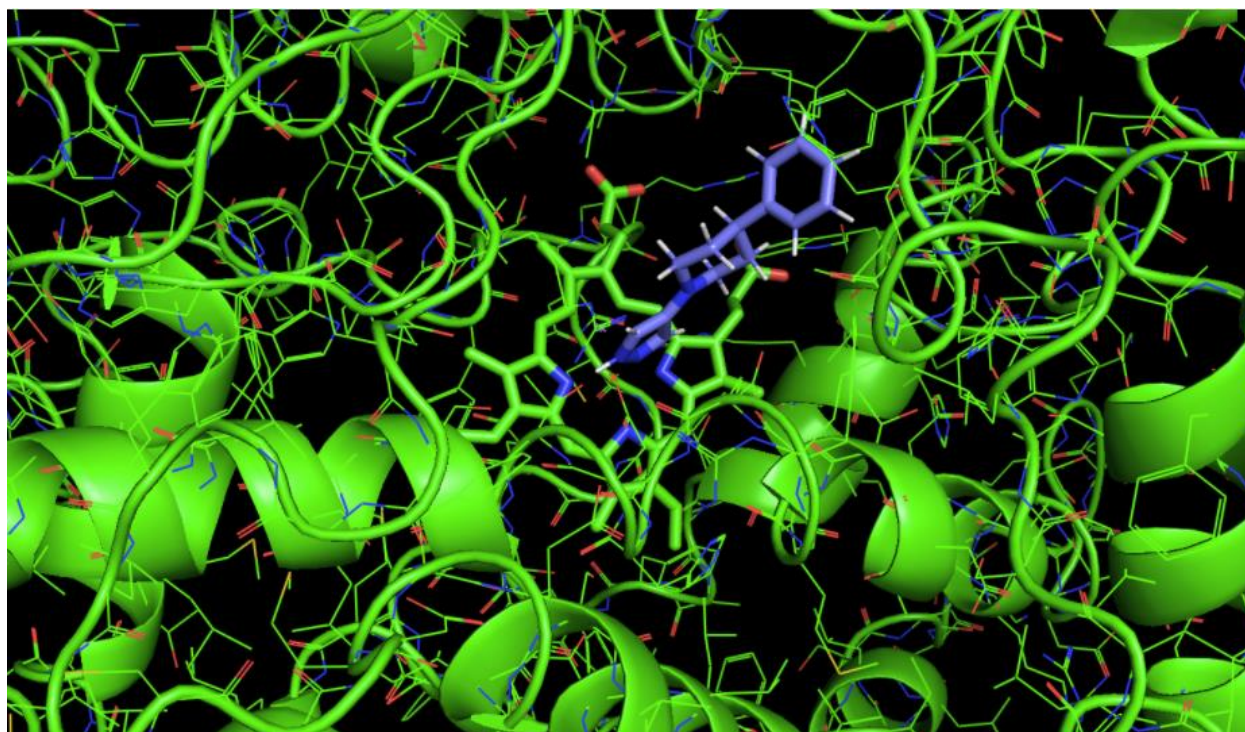



Compd <sup>a</sup> (UPMP)	R <sub>1</sub> , R <sub>2</sub> <sup>b</sup>	% of inhibition in RLM	Compd (UPMP)	R <sub>3</sub> , R <sub>4</sub>	% of inhibition in RLM
<b>021</b>	R <sub>1</sub> = CH <sub>2</sub>	0	<b>022</b>	R <sub>3</sub> = CH <sub>2</sub>	2.39
-	-	-	<b>103</b>	R <sub>3</sub> = CH <sub>2</sub> , R <sub>4</sub> = 4-OMe	4.00
-	-	-	<b>069</b>	R <sub>3</sub> = CH <sub>2</sub> , R <sub>4</sub> = 3-OMe	24.0
-	-	-	<b>142</b>	R <sub>3</sub> = CH <sub>2</sub> , R <sub>4</sub> = 4-CH <sub>3</sub>	59.6
<b>121</b>	R <sub>1</sub> = CH <sub>2</sub> , R <sub>2</sub> = 3-CH <sub>3</sub>	0	<b>118</b>	R <sub>3</sub> = CH <sub>2</sub> , R <sub>4</sub> = 3-CH <sub>3</sub>	13.5
-	-	-	<b>117</b>	R <sub>3</sub> = CH <sub>2</sub> , R <sub>4</sub> = 4-Cl	64.3
<b>115</b>	R <sub>1</sub> = CH <sub>2</sub> , R <sub>2</sub> = 3-Cl	0	<b>114</b>	R <sub>3</sub> = CH <sub>2</sub> , R <sub>4</sub> = 3-Cl	20.8
-	-	-	<b>133</b>	R <sub>3</sub> = CH <sub>2</sub> , R <sub>4</sub> = 4-pyrrolidone	63.6
<b>092</b>	R <sub>1</sub> = S, R <sub>2</sub> = 4-OMe	0	-	-	-
-	-	-	<b>100</b>	R <sub>3</sub> = S, R <sub>4</sub> = 3-OMe	0

-	-	-	<b>104</b>	R <sub>3</sub> = S, R <sub>4</sub> = 4-OMe	42.0
-	-	-	<b>094</b>	R <sub>3</sub> = S, R <sub>4</sub> = 4-F	35.7
-	-	-	<b>116</b>	R <sub>3</sub> = S, R <sub>4</sub> = 2-F	0

<sup>a</sup> Not all compounds with 4-phenyl-1-(1H-pyrazol-5-yl)piperidine core were synthesized.

<sup>b</sup> R<sub>2</sub> = H when R<sub>2</sub> is not defined in the table.



#### Appendix Figure 1 CYP4 homology model and docking of hit compound UPMP019

The hit compound **UPMP019** was positioned in CYP4F2 homology model assuming the coordination of pyrazole with the heme iron.

Previously, a crystal structure with rabbit CYP4B1 - HET0016 complex was reported and the binding of HET0016 in CYP4B1 active site was proposed. With the cis orientation of the N-hydroxyl group of HET0016, the nitrogen coordinates with ferric iron of the heme, the hydroxyl group binds with Thr-314 via hydrogen binding, and the long butyl chain fits in the active site cavity that could potentially increase the selectivity of  $\omega$ -1 hydroxylation (Jennings et al. 2018). A CYP4 homology model was built in our collaborator Dr. David Koes's lab (School of Medicine,

University of Pittsburgh) based on a published crystal structure of rabbit CYP4B1 complexed with octane. In our homology model, the hit compound **UPMP019** was positioned in CYP4F2 homology model assuming the pyrazole moiety coordinating with the heme (Appendix Figure 1). After optimization and validation of the CYP4F2 homology model, it could be applied to screen potential candidates as 20-HETE formation inhibitors, identify potential active binding site in the future to help discover new compounds.

Appendix B Supplementary data for Chapter 4 – PK and PD evaluation of UPMP107 in  
pediatric rats

**Appendix Table 7 Summary of structural model development process**

<b>Model description</b>	<b>AIC</b>
2cmt, additive RES, linear elimination	-
2cmt, proportional RES, linear elimination	1539.2
2cmt, combined RES, linear elimination	1438.0
1cmt, combined RES, linear elimination	1519.7
1cmt, combined RES, saturated elimination	1506.2
2cmt, combined RES, saturated elimination	1433.1

Cmt: compartment; RES: residual error; “-”: model did not converge.

The model selection was based on AIC values. A smaller AIC value supports the selection of the structural model.

**The control stream of UPMP107 popPK model:**

```

$PROBLEM 157 PK
$INPUT C ID TIME DV CONC=DROP LNDV=DROP DOSE WT AMT MDV EVID
$DATA 107_NONMEM_exc.csv IGNORE=C
$SUBROUTINE ADVAN6 TRANS1 TOL = 6
$MODEL
NCOMP = 2
COMP = (CENTRAL)
COMP = (PERIPHERAL)
$PK
V1 = THETA(1)*EXP(ETA(1))
KM = THETA(2)
VMAX = THETA(3)
Q = THETA(4)*EXP(ETA(2))
V2 = THETA(5)
S1 = V1/1000 ;S1 = V1/1000 ;DOSE in mg, CONC in ng/ml(ug/L)
K12 = Q/V1
K21 = Q/V2

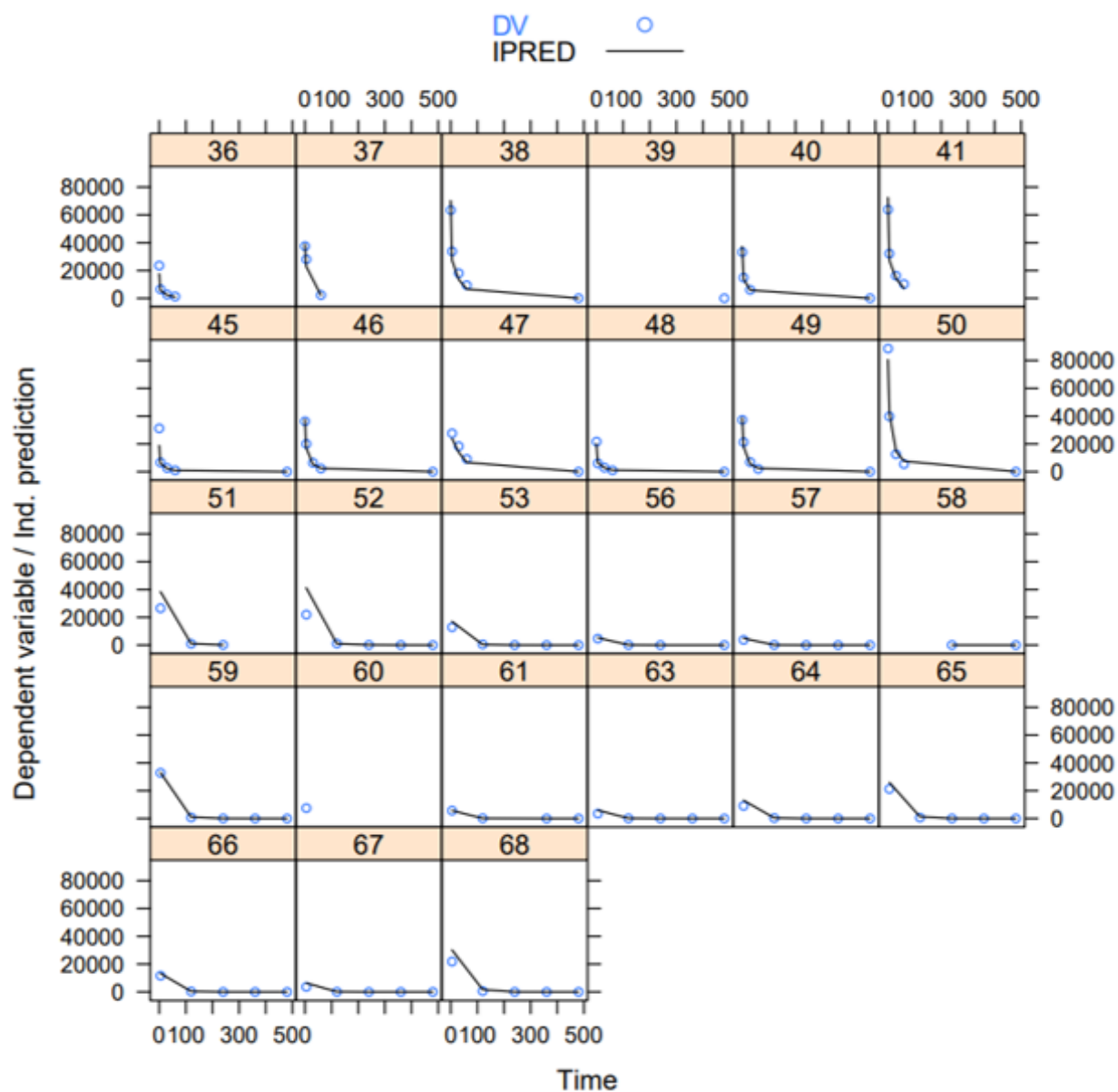
$ERROR
IPRED = F
W = SQRT(IPRED**2*SIGMA(1)+SIGMA(2))
IRES = DV- IPRED

```

```

Y = IPRED + IPRED* EPS(1) + EPS(2)
IWRES = IRES/W
$THETA
(0.00001,0.014,10) ; V1 in L
(0.00001, 47, 100000) ; Km
(0.00001,0.02,10) ; Vmax in L/min
(0.00001, 0.0056, 10) ;Q
(0.00001, 0.0171, 10) ;V2
$OMEGA
0.1 ; V
0.5 ; Q
$DES
C1 = A(1)/S1
DADT(1) = -K12*A(1) +K21*A(2) - (VMAX * A(1) /( KM*V1 + A(1) )
)
DADT(2) = K12*A(1) -K21*A(2)
$SIGMA
0.3 ; prop RV
300 ; additive RV
$COVARIANCE PRINT=E MATRIX=R
$EST METHOD=1 INTER MAXEVAL=9999 NOABORT SIG=2 PRINT=1 POSTHOC
$TABLE ID TIME DOSE MDV EVID PRED IPRED IRES IWRES CWRES CWRESI
ONEHEADER NOPRINT FILE=sdtab15
$TABLE ID V1 KM VMAX Q V2 ONEHEADER NOAPPEND NOPRINT FILE=patab15

```



**Appendix Figure 2 Observed concentrations versus individual predicted concentrations for each animal**

The blue dots represent the observed concentrations, the black line connects the individual predicted concentrations. Overall, there is good agreement in the predicted values and the observed values.

## Appendix C Supplementary data for Chapter 5 - Propofol popPK model

**Appendix Table 8 Summary of structural model development process**

Model description	AIC	Theta precision (%RSE)				Eta precision (%RSE)				Epsilon precision (%RSE)	
		CL	V1	Q	V2	IIV CL	IIV V1	IIV Q	IIV V2	prop	add
1cmt, CL~V, prop RES	3213.8	1	2			19	19			13	
1cmt, CL~V, additive RES	3454.2	18	27			26	27				7
1cmt, CL~V, combined RES	3207.0	13	18			18	18			21	305
2cmt, combined RES, no covariance	3162.9	35	156	18	27	10	5707	0	0	15	154
2cmt, combined RES, IIV V1 = 0, no covariance	3160.9	24	32	18	17	54		29	16	15	171
2cmt, combined RES, IIV V1 =0, CL~Q	3161.2	20	53	21	18	26		43	17	15	101
2cmt, combined RES, IIV V1 =0, CL~V2	3161.1	41	906	44	19	151		66	15	19	322
2cmt, combined RES, IIV V1 =0, block (3)	3186.4	94	9807	517	299	82		372	238	17	281
2cmt, combined RES, CL~V1, Q~V2	3166.6	30	102	51	18	58	503	162	14	15	33
2cmt, combined RES, CL~Q, V1~V2	3165.2	23	62	19	20	47	272	82	18	17	110
2cmt, combined RES, block(4)	3159.7	41	687	45	34	34	259	89	86	15	273

RES: residual error;

“~”: covariance between two parameters;

IIV: interindividual variability;

Block: block structure of the covariance matrix;

Prop: proportional residual error

Add: additive residual error

### Control stream of the final model:

```
$PROBLEM  PROP PK
$INPUT C ID DV LNDV=DROP DATE=DROP TIME TSFD TSLD DOSE MDV EVIDRATE
DUR SEX AMT aDUR SEVL MILDL LIVER BIL MAP SFLV SFCV WT AGE HT BMI CR
RACE SMOKE SFLVEN SFCVEN SFCNSEN SFRENALEN APACHE
$DATA  df_covariates.csv IGNORE=C

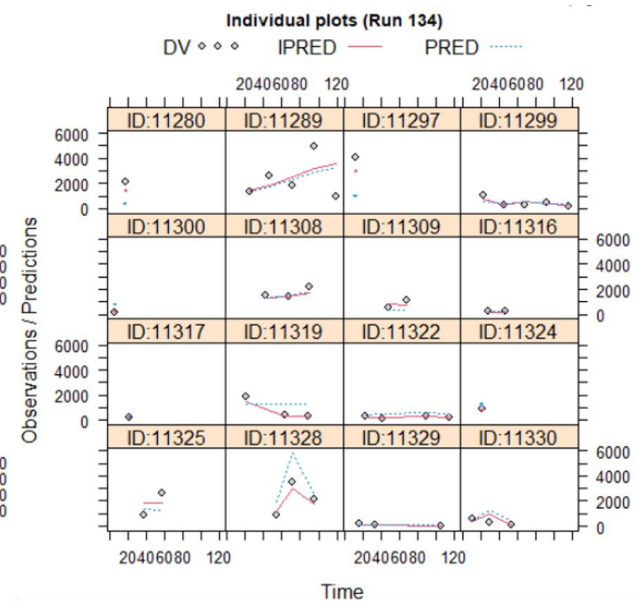
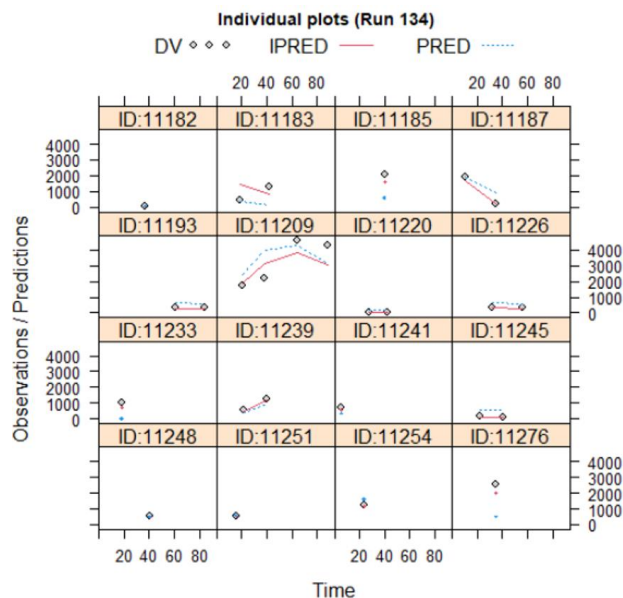
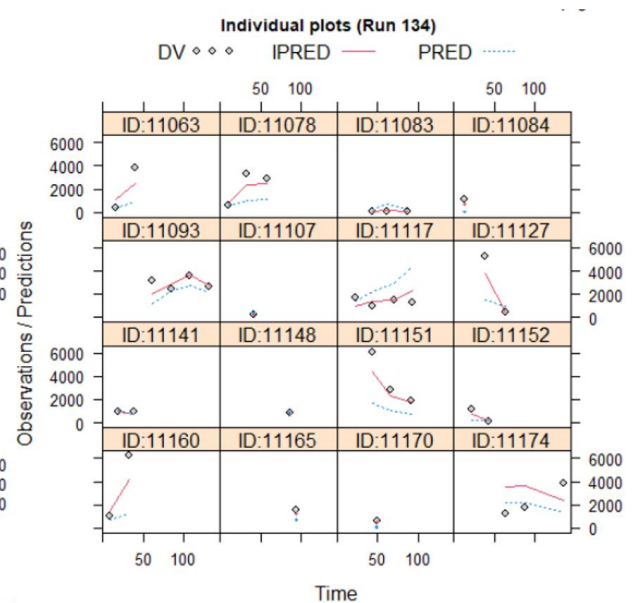
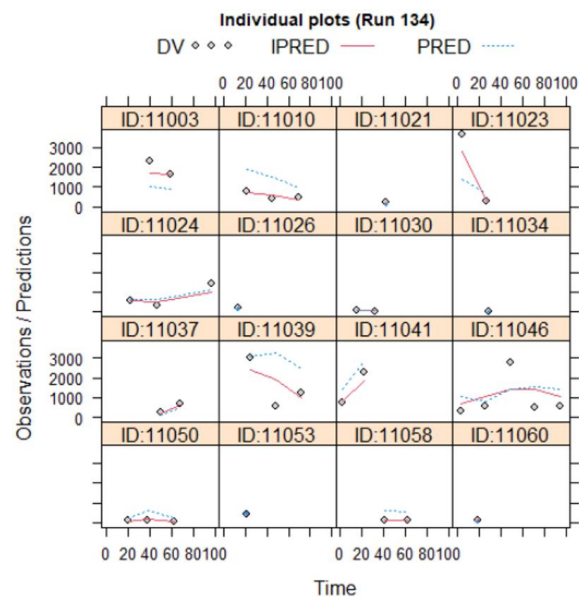
$SUBROUTINE  ADVAN3 TRANS4
$PK
CL = THETA(1)*EXP(ETA(1)) ;exponential model
V1 = THETA(2)
Q = THETA(3)*EXP(ETA(2))
IF (SFLV.LE.3) TVV2 = THETA(4)
IF (SFLV.GE.4) TVV2 = THETA(4)+THETA(5)*SFLV
V2 = TVV2*EXP(ETA(3))
S1 = V1/1000 ;DOSE in mg, CONC in ng/ml(ug/L)
$ERROR
IPRED = F
W = SQRT(IPRED**2*SIGMA(1)+SIGMA(2))
IRES = DV- IPRED
Y = IPRED + IPRED* EPS(1) + EPS(2)
IWRES = IRES/W
$THETA
(0.001, 40, 1000) ;CL in L/h
(0.001, 20, 1000) ;V1 in L
(0.001, 300, 1000) ;Q in L/h
(0.001, 8500, 100000) ;V2 in L
(-10000, -200, 0) ;SOFA on V2
$OMEGA BLOCK(2)
1.5 ; CL
0.5 1 ;Q
$OMEGA
1.9; V2
$SIGMA
(0, 0.18,10) ;prop RV
(0, 150,1000) ;add RV
$COVARIANCE PRINT=E MATRIX=R
$EST METHOD=1 INTER MAXEVAL=9999 NOABORT SIG=2 PRINT=1 POSTHOC
$TABLE ID TIME DOSE MDV EVID RATE IPRED IWRES CWRES CWRESI ONEHEADER
NOPRINT FILE=sdtab230
```

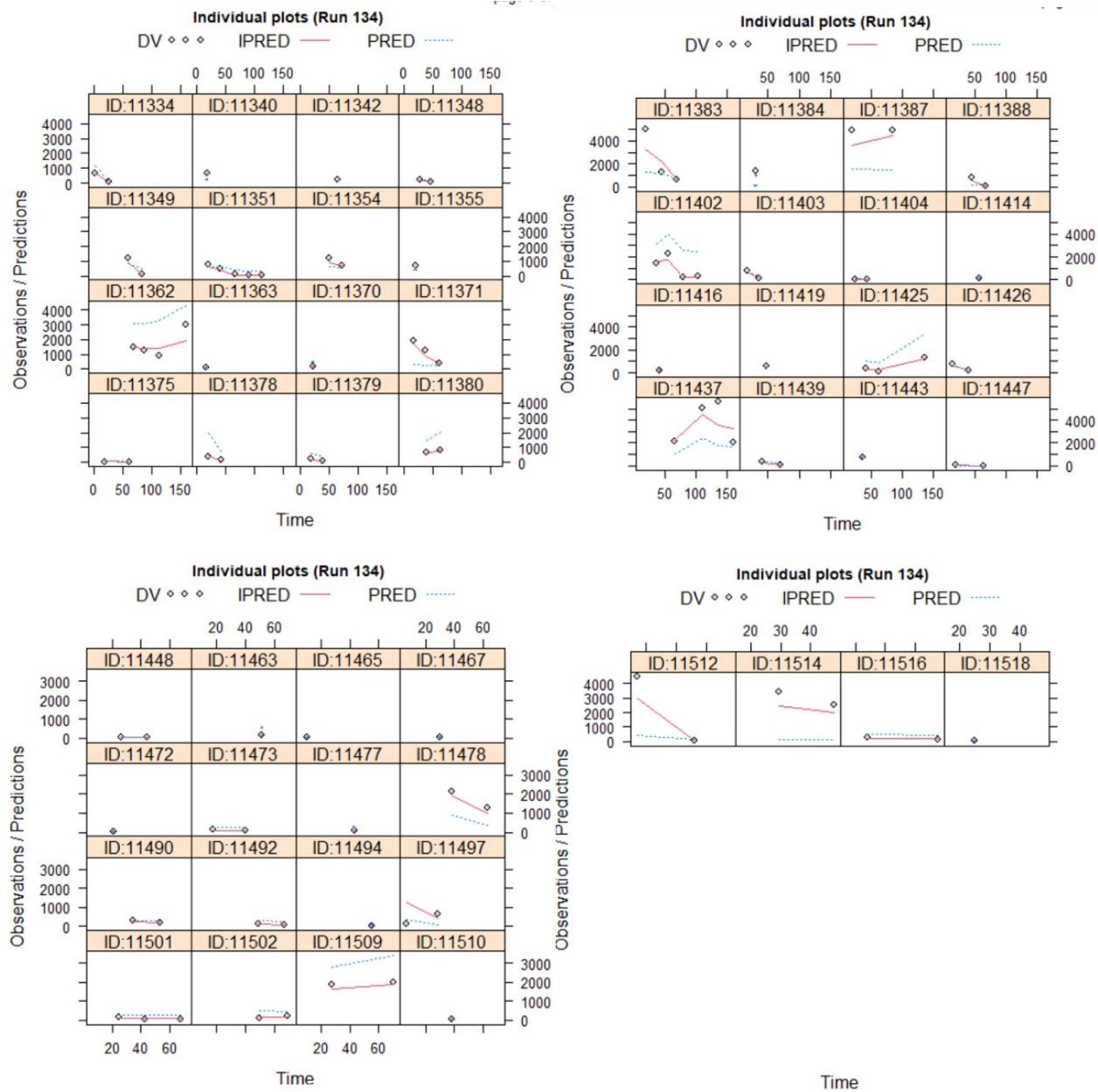


\$TABLE ID WT AGE HT BMI CR BIL MAP ONEHEADER NOAPPEND NOPRINT  
FILE=cotab134

\$TABLE ID SEX SEVL MILDL LIVER SFLV SFCV RACE SMOKE SFLVEN SFCVEN  
SFCNSN SFRENALEN APACHE ONEHEADER NOAPPEND NOPRINT FILE=catab134

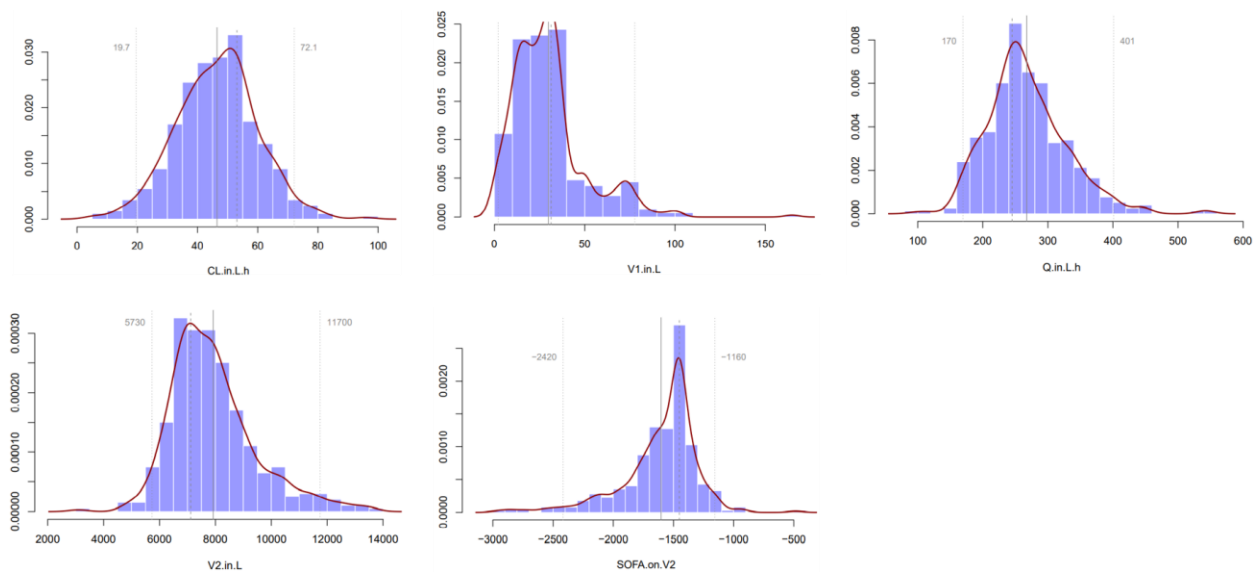
\$TABLE ID CL V1 V2 Q ETA1 ETA2 ETA3 ONEHEADER NOAPPEND NOPRINT  
FILE=patab230





**Appendix Figure 3 Individual plots of observed vs. predicted concentrations**

The open circles represent the observed concentrations, the red solid line connects the population predicted concentrations. The blue dashed line connects the individual predicted concentrations.



**Appendix Figure 4** Frequency distribution histograms of parameter mean estimates from bootstrap analysis (n=1000)

## Bibliography

- Absorption Systems. (2020). "BBB penetration Potential Determined - MDR1-MDCK Cell Monolayers." Retrieved Dec 30, 2020, from <https://www.absorption.com/shop/all-services/express-in-vitro-services/permeability/cell-based/ea203-blood-brain-barrier-mdr1-mdck/>.
- Adams Harold, P., et al. (2007). "Guidelines for the Early Management of Adults With Ischemic Stroke." *Circulation* **115**(20): e478-e534.
- Alavijeh, M. S., et al. (2005). "Drug metabolism and pharmacokinetics, the blood-brain barrier, and central nervous system drug discovery." *NeuroRx* **2**(4): 554-571.
- Alavijeh, M. S., et al. (2004). "The pivotal role of drug metabolism and pharmacokinetics in the discovery and development of new medicines." *IDrugs* **7**(8): 755-763.
- Albers, G. W., et al. (2006). "Magnetic resonance imaging profiles predict clinical response to early reperfusion: the diffusion and perfusion imaging evaluation for understanding stroke evolution (DEFUSE) study." *Ann Neurol* **60**(5): 508-517.
- Alexanian, A., et al. (2012). "20-HETE-producing enzymes are up-regulated in human cancers." *Cancer Genomics Proteomics* **9**(4): 163-169.
- Alonso-Galicia, M., et al. (1997). "Inhibition of 20-HETE production contributes to the vascular responses to nitric oxide." *Hypertension* **29**(1 Pt 2): 320-325.
- Alonso-Galicia, M., et al. (1999). "20-HETE agonists and antagonists in the renal circulation." *Am J Physiol* **277**(5): F790-796.
- Amaral, S. L., et al. (2003). "CYP4A metabolites of arachidonic acid and VEGF are mediators of skeletal muscle angiogenesis." *Am J Physiol Heart Circ Physiol* **284**(5): H1528-1535.
- Arnold, C., et al. (2010). "Arachidonic acid-metabolizing cytochrome P450 enzymes are targets of {omega}-3 fatty acids." *J Biol Chem* **285**(43): 32720-32733.
- Atkins, D. L., et al. (2009). "Epidemiology and outcomes from out-of-hospital cardiac arrest in children: the Resuscitation Outcomes Consortium Epistry-Cardiac Arrest." *Circulation* **119**(11): 1484-1491.
- Attwell, D., et al. (2010). "Glial and neuronal control of brain blood flow." *Nature* **468**(7321): 232-243.
- Baba, S., et al. (1963). "The mechanism of enzymatic hydroxylation at an enolizable position." *Steroids* **1**(2): 151-156.
- Baer, B. R., et al. (2006). "CYP4B1: An Enigmatic P450 at the Interface between Xenobiotic and Endobiotic Metabolism." *Drug Metabolism Reviews* **38**(3): 451-476.
- Bai, Q.-K., et al. (2019). "Treating ischaemic stroke with intravenous tPA beyond 4.5 hours under the guidance of a MRI DWI/T2WI mismatch was safe and effective." *Stroke and vascular neurology* **4**(1): 8-13.
- Bailie, G. R., et al. (1992). "Pharmacokinetics of Propofol During and After Long Term Continuous Infusion for Maintenance of Sedation in ICU Patients." *British Journal of Anaesthesia* **68**(5): 486-491.
- Balami, J. S., et al. (2011). "Neurological complications of acute ischaemic stroke." *Lancet Neurol* **10**(4): 357-371.

Baranczewski, P., et al. (2006). "Introduction to in vitro estimation of metabolic stability and drug interactions of new chemical entities in drug discovery and development." Pharmacol Rep **58**(4): 453-472.

Barr, J., et al. (2001). "Propofol Dosing Regimens for ICU Sedation Based upon an Integrated Pharmacokinetic– Pharmacodynamic Model." Anesthesiology **95**(2): 324-333.

Billington, S., et al. (2019). "Interindividual and Regional Variability in Drug Transporter Abundance at the Human Blood–Brain Barrier Measured by Quantitative Targeted Proteomics." Clinical Pharmacology & Therapeutics **106**(1): 228-237.

Blobaum, A. L., et al. (2013). "Heterotropic activation of the midazolam hydroxylase activity of CYP3A by a positive allosteric modulator of mGlu5: in vitro to in vivo translation and potential impact on clinically relevant drug-drug interactions." Drug Metab Dispos **41**(12): 2066-2075.

Blomqvist, P., et al. (1985). "Ischemic Brain Damage in Rats following Cardiac Arrest Using a Long-Term Recovery Model." Journal of Cerebral Blood Flow & Metabolism **5**(3): 420-431.

Blussé van Oud-Alblas, H. J., et al. (2019). "Population pharmacokinetic-pharmacodynamic model of propofol in adolescents undergoing scoliosis surgery with intraoperative wake-up test: a study using Bispectral index and composite auditory evoked potentials as pharmacodynamic endpoints." BMC anesthesiology **19**(1): 15-15.

Boobis, A. R., et al. (1990). "Species variation in the response of the cytochrome P-450-dependent monooxygenase system to inducers and inhibitors." Xenobiotica **20**(11): 1139-1161.

Borrello, S., et al. (1986). "Restoration of hydroperoxide-dependent lipid peroxidation by 3-methylcholanthrene induction of cytochrome P-448 in hepatoma microsomes." FEBS Letters **209**(2): 305-310.

Boullin, D. J., et al. (1979). "Responses of human and baboon arteries to prostaglandin endoperoxides and biologically generated and synthetic prostacyclin: their relevance to cerebral arterial spasm in man." British Journal of Clinical Pharmacology **7**(2): 139-147.

Bowman, C. M., et al. (2019). "In Vitro-In Vivo Extrapolation and Hepatic Clearance-Dependent Underprediction." J Pharm Sci **108**(7): 2500-2504.

Bruns, R. F., et al. (2012). "Rules for Identifying Potentially Reactive or Promiscuous Compounds." Journal of Medicinal Chemistry **55**(22): 9763-9772.

Buunk, G., et al. (1996). "Cerebral vasoconstriction in comatose patients resuscitated from a cardiac arrest?" Intensive Care Med **22**(11): 1191-1196.

Buunk, G., et al. (2000). "Cerebral blood flow after cardiac arrest." Neth J Med **57**(3): 106-112.

Cahill, J., et al. (2006). "Mechanisms of early brain injury after subarachnoid hemorrhage." J Cereb Blood Flow Metab **26**(11): 1341-1353.

CaJacob, C. A., et al. (1986). "Mechanism-based in vivo inactivation of lauric acid hydroxylases." Biochemistry **25**(16): 4705-4711.

Caldwell, G. W., et al. (2004). "Allometric scaling of pharmacokinetic parameters in drug discovery: Can human CL, Vss and t1/2 be predicted from in-vivo rat data?" European Journal of Drug Metabolism and Pharmacokinetics **29**(2): 133-143.

Capdevila, J., et al. (1981). "Liver microsomal cytochrome P-450 and the oxidative metabolism of arachidonic acid." Proceedings of the National Academy of Sciences **78**(9): 5362.

Capdevila, J., et al. (1988). "Inhibitors of cytochrome P-450-dependent arachidonic acid metabolism." Arch Biochem Biophys **261**(2): 257-263.

Carr, K. R., et al. (2013). "Inflammation, cerebral vasospasm, and evolving theories of delayed cerebral ischemia." Neurol Res Int **2013**: 506584.

Cavasotto, C. N., et al. (2009). "Homology modeling in drug discovery: current trends and applications." Drug Discov Today **14**(13-14): 676-683.

Cerchiari, E. L., et al. (1987). "Protective effects of combined superoxide dismutase and deferoxamine on recovery of cerebral blood flow and function after cardiac arrest in dogs." Stroke **18**(5): 869-878.

Chang, T. K., et al. "Differential inhibition and inactivation of human CYP1 enzymes by trans-resveratrol: evidence for mechanism-based inactivation of CYP1A2." (0022-3565 (Print)).

Chen, P., et al. (2005). "Inhibitors of cytochrome P450 4A suppress angiogenic responses." Am J Pathol **166**(2): 615-624.

Chen, S., et al. (2014). "Controversies and evolving new mechanisms in subarachnoid hemorrhage." Prog Neurobiol **115**: 64-91.

Chen, Z. H., et al. (2016). "An improved substrate cocktail for assessing direct inhibition and time-dependent inhibition of multiple cytochrome P450s." Acta Pharmacol Sin **37**(5): 708-718.

Chiba, M., et al. (2009). "Prediction of hepatic clearance in human from in vitro data for successful drug development." AAPS J **11**(2): 262-276.

Chiota, N. A., et al. (2011). "Hypoxic-ischemic brain injury and prognosis after cardiac arrest." Continuum (Minneapolis, Minn) **17**(5 Neurologic Consultation in the Hospital): 1094-1118.

Cho, S. S., et al. (2019). "Clazosentan for Aneurysmal Subarachnoid Hemorrhage: An Updated Meta-Analysis with Trial Sequential Analysis." World Neurosurg **123**: 418-424 e413.

Choi, Y. J., et al. (2018). "Discovery of rubiarbonone C as a selective inhibitor of cytochrome P450 4F enzymes." Archives of Toxicology **92**(11): 3325-3336.

Christmas, P., et al. (2001). "Alternative splicing determines the function of CYP4F3 by switching substrate specificity." J Biol Chem **276**(41): 38166-38172.

Chuang, S. S., et al. (2004). "CYP2U1, a novel human thymus- and brain-specific cytochrome P450, catalyzes omega- and (omega-1)-hydroxylation of fatty acids." J Biol Chem **279**(8): 6305-6314.

Crago Elizabeth, A., et al. (2011). "Cerebrospinal Fluid 20-HETE Is Associated With Delayed Cerebral Ischemia and Poor Outcomes After Aneurysmal Subarachnoid Hemorrhage." Stroke **42**(7): 1872-1877.

Dai, D., et al. (2016). "Epidemiology of Polypharmacy and Potential Drug-Drug Interactions Among Pediatric Patients in ICUs of U.S. Children's Hospitals." Pediatric critical care medicine : a journal of the Society of Critical Care Medicine and the World Federation of Pediatric Intensive and Critical Care Societies **17**(5): e218-e228.

Dakarapu, R., et al. (2019). "19-Hydroxyeicosatetraenoic acid analogs: Antagonism of 20-hydroxyeicosatetraenoic acid-induced vascular sensitization and hypertension." Bioorganic & Medicinal Chemistry Letters **29**(19): 126616.

Darvas, F., et al. (2002). "In Silico and Ex silico ADME approaches for drug discovery." Curr Top Med Chem **2**(12): 1287-1304.

Davies, B., et al. (1993). "Physiological parameters in laboratory animals and humans." Pharm Res **10**(7): 1093-1095.

De Buck, S. S., et al. (2007). "Prediction of human pharmacokinetics using physiologically based modeling: a retrospective analysis of 26 clinically tested drugs." Drug Metab Dispos **35**(10): 1766-1780.

De Paepe, P., et al. (2002). "Pharmacokinetic and Pharmacodynamic Considerations When Treating Patients with Sepsis and Septic Shock." Clinical Pharmacokinetics **41**(14): 1135-1151.

Deb, P., et al. (2010). "Pathophysiologic mechanisms of acute ischemic stroke: An overview with emphasis on therapeutic significance beyond thrombolysis." Pathophysiology **17**(3): 197-218.

Deng, S., et al. (2010). "CYP4F2 gene V433M polymorphism is associated with ischemic stroke in the male Northern Chinese Han population." Progress in Neuro-Psychopharmacology and Biological Psychiatry **34**(4): 664-668.

Devlin, J. W., et al. (2018). "Clinical Practice Guidelines for the Prevention and Management of Pain, Agitation/Sedation, Delirium, Immobility, and Sleep Disruption in Adult Patients in the ICU." Crit Care Med **46**(9): e825-e873.

Dhar, R., et al. (2012). "Relationship Between Angiographic Vasospasm and Regional Hypoperfusion in Aneurysmal Subarachnoid Hemorrhage." Stroke **43**(7): 1788-1794.

Di, L., et al. (2004). "Experimental design on single-time-point high-throughput microsomal stability assay." J Pharm Sci **93**(6): 1537-1544.

Di, L., et al. (2005). "Development and application of high throughput plasma stability assay for drug discovery." Int J Pharm **297**(1-2): 110-119.

Di, L., et al. (2003). "Optimization of a higher throughput microsomal stability screening assay for profiling drug discovery candidates." J Biomol Screen **8**(4): 453-462.

Di, L., et al. (2015). "Addressing the challenges of low clearance in drug research." AAPS J **17**(2): 352-357.

Donnelly, M. K., et al. (2015). "20-HETE is associated with unfavorable outcomes in subarachnoid hemorrhage patients." Journal of cerebral blood flow and metabolism : official journal of the International Society of Cerebral Blood Flow and Metabolism **35**(9): 1515-1522.

Donnelly, M. K., et al. (2015). "20-HETE is Associated with Unfavorable Outcomes in Subarachnoid Hemorrhage Patients." Journal of Cerebral Blood Flow & Metabolism **35**(9): 1515-1522.

Drolet, B., et al. (2017). "Altered Protein Expression of Cardiac CYP2J and Hepatic CYP2C, CYP4A, and CYP4F in a Mouse Model of Type II Diabetes-A Link in the Onset and Development of Cardiovascular Disease?" Pharmaceutics **9**(4): 44.

Dunn, K. M., et al. (2008). "Elevated production of 20-HETE in the cerebral vasculature contributes to severity of ischemic stroke and oxidative stress in spontaneously hypertensive rats." Am J Physiol Heart Circ Physiol **295**(6): H2455-2465.

Duraiaraj, P., et al. (2019). "Functional characterization and mechanistic modeling of the human cytochrome P450 enzyme CYP4A22." FEBS Letters **593**(16): 2214-2225.

Durrant, J. C., et al. (2015). "Rescue therapy for refractory vasospasm after subarachnoid hemorrhage." Curr Neurol Neurosci Rep **15**(2): 521.

Durukan, A., et al. (2007). "Acute ischemic stroke: overview of major experimental rodent models, pathophysiology, and therapy of focal cerebral ischemia." Pharmacol Biochem Behav **87**(1): 179-197.

Eagling, V. A., et al. (1998). "Differential selectivity of cytochrome P450 inhibitors against probe substrates in human and rat liver microsomes." British journal of clinical pharmacology **45**(2): 107-114.

Ebinger, M., et al. (2012). "MRI-based intravenous thrombolysis in stroke patients with unknown time of symptom onset." Eur J Neurol **19**(2): 348-350.

Edson, K. Z., et al. (2013). "CYP4 enzymes as potential drug targets: focus on enzyme multiplicity, inducers and inhibitors, and therapeutic modulation of 20-hydroxyeicosatetraenoic acid (20-HETE) synthase and fatty acid  $\omega$ -hydroxylase activities." Current topics in medicinal chemistry **13**(12): 1429-1440.



Eiichi, T., et al. (2004). "Continuous Elevation of Intracellular Ca<sup>2+</sup> Is Essential for the Development of Cerebral Vasospasm." Current Vascular Pharmacology **2**(1): 13-21.

El-Sherbeni, A. A., et al. (2013). "Determination of the dominant arachidonic acid cytochrome p450 monooxygenases in rat heart, lung, kidney, and liver: protein expression and metabolite kinetics." AAPS J **15**(1): 112-122.

El-Sherbeni, A. A., et al. (2016). "Repurposing Resveratrol and Fluconazole To Modulate Human Cytochrome P450-Mediated Arachidonic Acid Metabolism." Mol Pharm **13**(4): 1278-1288.

Elbarbry, F., et al. (2014). "Modulation of arachidonic Acid metabolism in the rat kidney by sulforaphane: implications for regulation of blood pressure." ISRN Pharmacol **2014**: 683508.

Eleveld, D. J., et al. (2018). "Pharmacokinetic&#x2013;pharmacodynamic model for propofol for broad application in anaesthesia and sedation." British Journal of Anaesthesia **120**(5): 942-959.

Elkhatali, S., et al. (2015). "19-Hydroxyeicosatetraenoic acid and isoniazid protect against angiotensin II-induced cardiac hypertrophy." Toxicol Appl Pharmacol **289**(3): 550-559.

Ellis, E. F., et al. (1990). "Dilation of cerebral arterioles by cytochrome P-450 metabolites of arachidonic acid." American Journal of Physiology-Heart and Circulatory Physiology **259**(4): H1171-H1177.

Ergul, A., et al. (2012). "Angiogenesis: a harmonized target for recovery after stroke." Stroke **43**(8): 2270-2274.

Eun, H. S., et al. (2018). "Profiling cytochrome P450 family 4 gene expression in human hepatocellular carcinoma." Mol Med Rep **18**(6): 4865-4876.

Eurofins Discovery. (2020). "SafetyScreen44 Panel, Cerep." Retrieved Dec 30, 2020, from <https://www.eurofinsdiscoveryservices.com/catalogmanagement/viewitem/SafetyScreen44-Panel-Cerep/P270>.

Falck, J. R., et al. (1997). "Eicosanoid biosynthesis: differential inhibition of cytochrome P450 epoxigenase and  $\omega$ -hydroxylase." Bioorganic & Medicinal Chemistry Letters **7**(23): 3053-3056.

Falck, J. R., et al. (1990). [40] Synthesis of epoxyeicosatrienoic acids and heteroatom analogs. Methods in Enzymology. R. C. Murphy and F. A. Fitzpatrick, Academic Press. **187**: 357-364.

Fan, F., et al. (2015). "Impaired myogenic response and autoregulation of cerebral blood flow is rescued in CYP4A1 transgenic Dahl salt-sensitive rat." American journal of physiology. Regulatory, integrative and comparative physiology **308**(5): R379-R390.

Fava, C., et al. (2008). "The V433M Variant of the CYP4F2 Is Associated With Ischemic Stroke in Male Swedes Beyond Its Effect on Blood Pressure." Hypertension **52**(2): 373-380.

FDA. (2017). "DIPRIVAN." Retrieved Jan 10, 2021, from [https://www.accessdata.fda.gov/drugsatfda\\_docs/label/2017/019627s066lbl.pdf](https://www.accessdata.fda.gov/drugsatfda_docs/label/2017/019627s066lbl.pdf).

FDA, U. (2017). In Vitro Metabolism and Transporter-Mediated Drug-Drug Interaction Studies-Guidance for Industry.

FDA, U. (2018). Bioanalytical Method Validation Guidance for Industry.

FDA, U. (2020). In Vitro Drug Interaction Studies — Cytochrome P450 Enzyme- and Transporter-Mediated Drug Interactions Guidance for Industry.

Fer, M., et al. (2008). "Cytochromes P450 from family 4 are the main omega hydroxylating enzymes in humans: CYP4F3B is the prominent player in PUFA metabolism." Journal of Lipid Research **49**(11): 2379-2389.

Fink, E. L., et al. (2016). "Unchanged pediatric out-of-hospital cardiac arrest incidence and survival rates with regional variation in North America." Resuscitation **107**: 121-128.

Fisher, M., et al. (2013). "Advanced imaging to extend the therapeutic time window of acute ischemic stroke." Ann Neurol **73**(1): 4-9.



Fisher, M. B., et al. (1998). "Positional specificity of rabbit CYP4B1 for omega-hydroxylation of short-medium chain fatty acids and hydrocarbons." Biochem Biophys Res Commun **248**(2): 352-355.

Fogel, D. B. (2018). "Factors associated with clinical trials that fail and opportunities for improving the likelihood of success: A review." Contemp Clin Trials Commun **11**: 156-164.

Folino, E. M. A. O. S. L. J. P. T. B. (2020). "Propofol." Retrieved Jan 10, 2021, from <https://www.ncbi.nlm.nih.gov/books/NBK430884/>.

Fraser, G. L., et al. (2013). "Benzodiazepine versus nonbenzodiazepine-based sedation for mechanically ventilated, critically ill adults: a systematic review and meta-analysis of randomized trials." Crit Care Med **41**(9 Suppl 1): S30-38.

Frenkel, C., et al. (1995). "Pharmacokinetics and pharmacodynamics of propofol/alfentanil infusions for sedation in ICU patients." Intensive Care Med **21**(12): 981-988.

Fu, Z., et al. (2008). "Haplotype-based case study of human CYP4A11 gene and cerebral infarction in Japanese subject." Endocrine **33**(2): 215-222.

Fu, Z., et al. (2008). "A Haplotype of the CYP4F2 Gene is Associated With Cerebral Infarction in Japanese Men." American Journal of Hypertension **21**(11): 1216-1223.

Gabrielsson, J., et al. (2019). "Dose-Response-Time Data Analysis: An Underexploited Trinity." Pharmacol Rev **71**(1): 89-122.

García Guzzo, M. E., et al. (2020). "Deep sedation using propofol target-controlled infusion for gastrointestinal endoscopic procedures: a retrospective cohort study." BMC Anesthesiology **20**(1): 195.

Garcia, V., et al. (2017). "20-HETE Signals Through G-Protein-Coupled Receptor GPR75 (Gq) to Affect Vascular Function and Trigger Hypertension." Circ Res **120**(11): 1776-1788.

Garcia, V., et al. (2015). "20-SOLA, a Novel Water Soluble 20-HETE Antagonist, Reduces Blood Pressure Through Regulation of Vascular ACE Expression via an IKK Dependent Pathway." The FASEB Journal **29**(1\_supplement): 647.649.

Gebremedhin, D., et al. (2000). "Production of 20-HETE and its role in autoregulation of cerebral blood flow." Circ Res **87**(1): 60-65.

Gebremedhin, D., et al. (1998). "Cat cerebral arterial smooth muscle cells express cytochrome P450 4A2 enzyme and produce the vasoconstrictor 20-HETE which enhances L-type Ca<sup>2+</sup> current." The Journal of physiology **507** ( Pt 3)(Pt 3): 771-781.

Gebremedhin, D., et al. (1992). "Mechanism of action of cerebral epoxyeicosatrienoic acids on cerebral arterial smooth muscle." American Journal of Physiology-Heart and Circulatory Physiology **263**(2): H519-H525.

Geocadin, R. G., et al. (2008). "Management of brain injury after resuscitation from cardiac arrest." Neurol Clin **26**(2): 487-506, ix.

Gleeson, M. P. (2008). "Generation of a set of simple, interpretable ADMET rules of thumb." J Med Chem **51**(4): 817-834.

Gonzalez-Fernandez, E., et al. (2020). "20-HETE Enzymes and Receptors in the Neurovascular Unit: Implications in Cerebrovascular Disease." Front Neurol **11**: 983.

Gonzalez-Fernandez, E., et al. (2019). "Localization of the CYP4A Enzymes that Produce 20-HETE and the 20-HETE Receptor in the Brain." The FASEB Journal **33**(S1): 500.512-500.512.

Gourley, J. K., et al. (1984). "Characteristics of reactive hyperemia in the cerebral circulation." American Journal of Physiology-Heart and Circulatory Physiology **246**(1): H52-H58.

Grabowski, H., et al. (2002). "Returns on research and development for 1990s new drug introductions." Pharmacoeconomics **20** Suppl 3: 11-29.

Grimm, S. W., et al. (2009). "The conduct of in vitro studies to address time-dependent inhibition of drug-metabolizing enzymes: a perspective of the pharmaceutical research and manufacturers of America." Drug Metab Dispos **37**(7): 1355-1370.

Guo, A. M., et al. (2007). "Activation of vascular endothelial growth factor through reactive oxygen species mediates 20-hydroxyeicosatetraenoic acid-induced endothelial cell proliferation." J Pharmacol Exp Ther **321**(1): 18-27.

Guo, A. M., et al. (2009). "20-HETE can act as a nonhypoxic regulator of HIF-1alpha in human microvascular endothelial cells." Am J Physiol Heart Circ Physiol **297**(2): H602-613.

Hacke, W., et al. (2008). "Thrombolysis with alteplase 3 to 4.5 hours after acute ischemic stroke." N Engl J Med **359**(13): 1317-1329.

Hamberg, M., et al. (1971). "-Oxidation of fatty acids. I. Mechanism of microsomal 1- and 2-hydroxylation." J Biol Chem **246**(24): 7411-7416.

Harder, D. R., et al. (1994). "Formation and action of a P-450 4A metabolite of arachidonic acid in cat cerebral microvessels." American Journal of Physiology-Heart and Circulatory Physiology **266**(5): H2098-H2107.

Harder, D. R., et al. (2011). "Pressure-induced myogenic tone and role of 20-HETE in mediating autoregulation of cerebral blood flow." Am J Physiol Heart Circ Physiol **300**(5): H1557-1565.

Hardwick, J. P. (2008). "Cytochrome P450 omega hydroxylase (CYP4) function in fatty acid metabolism and metabolic diseases." Biochem Pharmacol **75**(12): 2263-2275.

Harmon, S. D., et al. (2006). "Oxygenation of omega-3 fatty acids by human cytochrome P450 4F3B: effect on 20-hydroxyeicosatetraenoic acid production." Prostaglandins Leukot Essent Fatty Acids **75**(3): 169-177.

Hellinger, E., et al. (2012). "Comparison of brain capillary endothelial cell-based and epithelial (MDCK-MDR1, Caco-2, and VB-Caco-2) cell-based surrogate blood-brain barrier penetration models." Eur J Pharm Biopharm **82**(2): 340-351.

Hirani, V., et al. (2008). "Expression of CYP4F2 in human liver and kidney: assessment using targeted peptide antibodies." Arch Biochem Biophys **478**(1): 59-68.

Hoch, U., et al. (2000). "Structural determination of the substrate specificities and regioselectivities of the rat and human fatty acid omega-hydroxylases." Arch Biochem Biophys **373**(1): 63-71.

Honda Malca, S., et al. (2012). "Bacterial CYP153A monooxygenases for the synthesis of omega-hydroxylated fatty acids." Chem Commun (Camb) **48**(42): 5115-5117.

Hosea, N. A., et al. (2000). "Elucidation of distinct ligand binding sites for cytochrome P450 3A4." Biochemistry **39**(20): 5929-5939.

Hoshi, Y., et al. (2013). "Quantitative Atlas of Blood Brain Barrier Transporters, Receptors, and Tight Junction Proteins in Rats and Common Marmoset." Journal of Pharmaceutical Sciences **102**(9): 3343-3355.

Houston, J. B. (1994). "Utility of in vitro drug metabolism data in predicting in vivo metabolic clearance." Biochem Pharmacol **47**(9): 1469-1479.

Howard, A. D., et al. (2001). "Orphan G-protein-coupled receptors and natural ligand discovery." Trends in Pharmacological Sciences **22**(3): 132-140.

Hsu, M.-H., et al. (2017). "The Crystal Structure of Cytochrome P450 4B1 (CYP4B1) Monooxygenase Complexed with Octane Discloses Several Structural Adaptations for  $\omega$ -Hydroxylation." The Journal of biological chemistry **292**(13): 5610-5621.

Hsu, M. H., et al. (2007). "Human cytochrome p450 family 4 enzymes: function, genetic variation and regulation." Drug Metab Rev **39**(2-3): 515-538.

Hughes, C. G., et al. (2012). "Sedation in the intensive care setting." Clin Pharmacol **4**: 53-63.

Hutzler, J. M., et al. (2001). "Dapsone activation of CYP2C9-mediated metabolism: evidence for activation of multiple substrates and a two-site model." Drug Metab Dispos **29**(7): 1029-1034.

Hutzler, J. M., et al. (2002). "Activation of CYP2C9-mediated metabolism by a series of dapsone analogs: kinetics and structural requirements." Drug Metab Dispos **30**(11): 1194-1200.

Ignatov, A., et al. (2006). "RANTES stimulates Ca<sup>2+</sup> mobilization and inositol trisphosphate (IP<sub>3</sub>) formation in cells transfected with G protein-coupled receptor 75." Br J Pharmacol **149**(5): 490-497.

Iordanova, B., et al. (2017). "Alterations in Cerebral Blood Flow after Resuscitation from Cardiac Arrest." Front Pediatr **5**: 174.

Ito, O., et al. (1998). "Localization of cytochrome P-450 4A isoforms along the rat nephron." Am J Physiol **274**(2): F395-404.

Janicka, M., et al. (2020). "Predicting the Blood-Brain Barrier Permeability of New Drug-Like Compounds via HPLC with Various Stationary Phases." Molecules **25**(3).

Jarrar, B. Y., et al. (2019). "Molecular Functionality of Cytochrome P450 4 (CYP4) Genetic Polymorphisms and Their Clinical Implications." International Journal of Molecular Sciences **20**(17).

Jennings, G. K., et al. (2018). "Noncovalent interactions dominate dynamic heme distortion in cytochrome P450 4B1." The Journal of biological chemistry **293**(29): 11433-11446.

Jia, L., et al. (2007). "The conduct of drug metabolism studies considered good practice (II): in vitro experiments." Curr Drug Metab **8**(8): 822-829.

Jin, Y., et al. (2011). "CYP4F Enzymes Are Responsible for the Elimination of Fingolimod (FTY720), a Novel Treatment of Relapsing Multiple Sclerosis." Drug Metabolism and Disposition **39**(2): 191.

Joyce, M. G., et al. (2004). "A Single Mutation in Cytochrome P450 BM3 Induces the Conformational Rearrangement Seen upon Substrate Binding in the Wild-type Enzyme." Journal of Biological Chemistry **279**(22): 23287-23293.

Kakuda, W., et al. (2008). "Optimal definition for PWI/DWI mismatch in acute ischemic stroke patients." J Cereb Blood Flow Metab **28**(5): 887-891.

Kalsotra, A., et al. (2002). "Sexual Dimorphism and Tissue Specificity in the Expression of CYP4F Forms in Sprague Dawley Rats." Drug Metabolism and Disposition **30**(9): 1022.

Kalsotra, A., et al. (2002). "Sexual dimorphism and tissue specificity in the expression of CYP4F forms in Sprague Dawley rats." Drug Metab Dispos **30**(9): 1022-1028.

Kalsotra, A., et al. (2006). "Cytochrome P450 4F subfamily: At the crossroads of eicosanoid and drug metabolism." Pharmacology & Therapeutics **112**(3): 589-611.

Kausar, K., et al. (1991). "Inhibitors of cytochrome P-450 attenuate the myogenic response of dog renal arcuate arteries." Circ Res **68**(4): 1154-1163.

Kawakami, H., et al. (2011). "Simultaneous Absolute Quantification of 11 Cytochrome P450 Isoforms in Human Liver Microsomes by Liquid Chromatography Tandem Mass Spectrometry with In Silico Target Peptide Selection." Journal of Pharmaceutical Sciences **100**(1): 341-352.

Kehl, F., et al. (2002). "20-HETE contributes to the acute fall in cerebral blood flow after subarachnoid hemorrhage in the rat." American Journal of Physiology-Heart and Circulatory Physiology **282**(4): H1556-H1565.

Kehl, F., et al. (2002). "20-HETE contributes to the acute fall in cerebral blood flow after subarachnoid hemorrhage in the rat." Am J Physiol Heart Circ Physiol **282**(4): H1556-1565.

Kernan Walter, N., et al. (2014). "Guidelines for the Prevention of Stroke in Patients With Stroke and Transient Ischemic Attack." Stroke **45**(7): 2160-2236.

Khatri, R., et al. (2012). "Blood–brain barrier, reperfusion injury, and hemorrhagic transformation in acute ischemic stroke." Neurology **79**(13 Supplement 1): S52.

Knowles, J., et al. (2003). "A guide to drug discovery: Target selection in drug discovery." Nat Rev Drug Discov **2**(1): 63-69.

Korzekwa, K. R., et al. (1998). "Evaluation of Atypical Cytochrome P450 Kinetics with Two-Substrate Models: Evidence That Multiple Substrates Can Simultaneously Bind to Cytochrome P450 Active Sites." Biochemistry **37**(12): 4137-4147.

Krupinski, J., et al. (1994). "Role of angiogenesis in patients with cerebral ischemic stroke." Stroke **25**(9): 1794-1798.

Lasker, J. M., et al. (2000). "Formation of 20-hydroxyeicosatetraenoic acid, a vasoactive and natriuretic eicosanoid, in human kidney. Role of Cyp4F2 and Cyp4A11." J Biol Chem **275**(6): 4118-4126.

LeBrun, L. A., et al. (2002). "Autocatalytic Mechanism and Consequences of Covalent Heme Attachment in the Cytochrome P4504A Family." Journal of Biological Chemistry **277**(15): 12755-12761.

Lee, C.-Y. J., et al. (2008). "Different Patterns of Oxidized Lipid Products in Plasma and Urine of Dengue Fever, Stroke, and Parkinson's Disease Patients: Cautions in the Use of Biomarkers of Oxidative Stress." Antioxidants & Redox Signaling **11**(3): 407-420.

Lee, J. K., et al. (2011). "Cerebral blood flow and cerebrovascular autoregulation in a swine model of pediatric cardiac arrest and hypothermia." Crit Care Med **39**(10): 2337-2345.

Lee, J. Y., et al. (2014). "Fluoxetine inhibits transient global ischemia-induced hippocampal neuronal death and memory impairment by preventing blood–brain barrier disruption." Neuropharmacology **79**: 161-171.

Lee, S. K., et al. (1989). "Effect of cardiac arrest time on cortical cerebral blood flow during subsequent standard external cardiopulmonary resuscitation in rabbits." Resuscitation **17**(2): 105-117.

Li, C. S. W., et al. (2020). "Population pharmacokinetic modeling of PF-06439535 (a bevacizumab biosimilar) and reference bevacizumab (Avastin®) in patients with advanced non-squamous non-small cell lung cancer." Cancer Chemotherapy and Pharmacology **85**(3): 487-499.

Li, G., et al. (2015). "High-Throughput Cytochrome P450 Cocktail Inhibition Assay for Assessing Drug-Drug and Drug-Botanical Interactions." Drug metabolism and disposition: the biological fate of chemicals **43**(11): 1670-1678.

Li, J., et al. (2018). "Computational Insight Into Vitamin K(1)  $\omega$ -Hydroxylation by Cytochrome P450 4F2." Frontiers in pharmacology **9**: 1065-1065.

Li, L. (2019). Alteration of Cerebral Blood Flow after Neurovascular injury Unpublished Doctoral dissertation, Doctor of Philosophy, University of Pittsburgh, Pittsburgh, PA University of Pittsburgh

Li, L., et al. (2019). "Cerebral microcirculatory alterations and the no-reflow phenomenon in vivo after experimental pediatric cardiac arrest." J Cereb Blood Flow Metab **39**(5): 913-925.

Lin, T. H., et al. (1987). "Effects of albumin and alpha 1-acid glycoprotein on the transport of imipramine and desipramine through the blood-brain barrier in rats." Chem Pharm Bull (Tokyo) **35**(1): 294-301.

Liu, B., et al. "The novel chemokine receptor, G-protein-coupled receptor 75, is expressed by islets and is coupled to stimulation of insulin secretion and improved glucose homeostasis." (1432-0428 (Electronic)).

Liu, L.-Y., et al. (2015). "A sensitive and high-throughput LC-MS/MS method for inhibition assay of seven major cytochrome P450s in human liver microsomes using an in vitro cocktail of probe substrates." Biomedical Chromatography **29**(3): 437-444.

Liu, X., et al. (2014). "Rational Use of Plasma Protein and Tissue Binding Data in Drug Design." Journal of Medicinal Chemistry **57**(20): 8238-8248.

Liu, Y., et al. (2019). "Astrocytic cytochrome P450 4A/20-hydroxyeicosatetraenoic acid contributes to angiogenesis in the experimental ischemic stroke." Brain Res **1708**: 160-170.

Liu, Y., et al. (2014). "The protective effect of HET0016 on brain edema and blood-brain barrier dysfunction after cerebral ischemia/reperfusion." Brain Res **1544**: 45-53.

Lombardo, F., et al. (2013). "Comprehensive assessment of human pharmacokinetic prediction based on in vivo animal pharmacokinetic data, part 2: clearance." J Clin Pharmacol **53**(2): 178-191.

Lonardo, N. W., et al. (2014). "Propofol is associated with favorable outcomes compared with benzodiazepines in ventilated intensive care unit patients." Am J Respir Crit Care Med **189**(11): 1383-1394.

Loscher, W., et al. (2005). "Drug resistance in brain diseases and the role of drug efflux transporters." Nat Rev Neurosci **6**(8): 591-602.

Lu, L., et al. (2018). "20-HETE Inhibition by HET0016 Decreases the Blood–Brain Barrier Permeability and Brain Edema After Traumatic Brain Injury." **10**(207).

Lynch, T., et al. (2007). "The effect of cytochrome P450 metabolism on drug response, interactions, and adverse effects." Am Fam Physician **76**(3): 391-396.

Macdonald, R. L. (2014). "Delayed neurological deterioration after subarachnoid haemorrhage." Nat Rev Neurol **10**(1): 44-58.

Macdonald, R. L., et al. (2012). "Randomized trial of clazosentan in patients with aneurysmal subarachnoid hemorrhage undergoing endovascular coiling." Stroke **43**(6): 1463-1469.

Macdonald, R. L., et al. (1991). "A review of hemoglobin and the pathogenesis of cerebral vasospasm." Stroke **22**(8): 971-982.

Maier, K. G., et al. (2000). "Fluorescent HPLC assay for 20-HETE and other P-450 metabolites of arachidonic acid." Am J Physiol Heart Circ Physiol **279**(2): H863-871.

Manole, M. D., et al. (2009). "Magnetic resonance imaging assessment of regional cerebral blood flow after asphyxial cardiac arrest in immature rats." J Cereb Blood Flow Metab **29**(1): 197-205.

Marsh, B., et al. (1991). "Pharmacokinetic model driven infusion of propofol in children." Br J Anaesth **67**(1): 41-48.

Martignoni, M., et al. (2006). "Species differences between mouse, rat, dog, monkey and human CYP-mediated drug metabolism, inhibition and induction." Expert Opinion on Drug Metabolism & Toxicology **2**(6): 875-894.

Marumo, T., et al. (2010). "The inhibitor of 20-HETE synthesis, TS-011, improves cerebral microcirculatory autoregulation impaired by middle cerebral artery occlusion in mice." British Journal of Pharmacology **161**(6): 1391-1402.

Marumo, T., et al. (2010). "The inhibitor of 20-HETE synthesis, TS-011, improves cerebral microcirculatory autoregulation impaired by middle cerebral artery occlusion in mice." Br J Pharmacol **161**(6): 1391-1402.

Masica, A. L., et al. (2007). "Clinical sedation scores as indicators of sedative and analgesic drug exposure in intensive care unit patients." Am J Geriatr Pharmacother **5**(3): 218-231.

Masica, A. L., et al. (2007). "Clinical sedation scores as indicators of sedative and analgesic drug exposure in intensive care unit patients." The American Journal of Geriatric Pharmacotherapy **5**(3): 218-231.

Matthew Hutzler, J., et al. (2003). "Activation of cytochrome P450 2C9-mediated metabolism: mechanistic evidence in support of kinetic observations." Archives of Biochemistry and Biophysics **410**(1): 16-24.

Meanwell, N. A. (2016). "Improving Drug Design: An Update on Recent Applications of Efficiency Metrics, Strategies for Replacing Problematic Elements, and Compounds in Nontraditional Drug Space." Chemical Research in Toxicology **29**(4): 564-616.

Michaels, S., et al. (2014). "The Revised Human Liver Cytochrome P450 "Pie": Absolute Protein Quantification of CYP4F and CYP3A Enzymes Using Targeted Quantitative Proteomics." Drug Metabolism and Disposition **42**(8): 1241.

Miller, T. M., et al. (2009). "Rapid, simultaneous quantitation of mono and dioxygenated metabolites of arachidonic acid in human CSF and rat brain." J Chromatogr B Analyt Technol Biomed Life Sci **877**(31): 3991-4000.

Miyata, N., et al. (2005). "Beneficial Effects of a New 20-Hydroxyeicosatetraenoic Acid Synthesis Inhibitor, TS-011 [N-(3-Chloro-4-morpholin-4-yl) Phenyl-N'-hydroxyimido Formamide], on Hemorrhagic and Ischemic Stroke." Journal of Pharmacology and Experimental Therapeutics **314**(1): 77.

Miyata, N., et al. (2005). "Beneficial Effects of a New 20-Hydroxyeicosatetraenoic Acid Synthesis Inhibitor, TS-011 [N-(3-Chloro-4-morpholin-4-yl) Phenyl-N'-hydroxyimido Formamide], on Hemorrhagic and Ischemic Stroke." Journal of Pharmacology and Experimental Therapeutics **314**(1): 77.

Miyata, N., et al. (2001). "HET0016, a potent and selective inhibitor of 20-HETE synthesizing enzyme." British Journal of Pharmacology **133**(3): 325-329.

Mohs, R. C., et al. (2017). "Drug discovery and development: Role of basic biological research." Alzheimers Dement (N Y) **3**(4): 651-657.

Moncada, S., et al. (1979). "The role of prostacyclin in vascular tissue." Fed Proc **38**(1): 66-71.

Mongardon, N., et al. (2011). "Postcardiac arrest syndrome: from immediate resuscitation to long-term outcome." Ann Intensive Care **1**(1): 45.

Moore, L. E., et al. (1994). Role of Oxygen Free Radicals and Lipid Peroxidation in Cerebral Reperfusion Injury. Advances in Pharmacology. Z. J. Bosnjak and J. P. Kampine, Academic Press. **31**: 565-576.

Morofuji, Y., et al. (2020). "Drug Development for Central Nervous System Diseases Using In vitro Blood-brain Barrier Models and Drug Repositioning." Curr Pharm Des **26**(13): 1466-1485.

Mu, Y., et al. (2008). "Intravenous formulation of N-hydroxy-N'-(4-n-butyl-2-methylphenyl)formamidine (HET0016) for inhibition of rat brain 20-hydroxyeicosatetraenoic acid formation." Drug metabolism and disposition: the biological fate of chemicals **36**(11): 2324-2330.

Nakamura, T., et al. (2004). "Design and synthesis of 1-(4-benzoylphenyl)imidazole derivatives as new potent 20-HETE synthase inhibitors." Bioorganic & Medicinal Chemistry Letters **14**(21): 5305-5308.

Nakamura, T., et al. (2004). "Pyrazole derivatives as new potent and selective 20-hydroxy-5,8,11,14-eicosatetraenoic acid synthase inhibitors." Bioorganic & Medicinal Chemistry **12**(23): 6209-6219.

Nakamura, T., et al. (2004). "Imidazole derivatives as new potent and selective 20-HETE synthase inhibitors." Bioorganic & Medicinal Chemistry Letters **14**(2): 333-336.

Nakamura, T., et al. (2003). "Pyrazole and Isoxazole Derivatives as New, Potent, and Selective 20-Hydroxy-5,8,11,14-eicosatetraenoic Acid Synthase Inhibitors." Journal of Medicinal Chemistry **46**(25): 5416-5427.

Neumann, J. T., et al. (2013). "Global cerebral ischemia: synaptic and cognitive dysfunction." Curr Drug Targets **14**(1): 20-35.

Ng Felix, C., et al. (2018). "Persistently Elevated Microvascular Resistance Postrevascularization." Stroke **49**(10): 2512-2515.

Nguyen, X., et al. (1999). "Kinetic profile of the rat CYP4A isoforms: arachidonic acid metabolism and isoform-specific inhibitors." Am J Physiol **276**(6): R1691-1700.

Nolan, J. P., et al. (2008). "Post-cardiac arrest syndrome: epidemiology, pathophysiology, treatment, and prognostication. A Scientific Statement from the International Liaison Committee on Resuscitation; the American Heart Association Emergency Cardiovascular Care Committee; the Council on Cardiovascular Surgery and Anesthesia; the Council on Cardiopulmonary, Perioperative, and Critical Care; the Council on Clinical Cardiology; the Council on Stroke." Resuscitation **79**(3): 350-379.

Obach, R. S. (1997). "Nonspecific Binding to Microsomes: Impact on Scale-Up of <em>in Vitro</em> Intrinsic Clearance to Hepatic Clearance as Assessed Through Examination of Warfarin, Imipramine, and Propranolol." Drug Metabolism and Disposition **25**(12): 1359.

Obach, R. S. (2011). "Predicting clearance in humans from in vitro data." Curr Top Med Chem **11**(4): 334-339.

Ohkuma, H., et al. (2000). "Impact of Cerebral Microcirculatory Changes on Cerebral Blood Flow During Cerebral Vasospasm After Aneurysmal Subarachnoid Hemorrhage." Stroke **31**(7): 1621-1627.

Oliw, E. H., et al. (1981). "Arachidonic acid metabolism in rabbit renal cortex. Formation of two novel dihydroxyeicosatrienoic acids." Journal of Biological Chemistry **256**(19): 9924-9931.

Olsen, T. S., et al. (1981). "Focal cerebral hyperemia in acute stroke. Incidence, pathophysiology and clinical significance." Stroke **12**(5): 598-607.

Omura, T., et al. (2006). "Effect of a new inhibitor of the synthesis of 20-HETE on cerebral ischemia reperfusion injury." Stroke **37**(5): 1307-1313.

Ortiz de Montellano, P. R., et al. (1981). "Autocatalytic alkylation of the cytochrome P-450 prosthetic haem group by 1-aminobenzotriazole. Isolation of an NN-bridged benzyne-protoporphyrin IX adduct." The Biochemical journal **195**(3): 761-764.

Otite, F., et al. (2014). "Impaired cerebral autoregulation is associated with vasospasm and delayed cerebral ischemia in subarachnoid hemorrhage." Stroke **45**(3): 677-682.

Pajouhesh, H., et al. (2005). "Medicinal chemical properties of successful central nervous system drugs." NeuroRx : the journal of the American Society for Experimental NeuroTherapeutics **2**(4): 541-553.

Pan, J., et al. (2007). "Reperfusion injury following cerebral ischemia: pathophysiology, MR imaging, and potential therapies." Neuroradiology **49**(2): 93-102.

Park, J. H., et al. (2018). "Population pharmacokinetic analysis of propofol in underweight patients under general anaesthesia." British Journal of Anaesthesia **121**(3): 559-566.

Perkins, G. D., et al. (2015). "Part 3: Adult basic life support and automated external defibrillation: 2015 International Consensus on Cardiopulmonary Resuscitation and Emergency Cardiovascular Care Science with Treatment Recommendations." Resuscitation **95**: e43-69.

Pickard, J. D., et al. (1989). "Effect of oral nimodipine on cerebral infarction and outcome after subarachnoid haemorrhage: British aneurysm nimodipine trial." BMJ **298**(6674): 636-642.

Pisani, M. A., et al. (2009). "Benzodiazepine and opioid use and the duration of intensive care unit delirium in an older population." Critical care medicine **37**(1): 177-183.

Plummer, G. F. (1987). "Improved method for the determination of propofol in blood by high-performance liquid chromatography with fluorescence detection." Journal of Chromatography B: Biomedical Sciences and Applications **421**: 171-176.

Pluta, R. M., et al. (2009). "Cerebral vasospasm following subarachnoid hemorrhage: time for a new world of thought." Neurol Res **31**(2): 151-158.

Poloyac, S. M., et al. (2020). "Pharmacological Optimization for Successful Traumatic Brain Injury Drug Development." J Neurotrauma **37**(22): 2435-2444.

Poloyac, S. M., et al. (2004). "The effect of isoniazid on CYP2E1- and CYP4A-mediated hydroxylation of arachidonic acid in the rat liver and kidney." Drug Metab Dispos **32**(7): 727-733.

Poloyac, S. M., et al. (2006). "Protective effect of the 20-HETE inhibitor HET0016 on brain damage after temporary focal ischemia." J Cereb Blood Flow Metab **26**(12): 1551-1561.

Poulin, P., et al. (2013). "Toward a new paradigm for the efficient in vitro–in vivo extrapolation of metabolic clearance in humans from hepatocyte data." Journal of Pharmaceutical Sciences **102**(9): 3239-3251.

Powell, P. K., et al. (1998). "Metabolism of arachidonic acid to 20-hydroxy-5,8,11, 14-eicosatetraenoic acid by P450 enzymes in human liver: involvement of CYP4F2 and CYP4A11." J Pharmacol Exp Ther **285**(3): 1327-1336.

Preiss, B., et al. (1964). "Omega-Oxidation of Long Chain Fatty Acids in Rat Liver." J Biol Chem **239**: 85-88.

Puscas, I., et al. (2019). "IVIVC Assessment of Two Mouse Brain Endothelial Cell Models for Drug Screening." Pharmaceutics **11**(11).

Quartino, A. L., et al. (2016). "Population pharmacokinetic and exposure-response analysis for trastuzumab administered using a subcutaneous "manual syringe" injection or intravenously in women with HER2-positive early breast cancer." Cancer Chemother Pharmacol **77**(1): 77-88.

Ramadan, E., et al. (2014). "Transient postnatal fluoxetine leads to decreased brain arachidonic acid metabolism and cytochrome P450 4A in adult mice." Prostaglandins Leukot Essent Fatty Acids **90**(5): 191-197.

Rankovic, Z. (2015). "CNS drug design: balancing physicochemical properties for optimal brain exposure." J Med Chem **58**(6): 2584-2608.

Reade, M. C., et al. (2014). "Sedation and delirium in the intensive care unit." N Engl J Med **370**(5): 444-454.

Reed, M. D. (1999). "Optimal sampling theory: An overview of its application to pharmacokinetic studies in infants and children." Pediatrics **104**(3 Pt 2): 627-632.

Rehncrona, S., et al. (1981). "Brain Lactic Acidosis and Ischemic Cell Damage: 1. Biochemistry and Neurophysiology." Journal of Cerebral Blood Flow & Metabolism **1**(3): 297-311.

Reichel, A. (2009). "Addressing central nervous system (CNS) penetration in drug discovery: basics and implications of the evolving new concept." Chem Biodivers **6**(11): 2030-2049.

Renic, M., et al. (2009). "Effect of 20-HETE inhibition on infarct volume and cerebral blood flow after transient middle cerebral artery occlusion." J Cereb Blood Flow Metab **29**(3): 629-639.

Renic, M., et al. (2012). "Protective effect of 20-HETE inhibition in a model of oxygen-glucose deprivation in hippocampal slice cultures." Am J Physiol Heart Circ Physiol **302**(6): H1285-1293.



Ricciotti, E., et al. (2011). "Prostaglandins and inflammation." Arterioscler Thromb Vasc Biol **31**(5): 986-1000.

Rifkind, A. B., et al. (1995). "Arachidonic acid metabolism by human cytochrome P450s 2C8, 2C9, 2E1, and 1A2: regioselective oxygenation and evidence for a role for CYP2C enzymes in arachidonic acid epoxidation in human liver microsomes." Arch Biochem Biophys **320**(2): 380-389.

Riley, R. J., et al. (2005). "A unified model for predicting human hepatic, metabolic clearance from in vitro intrinsic clearance data in hepatocytes and microsomes." Drug Metab Dispos **33**(9): 1304-1311.

Robbins, K. C. (1968). "In vitro enzymic omega oxidation of medium-chain fatty acids in mammalian tissue." Arch Biochem Biophys **123**(3): 531-538.

Roman, R. J. (2002). "P-450 Metabolites of Arachidonic Acid in the Control of Cardiovascular Function." Physiological Reviews **82**(1): 131-185.

Roman, R. J., et al. (2006). "Evidence that 20-HETE contributes to the development of acute and delayed cerebral vasospasm." Neurological Research **28**(7): 738-749.

Rubanyi, G. M. (1991). "Endothelium-derived relaxing and contracting factors." J Cell Biochem **46**(1): 27-36.

Sahinovic, M. M., et al. (2018). "Clinical Pharmacokinetics and Pharmacodynamics of Propofol." Clin Pharmacokinet **57**(12): 1539-1558.

Sato, M., et al. (2001). "Discovery of a N'-hydroxyphenylformamidine derivative HET0016 as a potent and selective 20-HETE synthase inhibitor." Bioorganic & Medicinal Chemistry Letters **11**(23): 2993-2995.

Savas, U., et al. (2016). "20-Hydroxyeicosatetraenoic Acid (HETE)-dependent Hypertension in Human Cytochrome P450 (CYP) 4A11 Transgenic Mice: NORMALIZATION OF BLOOD PRESSURE BY SODIUM RESTRICTION, HYDROCHLOROTHIAZIDE, OR BLOCKADE OF THE TYPE 1 ANGIOTENSIN II RECEPTOR." J Biol Chem **291**(32): 16904-16919.

Savas, Ü., et al. "20-Hydroxyeicosatetraenoic Acid (HETE)-dependent Hypertension in Human Cytochrome P450 (CYP) 4A11 Transgenic Mice: NORMALIZATION OF BLOOD PRESSURE BY SODIUM RESTRICTION, HYDROCHLOROTHIAZIDE, OR BLOCKADE OF THE TYPE 1 ANGIOTENSIN II RECEPTOR." (1083-351X (Electronic)).

Savic, R. M., et al. (2009). "Importance of shrinkage in empirical bayes estimates for diagnostics: problems and solutions." AAPS J **11**(3): 558-569.

Scheps, D., et al. (2013). "Synthesis of omega-hydroxy dodecanoic acid based on an engineered CYP153A fusion construct." Microb Biotechnol **6**(6): 694-707.

Schnider, T. W., et al. (1998). "The influence of method of administration and covariates on the pharmacokinetics of propofol in adult volunteers." Anesthesiology **88**(5): 1170-1182.

Schubert, G. A., et al. (2008). "Clazosentan, an endothelin receptor antagonist, prevents early hypoperfusion during the acute phase of massive experimental subarachnoid hemorrhage: a laser Doppler flowmetry study in rats." J Neurosurg **109**(6): 1134-1140.

Schubert, G. A., et al. (2011). "Hypoperfusion in the acute phase of subarachnoid hemorrhage." Acta Neurochir Suppl **110**(Pt 1): 35-38.

Schuttler, J., et al. (2000). "Population pharmacokinetics of propofol: a multicenter study." Anesthesiology **92**(3): 727-738.

Schüttler, J., et al. (1985). "Pharmacokinetic and pharmacodynamic modelling of propofol ('Diprivan') in volunteers and surgical patients." Postgrad Med J **61 Suppl 3**: 53-54.

Sedláková, L., et al. (2018). "20-Hydroxyeicosatetraenoic acid antagonist attenuates the development of malignant hypertension and reverses it once established: a study in Cyp11a1-Ren-2 transgenic rats." Bioscience Reports **38**(5).

Sehba, F. A., et al. (1999). "Effects of S-nitrosoglutathione on acute vasoconstriction and glutamate release after subarachnoid hemorrhage." Stroke **30**(9): 1955-1961.

Sehba, F. A., et al. (2007). "Acute cerebral vascular injury after subarachnoid hemorrhage and its prevention by administration of a nitric oxide donor." J Neurosurg **106**(2): 321-329.

Sehba, F. A., et al. (2000). "Acute decrease in cerebral nitric oxide levels after subarachnoid hemorrhage." J Cereb Blood Flow Metab **20**(3): 604-611.

Seki, T., et al. (2005). "Cytochrome P450 4A Isoform Inhibitory Profile of N-hydroxy-N'-(4-butyl-2-methylphenyl)-formamidine (HET0016) a Selective Inhibitor of 20-HETE Synthesis." Biological and Pharmaceutical Bulletin **28**(9): 1651-1654.

Sessler, C. N., et al. (2008). "Patient-focused sedation and analgesia in the ICU." Chest **133**(2): 552-565.

Seyhan, A. A. (2019). "Lost in translation: the valley of death across preclinical and clinical divide – identification of problems and overcoming obstacles." Translational Medicine Communications **4**(1): 18.

Shafer, A., et al. (1988). "Pharmacokinetics and Pharmacodynamics of Propofol Infusions during General Anesthesia." Anesthesiology **69**(3): 348-356.

Shaik, J. S., et al. (2015). "20-Hydroxyeicosatetraenoic Acid Inhibition by HET0016 Offers Neuroprotection, Decreases Edema, and Increases Cortical Cerebral Blood Flow in a Pediatric Asphyxial Cardiac Arrest Model in Rats." J Cereb Blood Flow Metab **35**(11): 1757-1763.

Shaik, J. S. B., et al. (2014). "Rapid and simultaneous quantitation of prostanoids by UPLC–MS/MS in rat brain." Journal of Chromatography B **945-946**: 207-216.

Shak, S., et al. (1985). "Leukotriene B<sub>4</sub> omega-hydroxylase in human polymorphonuclear leukocytes. Suicidal inactivation by acetylenic fatty acids." J Biol Chem **260**(24): 13023-13028.

Shekhar, S., et al. (2019). "Conflicting Roles of 20-HETE in Hypertension and Stroke." Int J Mol Sci **20**(18).

Sheweita, S. A. (2000). "Drug-metabolizing enzymes: mechanisms and functions." Curr Drug Metab **1**(2): 107-132.

Silver, I. A., et al. (1992). "Ion Homeostasis in Rat Brain in vivo: Intra- and Extracellular [Ca<sup>2+</sup>] and [H<sup>+</sup>] in the Hippocampus during Recovery from Short-Term, Transient Ischemia." Journal of Cerebral Blood Flow & Metabolism **12**(5): 759-772.

Smith, B. P., et al. (2000). "Confidence interval criteria for assessment of dose proportionality." Pharm Res **17**(10): 1278-1283.

Smuszkiewicz, P., et al. (2016). "The pharmacokinetics of propofol in ICU patients undergoing long-term sedation." Biopharmaceutics & Drug Disposition **37**(8): 456-466.

Spaggiari, D., et al. (2014). "A cocktail approach for assessing the in vitro activity of human cytochrome P450s: an overview of current methodologies." J Pharm Biomed Anal **101**: 221-237.

Stec, D. E., et al. (2007). "Functional polymorphism in human CYP4F2 decreases 20-HETE production." Physiol Genomics **30**(1): 74-81.

Sterz, F., et al. (1992). "Multifocal cerebral blood flow by Xe-CT and global cerebral metabolism after prolonged cardiac arrest in dogs. Reperfusion with open-chest CPR or cardiopulmonary bypass." Resuscitation **24**(1): 27-47.

Sun, C.-W., et al. (1998). "Nitric Oxide-20-Hydroxyeicosatetraenoic Acid Interaction in the Regulation of K<sup>+</sup> Channel Activity and Vascular Tone in Renal Arterioles." Circulation Research **83**(11): 1069-1079.

Sun, Q., et al. (2011). "1-Aminobenzotriazole, a Known Cytochrome P450 Inhibitor, Is a Substrate and Inhibitor of <em>N</em>-Acetyltransferase." Drug Metabolism and Disposition **39**(9): 1674.

Sundgreen, C., et al. (2001). "Autoregulation of cerebral blood flow in patients resuscitated from cardiac arrest." Stroke **32**(1): 128-132.

Sundseth, S. S., et al. (1992). "Sex-dependent expression and clofibrate inducibility of cytochrome P450 4A fatty acid omega-hydroxylases. Male specificity of liver and kidney CYP4A2 mRNA and tissue-specific regulation by growth hormone and testosterone." J Biol Chem **267**(6): 3915-3921.

Sundt, T. M., Jr., et al. (1971). "Cerebral ischemia and reactive hyperemia. Studies of cortical blood flow and microcirculation before, during, and after temporary occlusion of middle cerebral artery of squirrel monkeys." Circ Res **28**(4): 426-433.

Sylvie Retout, F. M. (n.d.). "Sparse sampling design in design in population PK/PD population PK/PD studies." Retrieved March, 25, 2021, from [https://www.ema.europa.eu/en/documents/presentation/presentation-sparse-sampling-design-population-pharmacokinetic/pharmacodynamic-studies\\_en.pdf](https://www.ema.europa.eu/en/documents/presentation/presentation-sparse-sampling-design-population-pharmacokinetic/pharmacodynamic-studies_en.pdf).

Syvanen, S., et al. (2009). "Species differences in blood-brain barrier transport of three positron emission tomography radioligands with emphasis on P-glycoprotein transport." Drug Metab Dispos **37**(3): 635-643.

Takeuchi, K., et al. (2005). "Reversal of delayed vasospasm by an inhibitor of the synthesis of 20-HETE." Am J Physiol Heart Circ Physiol **289**(5): H2203-2211.

Tanaka, Y., et al. (2007). "Continuous inhibition of 20-HETE synthesis by TS-011 improves neurological and functional outcomes after transient focal cerebral ischemia in rats." Neurosci Res **59**(4): 475-480.

Tang, C. (2016). Unpublished Master's thesis, University of Pittsburgh, Pittsburgh, PA, USA.

Tang, Z., et al. (2010). "Human cytochrome P450 4F11: heterologous expression in bacteria, purification, and characterization of catalytic function." Arch Biochem Biophys **494**(1): 86-93.

Tarttelin, E. E., et al. (1999). "Cloning and Characterization of a Novel Orphan G-Protein-Coupled Receptor Localized to Human Chromosome 2p16." Biochemical and Biophysical Research Communications **260**(1): 174-180.

Tchertanov, L. (1999). "Structural metrics relationships in covalently bonded organic azides." Acta Crystallogr B **55**(Pt 5): 807-809.

The Human Protein Atlas. Retrieved Jan 13, 2021, from <https://www.proteinatlas.org/>.

The, N. t.-P. A. S. S. G. n. (1997). "Intracerebral Hemorrhage After Intravenous t-PA Therapy for Ischemic Stroke." Stroke **28**(11): 2109-2118.

Topjian Alexis, A., et al. (2019). "Pediatric Post-Cardiac Arrest Care: A Scientific Statement From the American Heart Association." Circulation **140**(6): e194-e233.

Tornio, A., et al. (2019). "Clinical Studies on Drug-Drug Interactions Involving Metabolism and Transport: Methodology, Pitfalls, and Interpretation." Clinical pharmacology and therapeutics **105**(6): 1345-1361.

Uniprot. Retrieved Jan 14, 2021, from <https://www.uniprot.org/uniprot/D3ZJX6>.

Vajkoczy, P., et al. (2005). "Clazosentan (AXV-034343), a selective endothelin A receptor antagonist, in the prevention of cerebral vasospasm following severe aneurysmal subarachnoid

hemorrhage: results of a randomized, double-blind, placebo-controlled, multicenter phase IIa study." J Neurosurg **103**(1): 9-17.

van den Brule, J. M. D., et al. (2017). "Middle cerebral artery flow, the critical closing pressure, and the optimal mean arterial pressure in comatose cardiac arrest survivors—An observational study." Resuscitation **110**: 85-89.

Veber, D. F., et al. (2002). "Molecular Properties That Influence the Oral Bioavailability of Drug Candidates." Journal of Medicinal Chemistry **45**(12): 2615-2623.

Verkade P.E., E. M., van der Lee J., DeWolff H.H., Verkade-Sandbergen A., van der Sande D. (1933). "Untersuchungen uber der Fett Stoffwechsel. ." Z. Phys. Chem. **215**: 225–257.

Virani, S. S., et al. (2020). "Heart Disease and Stroke Statistics-2020 Update: A Report From the American Heart Association." Circulation **141**(9): e139-e596.

Wakabayashi, K., et al. (1961). "Studies in vitro on the mechanisms of omega-oxidation of fatty acids." Biochim Biophys Acta **48**: 615-617.

Walker, D. K. (2004). "The use of pharmacokinetic and pharmacodynamic data in the assessment of drug safety in early drug development." British journal of clinical pharmacology **58**(6): 601-608.

Wanat, K. (2020). "Biological barriers, and the influence of protein binding on the passage of drugs across them." Molecular Biology Reports **47**(4): 3221-3231.

Wang, M. H., et al. (1998). "Cytochrome P450-derived arachidonic acid metabolism in the rat kidney: characterization of selective inhibitors." J Pharmacol Exp Ther **284**(3): 966-973.

Ward, N. C., et al. (2011). "Cytochrome P450 metabolites of arachidonic acid are elevated in stroke patients compared with healthy controls." Clin Sci (Lond) **121**(11): 501-507.

Waring, M. J., et al. (2015). "An analysis of the attrition of drug candidates from four major pharmaceutical companies." Nat Rev Drug Discov **14**(7): 475-486.

Williams, J. M., et al. (2010). "20-hydroxyeicosatetraenoic acid: a new target for the treatment of hypertension." Journal of cardiovascular pharmacology **56**(4): 336-344.

Wu Jason, H. Y., et al. (2009). "Inhibition of 20-Hydroxyeicosatetraenoic Acid Synthesis Using Specific Plant Lignans." Hypertension **54**(5): 1151-1158.

Wu, J. H., et al. "Inhibition of 20-hydroxyeicosatetraenoic acid synthesis using specific plant lignans: in vitro and human studies." (1524-4563 (Electronic)).

Xiang, J., et al. (2016). "Mechanisms Underlying Astrocyte Endfeet Swelling in Stroke." Acta Neurochir Suppl **121**: 19-22.

Xu, F., et al. (2004). "Catalytic Activity and Isoform-Specific Inhibition of Rat Cytochrome P450 4F Enzymes." Journal of Pharmacology and Experimental Therapeutics **308**(3): 887.

Xu, F., et al. (2002). "Antihypertensive effect of mechanism-based inhibition of renal arachidonic acid omega-hydroxylase activity." Am J Physiol Regul Integr Comp Physiol **283**(3): R710-720.

Xu, X., et al. (2011). "The roles of CYP450 epoxygenases and metabolites, epoxyeicosatrienoic acids, in cardiovascular and malignant diseases." Adv Drug Deliv Rev **63**(8): 597-609.

Xu, Y., et al. (2005). "Expression of CYP4A isoforms in developing rat placental tissue and rat trophoblastic cell models." Placenta **26**(2): 218-225.

Xu, Y., et al. (2009). "Faster recovery of cerebral perfusion in SOD1-overexpressed rats after cardiac arrest and resuscitation." Stroke **40**(7): 2512-2518.

Xu, Y., et al. (2017). "CYP4Z1 – A Human Cytochrome P450 Enzyme that Might Hold the Key to Curing Breast Cancer." Current Pharmaceutical Design **23**(14): 2060-2064.

Yamashita, S., et al. (2010). "Population pharmacokinetics of a propofol bolus administered in patients with major burns." Burns **36**(8): 1215-1221.

Yang, X. M., et al. (2018). "In vivo observation of cerebral microcirculation after experimental subarachnoid hemorrhage in mice." Neural Regen Res **13**(3): 456-462.

Yang, Z.-J., et al. (2012). "Attenuation of neonatal ischemic brain damage using a 20-HETE synthesis inhibitor." Journal of neurochemistry **121**(1): 168-179.

Yang, Z. J., et al. (2012). "Attenuation of neonatal ischemic brain damage using a 20-HETE synthesis inhibitor." J Neurochem **121**(1): 168-179.

Yi, K., et al. (2019). "Tissue Plasminogen Activator for Cortical Embolism Stroke with Magnetic Resonance Perfusion Imaging: A Report of Two Cases." Case Rep Neurol **11**(2): 222-229.

Yi, M., et al. (2017). "Functional characterization of a common CYP4F11 genetic variant and identification of functionally defective CYP4F11 variants in erythromycin metabolism and 20-HETE synthesis." Arch Biochem Biophys **620**: 43-51.

Yi, X., et al. (2016). "20-Hydroxyeicosatetraenoic Acid as a Predictor of Neurological Deterioration in Acute Minor Ischemic Stroke." Stroke **47**(12): 3045-3047.

Yuan, Z. X., et al. "Transient postnatal fluoxetine decreases brain concentrations of 20-HETE and 15-epi-LXA4, arachidonic acid metabolites in adult mice." (1532-2823 (Electronic)).

Yuan, Z. X., et al. (2015). "Transient postnatal fluoxetine decreases brain concentrations of 20-HETE and 15-epi-LXA4, arachidonic acid metabolites in adult mice." Prostaglandins Leukot Essent Fatty Acids **101**: 9-14.

Zaal, I. J., et al. (2015). "Benzodiazepine-associated delirium in critically ill adults." Intensive Care Med **41**(12): 2130-2137.

Zanger, U. M., et al. (2013). "Cytochrome P450 enzymes in drug metabolism: regulation of gene expression, enzyme activities, and impact of genetic variation." Pharmacol Ther **138**(1): 103-141.

Zeldin, D. C., et al. (1996). "Biochemical characterization of the human liver cytochrome P450 arachidonic acid epoxygenase pathway." Arch Biochem Biophys **330**(1): 87-96.

Zhang, H., et al. (2017). "Upregulation of 20-HETE Synthetic Cytochrome P450 Isoforms by Oxygen-Glucose Deprivation in Cortical Neurons." Cell Mol Neurobiol **37**(7): 1279-1286.

Zhang Rui, L., et al. (2008). "Synergistic Effect of an Endothelin Type A Receptor Antagonist, S-0139, With rtPA on the Neuroprotection After Embolic Stroke." Stroke **39**(10): 2830-2836.

Zhu, J., et al. (2015). "Additive Neuroprotection of a 20-HETE Inhibitor with Delayed Therapeutic Hypothermia after Hypoxia-Ischemia in Neonatal Piglets." Dev Neurosci **37**(4-5): 376-389.

Zou, A. P., et al. (1994). "Effects of 17-octadecynoic acid, a suicide-substrate inhibitor of cytochrome P450 fatty acid omega-hydroxylase, on renal function in rats." J Pharmacol Exp Ther **268**(1): 474-481.